HEAT TREATMENT, STRUCTURE-PROPERTY, STRESS CORROSION CRACKING AND ACOUSTIC EMISSION STUDIES ON 300M STEEL

Ramaswamy Padmanabhan
B.Sc., University of Madras, Madras, India, 1972
B.E., Indian Institute of Science, Bangalore, India, 1975

A dissertation submitted to the faculty
of the Oregon Graduate Center
in partial fulfillment of the
requirements for the degree
Doctor of Philosophy
in
Materials Science

March, 1982

The dissertation "Heat Treatment, Structure-Property, Stress Corrosion Cracking and Acoustic Emission Studies on 300M Steel" by Ramaswamy Padmanabhan has been examined and approved by the following Examination Committee:

William E. Wood, Thesis Advisor
Professor

Jack H. Devletian
Associate Professor

Nicholas G. Eror
Associate Professor

James J. Huntzicker
Associate Professor

DEDICATION

This work is dedicated to

AMMA
&
APPA

ACKNOWLEDGEMENT

I thank Prof. W. E. Wood for his guidance and support throughout this work. I also thank Drs. J. H. Devletian, N. G. Eror and J. J. Huntzicker for agreeing to examine my thesis. I am indebted to Drs. C. N. Sastry, D. K. Dedhia, K. H. Khan and V. C. Kannan for the many invaluable discussions I had with them. I also appreciate deeply the help provided by R. Turpin, M. Sprinker, M. Scholl, U. Balachandran, R. Gudimetla and S. Shankar during some phases of this work. Special thanks are due to Ms. C. Rathbun for her excellent typing and proofreading of the thesis manuscript, Ms. B. Ryall for the nice drawings and Ms. N. Suriyayothin for her assistance in experimental work, acoustic emission modelling and computer programming.

TABLE OF CONTENTS

LIST OF TABLES

LIST OF FIGURES

Page

Page

Page

Page

Page

Page

ABSTRACT

Heat Treatment, Structure-Property, Stress Corrosion Cracking and Acoustic Emission Studies on 300M Steel

Ramaswamy Padmanabhan, Ph.D.
Oregon Graduate Center, 1982

Supervising Professor: William E. Wood

Strength, ductility, impact toughness and plane strain fracture toughness of quenched and tempered 300M steel were studied as functions of grain size, martensite substructure, carbide type and dispersion, amounts of retained austenite and segregation. These microstructural variables were introduced by utilizing different austenitization temperatures and by thermal cycling between austenite and martensite phases. The results of these structure-property relationships were applied to design modified heat treatment processes to improve all the properties simultaneously. A critical carbide dispersion was achieved by controlling intermediate temper and reaustenitization steps. Grain size refinement, reduction in twin density and segregation, increased amounts of retained austenite and preferential formation of lath martensite, together with critical carbide dispersion were established to be the major factors in the improvement of properties.

Stress corrosion cracking behavior of 300M steel was also studied and acoustic emission testing was employed to predict threshold stress intensities and to monitor crack velocities. Threshold stress intensities were dependent chiefly upon the prior austenite grain size and amounts of retained austenite and segregation. The crack velocities were influenced by interparticle spacing, as well as, the prior austenite grain size. A model was proposed to explain the observed behavior in terms of a critical segregation concentration criterion. An energy approach was utilized to explain the dependence of acoustic emission responses upon applied stress intensity, prior austenite grain size and crack velocities.

1. INTRODUCTION

Ultrahigh strength low alloy steels are increasingly used in many applications, where, hitherto, more expensive alloy steels have been used. However, their usefulness in many instances is limited by their modest toughness at high strength levels. Detailed research has been carried out to improve the toughness of these steels, without compromising strength, through heat treating processes, which alter the basic microstructure. This approach is attractive, since it eliminates the need for expensive alloy additions. Among others, high temperature, step and cyclic heat treatments have been exhaustively studied in recent years for these steels with varying degrees of success. However, there is still a great need to understand the underlying principles involved in these heat treatments and the exact ways in which they affect the microstructure. Besides the study of these relationships between heat treatment processes and the resultant microstructure, the effects of the different microstructural parameters upon the mechanical properties have also to be thoroughly established. This investigation provides a basis for developing new alloys and new heat treatments for obtaining optimum mechanical properties.

High strength steels, which are highly susceptible to stress corrosion cracking failure, are commonly exposed to aggressive or even mild environments, which act as sources of hydrogen. Before a potential heat treatment is accepted, its effect upon the stress corrosion cracking characteristics should be understood. Although many heat treatments, like the high temperature heat treatment, have been designed for specifically increasing the fracture toughness at high strength levels of ultrahigh strength low alloy steels, few investigators have attempted to evaluate the effect of these heat treatments on the stress corrosion cracking behavior of the steel. In this investigation, these studies are attempted for not only the standard heat treatments, but also for new heat treatments, developed during the course of this work.

Many theories have been proposed to understand the phenomenon of stress corrosion cracking in high strength steels. Although these theories explain the mechanisms adequately on a macroscopic level, each one of them has limitations, due mostly to inadequacies in following the crack propagation on an atomistic level. The advent of acoustic emission in recent years has provided metallurgists with a new tool to monitor defects within a material and has been utilized in this investigation to study stress corrosion cracking in 300M steel.

1. INTRODUCTION

Ultrahigh strength low alloy steels are increasingly used in many applications, where, hitherto, more expensive alloy steels have been used. However, their usefulness in many instances is limited by their modest toughness at high strength levels. Detailed research has been carried out to improve the toughness of these steels, without compromising strength, through heat treating processes, which alter the basic microstructure. This approach is attractive, since it eliminates the need for expensive alloy additions. Among others, high temperature, step and cyclic heat treatments have been exhaustively studied in recent years for these steels with varying degrees of success. However, there is still a great need to understand the underlying principles involved in these heat treatments and the exact ways in which they affect the microstructure. Besides the study of these relationships between heat treatment processes and the resultant microstructure, the effects of the different microstructural parameters upon the mechanical properties have also to be thoroughly established. This investigation provides a basis for developing new alloys and new heat treatments for obtaining optimum mechanical properties.

High strength steels, which are highly susceptible to stress corrosion cracking failure, are commonly exposed to aggressive or even mild environments, which act as sources of hydrogen. Before a potential heat treatment is accepted, its effect upon the stress corrosion cracking characteristics should be understood. Although many heat treatments, like the high temperature heat treatment, have been designed for specifically increasing the fracture toughness at high strength levels of ultra-high strength low alloy steels, few investigators have attempted to evaluate the effect of these heat treatments on the stress corrosion cracking behavior of the steel. In this investigation, these studies are attempted for not only the standard heat treatments, but also for new heat treatments, developed during the course of this work.

Many theories have been proposed to understand the phenomenon of stress corrosion cracking in high strength steels. Although these theories explain the mechanisms adequately on a macroscopic level, each one of them has limitations, due mostly to inadequacies in following the crack propagation on an atomistic level. The advent of acoustic emission in recent years has provided metallurgists with a new tool to monitor defects within a material and has been utilized in this investigation to study stress corrosion cracking in 300M steel.

2. BACKGROUND

2.1. Heat Treatment, Microstructure and Mechanical Properties

Ultrahigh strength low alloy steels possess yield strength exceeding 1350 MNm^{-2}, making them extremely attractive for many applications for which, more expensive alloy steels are conventionally used. However, these low alloy steels offer only modest fracture toughness at such high strengths and whenever a combination of high strength and toughness is required, it is still not possible to replace high alloy steels with these less expensive steels. Achieving a good combination of strength and toughness in these steels is a constant challenge. Alloy modifications of base composition is one expensive way to realize this goal. A second, more attractive way, would be through suitable heat treatment processes which alter the basic microstructure in such a way as to offer the best combination of strength and toughness for a given composition. Several investigators have attempted such studies, wherein the conventional heat treatment process was altered to produce the desired microstructure.

The conventional heat treatment involves austenitizing the low alloy steel at about 850°C for usually 1 hour, to achieve maximum homogeneity and subsequently quenching at a high enough rate to transform the austenite to martensite, followed by tempering at a suitable temperature. By utilizing higher austenitization temperatures, many investigators [1-22] were able to achieve substantial improvement in the plane strain fracture toughness while maintaining yield and ultimate tensile strength at essentially the same levels. However, these investigators observed a dramatic decrease in tensile ductility. Most of them also observed a drop in impact toughness [3,4,6,12,13,20-22], and this was attributed to microstructural variations. These are discussed in Section 5. The major structural changes that were noted by higher austenitization treatments were:

1. coarsening of the prior austenite grain size [1-22],
2. reduction in the amount of twinned plate martensite and a concurrent increase in the amount of dislocated lath martensite [4,7,17,19],
3. increase in the amount of retained austenite, usually present in the form of interlath films [3-5,9,10,19],
4. reduction in the amount of segregation of impurity and alloying elements to the prior austenite grain boundaries [1,2,5,54,66] and
5. reduction in the amount of second phases at the prior austenite grain boundaries [1,3,5,8,14].

Although the above changes have generally been reported by many investigators, there is no complete agreement among these investigators. Some investigators claim, for instance, that no changes were observed with respect to twin density [16,60], amount of retained austenite [16,17, 20] and segregation [165] with increased austenitization temperatures. This investigation examines these claims and attempts to relate the observed changes in properties with the structural variations produced.

One variation of the high temperature heat treatment is the step heat treatment, which involves austenitizing the steel at high temperatures, followed by quenching to a lower temperature in the austenite phase and then quenching to transform the austenite to martensite. While this heat treatment reduced the problem of quench cracking that usually results in high temperature heat treatments (especially in thick sections where differential cooling rates exist), the fracture toughness dropped to an intermediate value, while tensile ductility, strength and impact toughness usually decreased to an even greater extent when compared with the conventional heat treatment [3,8,17-19]. The main structural changes between this and the direct high temperature heat treatment were the increased amounts of segregation to the prior austenite grain boundaries and an increase in the twin density [17-19]. Other variations of the basic conventional heat treatment have also been attempted, including isothermal holding prior to final quenching for different times at different temperatures in either the bainitic or the martensitic regions, but the reactions involved were difficult to control and the final product did not usually yield the high fracture toughness at strength levels similar to that of the conventional heat treatment, achieved through the high temperature heat treatment [18,19,28,253].

Rapid cyclic heat treatments between the austenite and the martensite phases produce ultrafine grains [24,46] and strength can be significantly improved. However, while this process increases the fracture toughness at similar or increased strength levels for certain steels like EN24, for 4340 and 300M steels, it improved only the yield strength while decreasing the fracture toughness [17,25,26].

Dispersion of particles in the austenite produces dislocation multiplication, during subsequent transformation of the austenite to martensite and enhances strength through dispersion strengthening [123-125]. While ausforming is one way to achieve this dispersion [122,273,274], the tempered martensite could alternatively be rapidly reaustenitized and requenched immediately to transform the austenite with undissolved carbides to martensite. This second approach improved the strength and ductility of some alloys but toughness did not improve significantly [124,125,275,276]. By reaustenitizing a lightly tempered martensite at low temperatures, grain refinement was achieved through the nucleating action of fine carbides, which subsequently dissolved and upon transformation to martensite, strength and impact toughness were improved in some low alloy steels [277-279]. In this investigation although isothermal heat treatments are not studied, step and cyclic heat treatments are examined. New heat treatment approaches are attempted to produce a dispersion strengthened, grain refined, lath martensitic structure that yields optimum mechanical properties.

Thus, while many heat treatments and processes have been studied, only limited success has been achieved in producing low alloy steels with high strength, ductility and toughness. While these various studies have provided valuable insight into the microstructural features that lead to better properties, there is no unified analysis of this subject. These are the main concerns of this investigation.

2.2. Stress Corrosion Cracking and Acoustic Emission

Stress corrosion cracking is particularly severe for high strength steels, which are extremely susceptible even under very mild environments with very low hydrogen content (less than a few parts per million). Although efforts to improve the general properties (like strength, toughness etc.) of these steels are not lacking, often the effects of such efforts upon stress corrosion characteristics are not studied. Especially in the case of 300M steel, little published work exists [17,27-31] and none examined the effects of high temperature and step heat treatments upon the crack growth behavior. Even among these limited studies, inconsistencies exist as to the actual values of threshold stress intensity and crack growth rate data. This investigation attempts to clear these inconsistencies, as well as providing the necessary data for those heat treatments not previously considered.

Many factors affect the stress corrosion cracking behavior of steels and these include the alloy strength level, applied stress intensity, microstructure (including the type, size, distribution and shape of carbides, dislocation density, twin density, amount of retained austenite, prior austenite grain size and segregation of impurity and alloying elements), steel composition, environment and temperature. Again, for 300M steel, little work has been carried out to analyze the effects of these various factors upon the stress corrosion cracking behavior. All these factors, including the relevant literature, are covered in Section 5.
In many cases even when reasonable data is available, there is some confusion as to the actual influence of these parameters upon the stress corrosion cracking behavior. As an example, some investigators reported an

increase in threshold stress intensity with an increase in prior austenite grain size [29,32,33], while others reported no grain size effect [17,26]. The influence of these various parameters upon stress corrosion cracking behavior are also studied in this investigation.

Several theories to explain hydrogen embrittlement have been put forth [229-233,236,237,239-242,282,286]. These can be broadly classified into:

1. the pressure-expansion theories [229-233], which postulate that large hydrogen pressures are generated within internal microcracks and voids and expand, causing coalescence of such cracks and voids,
2. the decohesion theories, which assume a critical hydrogen concentration above which the cohesive force between iron atoms at the crack tip is decreased and the crack advances, atom by atom [236,237,239-242] and
3. the adsorption theories, which propose that the surface free energy of an atomically clean metal is decreased by hydrogen adsorption, thus lowering the fracture stress [282,286].

None of these theories are adequate in explaining the observed behavior of UHSLA steels under hydrogen-containing environments. The pressure-expansion theories do not explain the observed cracking of high strength steels at atmospheric and low pressures [234,235]. The decohesion theories cannot account for the discontinuous crack propagation of these steels [32,238] and the adsorption theories are questionable from the standpoint of fracture strength of real materials, wherein the effect of surface energy on the total energy for fracture is negligible [97]. Hence, in this study, a new mechanism is proposed to explain the observed stress corrosion cracking behavior of high strength steels.

Since acoustic emissions are generated during transient changes in the local stress and strain fields within a material, the actual mechanism of stress corrosion cracking in high strength steels can be better understood by the use of acoustic emission techniques. When the stress corrosion crack propagates, a part of the elastic energy is released as a stress wave that can be detected by a transducer located on the surface of the specimen. Although several investigators have attempted to study stress corrosion cracking behavior of materials through acoustic emission monitoring, there are no established interpretative techniques [33,40, 254-267]. The analysis of the acoustic emission data is still in its infancy. In this study, acoustic emission methodology is used to better understand the stress corrosion cracking behavior and new interpretative techniques are presented to analyze the acoustic emission data.

2.3. Objectives of this Investigation

Briefly, the ultimate goal of this study is to obtain better properties in 300M steel through alterations in the basic microstructure, effected by new heat treatment processes. The starting point is the study of structure-property relationships, developed through several standard heat treatments. Subsequently, modified heat treatments are developed to achieve the necessary microstructural changes that yield the optimum properties in the steel. Although these modified heat treatments could be equally well or better applied to other medium or high alloy steels (or through additions of alloy elements to the base 300M steel), these studies are limited to commercially available vacuum arc remelted 300M steel. The impact of these heat treatments, as well as the standard heat treatments, upon the stress corrosion properties are also examined and the mechanisms of embrittlement are studied through acoustic emission monitoring.

3. EXPERIMENTAL PROCEDURE

3.1. Materials and Specimen Preparation

The alloy used in this investigation was 300M steel, a vacuum remelted silicon modified AISI 4340 steel, whose chemical composition is given in Table 3-1.

The steel was received in the form of 19 mm thick hot rolled plates and 12.7 mm drawn rods in a fully annealed condition. Tensile specimens were machined from the rods and compact tension (CT), Charpy V-notch (CVN) and double cantilever beam (DCB) specimens were all machined from the plate, in accordance with ASTM specifications, in L-T orientation, Figure 3-1. Dimensional details of the various specimens are shown in Figure 3-2. CT specimens were used for evaluation of plane strain fracture toughness, stress corrosion crack growth rates and acoustic emission studies. CVN specimens were used for evaluation of impact toughness (including fracture initiation and propagation energies), specimen deflection, dynamic fracture toughness and apparent yield strength and DCB specimens for threshold stress intensity evaluation.

3.2. Heat Treatment

Various austenitization and reaustenitization temperatures, both of which control the final microstructure obtained in the steel, various intermediate tempering temperatures and one final tempering temperature were used in this investigation and the exact heat treatment schedules are all listed in Table 3-2.

TABLE 3-1

CHEMICAL COMPOSITION OF 300M STEEL (WT.%)

C	Mn	Si	Cr	Ni	Mo	Cu	S	P	V	Fe
0.42	0.79	1.64	0.79	1.84	0.36	0.05	0.006	0.010	0.08	Rest

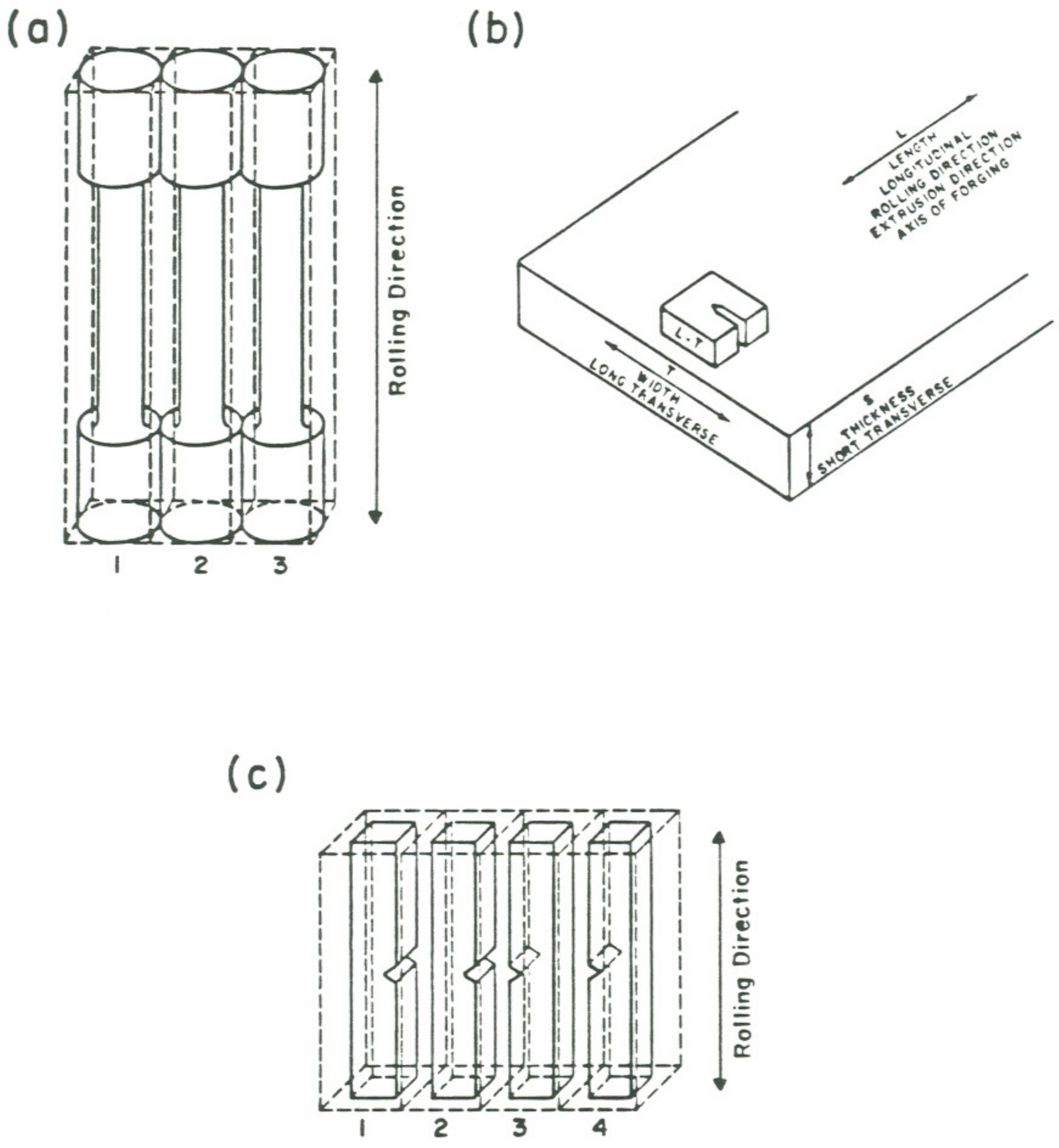

Figure 3-1: ORIENTATION DETAILS FOR
a) TENSILE,
b) CT AND DCB AND
c) CVN SPECIMENS.

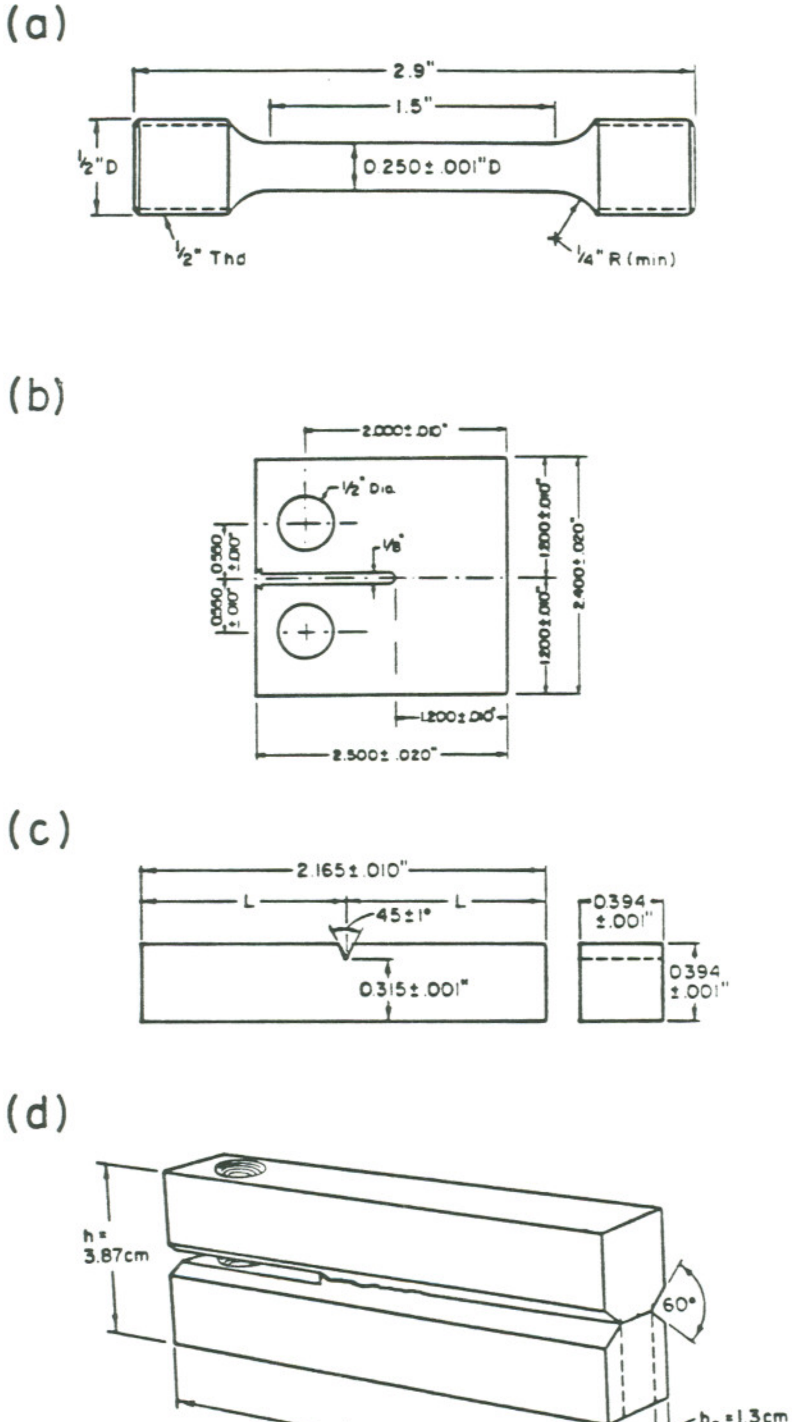

Figure 3-2: DIMENSIONAL DETAILS OF
a) TENSILE,
b) CT,
c) CVN AND
d) DCB SPECIMENS.

TABLE 3-2

HEAT TREATMENTS EMPLOYED

Code	Austenitization			Intermediate Temper			Reaustenitization			Final Temper		
	Temperature		Time	Temperature		Time	Temperature		Max.Time	Temperature		Time
	(°C)	(°F)	(min)	(°C)	(°F)	(min)	(°C)	(°F)	(min)	(°C)	(°F)	(min)
Conventional	870	1598	60	---	---	---	---	---	---	280	536	60
Cyclic	870	1598	60	---	---	---	850	1562	3	280	536	60
High Temperature	1200	2192	60	---	---	---	---	---	---	280	536	60
Step	1200→ 870	2192→ 1598	60→ 5	---	---	---	---	---	---	280	536	60
Modified Conventional	870	1598	60	650	1202	60	850	1562	3	280	536	60
Modified High Temperature	1200	2192	60	650	1202	60	850	1562	3	280	536	60
Modified Step	1200→ 870	2192→ 1598	60→ 5	650	1202	60	850	1562	3	280	536	60

All austenitizing heat treatments were carried out in controlled atmosphere (argon) "Mini Brute" Thermco vertical tube furnace, with a center 35.6 cm flat zone accuracy of ± 0.3°C. Intermediate and final tempering operations were carried out in a Thermodyne constant temperature salt bath furnace with an operating range of 175°C to 700°C and an accuracy of ± 0.3°C. A small salt bath furnace with a 45.7 cm long x 15.2 cm diameter pot, coupled to a Polytherm temperature controller, capable of maintaining temperature within ± 0.3°C, in a working range of 900°C to 1300°C was constructed to carry out reaustenitization operations. Dummy CT and tensile specimens with type K chromel-alumel thermocouple embedded in the core were used to monitor heating rates and times at reaustenitization temperature, whenever appropriate.

3.3. Mechanical Property Evaluation

3.3.1. Plane Strain Fracture Toughness Testing.

Room temperature plane strain fracture toughness of the steel, under various heat treated conditions, was evaluated in accordance with ASTM E 399-74 specifications. After machining of CT specimens, including the cutting of a crack starter notch, a 200 μm wide slot was further cut, after appropriate heat treatments, to act as a sharp notch during fatigue precracking. Fatigue precracking and fracture toughness testing were both carried out using a 10,000 kg capacity Instron Lawrence dynamic test system. Fatiguing was done at an R ratio of 0.5 with a mean load of 680 kgs and an alternating load of 340 kgs, and at 10 Hz or 20 Hz. In no case did the maximum stress intensity of the fatigue cycle exceed 60% of the K_{Ic} values and the minimum fatigue crack length was at least 1.27 mm, the total crack length being at least 22.9 mm. In order to evaluate the K_{Ic} values, a compliance calibration curve was generated (Figure 3-3). A computer program was used to carry out regression analysis and (a/W) vs (VBE/P) values were curve fitted using a polynomial of fourth degree, the actual expression being:

$$\frac{a}{W} = 0.15 + 8.71 \times 10^{-3} \left(\frac{VBE}{P}\right) - 5.71 \times 10^{-5} \left(\frac{VBE}{P}\right)^{2} + 1.84 \times 10^{-4} \left(\frac{VBE}{P}\right)^{3} - 2.26 \times 10^{-10} \left(\frac{VBE}{P}\right)^{4} \quad (3.1)$$

This curve was subsequently used to read off the a/W values for a given VBE/P and thereby, obtain the f(a/W) values in the Brown and Srawley [280] equation:

$$K_Q = (P_Q/BW^{1/2})f(a/W), \quad (3.2)$$

with $$f(a/W) = [29.6(a/W)^{1/2} - 185.5(a/W)^{3/2} + 655.2(a/W)^{5/2} - 1017.0(a/W)^{7/2} + 638.9(a/W)^{9/2}], \quad (3.3)$$

where K_Q equals conditional fracture toughness (equals K_{Ic}, the actual fracture toughness for a valid test), P_Q and P equal load, as determined in Section 9.1.1, E-399-74, B equals thickness of the specimen, W equals width of the specimen, a equals crack length and E equals the modulus of elasticity.

An Instron crack opening displacement gauge (COD), with a sensitivity of 250 μm/volt was used to monitor the crack length and the Instron machine was operated at a strain rate of 0.025 cm/min.

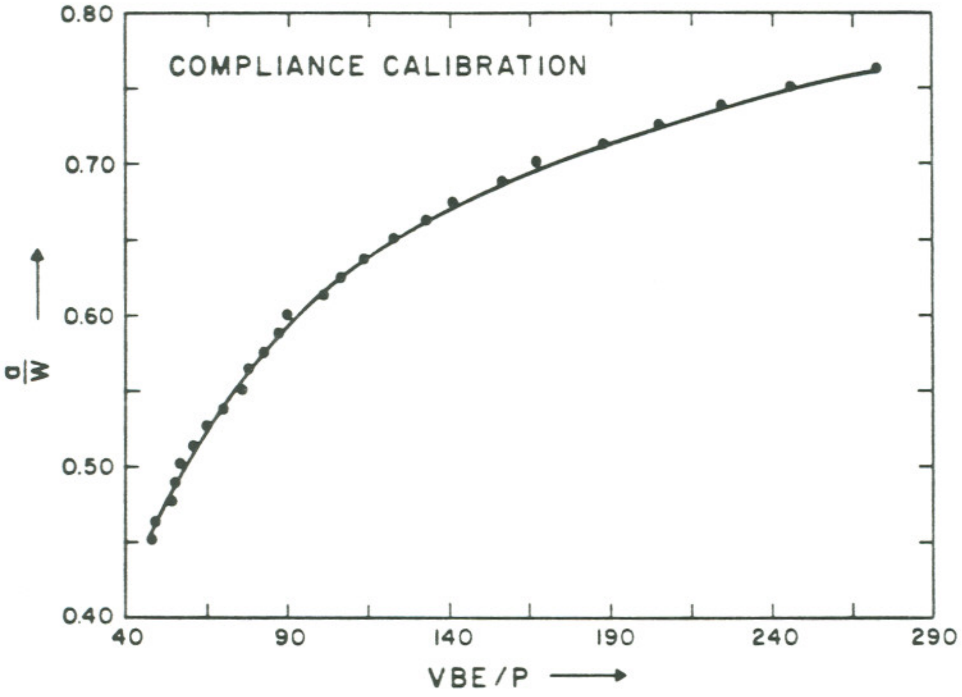

Figure 3-3: COMPLIANCE CALIBRATION CURVE.

3.3.2. Impact Toughness Testing. Room temperature longitudinal dynamic tests on ASTM Charpy V-notch specimens were done using a microprocessor based Instrumented Charpy impact machine with a 160 Nm capacity at Battelle Northwest Laboratories, Richland, Washington. On impact, the dynamic load on the specimen was measured through an electrical signal sent by the strain gauges on the tup of a Charpy hammer. The calibration method used to assure the reliability of load measurements is described in Appendix I.

Since load deflection data were also recorded, dynamic fracture toughness (K_{Id}) and apparent yield stress (σ_A) were also calculated, with K_{Id} given by the equation [280]:

$$K_{Id} = \frac{\left[1.5\ f\left(\frac{a}{W}\right) L\ P_m\ a^{1/2}\right]}{BW^2} \tag{3.4}$$

$$\text{with } f(a/W) = 1.93 - 3.07(a/W) + 14.53(a/W)^2 - 25.11(a/W)^3 + 25.8(a/W)^4 \quad , \tag{3.5}$$

where L equals length, W equals width, B equals thickness, a equals notch depth, and P_m equals applied load at fracture pop-in.

By substituting the appropriate values for the conventional Charpy V-notch specimen, the above equation reduces to:

$$K_{Id} = 38.7\ f(a/W)\ P_m\ a^{1/2} \tag{3.6}$$

In the Instrumented Charpy system, three more parameters, viz., specimen deflection and fracture initiation and fracture propagation energies were also obtained. The deflection at yield of the specimen is, as shown in Figure 3-4, obtained from the effective velocity (see Appendix I), V_{eff}, of the tup from the relationship, deflection $d = (V_{eff})t$, where t is the time taken for yielding the specimen.

The fracture initiation energy is the area (A_i) under the load deflection curve (see Figure 3-5) up to the maximum load, P_m, at fracture pop-in and the fracture propagation energy is the total area (A_t) under the load-deflection curve minus the area A_i. The total energy ($= A_i + A_t$) gives the Charpy impact energy.

3.3.3. Tensile Testing. Room temperature longitudinal tensile properties were determined using standard ASTM 6.35 mm diameter rods and pulling them in tension in the same 10,000 kg capacity Instron test system, used for fracture toughness evaluation. The strain rate applied was 0.025 cm/min and the strain was measured using a 2.54 cm gauge MTS extensometer. The yield strength (σ_{ys}) was read off from the load-strain curve at 0.2% total strain and the tensile strength, percent elongation and percent reduction in area were all evaluated according to standard procedures.

3.3.4. Stress Corrosion Cracking Testing.

3.3.4.1. Threshold Testing. Bolt loaded DCB specimens were used for the evaluation of threshold stress intensity values. 2.5 mm deep grooves were cut along the sides of these DCB specimens to prevent the crack from running out of the plane. After appropriate heat treatments, a 200 μm wide crack starter notch was cut and these DCB specimens were then loaded by tightening the bolts while monitoring the arm deflection accurately with a Gaertner cathetometer until a pre-selected

Figure 3-4: DEFLECTION AT YIELD OF CVN SPECIMEN.

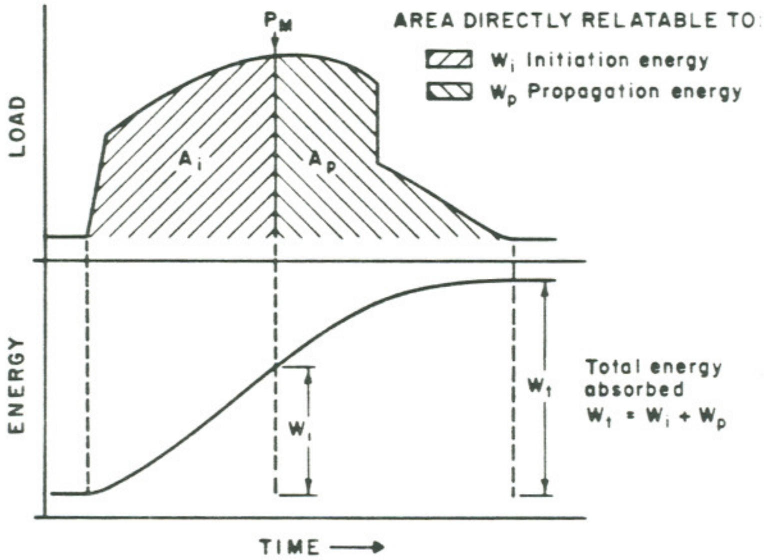

Figure 3-5: LOAD, ENERGY VS. TIME CURVES FOR CVN SPECIMEN.

deflection value was achieved. These were then immersed in a 3.5% aqueous solution of reagent grade sodium chloride and left under load for 100 hrs, after which they were broken open to measure the hydrogen assisted crack extension. For these specimens, for a fixed arm displacement, the stress intensity decreases as the crack grows, until at threshold stress intensity, the crack stops growing. From the arm deflection (v) and the crack length (a) data, the threshold stress intensity value $\left(K_{Iscc}\right)$ was calculated using the relationship [287]:

$$K_{Iscc} = \frac{vEh[3h(a + 0.6h)^2 + h^3]^{\frac{1}{2}}}{4[(a + 0.6h)^3 + h^2a]} \qquad (3.7)$$

where E equals modulus of elasticity and h equals half height of the DCB specimen.

These K_{Iscc} values were also crosschecked using CT specimens (with an acoustic emission detection system) kept immersed for 100 hrs in a 3.5% sodium chloride solution, under a load very near that corresponding to the K_{Iscc} values. A third method was also used, namely extrapolation of dc/de or dc/dt or de/dt or da/dt versus applied stress intensity curve, where c equals cumulative threshold counts, e equals cumulative events, t equals time interval and a equals crack length. This method is described in detail in Section 4.1.5. The K_{Iscc} values measured by these various methods were within $\pm$ 0.275 $MNm^{-3/2}$.

3.3.4.2. Crack Growth Testing. CT specimens conforming to ASTM E 399-74 specifications were used to study the crack growth rate as a function of stress intensity. After heat treating, a 200 μm wide slot was cut to act as a notch during fatigue precracking. A sharp crack was then introduced by fatiguing in the Instron test system, at 10 or 20 Hz, with a mean load of 680 kgs and an alternating load of 340 kgs (R ratio of 0.5) and decreasing these loads, while maintaining the R ratio constant, to minimize any residual stress effect. At each stage, the crack was allowed to grow through the plastic zone associated with the previous higher load. This procedure was necessary to obtain the crack growth rates at low stress intensity levels. The starting crack length (including the fatigue precrack) was at least 23 mm. These specimens were then immersed in a 3.5% sodium chloride solution and loaded to a predetermined stress intensity level. For this fixed load, the stress intensity increases as the crack propagates. Using an Instron crack opening displacement (COD) gauge, with a sensitivity of 250 μm/volt, the displacement was continuously monitored and plotted as a function of time. Through the compliance calibration data, the crack length, a, and the corresponding stress intensity, K_I, were then calculated for small increments of time. A Motorola microprocessor was used to record the displacement, time and the acoustic emission parameters, c (cumulative counts) and e (cumulative events), continuously onto a magtape. These data were then analyzed using a computer program which converts the digital values to real values and another program which calculates the crack length, a, the crack growth rate, da/dt, for da $\geq$ 125 μm, the average stress intensity, K_I, for every set of two successive a values, counts and counts rate dc/dt and dc/da, events and events rate de/dt and de/da, and counts per event dc/de data (Appendix II). Graphical plots of interest like da/dt or dc/de vs K_I were then generated using a third program.

3.4. Acoustic Emission Monitoring

A block diagram of the A.E. monitoring system is given in Figure 3-6. An AET model AC175L resonant frequency piezoelectric transducer was attached, using a viscous couplant (AET #SC4), to the CT specimen undergoing the stress corrosion test. After passing the transducer output through an AET model 160 filter with a bandpass range of 125-250 KHz to eliminate extraneous noise below 125 KHz, the signal was further amplified with a 60 dB preamplifier. This signal was then processed using AET model 201 signal processor (which can provide an addititonal gain of up to 40 dB) to record the cumulative threshold counts and AET model 203 amplitude distribution analyzer to record the cumulative events. Model 203 can also sort events according to their amplitude into 50 channels over a 60 dB dynamic range and the amplitude distribution can be obtained at any time during a test on a log or linear scale as a frequency or cumulative frequency histogram. In these tests, an actual gain of 70 dB was used, with the threshold stress intensity level set at 0.05 V which was slightly higher than the noise level of about 0.03 V. Cumulative counts and events were recorded as a function of time and crack length onto a magtape, and were further processed using the programs described earlier (Appendix II).

3.5. Structural Studies

3.5.1. Transmission Electron Microscopy.

Broken CT specimens were used to obtain thin foils for TEM study. 500 μm thick slices were cut from these specimens using a 0.79 mm abrasive cutoff wheel, while flooding with a coolant to avoid heating. These slices were then mechanically ground and polished to about 125 μm, followed by electropolishing to 50 μm.

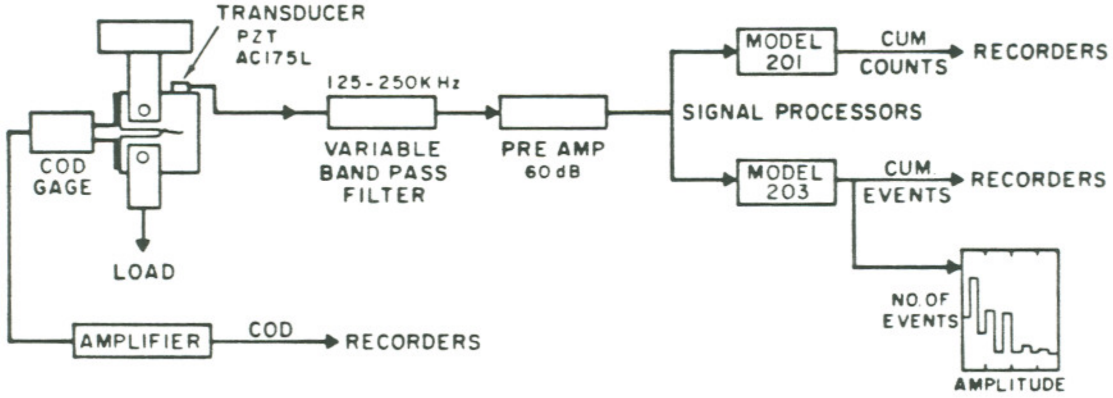

Figure 3-6: BLOCK DIAGRAM OF ACOUSTIC EMISSION TEST SYSTEM.

Discs of 3 mm diameter were then obtained from these 50 μm thick slices using a mechanical punch. Final jet polishing was done using a Fischione double jet polishing unit. For both window and jet polishing, the electrolyte used was 100 gms of chromic trioxide in 540 cc of glacial acetic acid and 28 cc of distilled water, under an applied voltage of 60 V for window polishing and 80 V for jet polishing at a current density of 0.5 to 0.6 amp/sq cm. By surrounding the electropolishing unit in an ice bath, the temperature of the electrolyte was maintained between 10°C to 15°C during polishing.

To identify the carbides in the steel, carbon extraction replication samples were prepared and examined in TEM. After successive grinding in 120, 240, 400 and 600 grits, followed by final polishing in selvyt cloths impregnated with 5 μm, 0.3 μm and 0.05 μm alumina particles suspended in water, the samples were etched in a 5% nital solution. Fine carbon particles were deposited onto these surfaces to a thickness of about 200 μm by the following method: Specimens were placed on glass slides and held flat using cellotape. They were then transferred to an evaporating unit, capable of reducing pressure up to 10^{-4} mm of Hg. Two carbon rods, one blunt and the other sharp (to give a point source) were placed just touching each other, about 25 cm above the sample and at a pressure of 10^{-4} mm of Hg, carbon was evaporated by resistance heating of the rods at the contact point to produce a film on the specimen surfaces. For judging the thickness of the film, a drop of diffusion pump oil was deposited onto a piece of clean white porcelain placed alongside the specimens. Carbon film does not form on the oil droplet itself, but the surrounding areas become deeply tinted as the film thickness increases. After about 3 to 4 seconds, when the tint becomes light gray, the carbon film will be about 200 Å thick. Squares of 2 mm side were scribed on these surfaces using a fine blade, followed by re-etching for a short time. The carbon films were then freed by electropolishing in 10% nitric acid in ethyl alcohol for 5 to 10 seconds, at a current density of 1.5 amps/sq cm under 10 V, followed by washing in ethanol and lowering in distilled water until freed. The floating pieces of carbon film were caught on perforated copper grids (75 x 300 mesh), which were previously washed in alcohol and thoroughly dried, and then examined in the TEM.

Both the thin foil specimens and extraction replica films were examined in a Hitachi HU-11B TEM under accelerating voltages of 75, 100 or 125 KV.

3.5.2. Scanning Electron Microscopy. All fracture surfaces, be they broken CT specimens, tensile specimens, Charpy specimens or stress corrosion cracking specimens, were coated with a protective clear plastic "Dem-Kote" spray to prevent them for oxidizing. Whenever ready for examination, the coating was dissolved in acetone and ultrasonically cleaned in petroleum ether.

For structural studies with SEM, polished and etched specimens (with a somewhat heavier etch than in the case of optical microscopy specimens) were used and these were examined under either direct contrast mode for topology studies or inverse contrast mode (to highlight structural features like carbides, lath and prior austenite grain boundaries).

All these specimens were examined in a JEOL (JSM-35) SEM under secondary electron accelerating voltages of 15 or 25 KV and at various magnifications.

3.5.3. Optical Microscopy. Specimens for optical microscopy work (cut from the central portion of CT specimens) were ground successively in 120, 280, 400 and 600 grits and then polished successively in selvyt cloths impregnated with 5 μm, 0.3 μm, and 0.05 μm size alumina particles suspended in water. These were then etched in a 5% picral and nital solution with a few drops of zephyron trichloride. The final polishing and etching steps were repeated 3 to 4 times. The microscope used was a Carl-Zeiss optical microscope. For determination of grain sizes, especially for fine grained structures, the specimens were embrittled by tempering at 650°C for 10 hours, followed by step cooling at the rate of 10°C/hr. The grain sizes were measured by Jeffrey's intercept method (ASTM spc. #E112-81).

3.5.4. X-Ray Analysis. Powders for x-ray diffraction were obtained by filing CT specimens. For carbide identification, the carbon films obtained by the extraction technique were used as such. The diffraction patterns were obtained using a 57.3 mm Debye-Scherrer camera on Siemens Kristalloflex-2 diffraction unit, using either Cr-K_α or Co-K_α radiation.

Elemental analysis was also done using the Ortec energy dispersive x-ray analysis unit attached to the JSM-35 SEM.

---

heat treatment these values increased marginally by 1.2% and 3.1%.

Impact toughness also decreased for the high temperature and step heat treatments, by 9.5 Nm and 14.8 Nm, respectively, whereas it increased by 3.4 Nm for the cyclic heat treatment. The fracture initiation (FIE) and the fracture propagation (FPE) energies, measured during

TABLE 4-1
TENSILE PROPERTIES

Heat Treatment	Specimen #	Yield Strength		Ultimate Tensile Strength		Elongation (%)	Reduction in Area (%)
		(Ksi)	(MNm^{-2})	(Ksi)	(MNm^{-2})		
Conventional	D189	234.7	1616.9	285.6	1967.5	11.3	39.8
	D190	235.9	1625.1	284.3	1958.5	10.8	39.2
	Mean	235.3	1621.0	285.0	1963.0	11.1	39.5
Cyclic	D139	260.1	1791.8	301.2	2075.0	13.0	43.4
	D140	252.7	1740.9	290.4	2000.6	11.5	41.8
	Mean	256.4	1766.4	295.8	2037.8	12.3	42.6
High Temperature	D187	241.0	1660.2	293.2	2019.9	6.4	12.4
	D188	239.8	1652.0	288.1	1984.7	5.1	10.9
	Mean	240.4	1656.1	290.7	2002.3	5.8	11.7
Step	D185	223.2	1537.6	269.0	1853.1	6.9	13.9
	D186	210.5	1450.1	258.8	1782.9	10.0	18.3
	Mean	216.9	1493.9	263.9	1818.0	8.5	16.1

TABLE 4-2.

FRACTURE TOUGHNESS AND IMPACT PROPERTIES

Heat Treatment	* Specimen #	Plane Strain Fracture Toughness		Fracture Initiation Energy		Fracture Propagation Energy		Charpy V-Notch Energy		Dynamic Fracture Toughness		Apparent Yield Strength		Deflection at Yield	
		(Ksi$\sqrt{in}$)	(MNm$^{-3/2}$)	(ft-lbs)	(Nm)	(ft-lbs)	(Nm)	(ft-lbs)	(Nm)	(Ksi$\sqrt{in}$)	(MNm$^{-3/2}$)	(Ksi)	(MNm^{-2})	(x10^{-3}in)	(x10^{-4}m)
Conventional	E5,E6	50.7	55.7	16.5	22.4	3.1	4.2	19.7	26.7	126.4	138.9	234.7	1616.9	42.0	10.7
	BC189,BC190	51.0	56.0	16.7	22.7	3.5	4.8	20.2	27.4	111.7	122.8	235.9	1625.1	42.0	10.7
	Mean	50.9	55.9	16.6	22.6	3.3	4.5	20.0	27.1	119.1	130.9	235.3	1621.0	42.0	10.7
Cyclic	E35,E36	50.6	55.6	16.7	22.7	6.1	8.3	22.8	30.9	136.8	150.3	229.9	1583.8	36.3	9.2
	BC158,BC160	46.0	50.6	18.2	24.7	3.4	4.6	21.7	29.4	172.5	189.6	304.6	2098.4	44.3	11.3
	Mean	48.3	53.1	17.5	23.7	4.8	6.5	22.5	30.2	154.7	170.0	267.3	1841.1	40.3	10.3
High Temperature	E11,E12	83.2	91.4	10.0	13.6	3.2	4.3	13.2	17.9	112.1	123.2	243.4	1676.8	32.5	8.3
	BC187,BC188	82.7	90.9	9.8	13.3	2.9	3.9	12.8	17.4	109.1	119.9	247.3	1703.7	32.5	8.3
	Mean	83.0	91.2	9.9	13.5	3.1	4.1	13.0	17.7	110.6	121.6	245.4	1690.3	32.5	8.3
Step	E18,E23	64.7	71.1	5.9	8.0	2.3	3.1	8.2	11.1	127.5	140.1	194.9	1342.7	26.9	6.8
	BC185,BC186	78.8	86.6	7.6	10.3	2.3	3.1	10.0	13.6	126.8	139.3	223.9	1542.5	29.4	7.5
	Mean	71.8	78.9	6.8	9.2	2.3	3.1	9.1	12.4	127.2	139.7	209.4	1442.6	28.2	7.9

*Code: E = Charpy V-notch Specimen
BC = Compact Tension Specimen

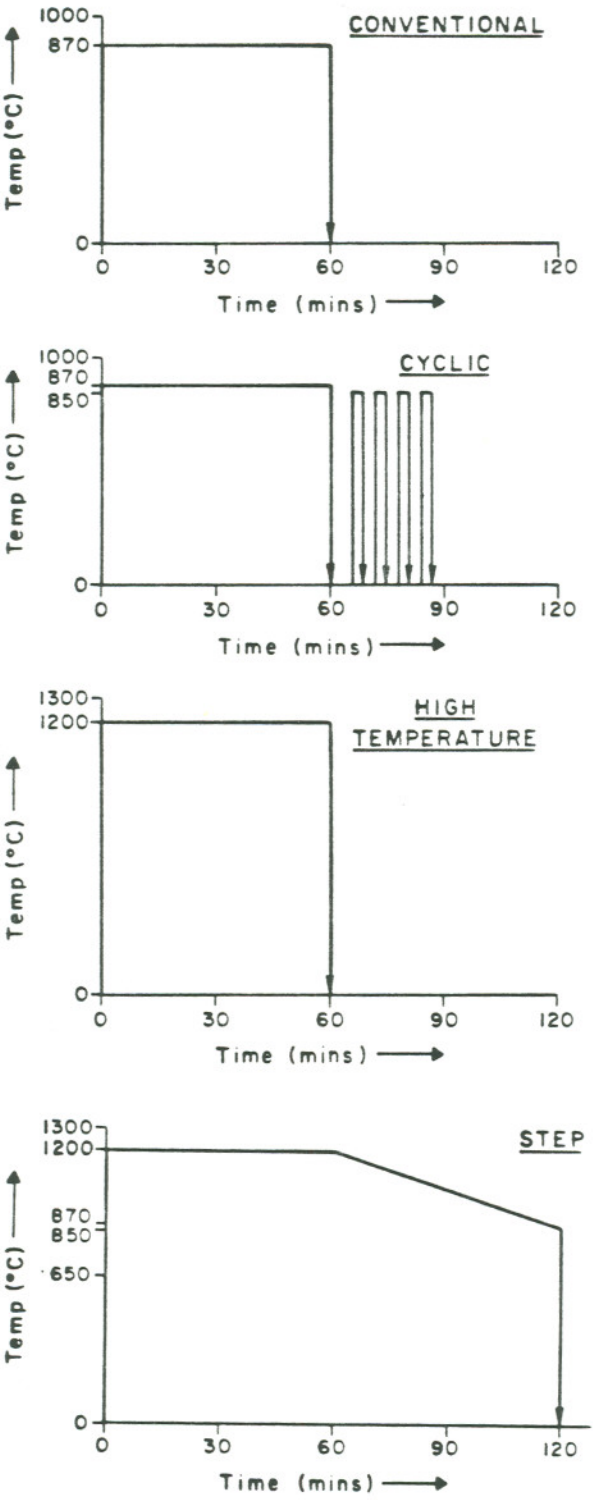

Figure 4-1: HEAT TREATMENT SCHEMATIC

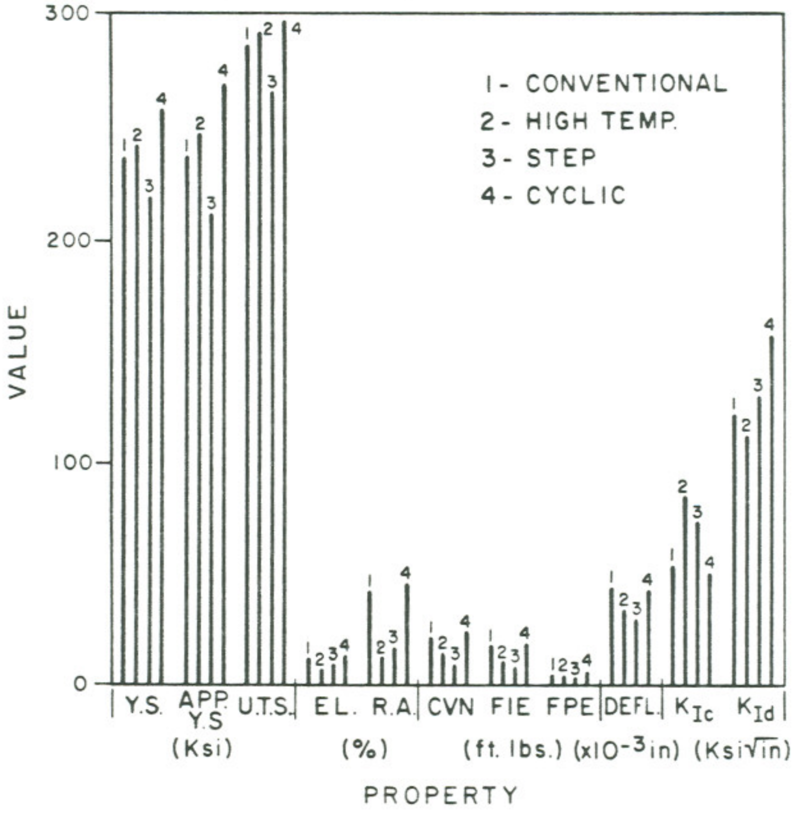

Figure 4-2: COMPARISON OF MECHANICAL PROPERTIES OF VARIOUS HEAT TREATMENTS.

instrumented impact testing were also slightly higher for the cyclic heat treatment, by 1.2 Nm and 2.0 Nm, respectively, when compared with the conventional heat treatment, but were significantly lower for the high temperature heat treatment, by 9.1 Nm and 0.27 Nm, respectively, and for the step heat treatment, by 13.3 Nm and 1.36 Nm, respectively. The maximum variation was thus noted in the FIE. Specimen deflection, also measured during impact testing, decreased by 0.241 mm and 0.352 mm for the high temperature and step heat treatments, respectively, while it decreased very marginally by 0.043 mm for the cyclic heat treatment. Thus, in general, the variation in the impact toughness, FIE, FPE and specimen deflection followed similar trends.

From the Charpy load vs. deflection curves, dynamic fracture toughness (K_{Id}) and apparent yield strength (σ_A) were also measured. For the high temperature heat treatment, K_{Id} decreased by 9.3 $MNm^{-3/2}$ but for step and cyclic heat treatments, it increased by 8.9 $MNm^{-3/2}$ and 39.1 $MNm^{-3/2}$, respectively. The apparent yield strength increased by 69.6 MNm^{-2} and 220.5 MNm^{-2} for the high temperature and cyclic heat treatments, respectively, while it decreased by 178.4 MNm^{-2} for the step heat treatment. Although the absolute values were not identical, the change in apparent yield strength was exactly similar to the change in actual yield strength for the various heat treatments. However, the change in K_{Id} did not always follow the trend of either K_{Ic} or CVN toughness.

Significant improvements in the fracture toughness of 300M and other UHSLA steels at similar yield strength levels but with reduced ductility, was also observed by other investigators [1-22]. Most of these investigators [3,4,6,12,13,20-22] noted a decrease in the impact toughness with an increase in the austenitization temperature. On the contrary, Datta [23] noted an increase in CVN energy with an increase in austenitization temperature but did not explain this behavior. However, in agreement with the present investigation, he noted identical trends for deflection, CVN energy and FIE. Thus, in general, the observed differences in toughness and tensile properties between the high temperature, step, and conventional heat treatments are consistent with the results obtained by other investigators. Cyclic heat treatment was shown to improve the strength of various steels by Grange [24]. This technique improved the toughness of EN24 steel at similar strength levels [25] but when extended to 4340 and 300M steels, improved only the strength while the fracture toughness decreased [17,26]. This is also consistent with the results obtained in this investigation for cyclic heat treatment.

4.1.2. Heat Treatment Standardization.

A new series of heat treatments was developed to achieve optimum mechanical properties. Initial standardization work was carried out to determine the optimum time and temperature for the intermediate tempering step and also for the reaustenitization step. The general heat treatment principle was the same in all cases, viz., austenitize the specimen at the desired solutioning temperature, quench in oil (agitated) to room temperature to transform the austenite to martensite, temper the martensite at the desired intermediate tempering temperature for specific time intervals, reaustenitize the specimen at the desired temperature for specific short time periods, quench the specimen again in agitated oil to room temperature and temper the martensite at the final tempering temperature and quench in water to room temperature (see Figure 4-3). Fracture toughness and tensile results are shown as functions of reaustenitization times for a constant 850°C reaustenitization temperature for three intermediate tempering temperatures, viz., 600°C, 650°C and 675°C, respectively, in Figures 4-4, 4-5, and 4-6. K_{Ic} and σ_{ys} values are also compared in Figure 4-7 for all three cases. In all cases, the intermediate tempering time was held constant at 1 hr, the initial austenitization temperature was chosen as 870°C (with a solutioning time of 1 hr) and the final tempering temperature and time were 280°C and 1 hr, respectively. A minimum reaustenization time of 3 min was necessary for the core of the CT (and DCB) specimen to achieve the reaustenitization temperature of 850°C. This was determined using a chromel-alumel thermocouple embedded in the core of a dummy CT specimen. Similarly, for the tensile specimens, the minimum reaustenitization time was determined to be 1 min. It is seen from Figures 4-4, 4-5, 4-6 and 4-7 that the best combination of properties was achieved in all the cases when the reaustenitization time was 3 min for the CT specimens, corresponding to 1 min for the tensile specimens. (Since the core of tensile specimens reaches 850°C 2 min earlier than the CT specimens, holding the CT specimens for 3 min at 850°C is equivalent to holding the tensile specimens for 1 min at 850°C and holding the CT specimens at 850°C for 10 min is equivalent to holding the tensile specimens at 850°C for 8 min and so on.) Hence, in these figures, the x-axis refers to the reaustenitization time for CT specimens and the tensile properties plotted against a particular x-value would refer in

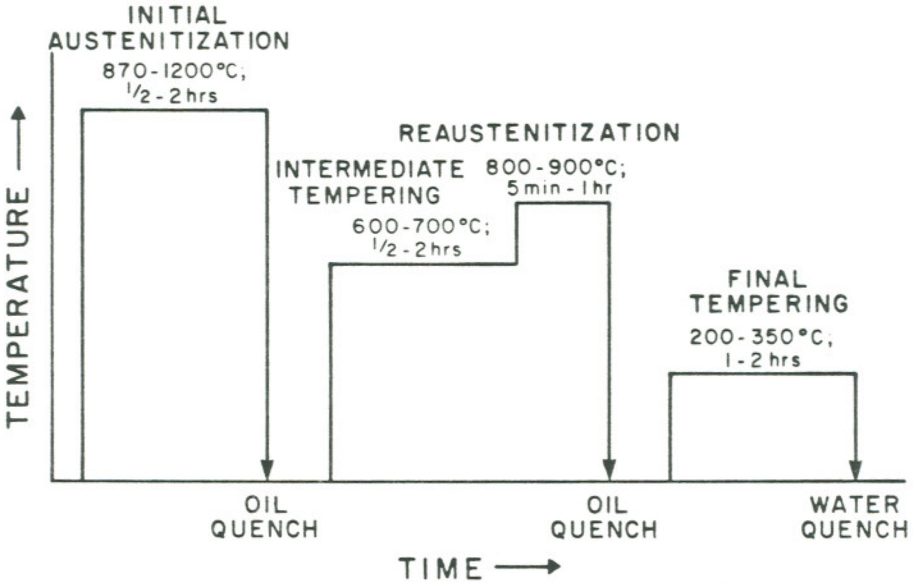

Figure 4-3: TRIAL HEAT TREATMENT SCHEMATIC.

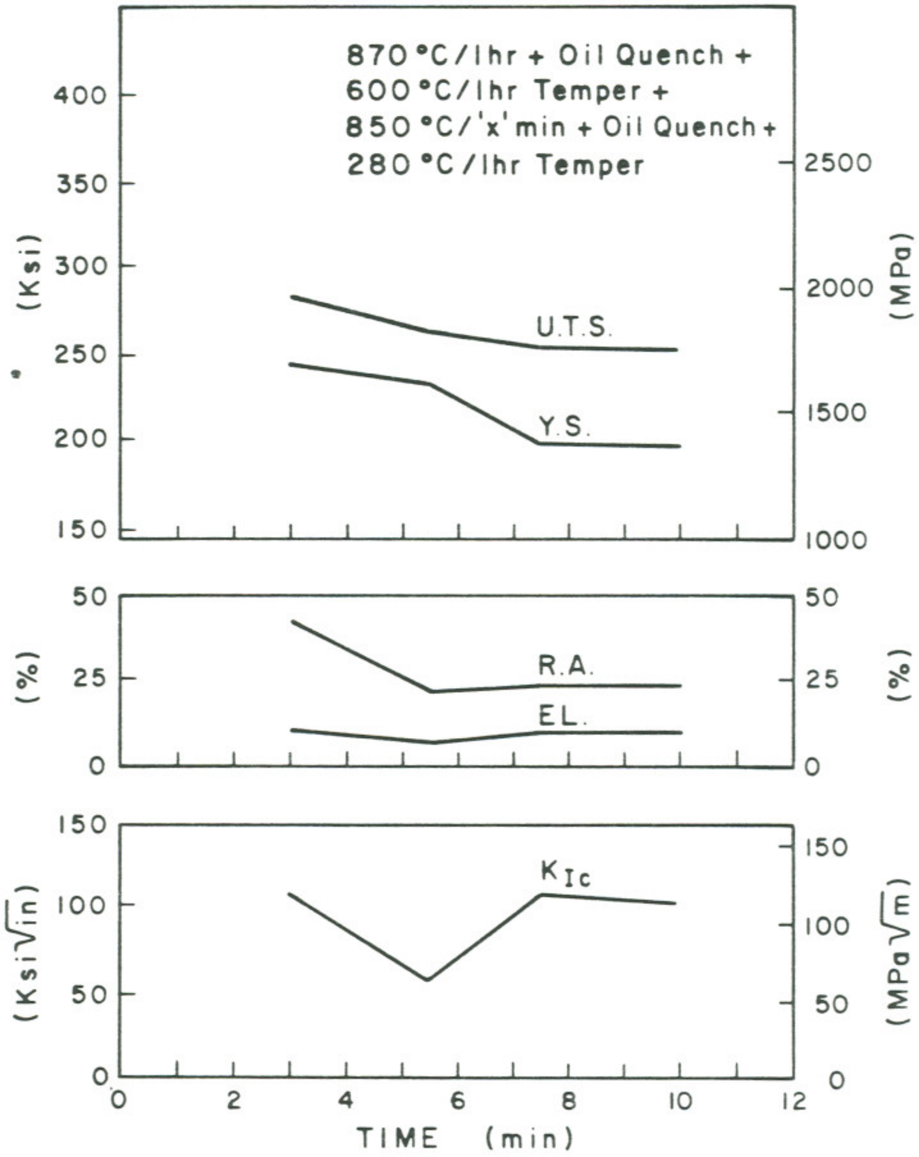

Figure 4-4: MECHANICAL PROPERTIES OF TRIAL HEAT TREATMENT WITH AN INTERMEDIATE TEMPERING TEMPERATURE OF 600°C.

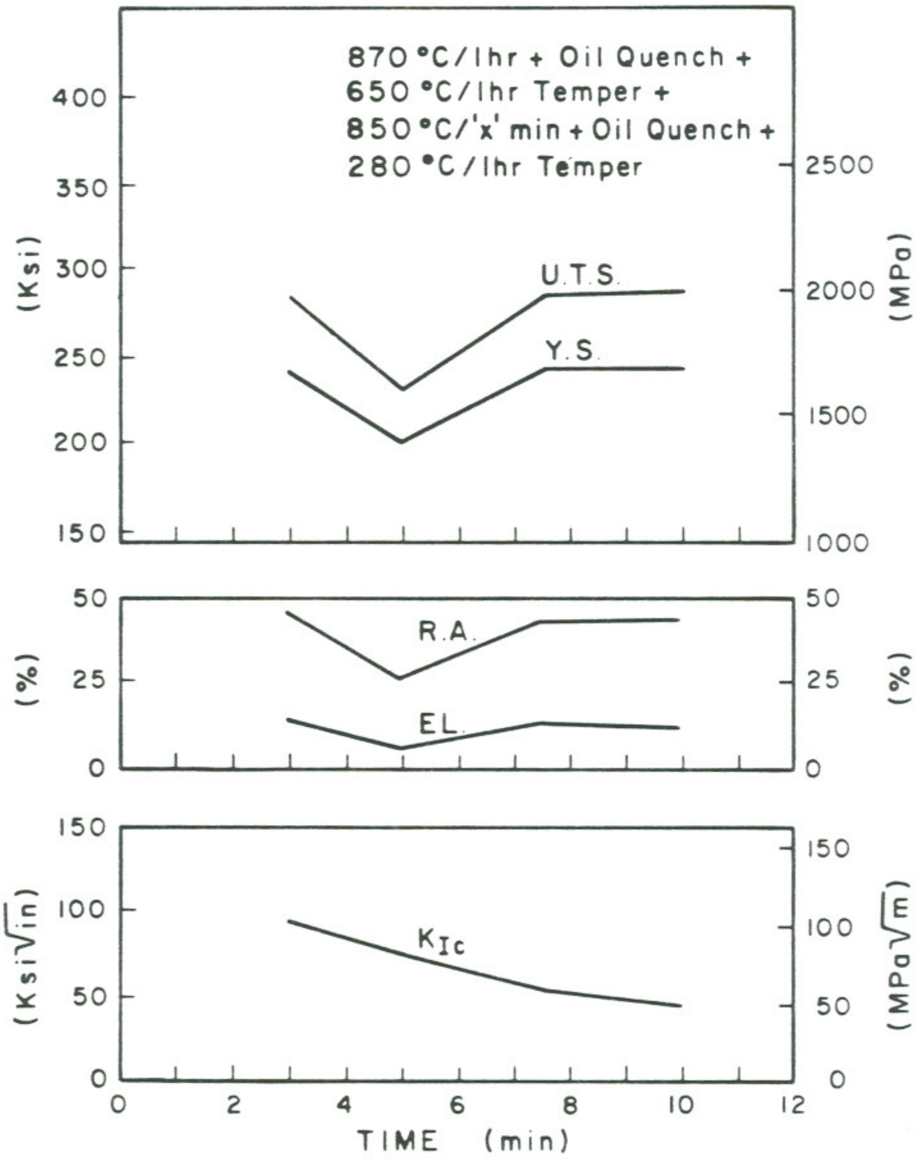

Figure 4-5: MECHANICAL PROPERTIES OF TRIAL HEAT TREATMENT WITH AN INTERMEDIATE TEMPERING TEMPERATURE OF 650°C.

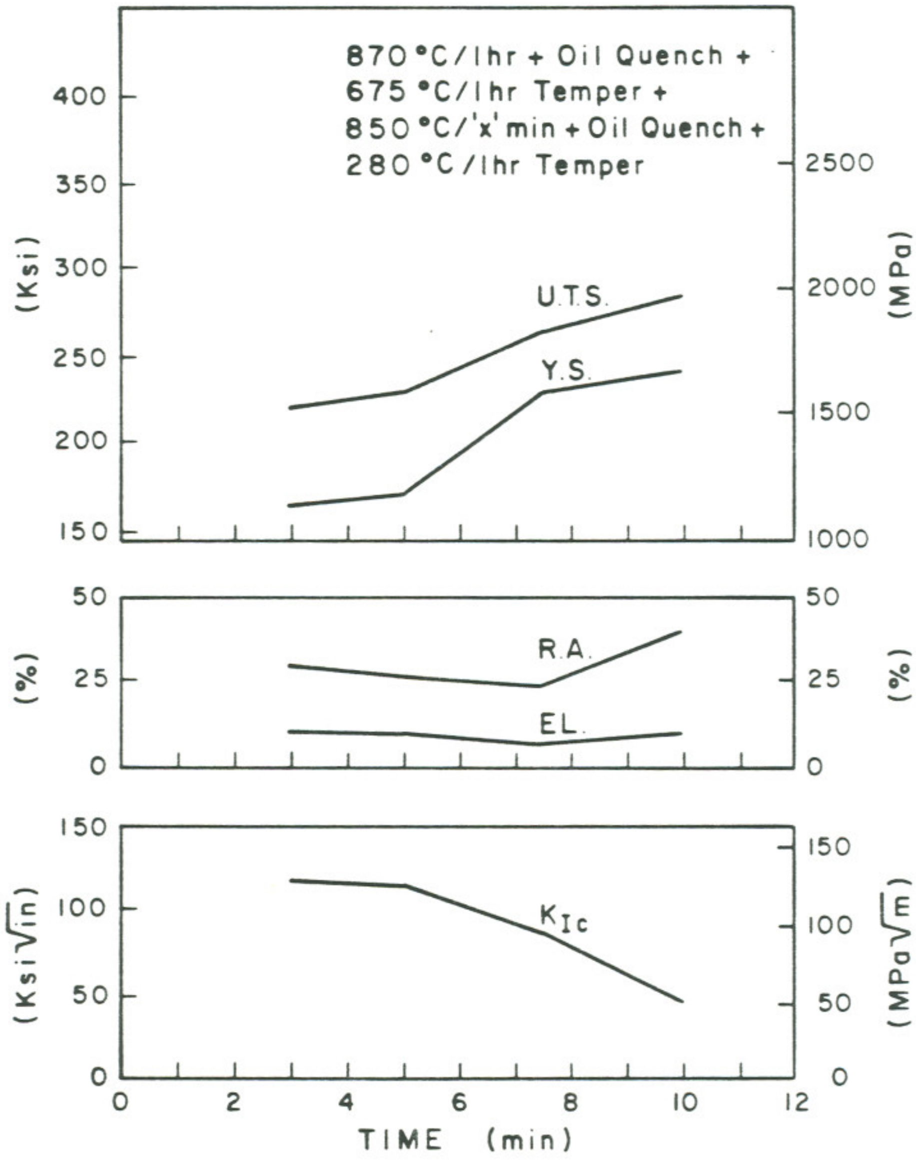

Figure 4-6: MECHANICAL PROPERTIES OF TRIAL HEAT TREATMENT WITH AN INTERMEDIATE TEMPERING TEMPERATURE OF 675°C.

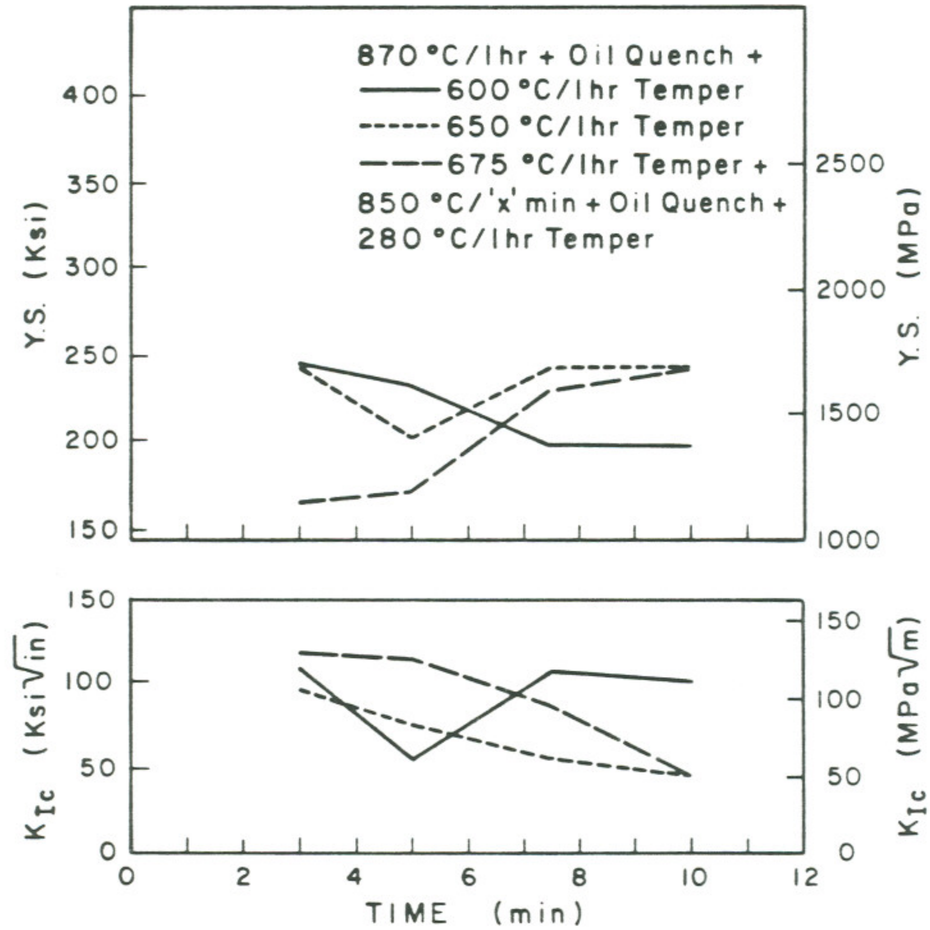

Figure 4-7: COMPARISON OF MECHANICAL PROPERTIES OF DIFFERENT TRIAL HEAT TREATMENTS.

actuality to the value corresponding to (x - 2) min. The actual values are also listed in Table 4-3. While it is obvious that the best combinations of K_{Ic} and yield strength were achieved with an intermediate tempering temperature of 600°C, the drop in K_{Ic} with increasing time was more rapid than when the intermediate tempering temperature was 650°C. Also, the initial differences for these two cases were not significant. However, when the intermediate tempering temperature was 675°C, the toughness-strength combinations were poor. Based on these results, intermediate tempering temperature of 650°C and reaustenitization temperature of 850°C were chosen for further study. For these conditions, the complete property plot as a function of reaustenitization time is given in Figure 4-8. Beyond 10 min reaustenitization times, all the properties remained essentially unchanged, with the actual values corresponding to those of the conventionally heat treated specimen (Table 4-4). From these results, it was concluded that 3 min reaustenitization time gave the most beneficial results and for further studies, this time was chosen. Henceforth, this heat treatment will be referred to as the modified conventional, modified high temperature or modified step heat treatment, depending upon the initial austenitization temperature.

4.1.3. Modified Heat Treatments. Tables 4-5 and 4-6 list the mechanical properties of conventional, high temperature, step, modified conventional, modified high temperature and modified step heat treatments. The heat treatment schedules are shown separately in Figure 4-9. A histogram analysis of the mechanical properties is presented in Figure 4-10. It is clear that all the modified heat treatments exhibited better

TABLE 4-3.

MECHANICAL PROPERTIES OF TRIAL HEAT TREATMENTS

Heat Treatment	*Specimen #	Reaustenitization Time 'x' (min)	Yield Strength		Ultimate Tensile Strength		Plane Strain Fracture Toughness		Elongation (%)	Reduction in Area (%)
			(Ksi)	(MNm^{-2})	(Ksi)	(MNm^{-2})	(Ksi$\sqrt{in}$)	($MNm^{-3/2}$)		
870°C/1hr+ Oil Quench+	D 203 BC 203	3	244.8	1686.4	284.3	1958.5	107.5	118.1	11.0	44.1
600°C/1hr+	D 205 BC 205	5½	232.1	1598.9	263.9	1818.0	57.1	62.8	6.7	22.6
850°C/'x'min+ Oil Quench+	D 204 BC 204	7½	197.8	1362.6	255.0	1756.7	106.0	116.5	9.6	23.3
280°C/1hr	D 202 BC 202	10	196.5	1353.7	252.5	1739.5	100.5	110.4	9.4	23.3
870°C/hr+ Oil Quench+	D 197 BC 197	3	242.3	1669.2	284.3	1958.5	94.9	104.3	13.4	45.8
650°C/1hr+	D1911 BC 191	5	201.6	1388.8	232.1	1598.9	75.9	83.4	6.0	25.4
850°C/'x'min+ Oil Quench+	D 198 BC 198	7½	243.6	1678.2	285.6	1967.5	57.1	62.8	13.1	44.1
280°C/1hr	D 192 BC 192	10	243.6	1678.2	288.1	1984.7	47.4	52.1	11.1	44.1
870°C/1hr+ Oil Quench+	D 209 BC 209	3	163.5	1126.4	220.7	1520.4	117.0	128.6	10.0	28.8
675°C/1hr+	D 208 BC 208	5	171.1	1178.7	229.6	1581.7	113.7	125.0	9.4	27.4
850°C/'x'min+ Oil Quench+	D 207 BC 207	7½	229.6	1581.7	265.2	1827.0	85.8	94.3	6.7	24.0
280°C/1hr	D 206 BC 206	10	242.3	1669.2	286.8	1975.8	47.5	52.2	11.1	42.2

*Code: D = Tensile Specimen
BC = Compact Tension Specimen

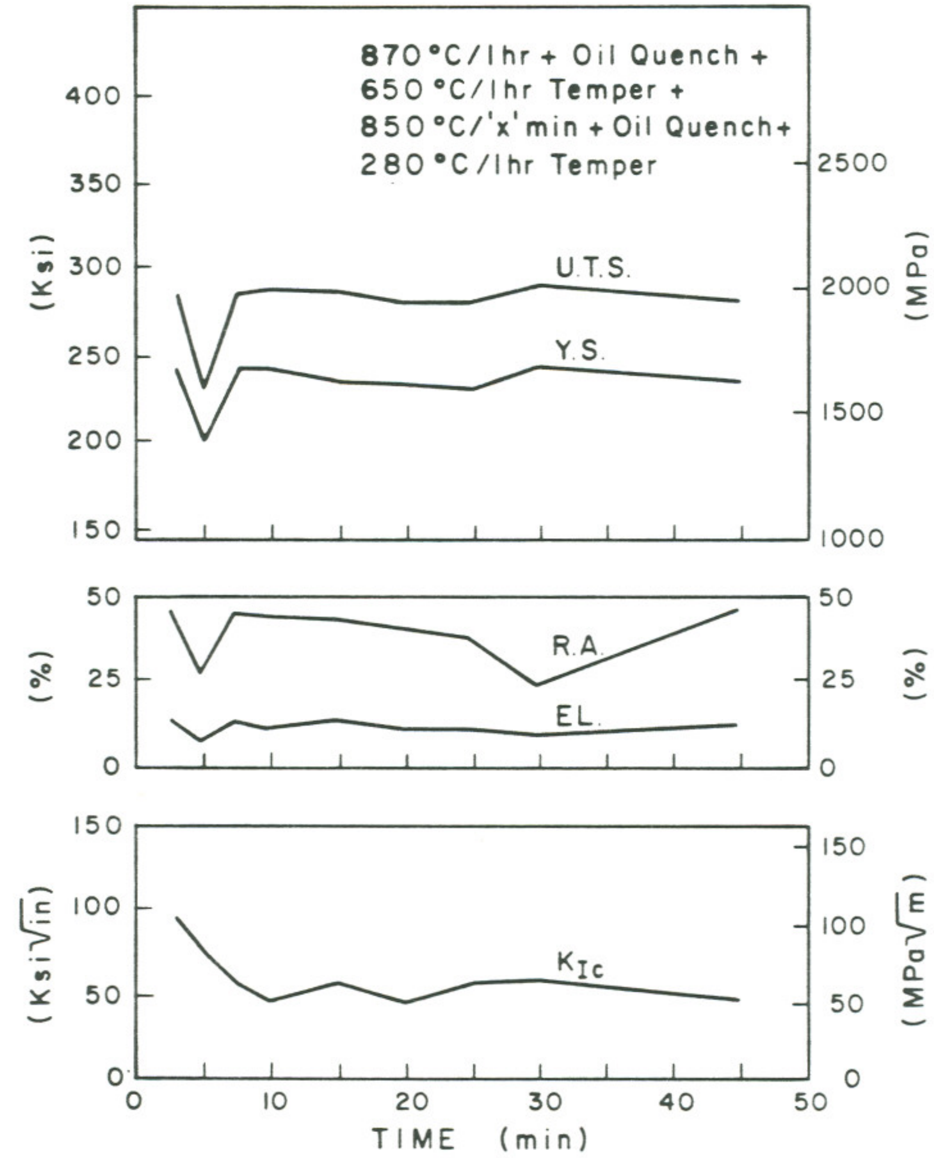

Figure 4-8: MECHANICAL PROPERTIES OF TRIAL HEAT TREATMENT WITH AN INTERMEDIATE TEMPERING TEMPERATURE OF 650°C.

TABLE 4-4.

MECHANICAL PROPERTIES OF TRIAL HEAT TREATMENTS

Heat Treatment	*Specimen #	Reaustenitization Time 'x' (min)	Yield Strength		Ultimate Tensile Strength		Plane Strain Fracture Toughness		Elongation (%)	Reduction in area (%)
			(Ksi)	(MNm^{-2})	(Ksi)	(MNm^{-2})	(Ksi$\sqrt{in}$)	(MNm$^{-3/2}$)		
870°C/1hr+ Oil Quench+ 650°C/1hr+ 850°C/'x'min+ Oil quench+ 280°C/1hr	D 197 BC 197	3	242.3	1669.2	284.3	1958.5	94.9	104.3	13.4	45.8
	D1911 BC 191	5	201.6	1388.8	232.1	1598.9	75.9	83.4	6.0	25.4
	D 198 BC 198	7½	243.6	1678.2	285.6	1967.5	57.1	62.8	13.1	44.1
	D 192 BC 192	10	243.6	1678.2	288.1	1984.7	47.4	52.1	11.1	44.1
	D 193 BC 193	15	235.9	1625.1	286.8	1975.8	58.4	64.2	12.0	44.1
	D 194 BC 194	20	234.7	1616.9	280.5	1932.4	47.4	52.1	11.2	40.4
	D 195 BC 195	25	232.1	1598.9	280.5	1932.4	57.8	63.5	11.0	37.9
	D 196 BC 196	30	244.8	1686.4	290.7	2002.6	59.2	65.1	8.9	22.6
	D 199 BC 199	45	235.9	1625.1	281.7	1940.6	48.5	53.3	12.4	45.2

*Code: D = Tensile Specimen
BC = Compact Tension Specimen

TABLE 4-5.

TENSILE PROPERTIES

Heat Treatment	Specimen #	Yield Strength		Ultimate Tensile Strength		Elongation (%)	Reduction in Area (%)
		(Ksi)	(MNm^{-2})	(Ksi)	(MNm^{-2})		
Conventional	D189	234.7	1616.9	285.6	1967.5	11.3	39.8
	D190	235.9	1625.1	284.3	1958.5	10.8	39.2
	Mean	235.3	1621.0	285.0	1963.0	11.1	39.5
Modified Conventional	D197	242.3	1669.2	284.3	1958.5	13.4	45.8
	D127	260.2	1792.5	290.0	1997.8	14.1	47.6
	Mean	251.3	1730.9	287.2	1978.2	13.8	46.7
High Temperature	D187	241.0	1660.3	293.2	2019.9	6.4	12.4
	D188	239.8	1652.0	288.1	1984.7	5.1	10.9
	Mean	240.4	1656.2	290.7	2002.3	5.8	11.7
Modified High Temperature	D191	242.3	1669.2	288.1	1984.7	9.4	23.1
	D213	244.8	1686.4	285.6	1967.5	8.0	28.1
	Mean	243.6	1677.8	286.9	1976.1	8.7	25.6
Step	D185	223.2	1537.6	269.0	1853.1	6.9	13.9
	D186	210.5	1450.1	258.8	1782.9	10.0	18.3
	Mean	216.9	1493.9	263.9	1818.0	8.5	16.1
Modified Step	D170	229.6	1581.7	265.2	1827.0	7.2	21.6
	D171	242.3	1669.2	265.2	1827.0	8.1	21.6
	Mean	236.0	1625.5	265.2	1827.0	7.7	21.6

TABLE 4-6.

FRACTURE TOUGHNESS AND IMPACT PROPERTIES

Heat Treatment	Specimen #	Plane Strain Fracture Toughness		Fracture Initiation Energy		Fracture Propagation Energy		Charpy V-Notch Energy		Dynamic Fracture Toughness		Apparent Yield Strength		Deflection at Yield	
		$(\text{Ksi}\sqrt{\text{in}})$	$(\text{MNm}^{-3/2})$	(ft-lbs)	(Nm)	(ft-lbs)	(Nm)	(ft-lbs)	(Nm)	$(\text{Ksi}\sqrt{\text{in}})$	$(\text{MNm}^{-3/2})$	(Ksi)	(MNm^{-2})	$(\text{x}10^{-3}\text{in})$	$(\text{x}10^{-4}\text{m})$
Conventional	E5,E6	50.7	55.7	16.5	22.4	3.1	4.2	19.7	26.7	126.4	138.9	234.7	1616.9	42.0	10.7
	BC189,BC190	51.0	56.0	16.7	22.7	3.5	4.8	20.2	27.4	111.7	122.8	235.9	1625.1	42.0	10.7
	Mean	50.9	55.9	16.6	22.6	3.3	4.5	20.0	27.1	119.1	130.9	235.3	1621.0	42.0	10.7
Modified Conventional	E1,E2	94.9	104.3	16.9	22.9	3.5	4.8	20.4	27.7	126.8	139.3	294.8	2030.9	45.0	11.4
	BC197,BC127	89.7	98.6	16.6	22.5	3.0	4.1	19.6	26.6	140.4	154.3	293.5	2021.9	42.9	10.9
	Mean	92.3	101.5	16.8	22.7	3.3	4.5	20.0	27.2	133.6	146.8	294.2	2026.4	44.0	11.2
High Temperature	E11,E12	83.2	91.4	10.0	13.6	3.2	4.3	13.2	17.9	112.1	123.2	243.4	1676.8	32.5	8.3
	BC187,BC188	82.7	90.9	9.8	13.3	2.9	3.9	12.8	17.4	109.1	119.9	247.3	1703.7	32.5	8.3
	Mean	83.0	91.2	9.9	13.5	3.1	4.1	13.0	17.7	110.6	121.6	245.4	1690.3	32.5	8.3
Modified High Temperature	E7,E8	97.2	106.8	16.2	22.0	3.1	4.2	19.4	26.3	133.5	146.7	292.9	2017.8	42.3	10.7
	BC 68,BC152	99.1	108.9	14.1	19.1	3.4	4.6	17.5	23.7	145.2	159.6	266.8	1838.0	39.2	10.0
	Mean	98.2	107.9	15.2	20.6	3.3	4.4	18.5	25.0	139.4	153.2	279.9	1927.9	40.8	10.4
Step	E18,E23	64.7	71.1	5.9	8.0	2.3	3.1	8.2	11.1	127.5	140.1	194.9	1342.7	26.9	6.8
	BC185,BC186	78.8	86.6	7.6	10.3	2.3	3.1	10.0	13.6	126.8	139.3	223.9	1542.5	29.4	7.5
	Mean	71.8	78.9	6.8	9.2	2.3	3.1	9.1	12.4	127.2	139.7	209.4	1442.6	28.2	7.9
Modified Step	E13,E14	93.2	102.4	16.4	22.2	3.6	4.9	20.0	27.1	140.1	154.0	292.2	2013.0	42.9	10.9
	BC 70,BC171	92.3	101.4	14.6	19.8	3.3	4.5	18.0	24.4	165.5	181.9	257.7	1775.3	41.2	10.5
	Mean	92.8	101.9	15.5	21.0	3.5	4.7	19.0	25.8	152.8	168.0	275.0	1894.2	42.1	10.7

*Code: E = Charpy V-Notch Specimen
BC = Compact Tension Specimen

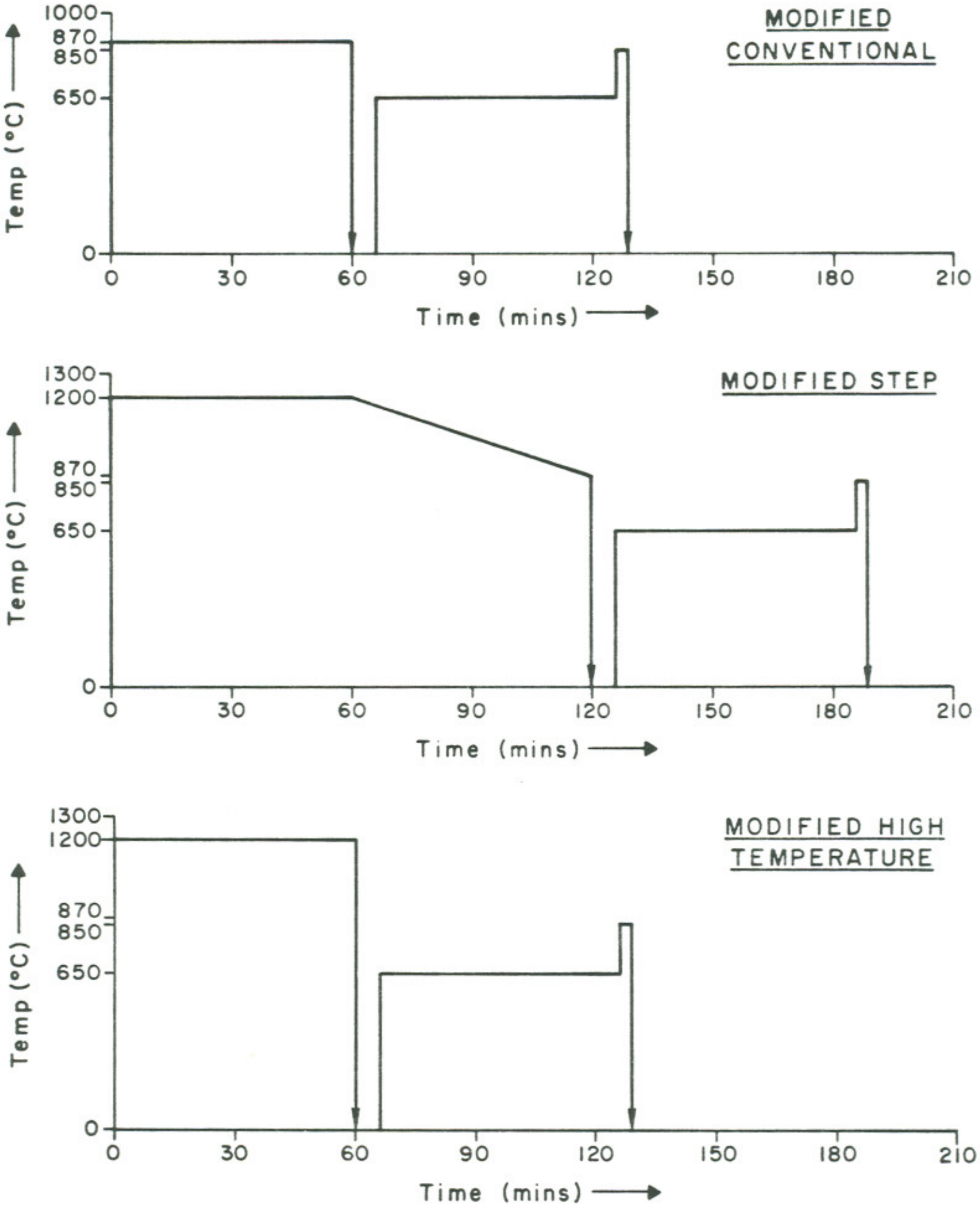

Figure 4-9: HEAT TREATMENT SCHEMATIC.

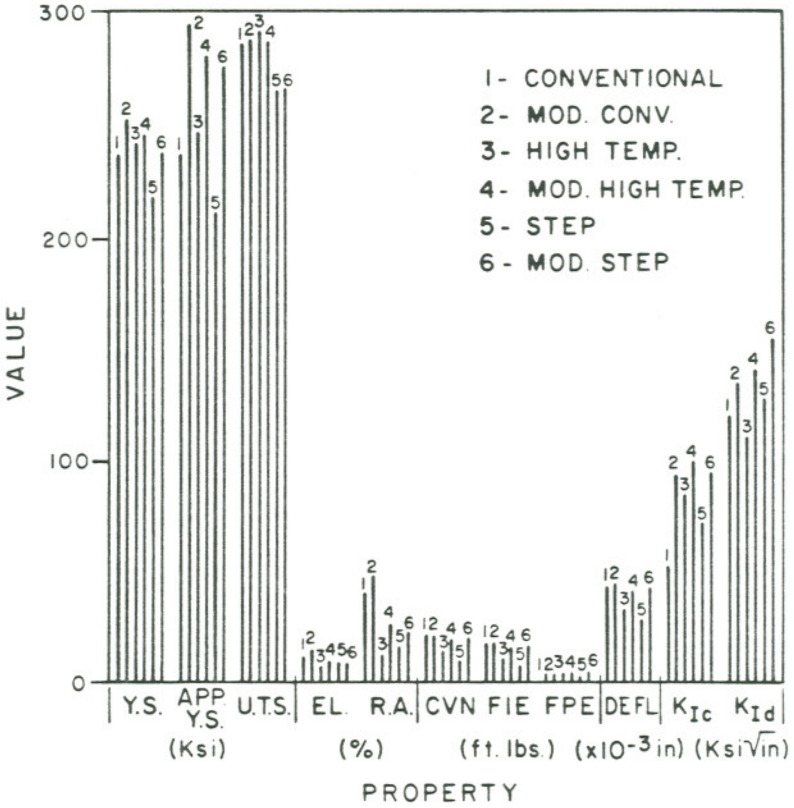

Figure 4-10: COMPARISON OF MECHANICAL PROPERTIES OF VARIOUS HEAT TREATMENTS.

properties. The modified conventional heat treatment improved yield strength by 110.2 MNm^{-2}, elongation by 2.7%, reduction in area by 7.2% and deflection at yield by 0.025 mm, when compared with the conventional heat treatment. While CVN energy, ultimate tensile strength, FIE and FPE remained essentially unchanged, all other properties showed even better improvement. Fracture toughness improved by 45.1 $\mathrm{MNm}^{-3/2}$, K_{Id} by 15.9 $\mathrm{MNm}^{-3/2}$, and apparent yield strength by 405.8 MNm^{-2}. The modified high temperature heat treatment improved yield strength by 22 MNm^{-2}, apparent yield strength by 237.7 MNm^{-2}, elongation by 2.9%, reduction in area by 13.9%, K_{Ic} by 13.7 $\mathrm{MNm}^{-3/2}$, CVN energy by 7.5 Nm, FIE by 7.2 Nm, deflection at yield by 0.203 mm, and K_{Id} by 31.7 $\mathrm{MNm}^{-3/2}$, when compared with the high temperature heat treatment. Ultimate tensile strength and FPE remained virtually unaffected. While the high temperature heat treatment improved the plane strain fracture toughness relative to the conventional heat treatment at essentially the same strength levels, ductility and impact properties exhibited a marked decrease.

However, the modified high temperature heat treatment, while improving K_{Ic} relative to the conventional heat treatment even more at the same strength levels, resulted in lesser drops in overall ductility and impact properties (K_{Id} and apparent yield strength, in fact, improved). The modified step heat treatment improved yield strength by 131.6 MNm^{-2}, apparent yield strength by 451.9 MNm^{-2}, reduction in area by 5.5%, K_{Ic} by 23.1 $\mathrm{MNm}^{-3/2}$, K_{Id} by 72.1 $\mathrm{MNm}^{-3/2}$, impact toughness by 13.7 Nm, FIE by 11.8 Nm, and deflection at yield by 0.353 mm. All other properties remained essentially unchanged. While the step heat treatment improved K_{Ic}

and K_{Id} compared to the conventional heat treatment, significant reductions in other properties resulted. In the case of the modified step heat treatment, both K_{Ic} and K_{Id} improved even more, and the loss in other properties was less severe, while impact properties remained more or less unchanged. Thus, the modified heat treatments improved the mechanical properties of the corresponding conventional, high temperature and step heat treatments, and the reduction in some properties when compared with the conventional heat treatment was also less severe than for the high temperature or step heat treatments.

4.1.4. Stress Corrosion Cracking Properties.

4.1.4.1. Threshold Stress Intensity. The threshold stress intensity (K_{Iscc}) values, below which hydrogen assisted cracking did not occur, are listed in Table 4-7. These values were obtained using bolt loaded DCB specimens. For the purposes of stress corrosion cracking studies, only one modified heat treatment was chosen, viz., the modified conventional heat treatment. As seen from Table 4-7, the high temperature and step heat treatments resulted in almost identical K_{Iscc} values, 21.5 $MNm^{-3/2}$ and 21.2 $MNm^{-3/2}$, respectively. For conventional heat treatment, the value was 17.0 $MNm^{-3/2}$. In the case of the modified conventional heat treatment, the K_{Iscc} value was 35.4 $MNm^{-3/2}$, double that of the conventional heat treatment.

Ritchie et al. [27] and Cedeno [28] reported a value of 18.6 $MNm^{-3/2}$ for 300M steel austenitized at 870°C and tempered at 300°C for 1 hr, which is close to the value obtained in this investigation for the conventional heat treatment. This value also agrees well with the K_{Iscc} value

TABLE 4-7

THRESHOLD STRESS INTENSITY VALUES

Heat Treatment	Specimen #	Threshold stress Intensity ($Ksi\sqrt{in}$)	Threshold stress Intensity ($MNm^{-3/2}$)
Conventional	BD 23	15.3	16.8
	BD 24	15.7	17.3
	Mean	15.5	17.1
High Temperature	BD 21	19.4	21.3
	BD 22	19.7	21.7
	Mean	19.6	21.5
Step	BD 25	19.4	21.3
	BD 26	19.1	21.0
	Mean	19.3	21.2
Modified Conventional	BD 33	32.8	36.0
	BD 34	31.6	34.7
	Mean	32.2	35.4

reported by Carter [29] and by Speidel [30] for 4340 steel modified with 1.5 wt.% Si, and Mostovoy et al. [31] for 300M steel. However, McDarmaid [17] reported a much lower value of 11.5 $MNm^{-3/2}$ for 300M steel quenched and tempered at 320°C, irrespective of austenitization temperature, that is, independent of prior austenite grain size, a conclusion similar to that of Proctor and Paxton [26] who studied stress corrosion behavior for 4340 steel. Contrary to this, Carter [29], Lessar and Gerberich [32] and Dilip Kumar [33] all observed an increase in K_{Iscc} with an increase in prior austenite grain size. In this study, except in the case of the modified heat treatment, for the other heat treatments, an increase in K_{Iscc} was observed with increasing prior austenite grain size.

4.1.4.2. Crack Growth Analysis. Crack extension as a function of time for conventional, high temperature, step and modified conventional heat treatments are presented in Figure 4-11. As seen from this figure, an initial fast crack growth, followed by a steady state crack growth and a final fast crack growth at the onset of failure or crack instability were observed in all cases. The initial and final growth regions were, however, limited to very small time intervals and the steady growth region encompassed almost the entire test time. In order to make meaningful comparisons and to understand the stress corrosion cracking phenomenon better for each heat treatment, it was necessary to present these results in several forms. Crack growth rates [log (da/dt)] as a function of instantaneous stress intensity (K_I) values are given in Figures 4-12 through 4-15 for conventional, high temperature,

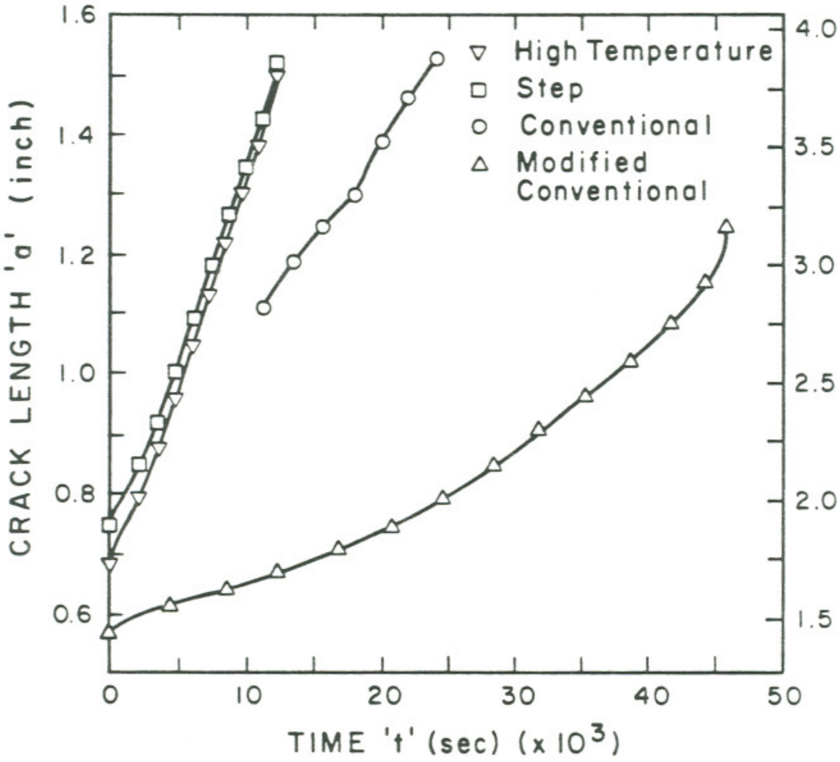

Figure 4-11: CRACK LENGTH VS. TIME CURVES FOR DIFFERENT HEAT TREATMENTS.

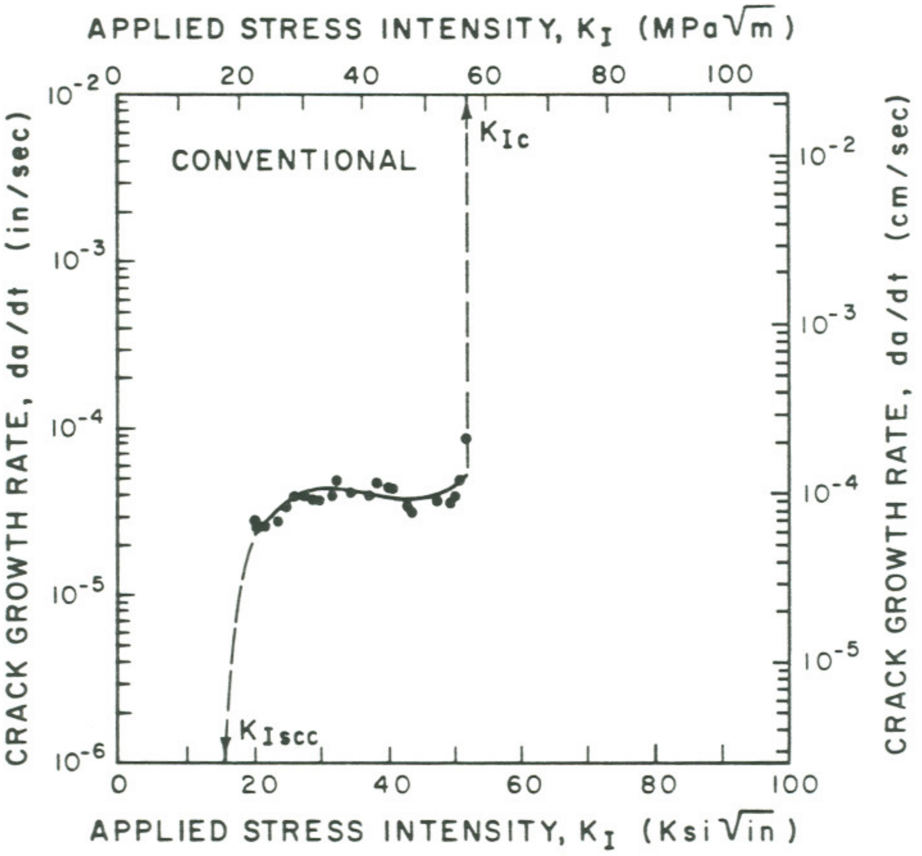

Figure 4-12: CRACK GROWTH RATE VS. APPLIED STRESS INTENSITY FOR CONVENTIONAL HEAT TREATMENT.

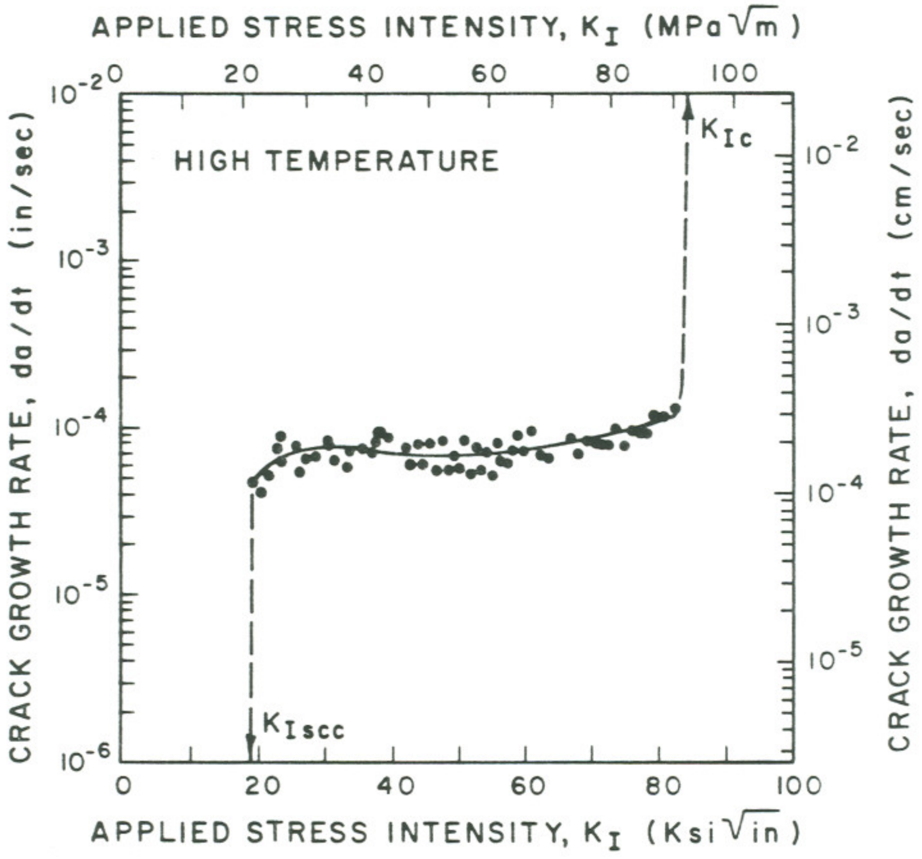

Figure 4-13: CRACK GROWTH RATE VS. APPLIED STRESS INTENSITY FOR HIGH TEMPERATURE HEAT TREATMENT.

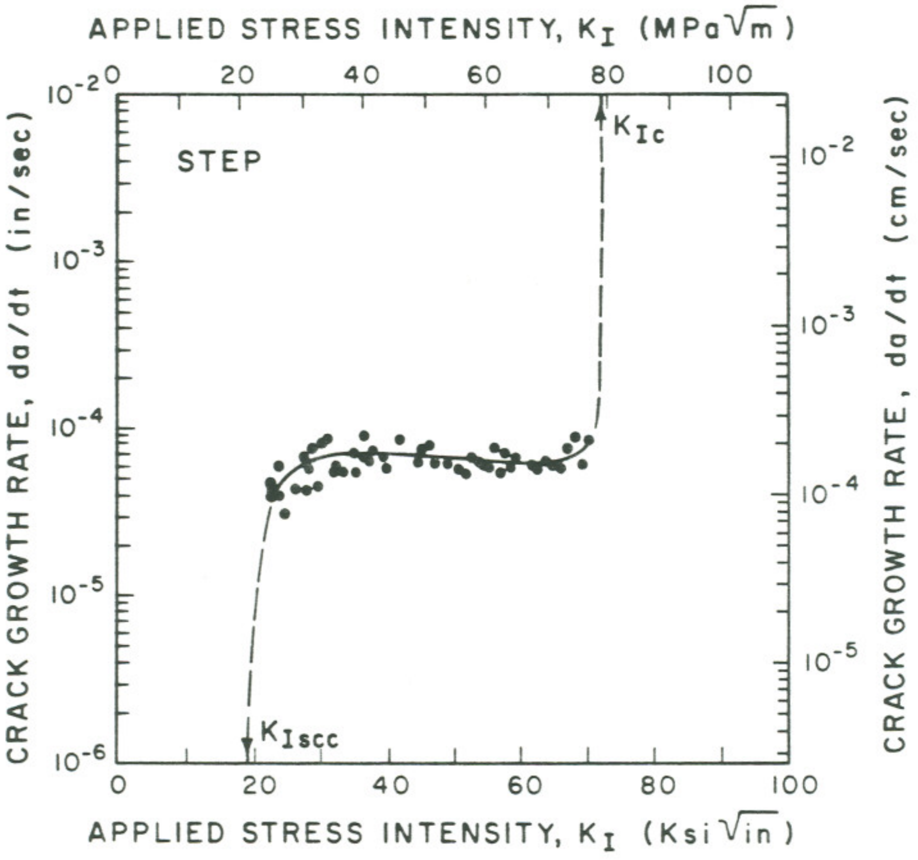

Figure 4-14: CRACK GROWTH RATE VS. APPLIED STRESS INTENSITY FOR STEP HEAT TREATMENT.

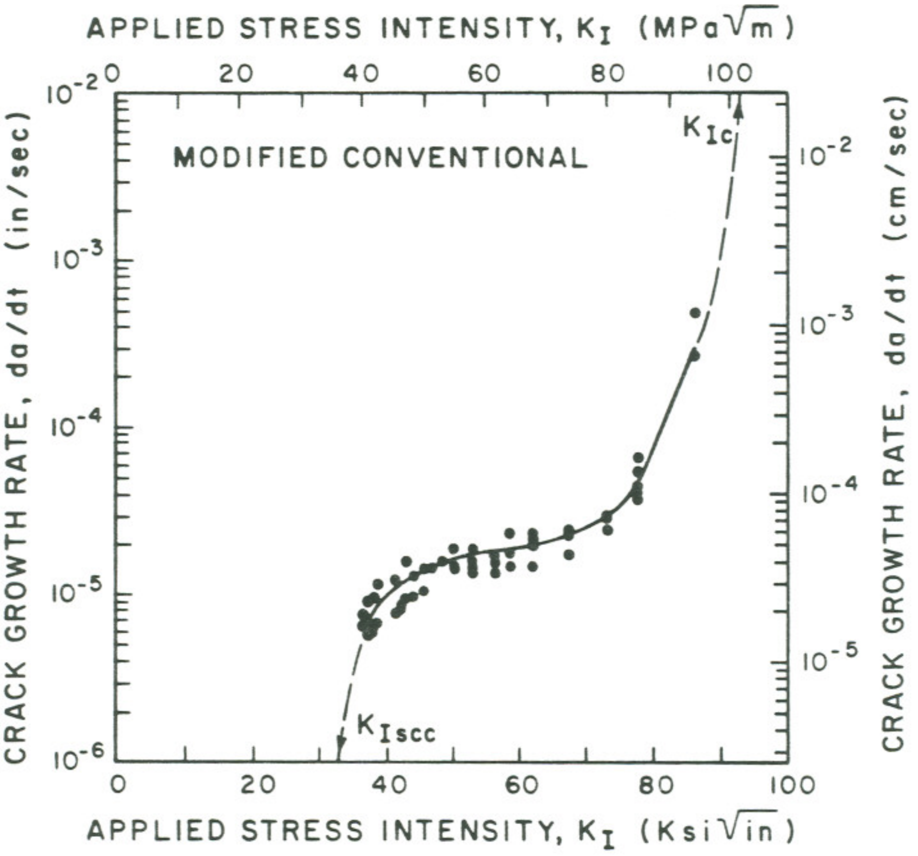

Figure 4-15: CRACK GROWTH RATE VS. APPLIED STRESS INTENSITY FOR MODIFIED CONVENTIONAL HEAT TREATMENT.

step and modified conventional heat treatments, respectively. It is a standard practice to represent stress corrosion data in this form [log (da/dt) vs K_I] [33-37]. All these curves exhibited three distinct regions as depicted in Figure 4-16 for a typical case. The crack velocity increased exponentially with stress intensity in region I, remained constant with K_I in region II (plateau region) and increased again with K_I in region III. Time to failure tests are not suitable for mechanistic studies, because failure time may encompass all these three regions as well as the initiation period and supercritical crack growth. Hence, log (da/dt) vs K_I studies were conducted in this investigation. Since regions I and III occupy only small time intervals, sometimes these regions were not well defined (Figures 4-13 and 4-14). Also, similar to the observations of Gerberich et al. [42] and Carter [43], in stage II, except in the case of modified conventional heat treatment, the crack velocity actually decreased slightly with stress intensity. The crack velocities for all heat treatments are compared in Figure 4-17 and in Table 4-8 as a function of stress intensity. The lowest stage II growth rate was obtained with modified conventional heat treatment (5.18×10^{-5} cm/sec) followed by conventional heat treatment (1.11×10^{-4} cm/sec), step (1.68×10^{-4} cm/sec) and high temperature (1.70×10^{-4} cm/sec) heat treatments. Thus, it is seen that the stage II velocity is directly dependent upon the reciprocal of prior austenite grain size with the finest grain sized material yielding the lowest crack growth rate. Although this conclusion is in agreement with the results reported by other investigators [26,33] for 4340 steels, Lessar and Gerberich [32]

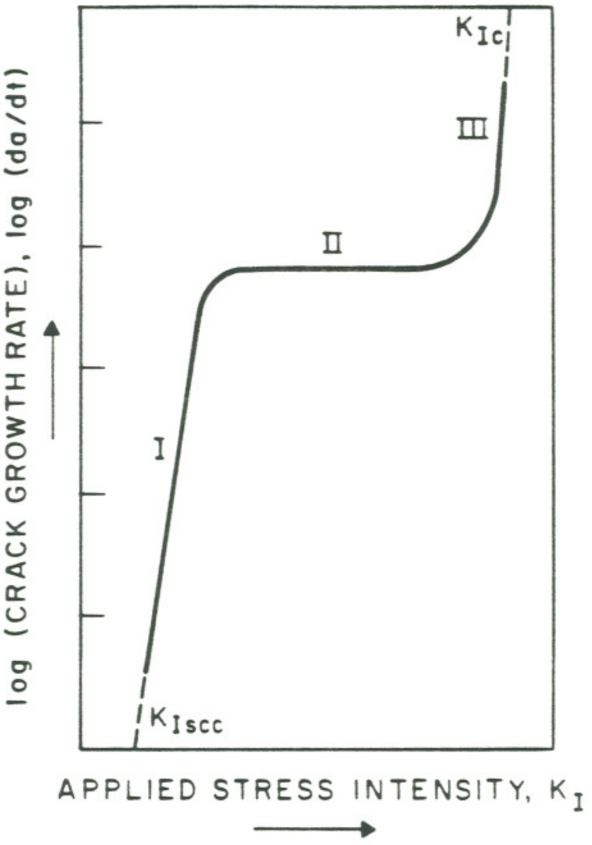

Figure 4-16: THE DIFFERENT STAGES OF A TYPICAL CRACK GROWTH RATE VS. APPLIED STRESS INTENSITY CURVE.

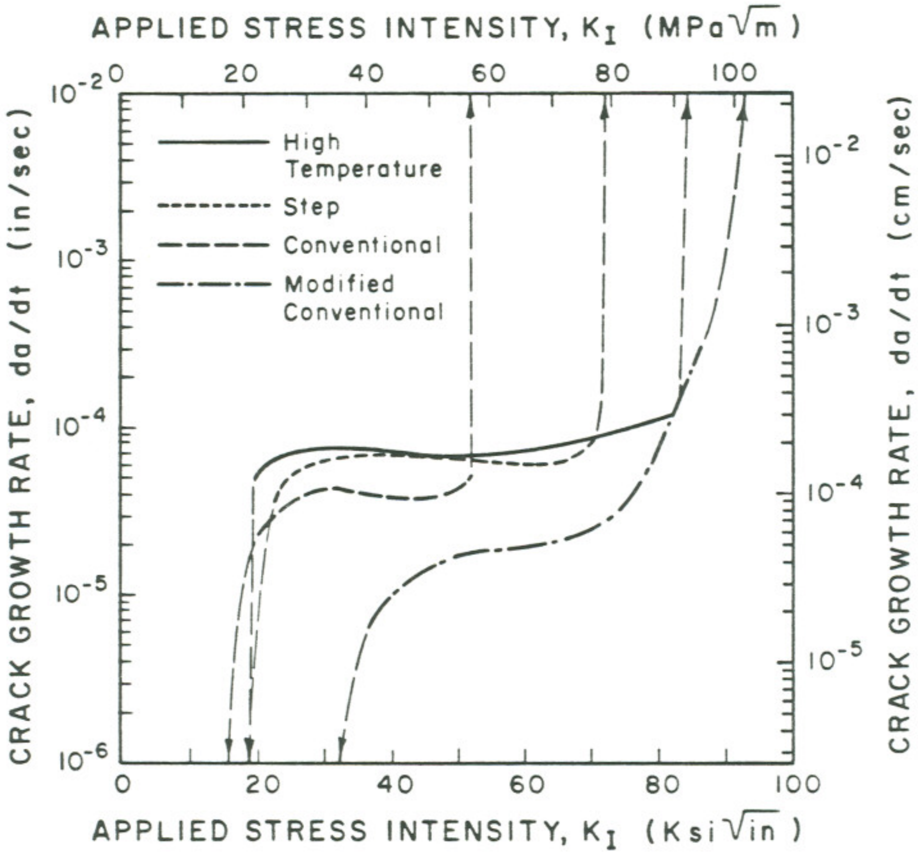

Figure 4-17: COMPARISON OF STRESS CORROSION CRACKING BEHAVIOR OF DIFFERENT HEAT TREATMENTS.

TABLE 4-8.

STRESS CORROSION CRACKING PROPERTIES

Heat Treatment	*Specimen #	Plane Strain Fracture Toughness K_{IC}		Threshold Stress Intensity K_{Iscc}		$K_M = \left[\frac{K_{Ic}+K_{Iscc}}{2}\right]$		Stage II Crack ** Velocity $\left(\frac{da}{dt}\right)_{II}$		Total Time to Failure
		(Ksi$\sqrt{in}$)	(MNm$^{-3/2}$)	(Ksi$\sqrt{in}$)	(MNm$^{-3/2}$)	(Ksi$\sqrt{in}$)	(MNm$^{-3/2}$)	(x10^{-5} in/sec)	(x10^{-5} cm/sec)	(hr:min)
Conventional	BC189, BC190 BC226, BC241 BD23, BD24 BC187, BC188	50.9	55.9	15.5	17.1	33.2	36.5	4.37	11.10	6:40
High Temperature	BC229, BC230 BD21, BD22	83.0	91.2	19.6	21.5	51.3	56.4	6.68	17.80	3:20
Step	BC185, BC186 BC232, BC235 BD25, BD26	71.8	78.9	19.3	21.2	45.6	50.1	6.62	17.00	3:15
Modified Conventional	BC197, BC127 BC211, BC212 BD33, BD34	92.3	101.5	32.2	35.4	62.3	68.5	2.04	5.18	12:30

*Code: BC = Compact Tension Specimens
BD = Double Cantilever Beam Specimens

**$\left(\frac{da}{dt}\right)_{II}$ Determined at K_M.

reported an opposite effect of prior austenite grain size on stage II crack velocity for 4340 steels. However, in their comparison, the yield strength varied widely with grain size unlike in this investigation and the lower growth rates could have been a result of this lowered yield strength for coarser grains. The log (da/dt) vs. K_I curves were drawn using regression analyses. The actual curves, in stage II, exhibited several peaks and valleys, as illustrated in Figure 4-18 for the high temperature heat treatment. Also, as seen from Figure 4-18, the peaks and valleys decreased in amplitude with increasing stress intensity. Such intermittent slow and fast growth regions have also been reported by other investigators [42, 44] for similar high strength steels.

4.1.5. Acoustic Emission Analysis. During stress corrosion cracking tests, both cumulative counts and events were continuously monitored. Cumulative counts vs. time and cumulative events vs. time data are presented in Figures 4-19 and 4-20 for all the heat treatments. In all cases, the increase in counts or events with time was almost exponential, except for the modified conventional heat treatment, where the increase was constant. Also, for the same heat treatment, the change in counts with time followed exactly the same trend as the change in events with time. The maximum number of counts and events were obtained for the step heat treatment followed by high temperature, conventional and modified conventional heat treatments in decreasing order. This was consistent with the decreasing prior austenite grain size obtained for these respective heat treatments. In Figures 4-21 and 4-22, counts vs. crack length and events vs. crack length data are presented for all heat

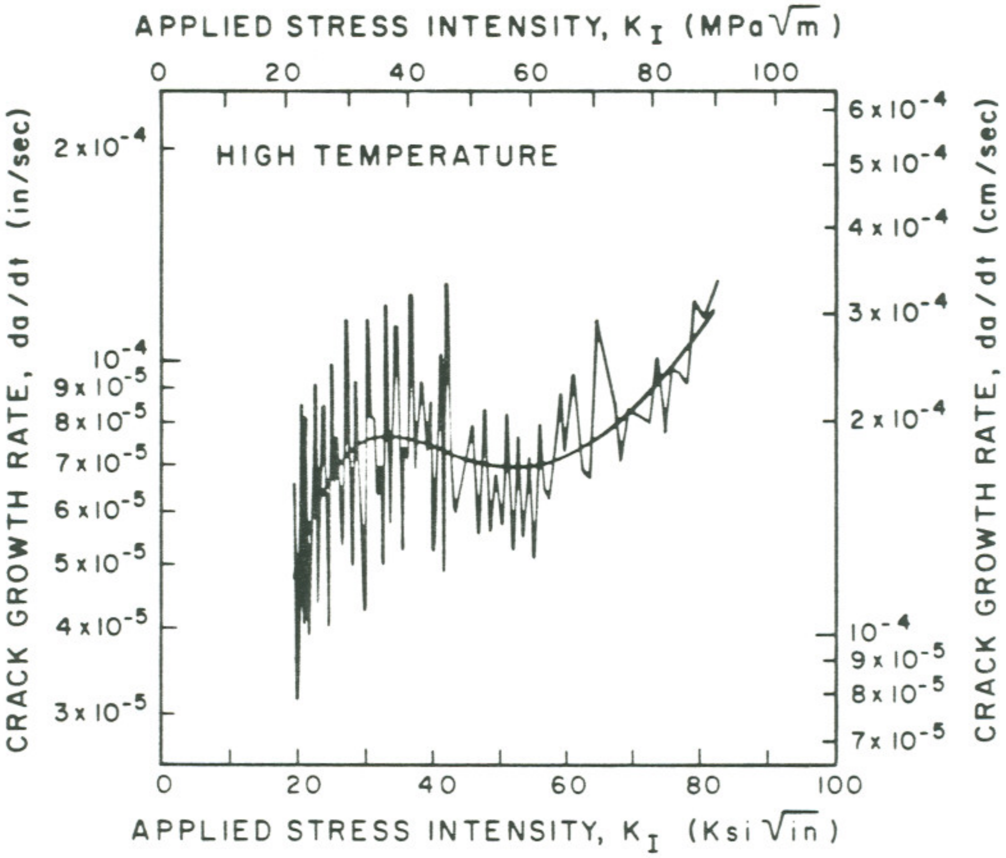

Figure 4-18: ACTUAL CRACK GROWTH RATE VS. APPLIED STRESS INTENSITY FOR HIGH TEMPERATURE HEAT TREATMENT.

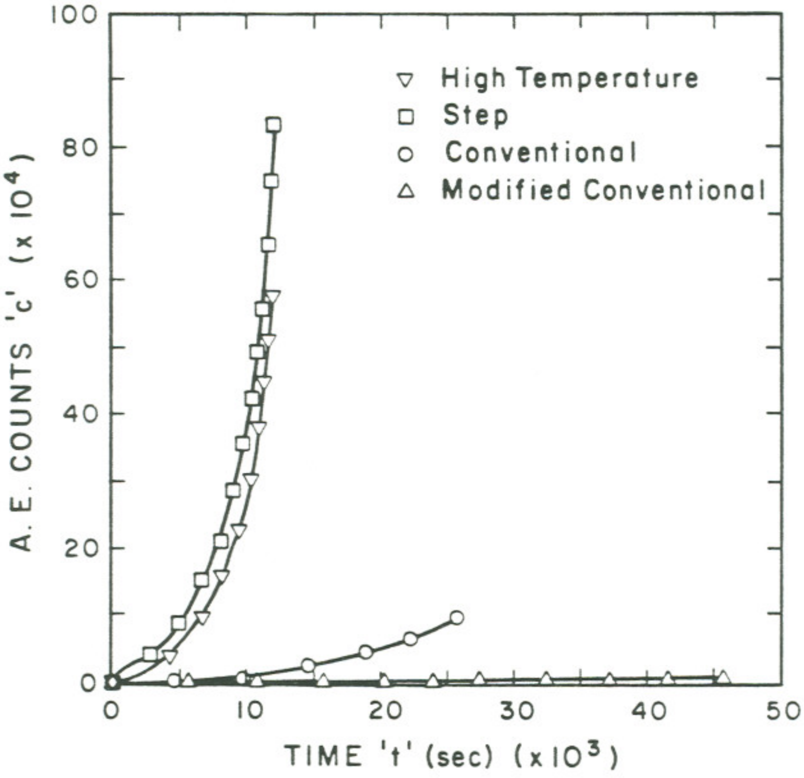

Figure 4-19: CUMULATIVE COUNTS VS. TIME FOR DIFFERENT HEAT TREATMENTS.

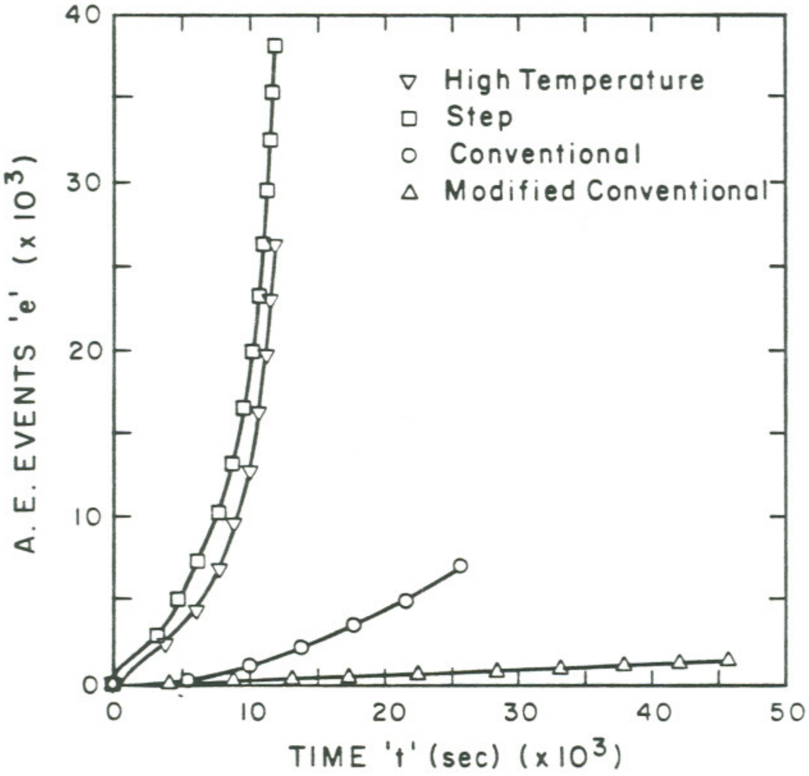

Figure 4-20: CUMULATIVE EVENTS VS. TIME FOR DIFFERENT HEAT TREATMENTS.

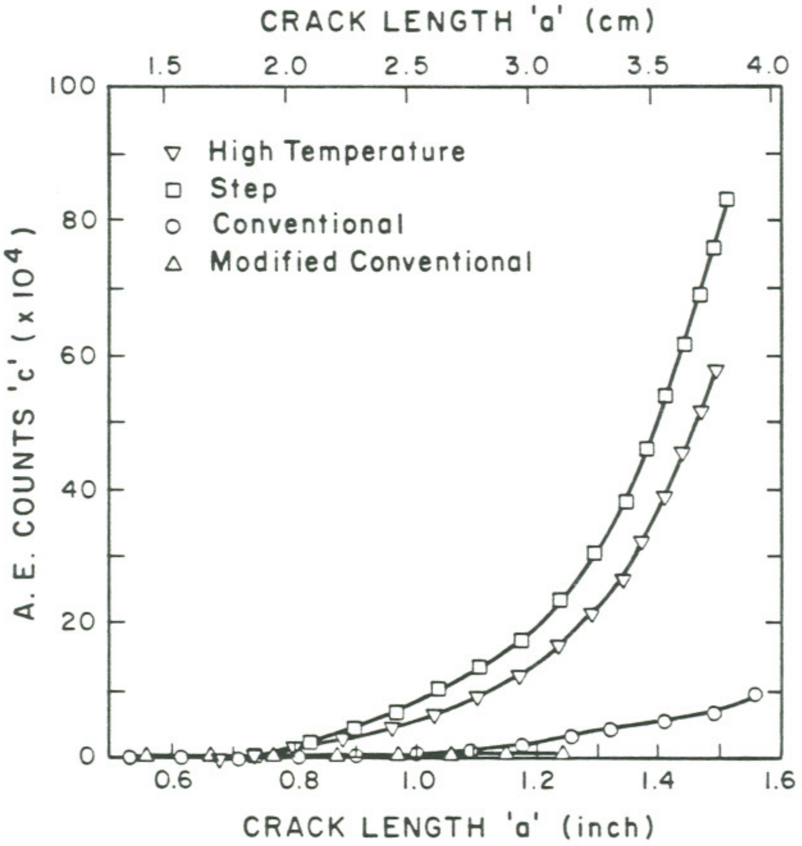

Figure 4-21: CUMULATIVE COUNTS VS. CRACK LENGTH FOR DIFFERENT HEAT TREATMENTS.

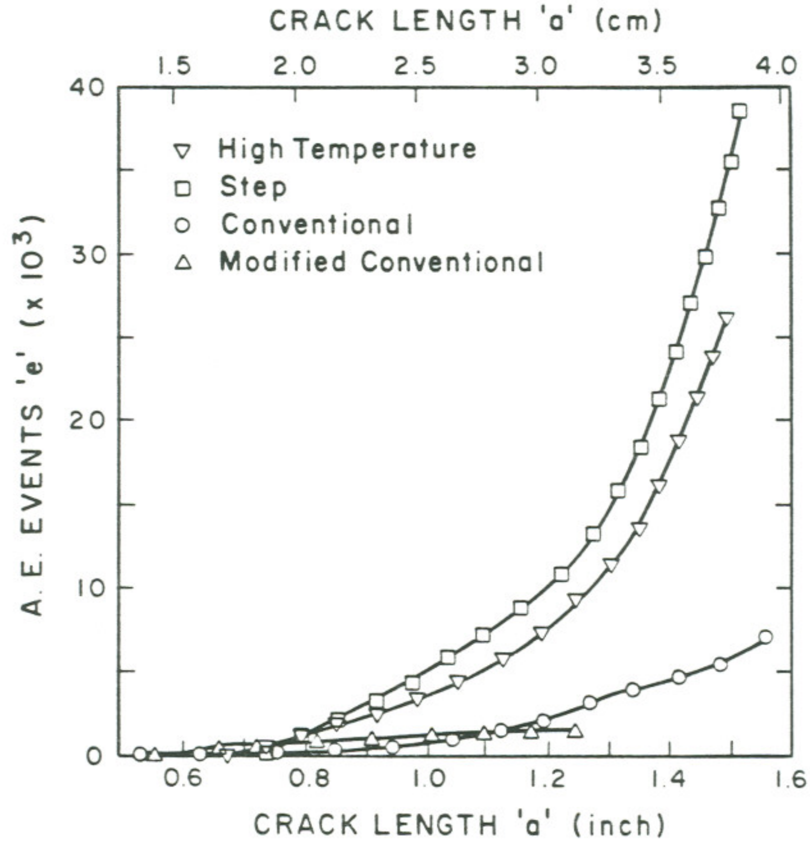

Figure 4-22: CUMULATIVE EVENTS VS. CRACK LENGTH FOR DIFFERENT HEAT TREATMENTS.

treatments. The trends in these data were exactly similar to the trend in the counts or events vs. time data, viz., the increase in counts or events with crack length was exponential except for modified conventional heat treatment where the increase was linear, for a given heat treatment. Also, the change in counts or events with respect to crack length was identical and the number of counts or events obtained was proportional to the prior austenite grain size. Since the change in counts and events with respect to either time or crack length was identical, crack extension with respect to time should be almost linear, and from the a vs. t diagrams (Figure 4-11), except for the initial and final regions of accelerated growth (which are limited to small intervals of time), the change in crack length with time was nearly linear. Also, since the change in counts or events with respect to time or crack length was identical, a plot of counts vs. events was also expected to be linear. This was confirmed in Figure 4-23.

The slopes of the a vs. t curves and counts vs. events curves were also evaluated. da/dt was determined at the midregion of the a vs. t curves to represent stage II crack growth rates. For conventional, high temperature, step and modified conventional heat treatments, the da/dt values obtained were respectively 8.46×10^{-5} cm/sec, 1.82×10^{-4} cm/sec, 1.69×10^{-4} cm/sec, and 6.38×10^{-5} cm/sec. These values were close to the stage II crack growth rates determined from the log (da/dt) vs. K_I curves. The dc/de values, determined from the center of counts vs. events curves for these heat treatments, were 14.21, 23.13, 23.03, and 4.88, respectively. It is apparent that dc/de was related to both the prior austenite grain size and the crack growth rate.

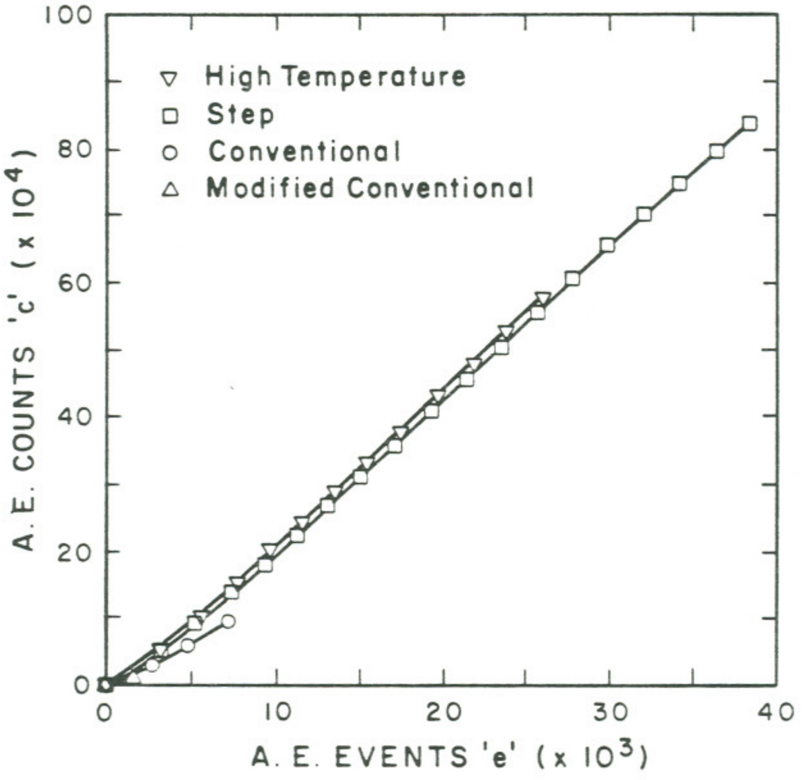

Figure 4-23: CUMULATIVE COUNTS VS. CUMULATIVE EVENTS FOR DIFFERENT HEAT TREATMENTS.

The counts rate and the events rate with respect to both time and crack extension, viz., dc/dt, de/dt, dc/da and de/da were plotted as a function of instantaneous stress intensity, in order to better analyze the different parameters. These results are presented in Figures 4-24 to 4-27. From Figure 4-24, it is seen that the counts rate increased continuously with K_I and also with respect to prior austenite grain size. The de/dt vs. K_I curves of Figure 4-25 also show the same dependence on both K_I and prior austenite grain size. In addition, there was a one-to-one correspondence between the counts and events rates. Identical results were obtained with dc/da and de/da vs. K_I curves (Figures 4-26 and 4-27). In addition, these curves exhibited a steady state region, corresponding to stage II region, where the rate of change of counts and events with respect to t or a was constant with K_I. An initial and final fast rate region, corresponding to stages I and III, respectively, were also observed in some cases. Extrapolation of these curves to zero rate coincided with the threshold stress intensity for any heat treatment.

Since the number of threshold counts per event for a given transducer depends on the energy released, these data were also analyzed. Figure 4-28 is a plot of dc/de vs. K_I for all the heat treatments. The shape of these curves was similar to the typical stress corrosion crack velocity curves [log (da/dt) vs. K_I]. Three regions, corresponding to stages I, II and III, were readily apparent. The extrapolation of stage I to zero counts/event coincided with the threshold stress intensity for that particular heat treatment. The stage II value of dc/de

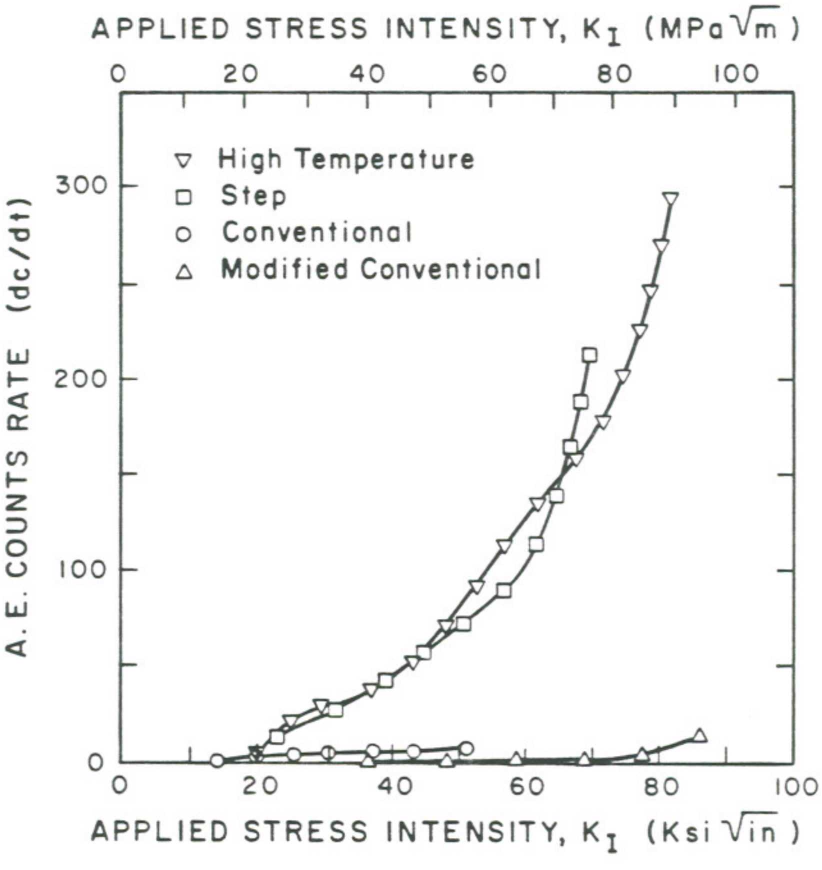

Figure 4-24: CUMULATIVE COUNTS RATE (dc/dt) VS. APPLIED STRESS INTENSITY FOR DIFFERENT HEAT TREATMENTS.

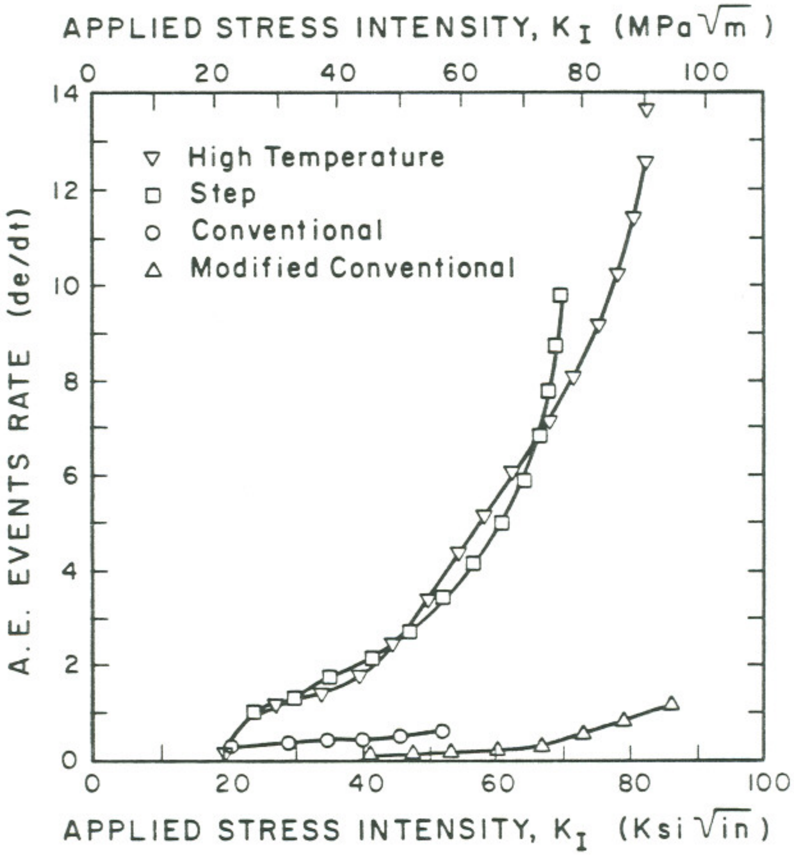

Figure 4-25: CUMULATIVE EVENTS RATE (de/dt) VS. APPLIED STRESS INTENSITY FOR DIFFERENT HEAT TREATMENTS.

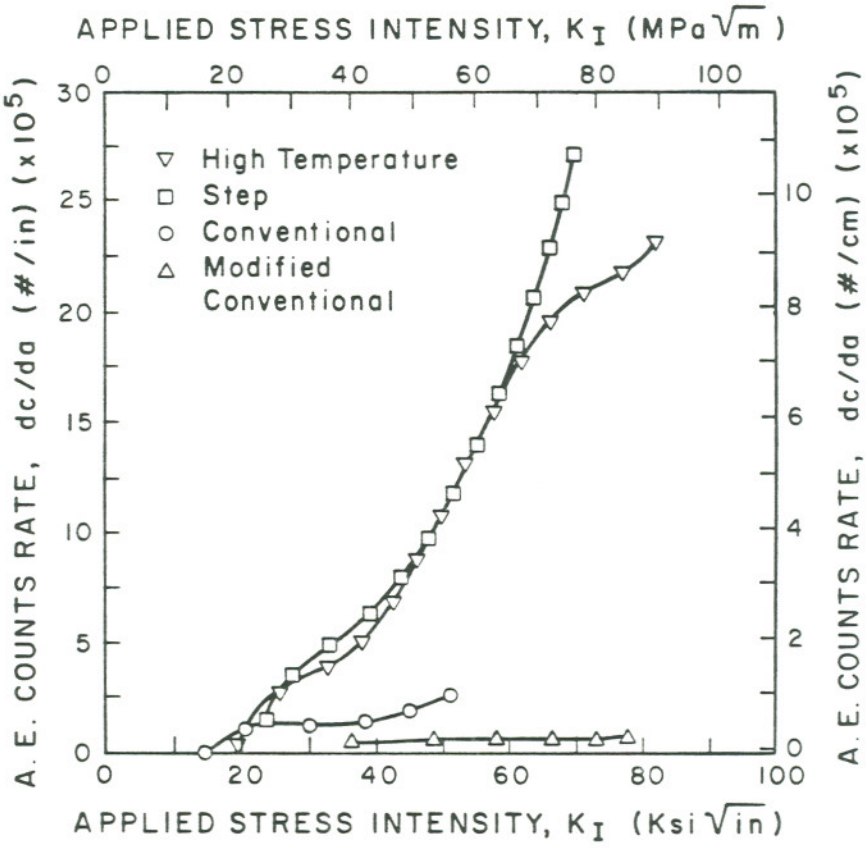

Figure 4-26: CUMULATIVE COUNTS RATE (dc/da) VS. APPLIED STRESS INTENSITY FOR DIFFERENT HEAT TREATMENTS.

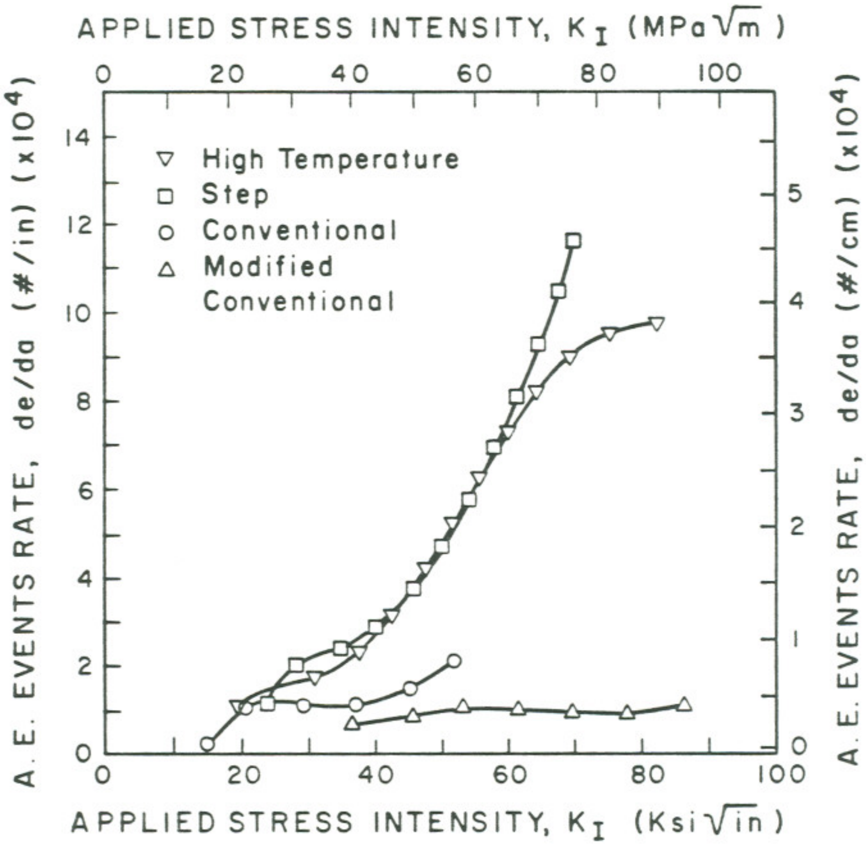

Figure 4-27: CUMULATIVE EVENTS RATE (de/da) VS. APPLIED STRESS INTENSITY FOR DIFFERENT HEAT TREATMENTS.

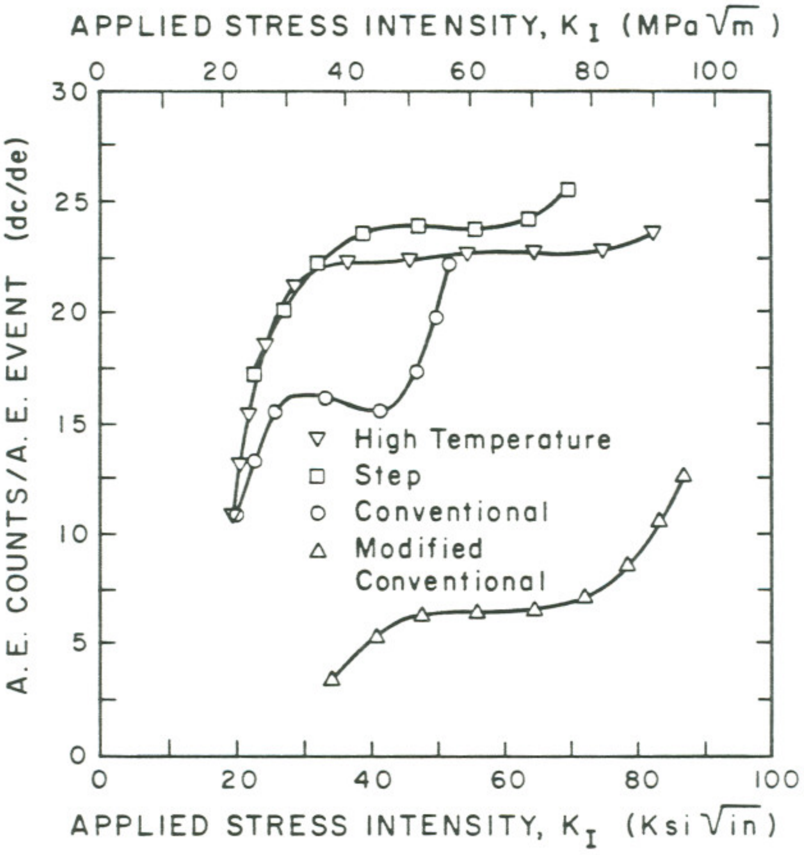

Figure 4-28: CUMULATIVE COUNTS PER EVENT (dc/de) FOR DIFFERENT HEAT TREATMENTS.

was dependent on the stage II crack growth rate and also on the prior austenite grain size, with higher crack growth rates and coarser grains yielding higher counts per event. Stage II dc/de values were also the same as those determined from the counts vs. events diagrams of Figure 4-23. The actual stage II dc/de values $[(dc/de)_{II}]$ were evaluated from these curves as 16.21, 22.51, 23.82 and 6.27, respectively, for conventional, high temperature, step and modified conventional heat treatments.

4.1.6. Summary: Mechanical Properties.

1. When compared with conventional heat treatment, the high temperature heat treatment improved the plane strain fracture toughness markedly at similar strength levels. However, impact properties and ductility showed a pronounced drop.

2. Step heat treatment also resulted in higher K_{Ic} as well as K_{Id}, but all other properties including yield strength and ultimate tensile strength decreased.

3. Cyclic heat treatment improved strength, ductility and impact properties, but fracture toughness decreased.

4. Modified heat treatments improved all mechanical properties when compared with the corresponding conventional, high temperature and step heat treatments.

5. When compared with conventional heat treatment, modified high temperature and modified step heat treatments improved fracture toughness even more than the corresponding high temperature and step heat treatments, while other properties showed lesser or no drop. The modified

conventional heat treatment, on the other hand, improved all the properties.

6. The threshold stress intensity (K_{Iscc}) values of high temperature and step heat treatments were identical and higher than for the conventional heat treatment.

7. K_{Iscc} of the modified conventional heat treatment was substantially higher than for all other heat treatments.

8. In region II, the average crack growth rate decreased slightly with stress intensity and the actual growth rate exhibited several sharp peaks and valleys, whose amplitudes decreased with increasing K_I.

9. State II crack growth rates were highest for high temperature and step heat treatments and lowest for modified conventional heat treatment with conventional heat treatment yielding an intermediate value.

10. The crack extension vs. time diagrams were almost linear, except for an initial and a final short region of fast extension. The slope of the a vs. t diagrams, evaluated at the mid-region, was indicative of stage II crack growth rate.

11. The number of threshold counts and cumulative events increased continuously with respect to both time and crack length.

12. The maximum number of counts and events were obtained for step heat treatment, followed by high temperature, conventional and modified conventional heat treatments, respectively.

13. The counts per event with respect to K_I curves showed a remarkable similarity to the stress corrosion curves, with three distinct regions, corresponding to stages I, II and III. The number of counts per

event was highest for step and high temperature heat treatments, followed by conventional and modified conventional heat treatments. Counts and events rate with respect to both time and crack extension increased continuously with respect to applied stress intensity, with the maximum rates obtained for step and high temperature heat treatments, followed by conventional and modified conventional heat treatments. In general, the counts and events rate curves exhibited three regions, similar to the stress corrosion crack velocity curves, with a pronounced steady state region, corresponding to stage II region.

14. The dc/de value corresponding to stage II was dependent upon da/dt, with high temperature and step heat treatments yielding the maximum value, followed by conventional and modified conventional heat treatments.

15. The extrapolation of the counts and events rates and the counts per event curves to zero rate coincided with threshold stress intensity values.

16. With respect to a given parameter, the change in cumulative counts or counts rate exhibited a one-to-one correspondence with the change in events or events rate.

4.2. Microstructure

4.2.1. Optical Microscopy. The prior austenite grain sizes of 300M steel, under various heat treated conditions, are presented in Figure 4-29 and the actual grain size values measured from these micrographs are listed in Table 4-9. High temperature and step heat treatments resulted in an order of magnitude higher grain size (220 μm) compared with conventional heat treatment (20 μm), whereas cyclic heat treatment refined the grains considerably (10 μm). All the modified heat treatments resulted in finer grains when compared with the non-modified heat treatments--the modified conventional, modified high temperature and modified step heat treatments resulting in grain sizes of 15 μm, 80 μm, and 80 μm, respectively. In the case of high temperature and step heat treatments, the grain sizes were observed directly after polishing and etching, while for all the other heat treatments, temper embrittling was necessary to highlight the grain boundaries. Thus, grain refinement occurred in cyclic and modified heat treatments, and the extent of refinement increased with the number of cycles between austenite and martensite phases. This is consistent with the observations of other investigators [24-26, 46].

Polished and etched specimens subjected to conventional, high temperature and step heat treatments were also examined at high magnifications. As seen in Figure 4-30, a distinctive etching (usually dark) constituent was often observed at the prior austenite grain boundaries. Similar dark etching phases were also observed by other investigators [1, 3,5,8,14] for many steels. However, this phase was noted only for high

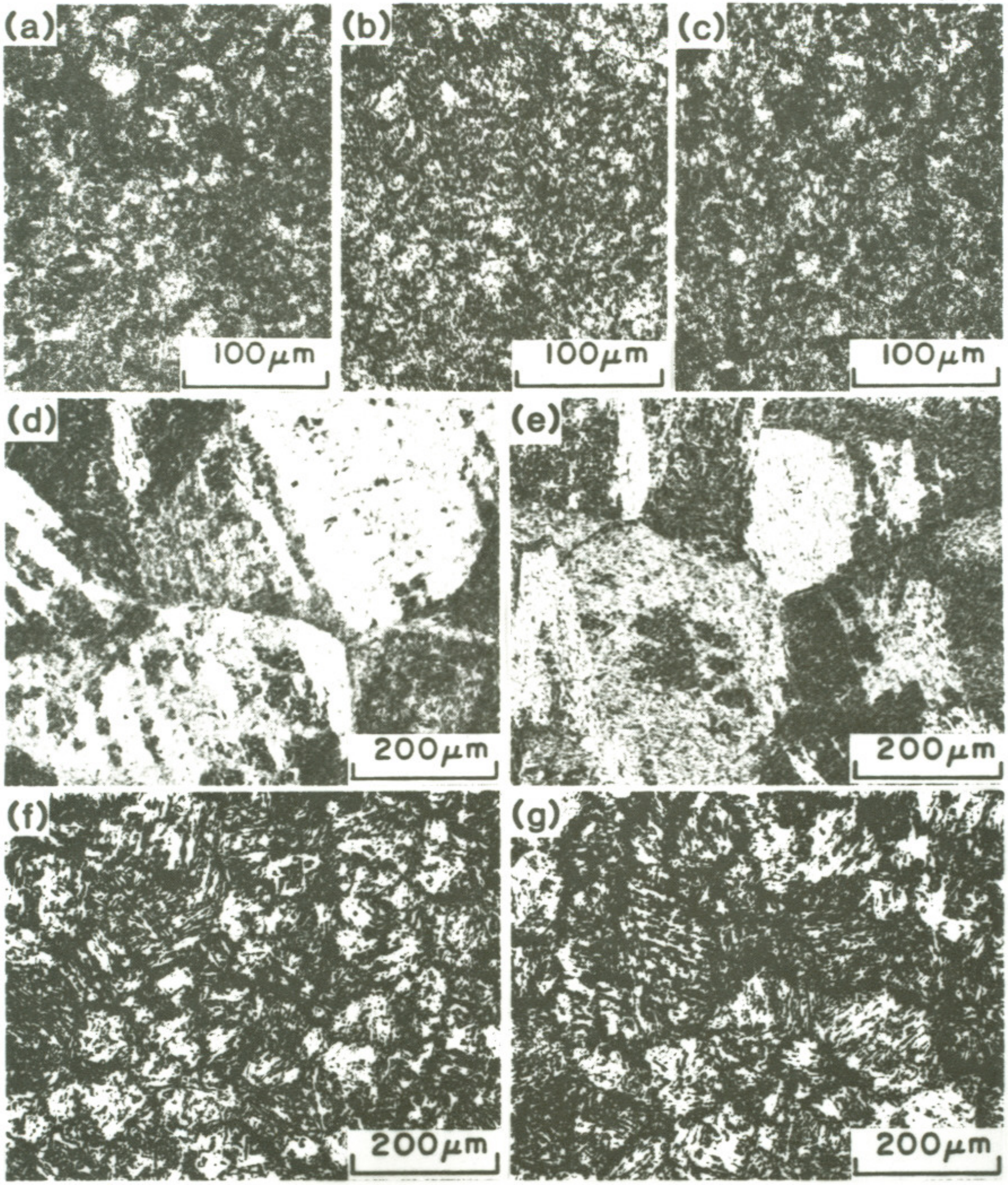

Figure 4-29: OPTICAL MICROGRAPHS COMPARING PRIOR AUSTENITIC GRAIN SIZES OF (a) CONVENTIONAL, (b) CYCLIC, (c) MODIFIED CONVENTIONAL, (d) HIGH TEMPERATURE, (e) STEP, (f) MODIFIED HIGH TEMPERATURE, AND (g) MODIFIED STEP HEAT TREATMENTS.

TABLE 4-9

PRIOR AUSTENITIC GRAIN SIZE OF 300M STEEL UNDER DIFFERENT HEAT TREATED CONDITIONS.

Heat Treatment	Grain Size (μm)
Conventional (870°C/280°C)	20 (± 2)
Cyclic (870°C/850°C/280°C) (4 cycles)	10 (± 2)
High Temperature (1200°C/280°C)	220 (±20)
Step (1200°C/870°C/280°C)	220 (±20)
Modified Conventional (870°C/650°C/850°C/280°C)	15 (± 2)
Modified High Temperature (1200°C/650°C/850°C/280°C)	80 (±10)
Modified Step (1200°C/870°C/650°C/850°C/280°C)	80 (±10)

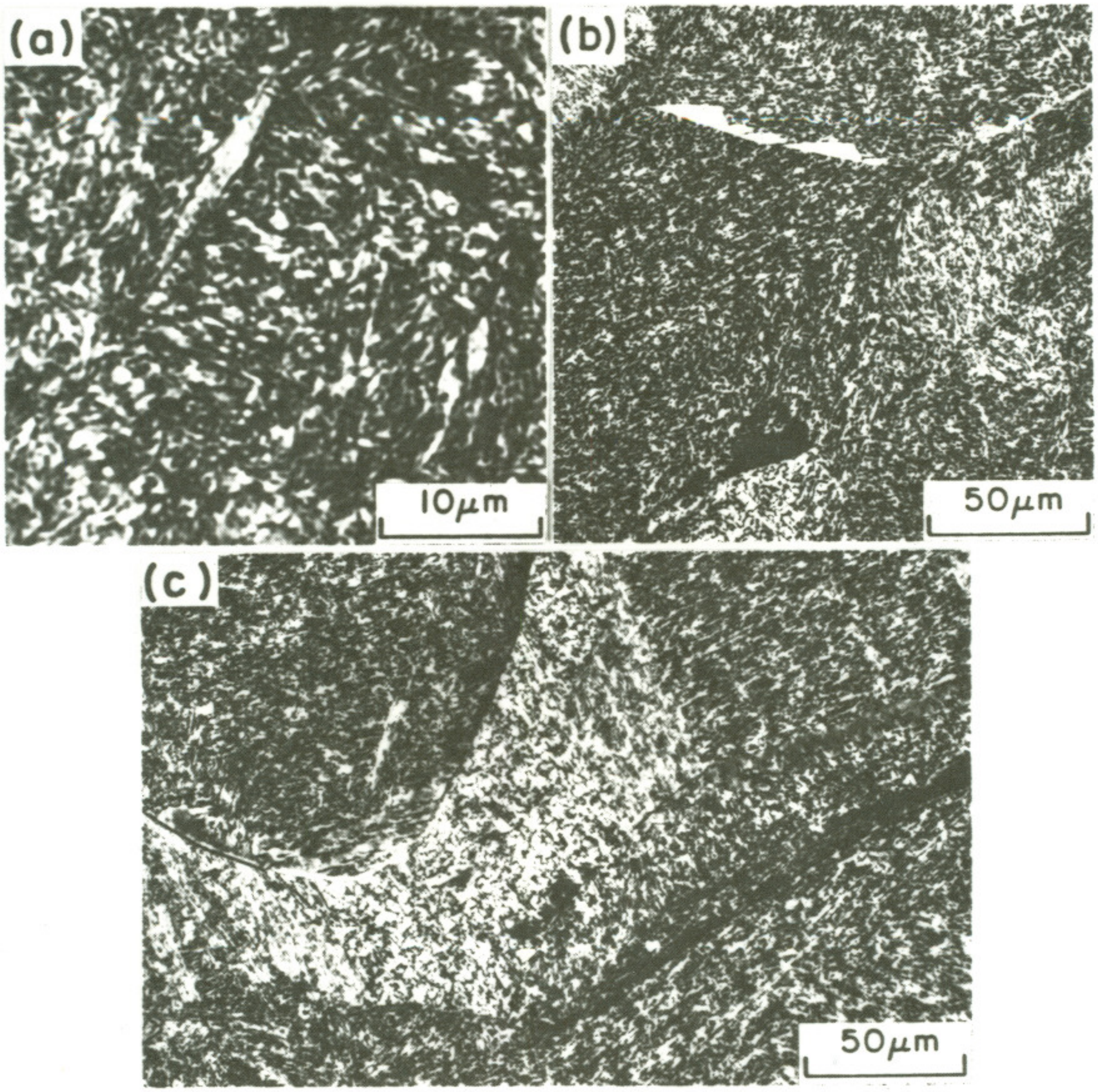

Figure 4-30: OPTICAL MICROGRAPHS SHOWING GRAIN BOUNDARY CONSTITUENT IN (a) CONVENTIONAL, (b) HIGH TEMPERATURE AND (c) STEP HEAT TREATMENTS.

temperature heat treatment in 300M steel. It was suggested by these investigators that this dark etching phase was bainite or other non-martensitic product. The examination of this phase by methods other than optical microscopy was carried out to positively identify this phase and these results are presented in the next sections.

4.2.2. Scanning Electron Microscopy. Polished and etched specimens (with a heavier etch than for optical microscopy) subjected to conventional, high temperature and step heat treatments, were observed in SEM. From the low magnification pictures of Figure 4-31, the basic difference in the general martensitic structure of the high temperature and step heat treatments on the one hand and the conventional heat treatment on the other was immediately seen. The conventional heat treatment produced more lenticular, platelike martensite, whereas the high temperature and step heat treatments resulted in lathlike martensite. This is discussed in Section 4.2.3.1. The grain boundary phase initially observed by optical microscopy (Section 4.2.1.) was visible. These SEM pictures confirmed that this grain boundary constituent (ranging in size from 1 μm to 10 μm) occurred irrespective of the austenitization temperature in both coarse and fine grained material unlike the observations of earlier investigators [1,3,5,8,14]. Additionally, the high magnification pictures of this phase (Figure 4-32) revealed the presence of parallel rows of wavy particles, probably iron carbide, inclined at an angle of almost 55° to the boundary (long axis) of the phase. Attempts to establish the composition of these carbides through energy dispersive analysis proved futile, since the particle size was less than 1 μm. Since the

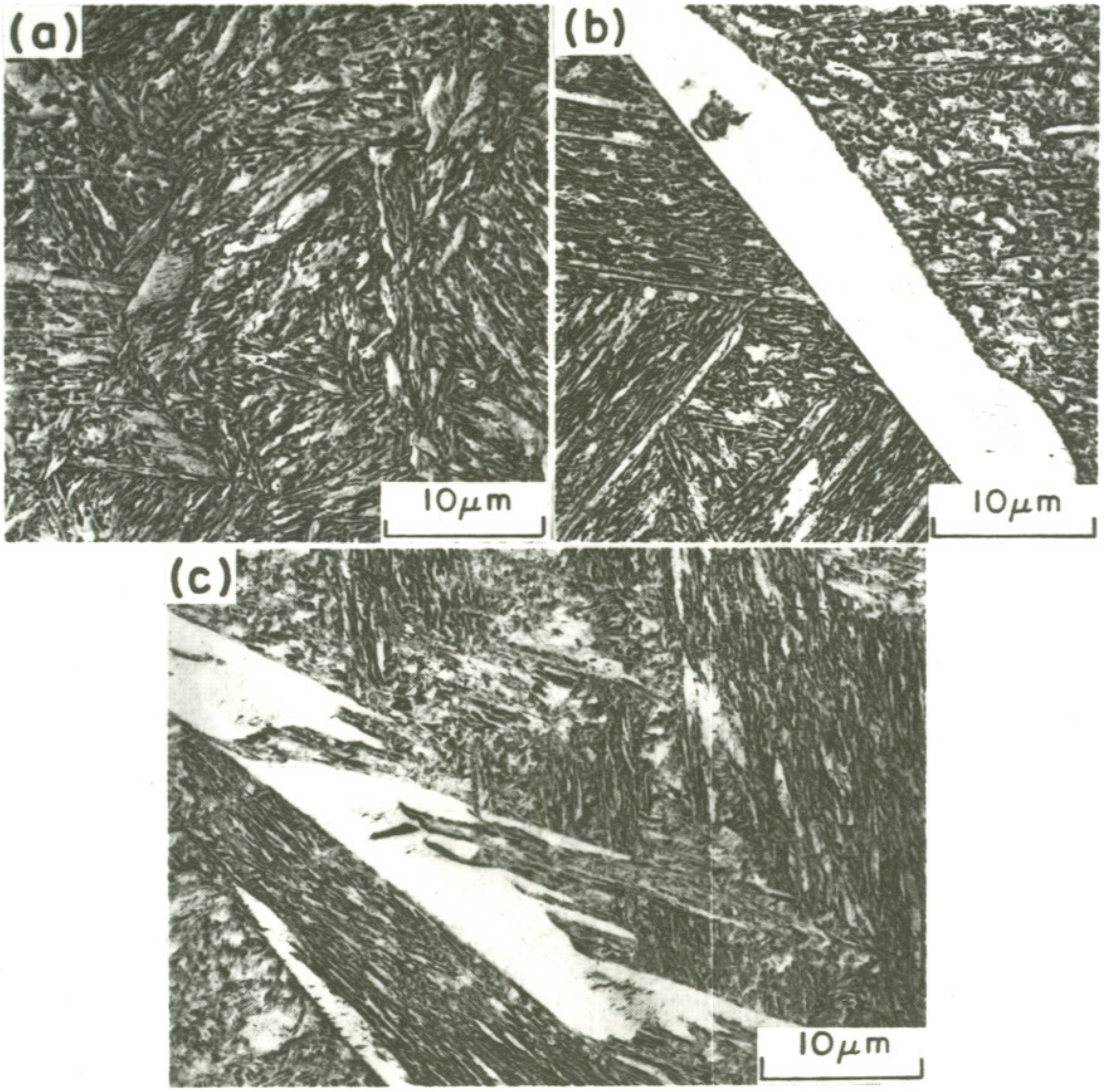

Figure 4-31: SEM MICROGRAPHS SHOWING THE STRUCTURE OF (a) CONVENTIONAL, (b) HIGH TEMPERATURE AND (c) STEP HEAT TREATMENTS. THE GRAIN BOUNDARY CONSTITUENT IS ALSO SEEN IN ALL CASES.

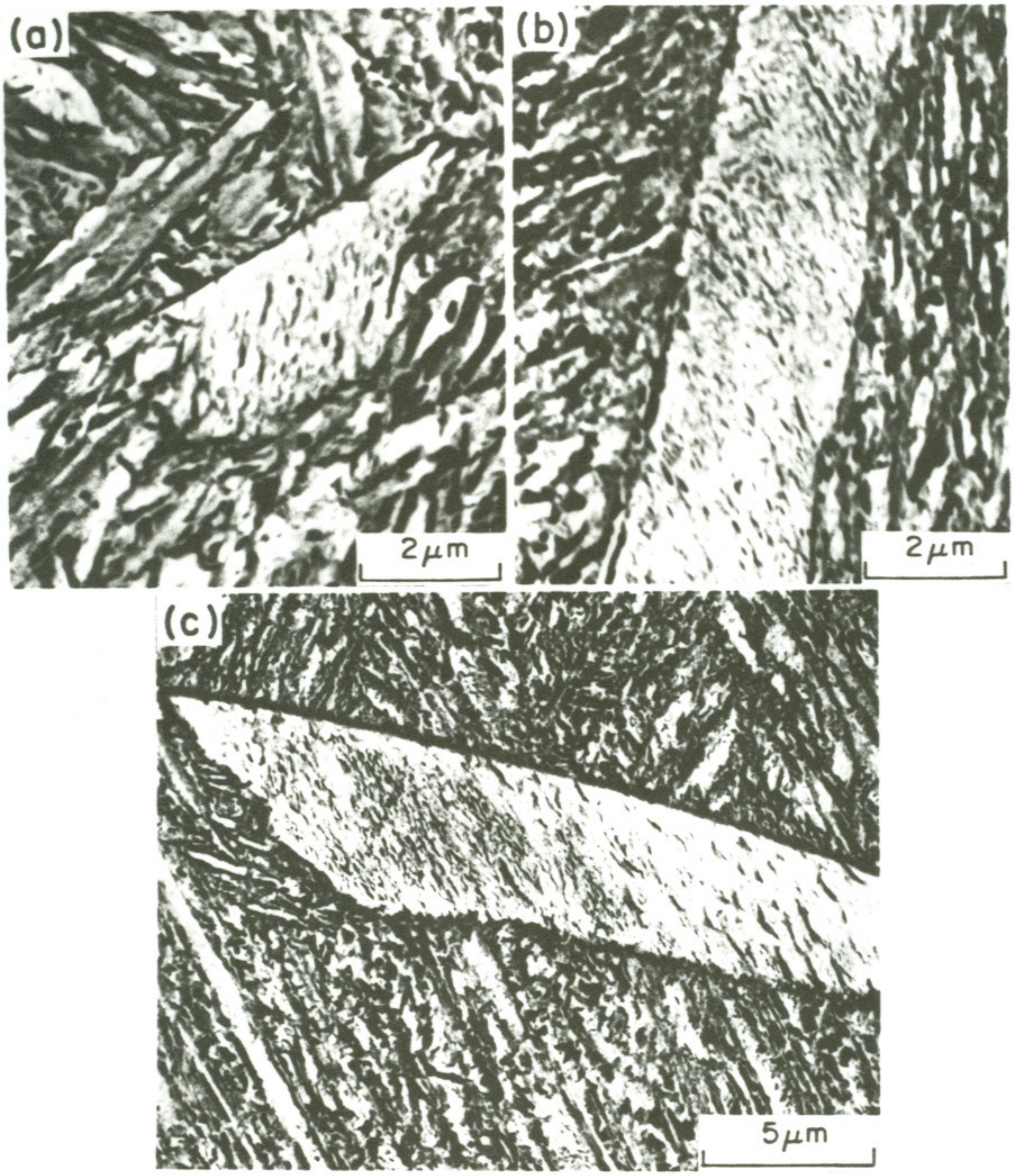

Figure 4-32: SEM MICROGRAPHS SHOWING CARBIDE PRECIPITATION WITHIN GRAIN BOUNDARY CONSTITUENT IN

(a) CONVENTIONAL, (b) STEP AND (c) HIGH TEMPERATURE HEAT TREATMENTS.

arrangement of carbides within this phase resembled the characteristic lower bainite feature [48-53] and since the quenching rate obtained in these steels was believed to be sufficient to prevent any bainitic formation, this phase was studied further through TEM and these results are presented in Section 4.2.3.5.

The modified heat treatments were also studied by SEM. The grain boundary phases seen in Figures 4-31 and 4-32 for the other heat treatments were also seen in these heat treatments (Figure 4-33). However, the particle morphology varied within these phases. In addition to wavy particles arranged along parallel rows at an angle of 55° to the longitudinal axis of these phases, a random distribution of spheroidal particles within these phases (the dark spots seen in Figure 4-33 are not to be confused with etch pits) was visible. In the inverse contrast mode, the topology is also reversed and, hence, the true topology was studied under normal contrast mode. Identification of these carbides by energy dispersive analysis was again not possible due to their size. Hence, a conventionally heat treated specimen was further tempered at 650°C for 1 hour and quenched directly to room temperature, without reaustenitizing at 850°C for short times as in the case of modified conventional heat treatment. The nature of the carbides precipitated at 650°C in this heat treatment should be the same as in the case of the modified conventional heat treatment, except that the size of these carbides will be much coarser. Figure 4-34 shows these carbides in both normal and inverse contrast modes. Although these carbides were much coarser than those shown in Figure 4-33, for the modified heat treatments, these were still

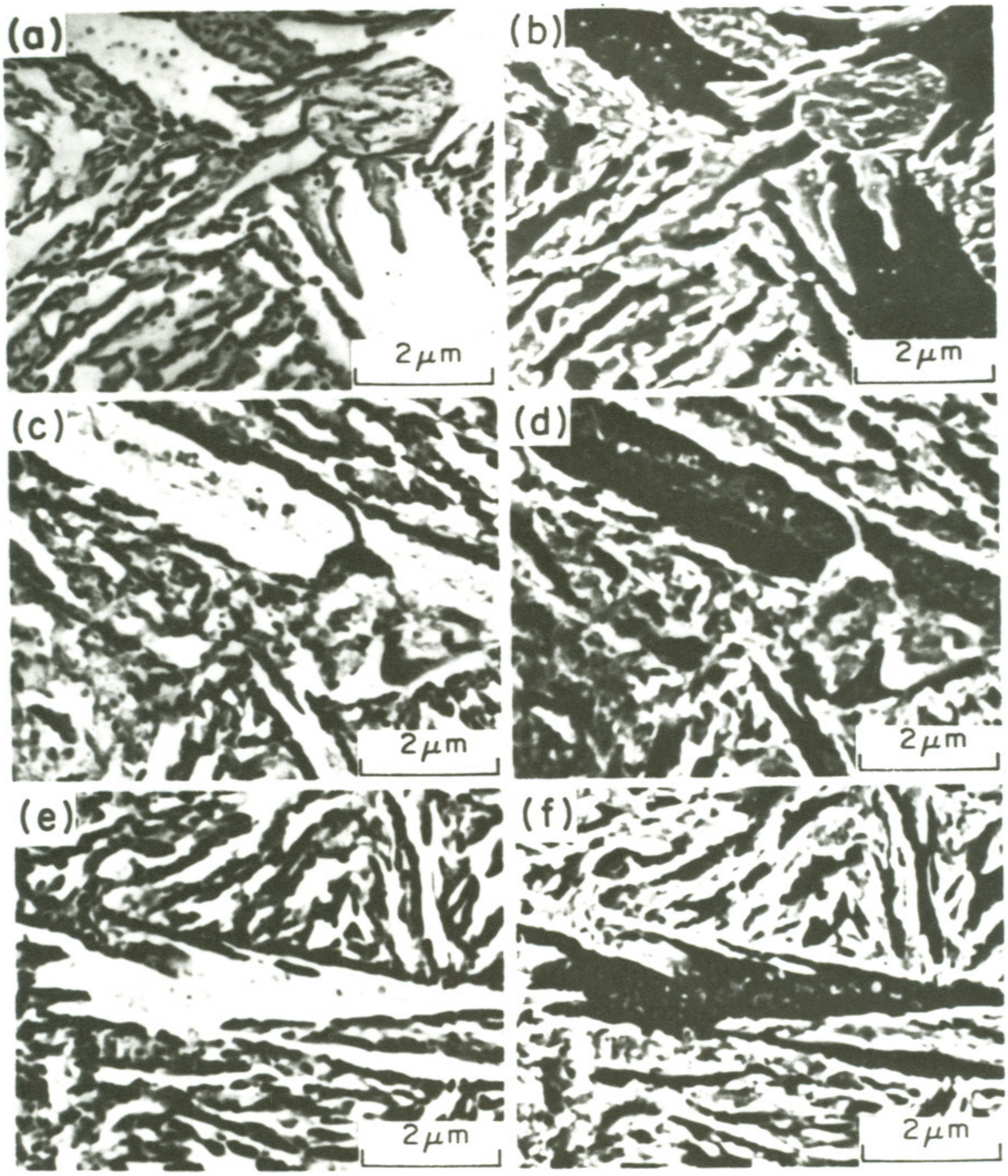

Figure 4-33: SEM MICROGRAPHS SHOWING RANDOM DISTRIBUTION OF CARBIDES IN (a) and (b) MODIFIED CONVENTIONAL, (c) AND (d) MODIFIED HIGH TEMPERATURE AND (e) AND (f) MODIFIED STEP HEAT TREATMENTS.

NOTE: (a), (c) AND (e) UNDER INVERSE AND (b), (d) AND (f) UNDER NORMAL CONTRAST MODES.

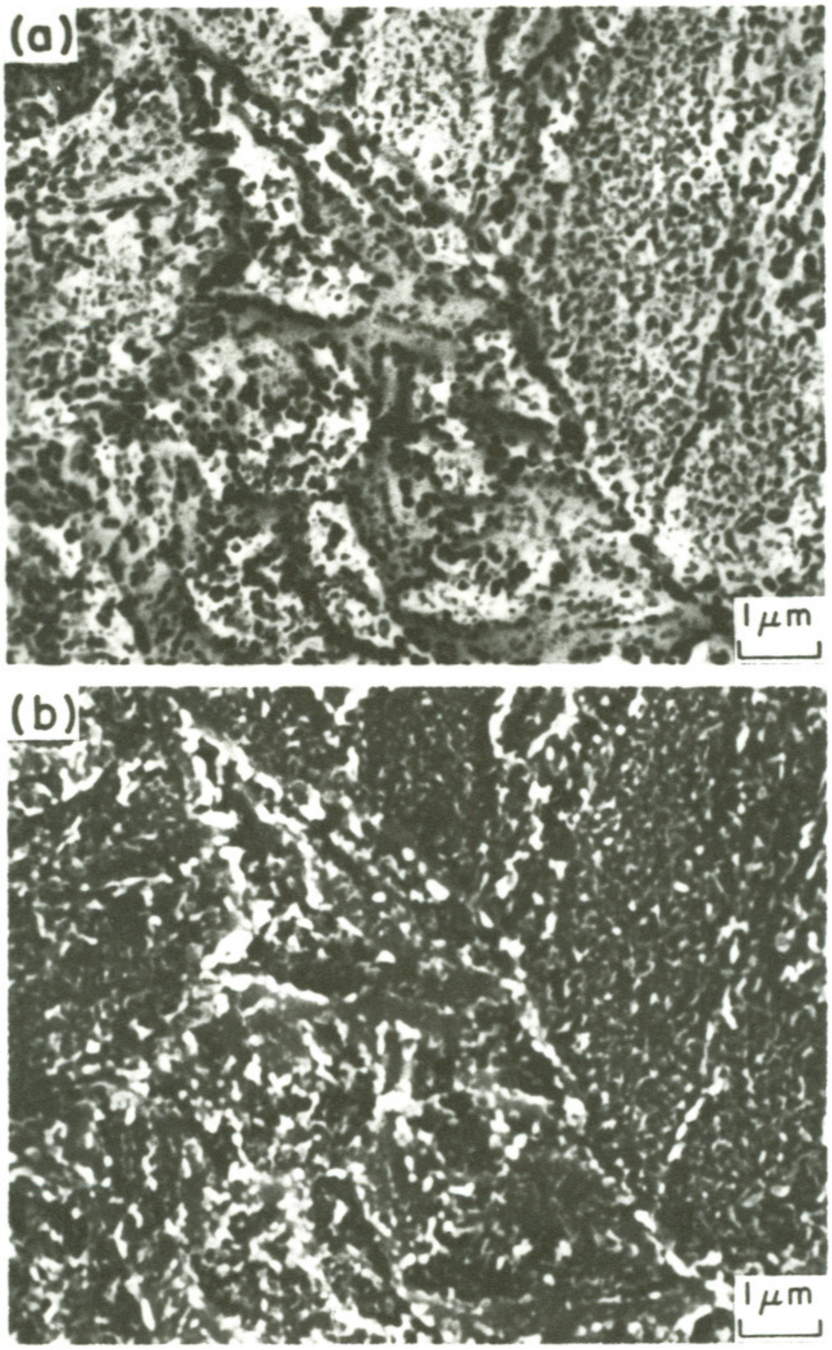

Figure 4-34: SEM MICROGRPAHS SHOWING EXTENSIVE CARBIDE PRECIPITATION IN A SPECIMEN QUENCHED DIRECTLY TO ROOM TEMPERATURE AFTER INTERMEDIATE TEMPERING STEP.
NOTE: (a) INVERSE AND (b) NORMAL CONTRAST MODES.

not coarse enough to yield sufficient electron counts for energy dispersive analysis. Hence, the modified heat treated specimens were examined under TEM.

4.2.3. Transmission Electron Microscopy.

4.2.3.1. General Microstructure. TEM studies were carried out for all heat treatments and the results are presented in these sections.

The microstructure obtained as a result of conventional heat treatment is typified in the bright field picture of Figure 4-35a. It consisted of both lath and plate type martensite, with the amount of plate martensite predominating. Internal faults like twins and dislocations were extensively present and the martensite plates or laths in many instances extended across the whole grain. The average lath width was 0.3 μm.

The microstructure of cyclic heat treatment is indicated in Figure 4-35b. All the observations made for the conventional heat treatment apply in this case, too. Both types of martensite (with plate martensite predominating) were seen and twins and dislocations were also extensively present. In many instances, the plate or lath extended across the whole grain. The average lath width in this case was 0.25 μm.

Figure 4-35c shows the microstructure of high temperature heat treatment, and although both types of martensite were seen, the amount of lath martensite predominated. While dislocations and twins were still present, twins were seen only very occasionally. Also, the lath or plate rarely

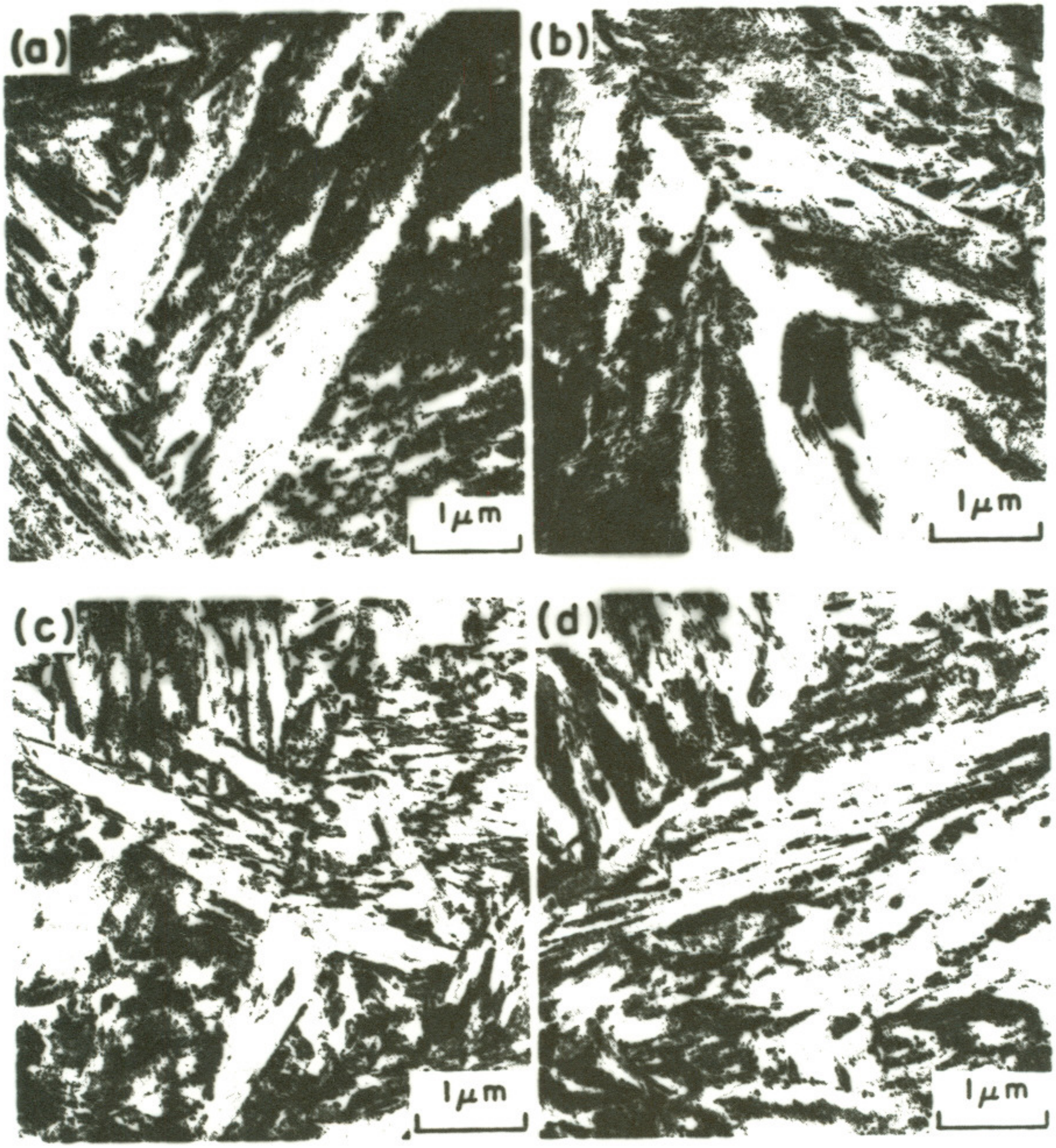

Figure 4-35: BRIGHT FIELD TEM MICROGRAPHS SHOWING PREDOMINANTLY PLATE MARTENSITE FOR (a) CONVENTIONAL AND (b) CYCLIC HEAT TREATMENTS AND PREDOMINANTLY LATH MARTENSITE FOR (c) HIGH TEMPERATURE AND (d) STEP HEAT TREATMENTS. TWINNED REGIONS CAN BE IDENTIFIED IN (a), (b) and (c).

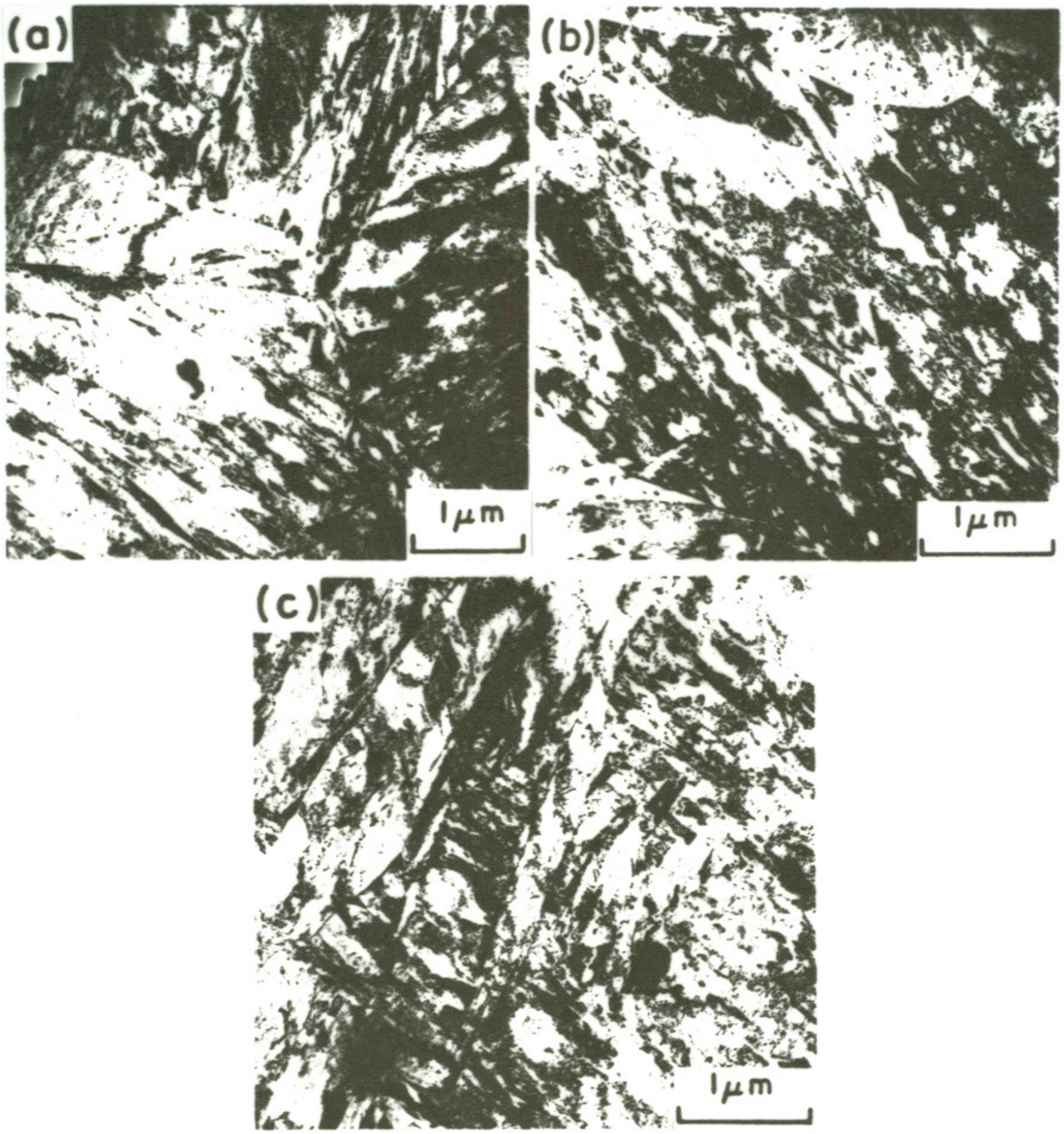

Figure 4-36: BRIGHT FIELD MICROGRAPHS SHOWING PREDOMINANTLY LATH MARTENSITE FOR (a) MODIFIED CONVENTIONAL, (b) MODIFIED HIGH TEMPERATURE AND (c) MODIFIED STEP HEAT TREATMENTS.

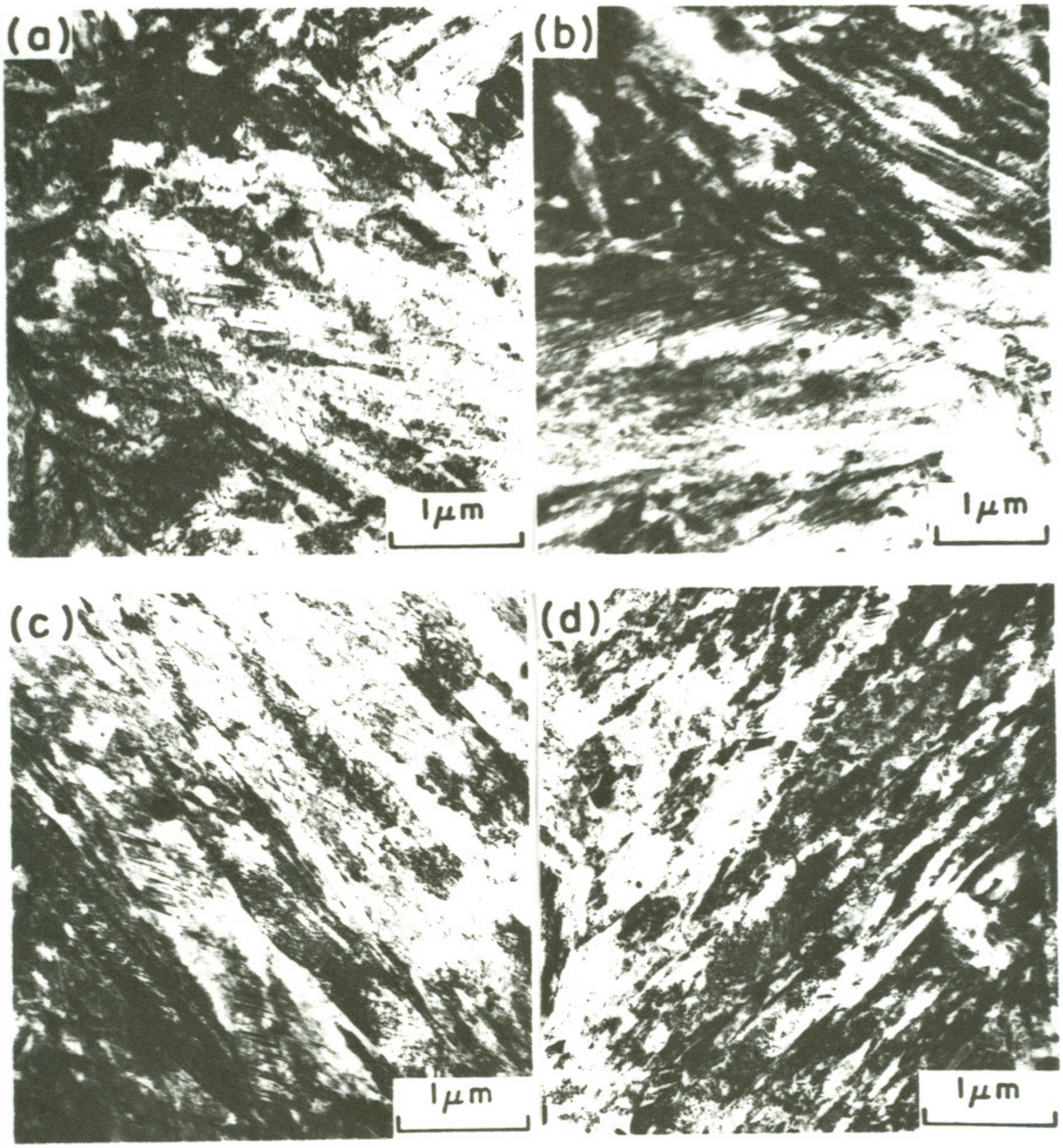

Figure 4-37: BRIGHT FIELD TEM MICROGRAPHS SHOWING EXTENSIVE TWINNING IN PLATE MARTENSITIC REGIONS OF (a) AND (b) CYCLIC HEAT TREATMENT AND LIMITED MICROTWINNING WITHIN LATHS OF (c) AND (d) HIGH TEMPERATURE HEAT TREATMENTS.

in a twin-related fashion. The predominant orientations were <100> and <111>, although <113> and <110> zone axes were also regularly observed. Three basic lath morphologies were observed, viz., convergent, parallel and large laths. Figure 4-38a shows a typical convergent lath morphology, wherein the laths merged together along curved boundaries. Regular parallel laths are shown in Figure 4-38b. These laths were usually separated along planar boundaries. Figure 4-38c is an example of large laths, containing extensive carbide precipitation within, which suggests that these laths were formed in the early stages of the austenite to martensite transformation.

As noted earlier, microtwins within laths were also reported by other investigators [54-57] in plain carbon and alloy steels. Law et al. [57] as well as Chilton et al. [58] also noted the occurrence of different lath morphologies, similar to the observations in the present investigation. Law et al. [57] utilized dark field imaging to eliminate sectioning effects as the reason for variation in lath morphology. Rao et al. [59] reported that laths of martensite occur predominantly in juxtaposition to <100> and <111> orientations. This is consistent with the observations of this investigation.

4.2.3.2. Effect of Heat Treatment on Twinning. Figures 4-39 to 4-41 show typically twinned regions for 300M steel subjected to conventional, cyclic and high temperature and step heat treatments, respectively. Twins occurred along {112} planes, which is the case for bcc structures [67-71]. The dark field pictures obtained using {110} type twin spots highlighted these twins clearly. The maximum amount of

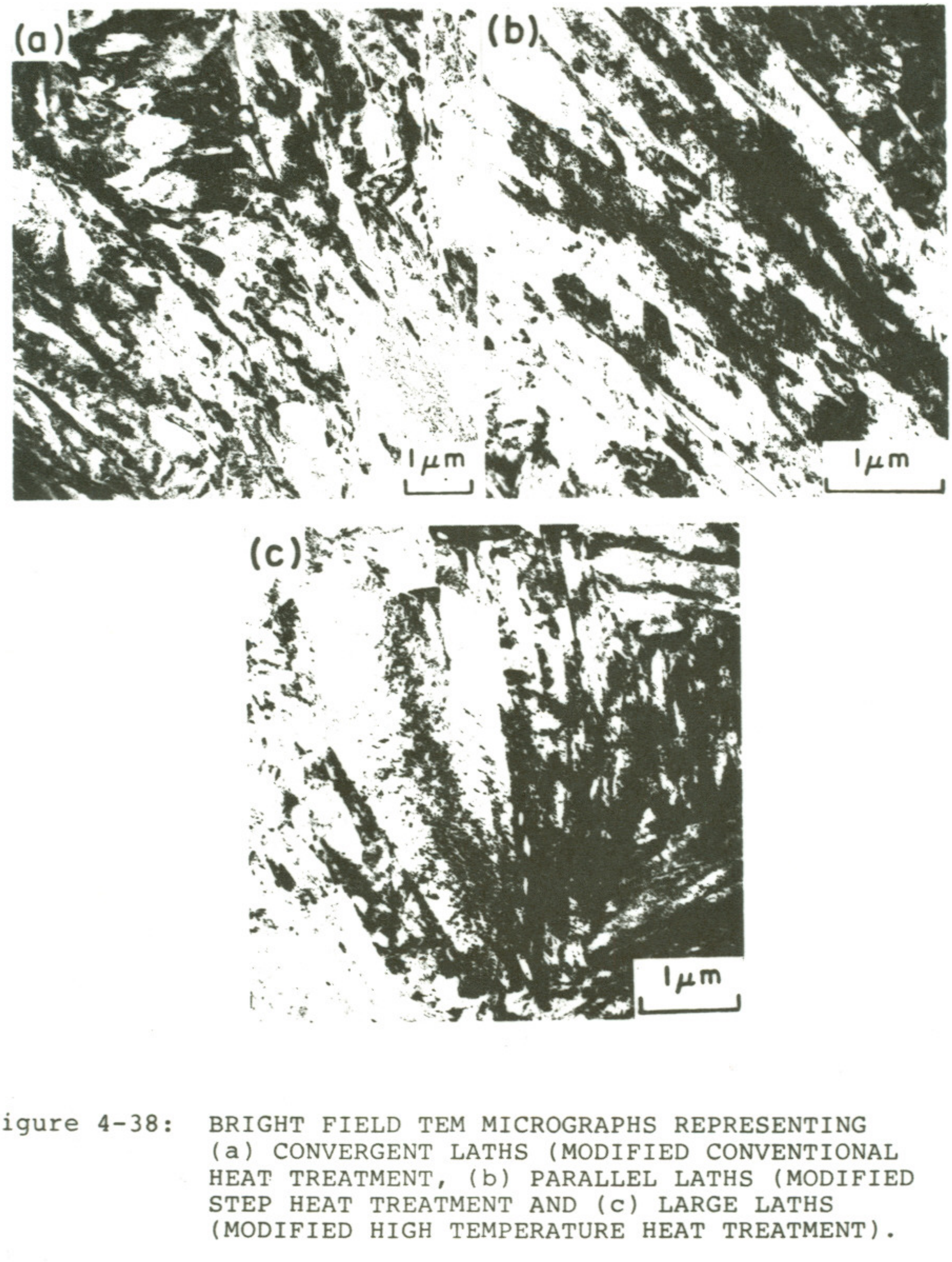

Figure 4-38: BRIGHT FIELD TEM MICROGRAPHS REPRESENTING (a) CONVERGENT LATHS (MODIFIED CONVENTIONAL HEAT TREATMENT, (b) PARALLEL LATHS (MODIFIED STEP HEAT TREATMENT AND (c) LARGE LATHS (MODIFIED HIGH TEMPERATURE HEAT TREATMENT).

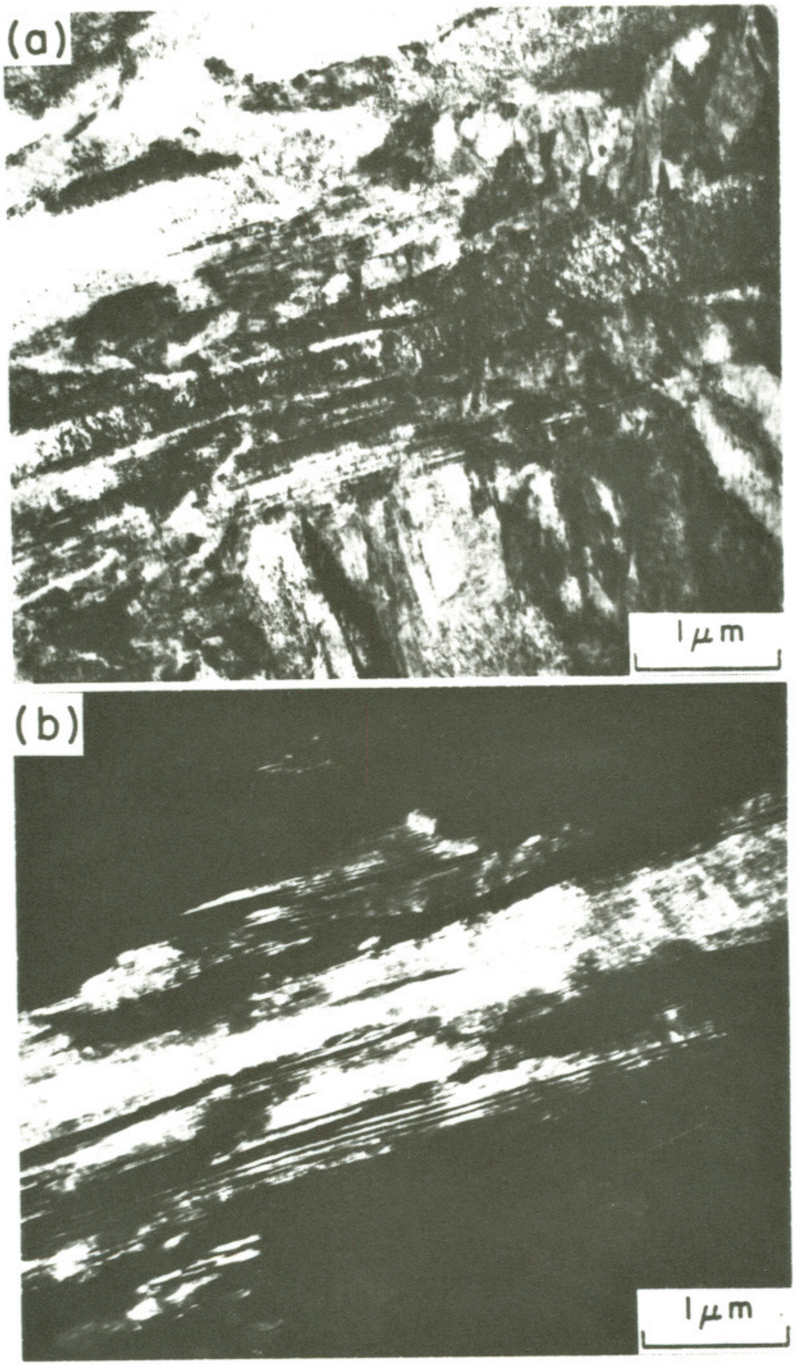

Figure 4-39: (a) BRIGHT FIELD TEM MICROGRAPH SHOWING A TWINNED REGION IN A CONVENTIONALLY HEAT TREATED SPECIMEN AND (b) DARK FIELD IMAGE USING $(01\bar{1})$ TWIN SPOT, HIGHLIGHTING THE TWINS. S.A.D. PATTERN WAS SIMILAR TO THE ONE IN FIGURE 4-40.

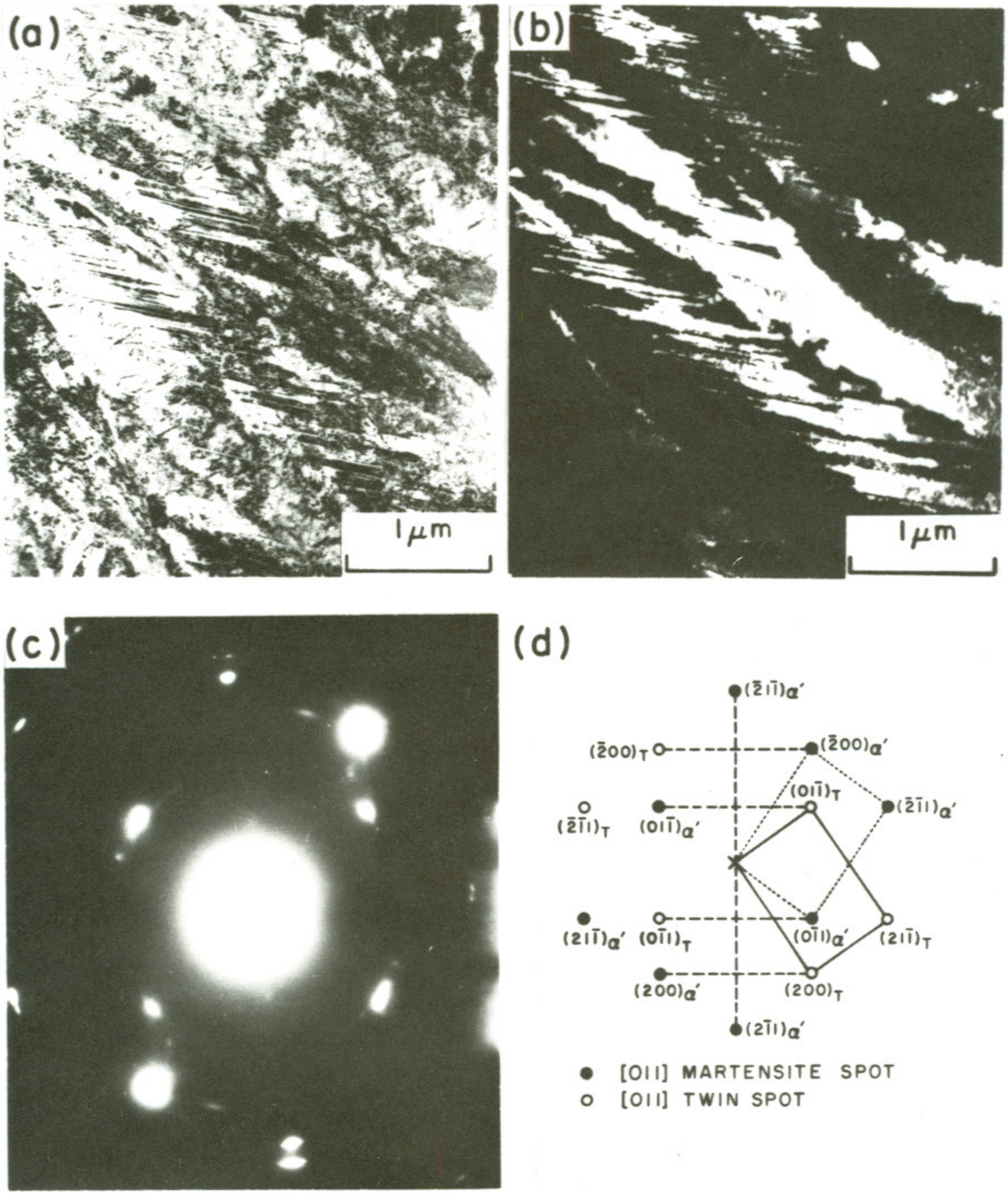

Figure 4-40: (a) BRIGHT FIELD TEM MICROGRAPH SHOWING A TWINNED REGION IN A CYCLICALLY HEAT TREATED STEEL, (b) DARK FIELD IMAGE USING $(01\bar{1})$ TYPE TWIN SPOT, (c) SELECTED AREA DIFFRACTION PATTERN FROM THE TWINNED REGION AND (d) INTERPRETATION OF THE S.A.D. PATTERN.

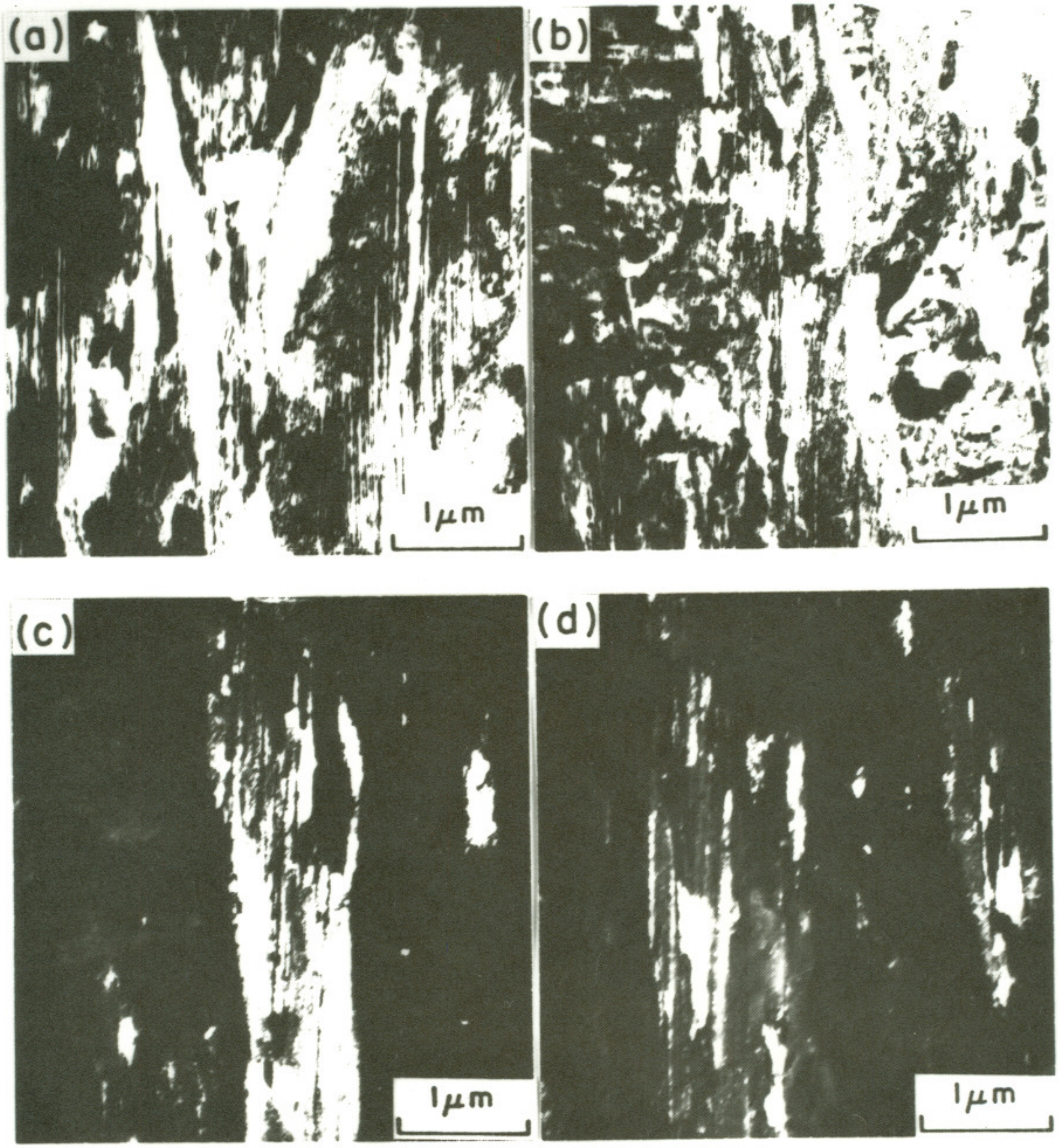

Figure 4-41: TEM BRIGHT FIELD MICROGRAPHS (a) AND (b) SHOWING TWINNED REGIONS IN HIGH TEMPERATURE AND STEP HEAT TREATMENTS RESPECTIVELY. DARK FIELD IMAGES (c) AND (d) HIGHLIGHT THE TWINS IN (b) AND WERE OBTAINED USING $(0\bar{1}1)$ AND (200) TYPE TWIN SPOTS (S.A.D. PATTERN WAS SIMILAR TO THE ONE IN FIGURE 4-40).

twinning was observed in the case of conventional and cyclic heat treatments and the high temperature heat treatment contained very few twinned regions. The step heat treatment resulted in more twins than the high temperature heat treatment, and all the modified heat treatments produced very few, if any, twins and a rare twinned region is shown in Figure 4-42 for modified conventional heat treatment.

The above results are, in general, consistent with the observations of earlier investigators. Increased amounts of lath martensite and reduced twinning with increasing austenitization temperatures were reported for 4340 and 300M steels [4,7,17,19]. On the other hand, Carlson et al. [60] reported increased twinning with increased austenitization temperature, due to greater carbon dissolution. While dissolution of carbon should lower M_s temperature, an increase in M_s temperature was reported for many steels, including low alloy steels, with increasing austenitization temperatures [4,61-64], which should decrease the tendency for formation of twins [65]. This was, in fact, confirmed in this investigation, where an increase in austenitization temperature resulted in decreased twin density. Lai et al. [4] also reported that plate martensite obtained from high temperature heat treatment was twin free. However, in this investigation, twinned plate martensite was occasionally observed (Figure 4-41). The observed decrease in twinning with increasing austenitization temperature is also consistent with segregation effects in these steels. It was reported that higher austenitization temperatures reduce segregation and increase homogeneity of steel [1,2,5,54,66]. The change in stacking fault energy with local variations of alloying and

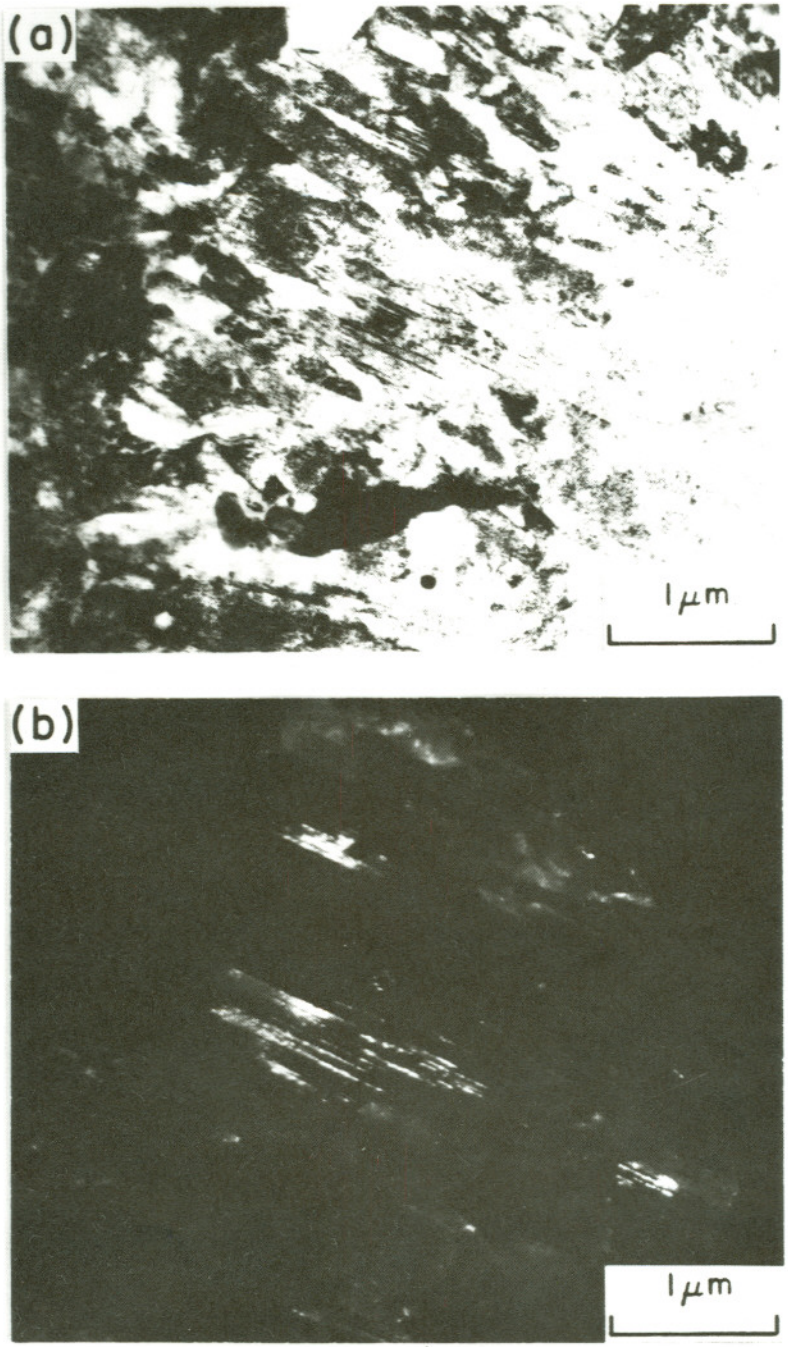

Figure 4-42: (a) BRIGHT FIELD TEM MICROGRAPH SHOWING A TWINNED REGION IN MODIFIED CONVENTIONAL HEAT TREATMENT AND (b) DARK FIELD IMAGE USING (011) TYPE TWIN SPOT HIGHLIGHTING THE TWINS (S.A.D. PATTERN WAS SIMILAR TO THE ONE IN FIGURE 4-40).

impurity elements was shown to have an effect on twin density by Khan and Wood [18], who found an increase in twin density in step heat treatments, the amount depending upon both intermediate holding temperatures and holding times at these temperatures. This was also confirmed in this investigation where twin density increased by step cooling the steel.

4.2.3.3. Effect of Heat Treatment on Retained Austenite.

All heat treatments resulted in some predominantly interlath films of retained austenite, although retained austenite was also seen occasionally at prior austenite grain boundaries and packet boundaries. The amount of retained austenite depended upon austenitization temperature, with high temperature and step heat treatments resulting in more retained austenite than conventional heat treatment. Cyclic heat treatment produced more retained austenite than conventional heat treatment. However, all modified heat treatments resulted in increased amounts of retained austenite when compared with the ocrresponding non-modified heat treatments. The modified conventional heat treatment produced less retained austenite than the modified step and modified high temperature heat treatments.

Figures 4-43 to 4-49 show mostly interlath films of retained austenite, ranging in thickness between 100 Å and 200 Å, for conventional, cyclic, high temperature, step, modified conventional, modified high temperature and modified step heat treatments, respectively. Dark field pictures revealed the retained austenite morphology and were all taken using {002} or {111} type retained austenite spots. Films of retained austenite at packet and prior austenite grain boundaries were also

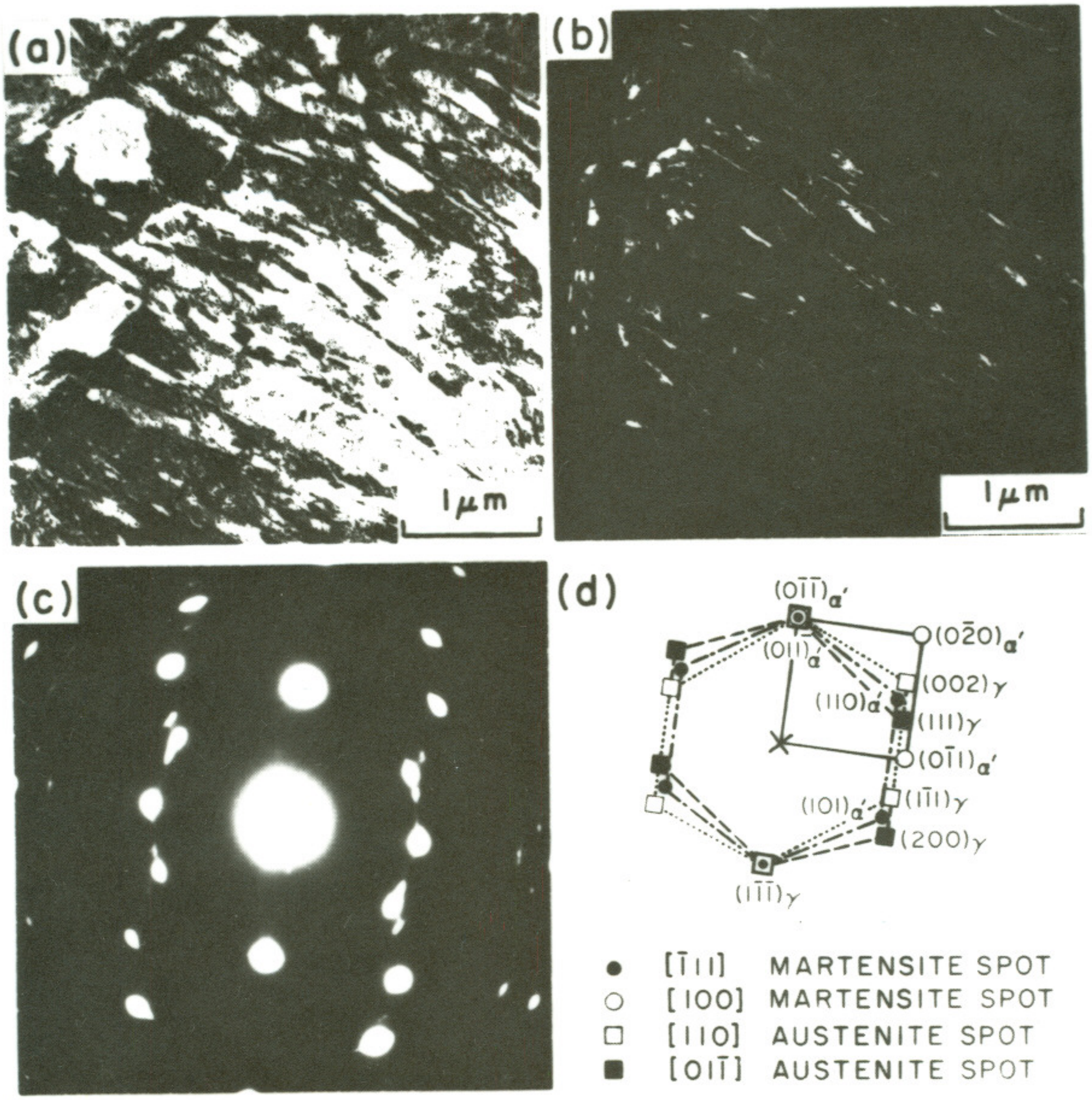

Figure 4-43: (a) BRIGHT FIELD TEM MICROGRAPH SHOWING A PREDOMINANTLY LATH MARTENSITIC REGION IN A CONVENTIONALLY HEAT TREATED SPECIMEN, (b) DARK FIELD IMAGE HIGHLIGHTING RETAINED AUSTENITE, PRESENT MOSTLY AS INTERLATH FILMS [$(\bar{2}00)_{\gamma}$ SPOT WAS USED], (c) S.A.D. PATTERN FROM (a) & (d) INTERPRETATION OF (c), SHOWING TWO AUSTENITE AND MARTENSITE ORIENTATIONS. BOTH K-S & N-W RELATIONSHIPS ARE OBSERVED - VIZ., $(01\bar{1})_{\alpha'} \parallel (1\bar{1}\bar{1})_{\gamma}$ and $[\bar{1}11]_{\alpha'} \parallel [110]_{\gamma}$ (K-S) AND $[001]_{\alpha'} \parallel [\bar{1}01]_{\gamma}$ (N-W).

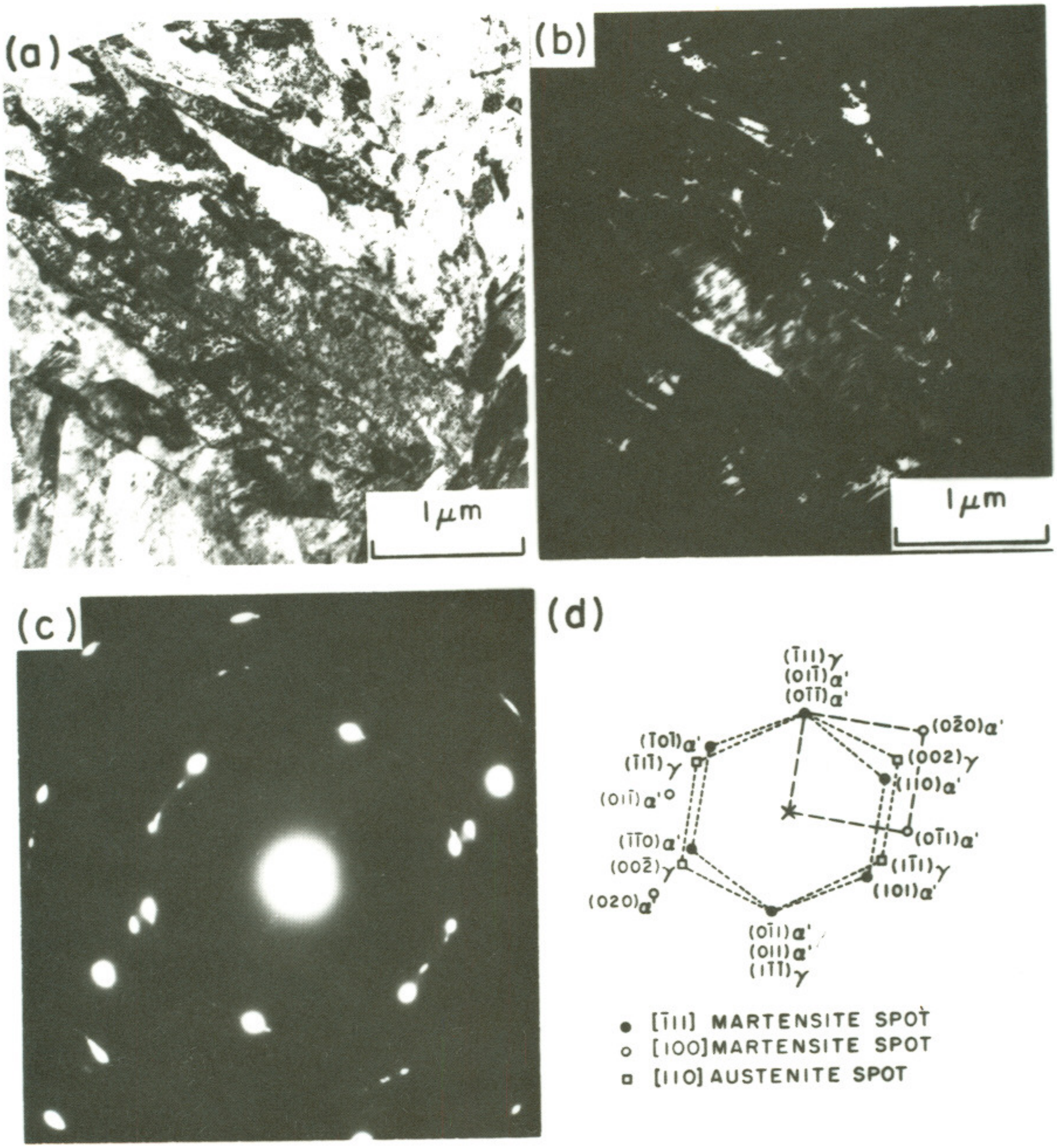

Figure 4-44: (a) BRIGHT FIELD TEM MICROGRAPH SHOWING A PREDOMINANTLY LATH MARTENSITIC REGION IN A CYCLICALLY HEAT TREATED SPECIMEN, (b) DARK FIELD IMAGE, USING $(002)_\gamma$ SPOT, HIGHLIGHTING INTERLATH AND SOME GRAIN BOUNDARY RETAINED AUSTENITE, (c) S.A.D. PATTERN FROM (a) AND (d) INTERPRETATION OF (c). BOTH K-S AND N-W RELATIONSHIPS ARE OBSERVED.

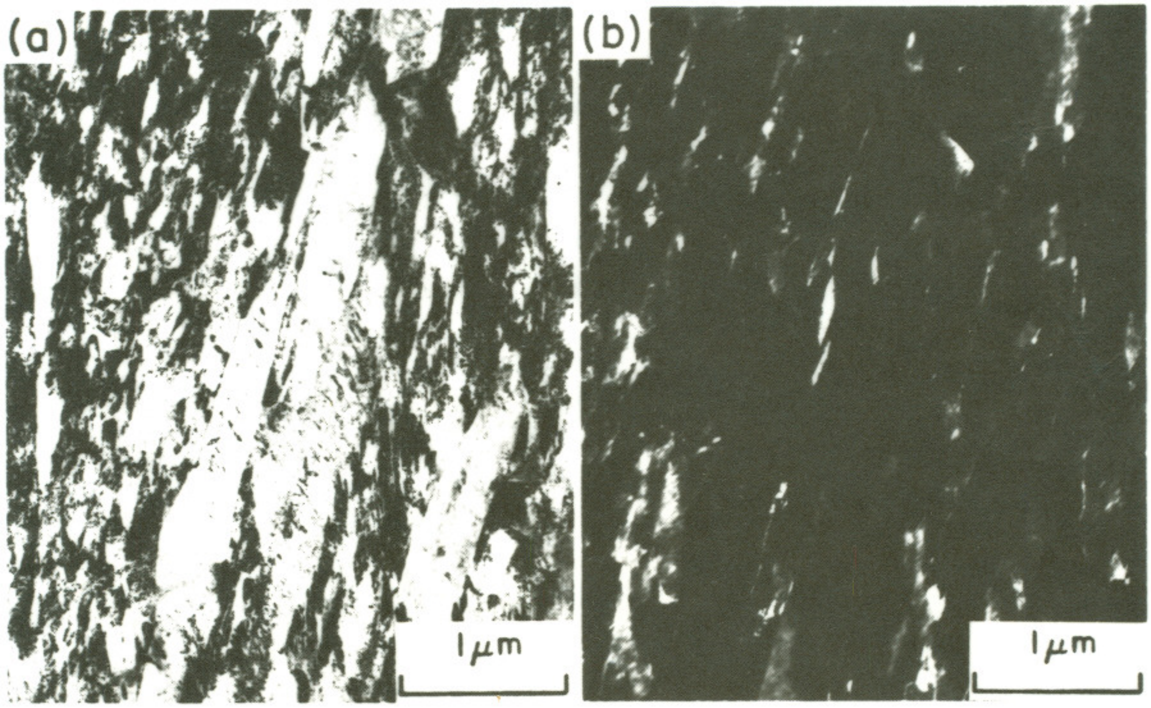

Figure 4-45: (a) BRIGHT FIELD TEM MICROGRAPH SHOWING PACKETS OF LATH MARTENSITE IN A SPECIMEN SUBJECTED TO HIGH TEMPERATURE HEAT TREATMENT AND (b) DARK FIELD IMAGE USING (002) TYPE AUSTENITE SPOT HIGHLIGHTING INTERLATH FILMS OF RETAINED AUSTENITE. SOME PACKET BOUNDARY RETAINED AUSTENITE IS ALSO SEEN (S.A.D. PATTERN WAS SIMILAR TO THAT IN FIGURE 4-43).

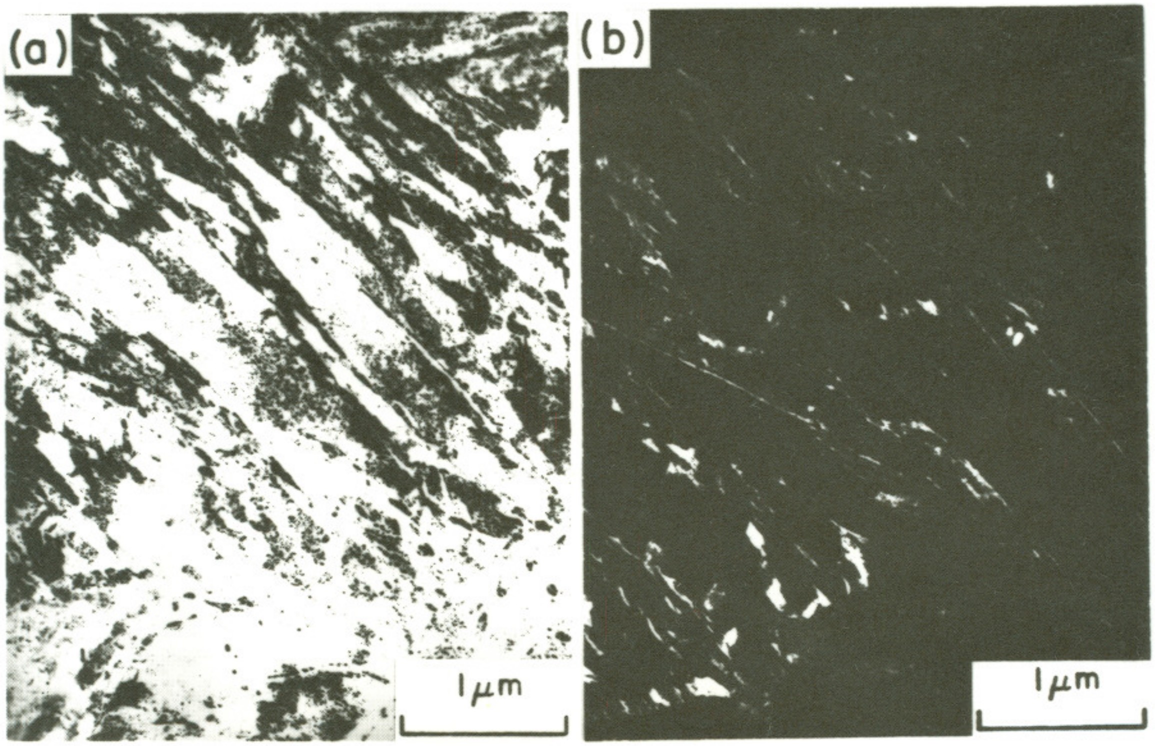

Figure 4-46: (a) BRIGHT FIELD TEM MICROGRAPH SHOWING PACKETS OF LATH MARTENSITE IN A SPECIMEN SUBJECTED TO STEP HEAT TREATMENT AND (b) DARK FIELD IMAGE USING (002) TYPE AUSTENITE SPOT HIGHLIGHTING INTERLATH FILMS OF RETAINED AUSTENITE. SOME PACKET BOUNDARY RETAINED AUSTENITE IS ALSO SEEN (S.A.D. PATTERN WAS SIMILAR TO THAT IN FIGURE 4-43).

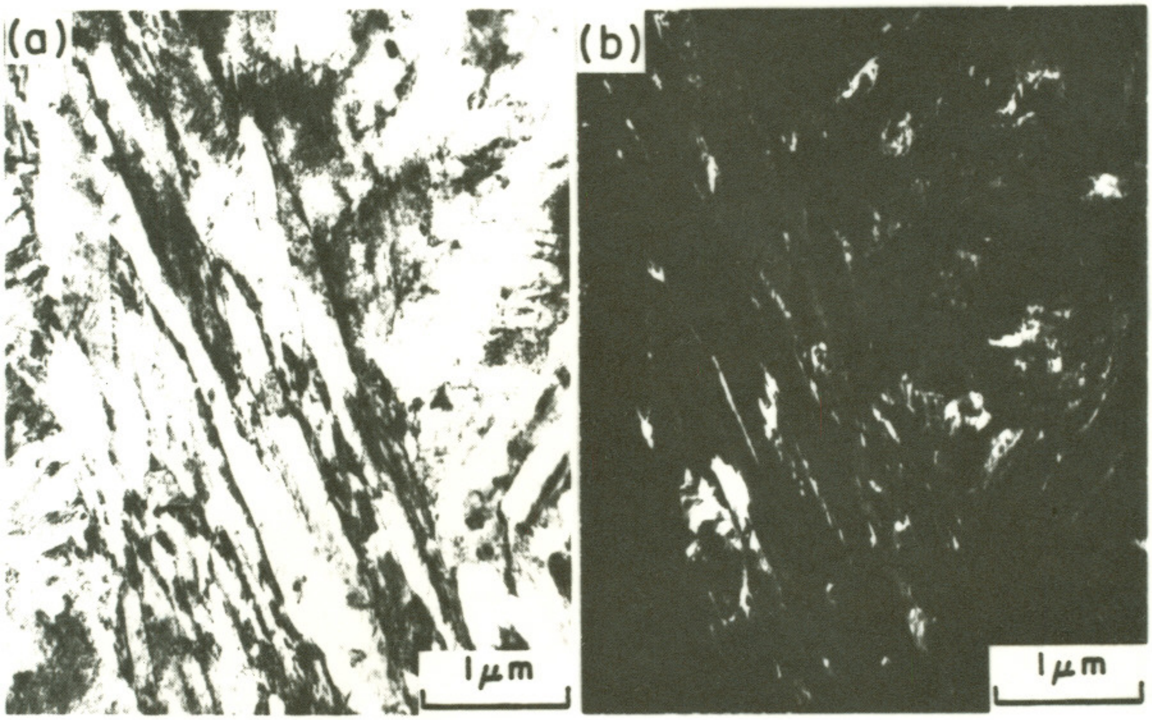

Figure 4-47: (a) BRIGHT FIELD TEM MICROGRAPH SHOWING PACKETS OF LATH MARTENSITE IN A SPECIMEN SUBJECTED TO MODIFIED CONVENTIONAL HEAT TREATMENT AND (b) DARK FIELD IMAGE HIGHLIGHTING INTERLATH AND PACKET BOUNDARY RETAINED AUSTENITE [(002) TYPE AUSTENITE SPOT WAS USED]. S.A.D. PATTERN WAS SIMILAR TO THE ONE IN FIGURE 4-43.

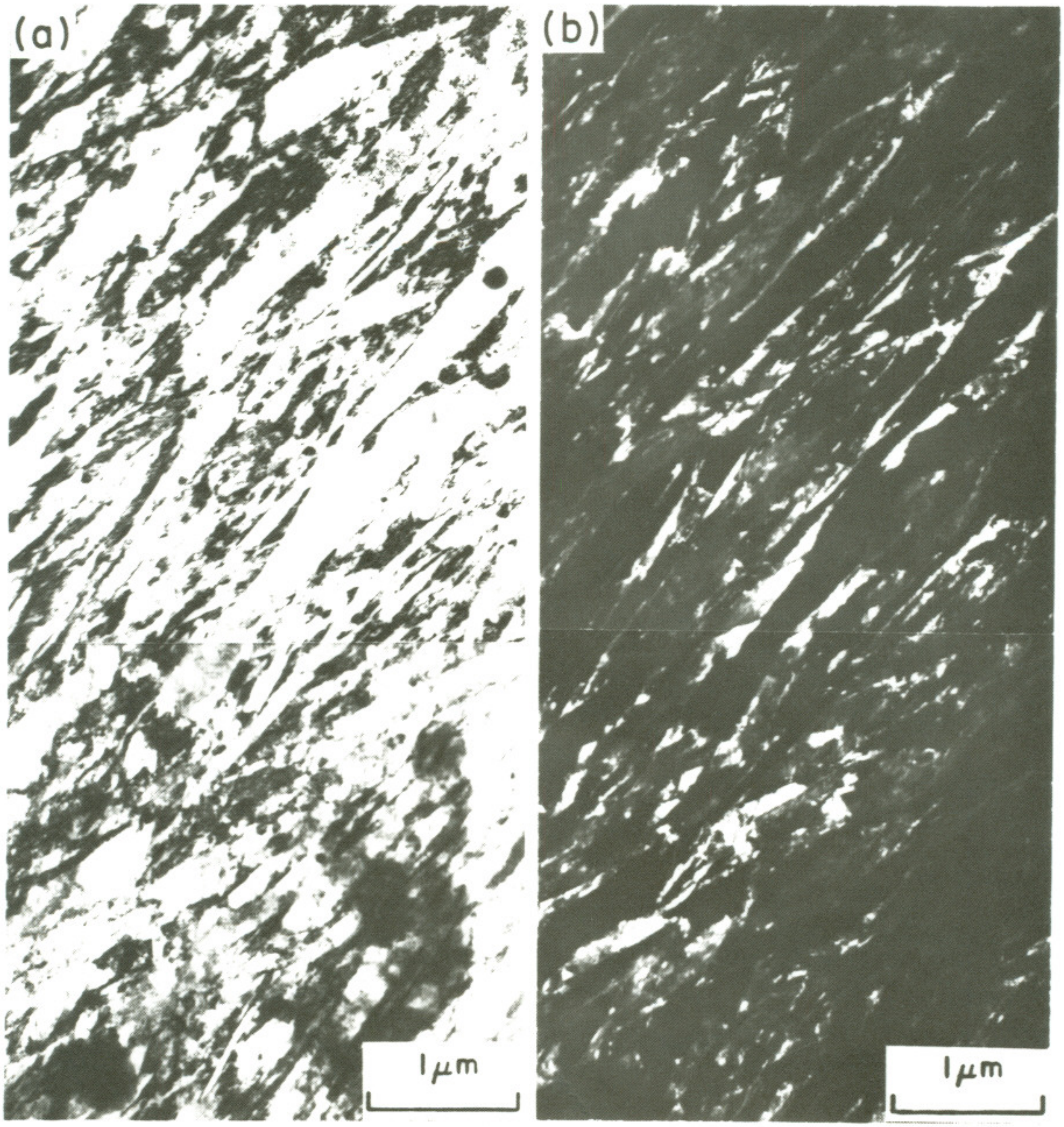

Figure 4-48: (a) COMPOSITE BRIGHT FIELD TEM MICROGRAPHS SHOWING AN EXTENSIVE LATH MARTENSITIC REGION IN A SPECIMEN SUBJECTED TO MODIFIED HIGH TEMPERATURE HEAT TREATMENT AND (b) DARK FIELD IMAGE, USING (111) TYPE AUSTENITE SPOT, HIGHLIGHTING INTERLATH FILMS OF RETAINED AUSTENITE. S.A.D. PATTERN WAS SIMILAR TO THE ONE IN FIGURE 4-44.

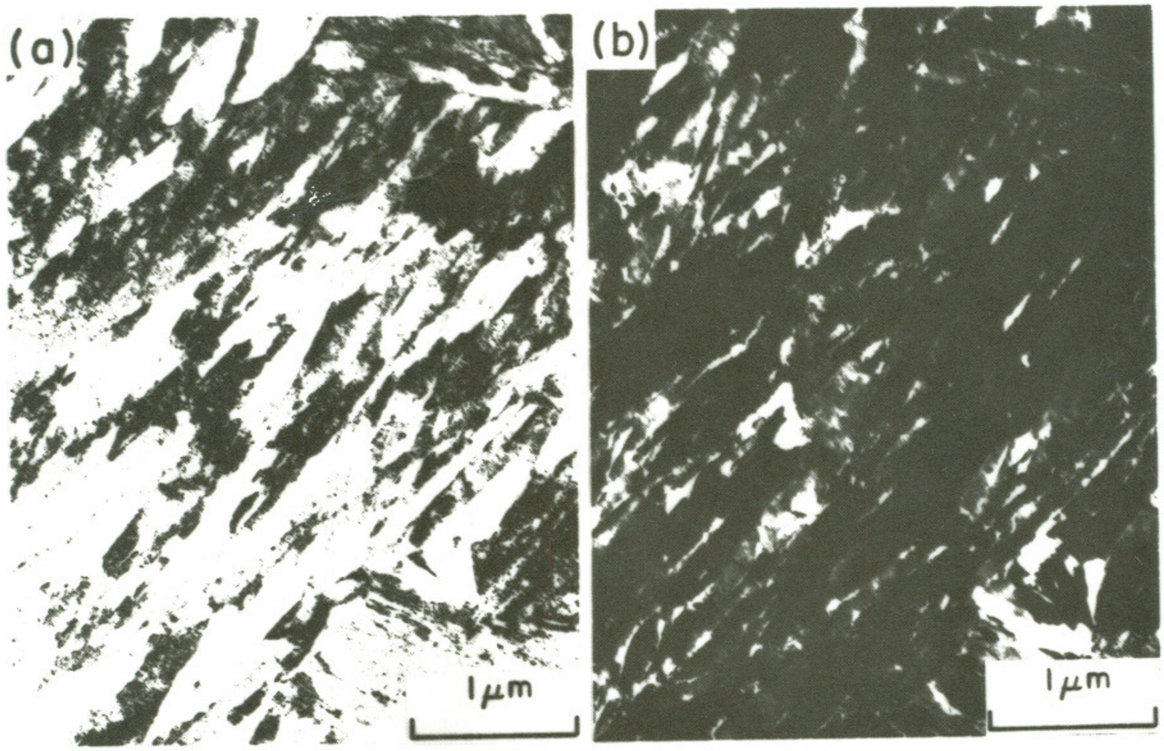

Figure 4-49: (a) BRIGHT FIELD TEM MICROGRAPH SHOWING AN EXTENSIVE LATH MARTENSITIC REGION IN A SPECIMEN SUBJECTED TO MODIFIED STEP HEAT TREATMENT AND (b) DARK FIELD IMAGE USING (002) TYPE AUSTENITE SPOT, HIGHLIGHTING INTER-LATH FILMS AND PACKET BOUNDARY RETAINED AUSTENITE. S.A.D. PATTERN WAS SIMILAR TO THE ONE IN FIGURE 4-44.

evident in some micrographs. Interlath austenite films were present irrespective of whether the laths were regular, large, or convergent.

These micrographs were representative of the amounts of retained austenite obtained due to the various heat treatments. Based on such extensive examination of many samples for each heat treatment, qualitative estimates of retained austenite amounts were made and the results are summarized in Table 4-10. From Figures 4-43 to 4-49, it was also clear that while conventional and cyclic heat treatments resulted in discontinuous films of retained austenite, for all other heat treatments, the films were more continuous around the laths, the degree of discontinuity depending upon the amount of retained austenite. From the diffraction patterns, it is also apparent that two basic orientation relationships between austenite and martensite were obtained, satisfying both the Kurdjumov-Sachs [72], viz., $(01\bar{1})_{\alpha'} \parallel (1\bar{1}\bar{1})_{\gamma}$ and $[\bar{1}11]_{\alpha'} \parallel [110]_{\gamma}$ and the Nishiyama-Wasserman relationships [73,74], viz., $(0\bar{1}\bar{1})_{\alpha'} \parallel (1\bar{1}\bar{1})_{\gamma}$ and $[001]_{\alpha'} \parallel [101]_{\gamma}$. While K-S relationship was observed more frequently, N-W relationship was observed only in conjunction with K-S relationship.

While most estimates of retained austenite, based on qualitative TEM studies, point to increased amounts of retained austenite with increasing austenitization temperature [3-5,7,9,10,19], Ritchie and Horn [20] did not observe any change in retained austenite amounts with austenitization temperatures for 4340 steel, which was the same conclusion of Youngblood and Raghavan [16] in their work with 300M steel. While McDarmaid [17] also did not observe any change in retained austenite

Table 4-10

QUALITATIVE TEM ESTIMATES OF RETAINED AUSTENITE AMOUNTS IN 300M STEEL UNDER DIFFERENT HEAT TREATED CONDITIONS

Heat Treatment	Retained Austenite(%)
Conventional (870°C/280°C)	3
Cyclic (870°C/850°C/280°C) 4 cycles	4
High Temperature (1200°C/280°C)	8
Step (1200°C/870°C/280°C)	7
Modified Conventional (870°C/650°C/850°C/280°C)	6
Modified High Temperature (1200°C/650°C/850°C/280°C)	10
Modified Step (1200°C/870°C/650°C/850°C/280°C)	10

amounts for 300M steel with austenitization temperatures, over the tempering temperature range of 230°C-560°C, careful examination of his data shows a difference of 3-4% between steels austenitized at 880°C and 1165°C and subsequently tempered at 230°C (conditions close to those employed in this investigation). His data also showed an increase of about 1-2% for cyclically heat treated steel. McDarmaid [17] and Khan and Wood [18] also reported no difference in retained austenite amounts between step and high temperature heat treatments, while in this study a slight decrease was obtained for the step heat treatment when compared to the high temperature heat treatment. A significant difference in retained austenite amounts between conventional and high temperature heat treatments was also noted in this study, as well as a small increase for the cyclic heat treatment when compared with the conventional heat treatment. The results of this study were based solely upon qualitative TEM estimates and the stability of retained austenite upon subsequent loading of samples was not considered.

Simultaneous observation of K-S and N-W orientation relationships from within the same packet of martensite, between austenite and martensite was reported by many investigators [4,7,18,75-77] and also noted in this investigation.

4.2.3.4. Effect of Heat Treatment on Carbides. All heat treatments resulted in a mixture of predominantly cementite and small amounts of ε-carbide after tempering at 280°C. The ε-carbide particles were considerably coarser than cementite particles and mostly precipitated inside large laths and on dislocations. Cementite particles, on the other hand, were precipitated inside laths or plates, at lath, plate, packet or grain boundaries and on dislocations and twins. The precipitation of cementite on twins, in particular, was an inverse function of austenitization temperature. While the orientation between ε-carbide and martensite was mostly the Jack [78] relationship, between cementite and martensite satisfied either the Bagaryatskii [79] or the Pitsch [80] relationships. Bright field pictures of Figure 4-50 all showed characteristic, wavy, ε-carbide precipitation within large laths and on dislocations. These carbides were typically 50 Å to 100 Å thick and about 1000 Å to 1500 Å long and were precipitated usually along parallel rows at an angle to the longitudinal axis of the ferrite. The small amount of these carbides made obtaining diffraction patterns with ε-carbide spots from these regions extremely difficult. However, in a few instances, diffraction patterns were obtained and the results are given in Figures 4-51 to 4-53 for conventional, high temperature and modified conventional heat treatments. In all the cases, the diffraction pattern was the same as in Figure 4-51c. To determine the orientation relationships, the orientations determined from the diffraction pattern were plotted on a stereographic projection (Figure 4-54). From Figure 4-54, $(0001)_{\varepsilon}$ was parallel to $(0\bar{1}1)_{\alpha'}$, $(10\bar{1}0)_{\varepsilon}$ was parallel to $(2\bar{1}1)_{\alpha'}$ and $(10\bar{1}1)_{\varepsilon}$ was only about 1° away from $(101)_{\alpha'}$. Also, $[0001]_{\varepsilon}$ was parallel to $[011]_{\alpha'}$. This was the same as the Jack orientation relationship [78] and the 1° variation of $(10\bar{1}1)_{\varepsilon}$ and $(101)_{\alpha'}$ planes could be due to inaccuracies in measurements. Dark field imaging for all these figures (Figures 4-51 to 4-53) was done using $\{1\bar{1}00\}_{\varepsilon}$ type spots and the ε-carbide

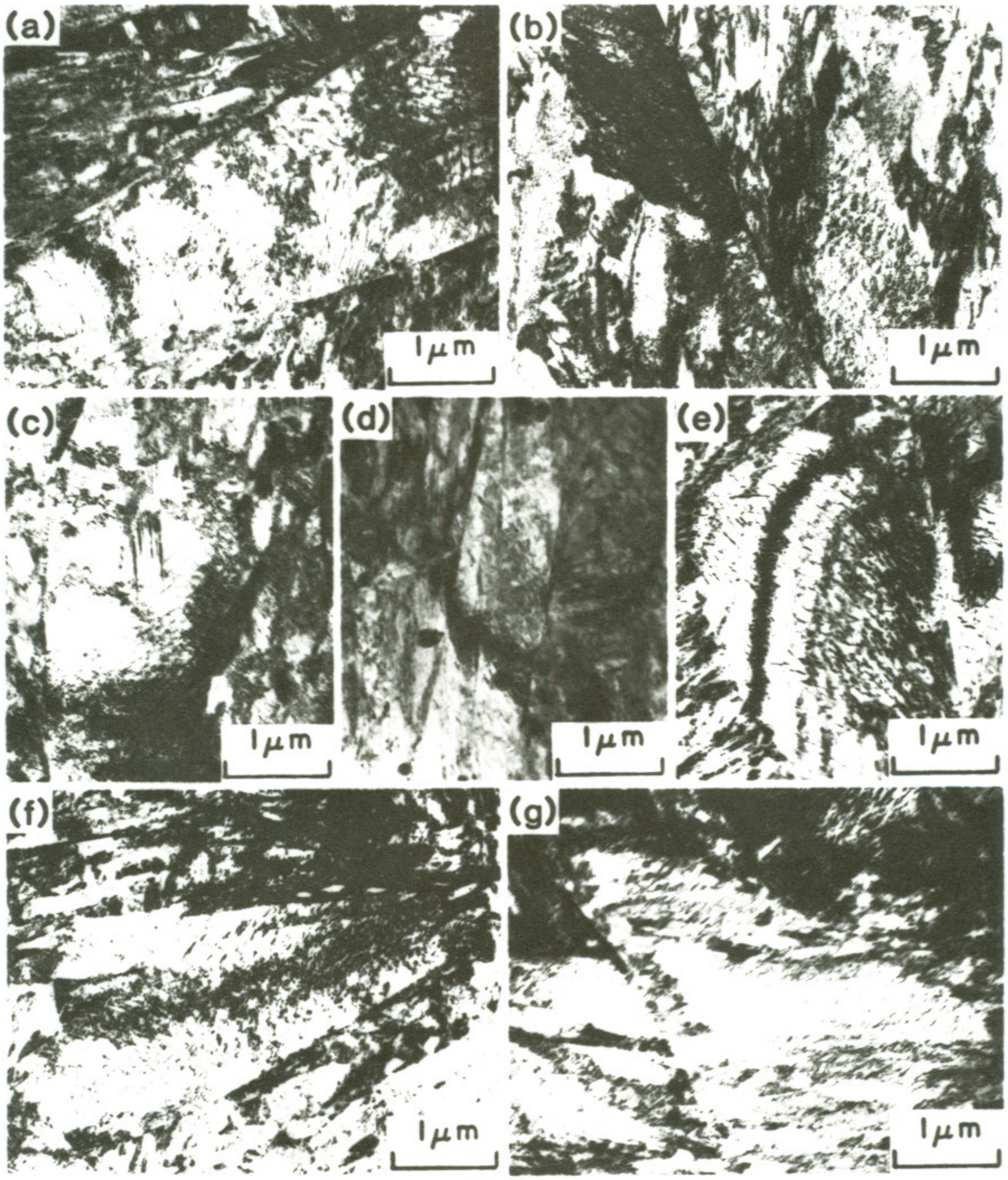

Figure 4-50: BRIGHT FIELD TEM MICROGRAPHS SHOWING EXTENSIVE ε-CARBIDE PRECIPITATION WITHIN LARGE LATHS AND ON DISLOCATIONS FOR (a) CONVENTIONAL, (b) CYCLIC, (c) HIGH TEMPERATURE, (d) STEP, (e)MODIFIED CONVENTIONAL, (f) MODIFIED HIGH TEMPERATURE AND (g) MODIFIED STEP HEAT TREATMENTS.

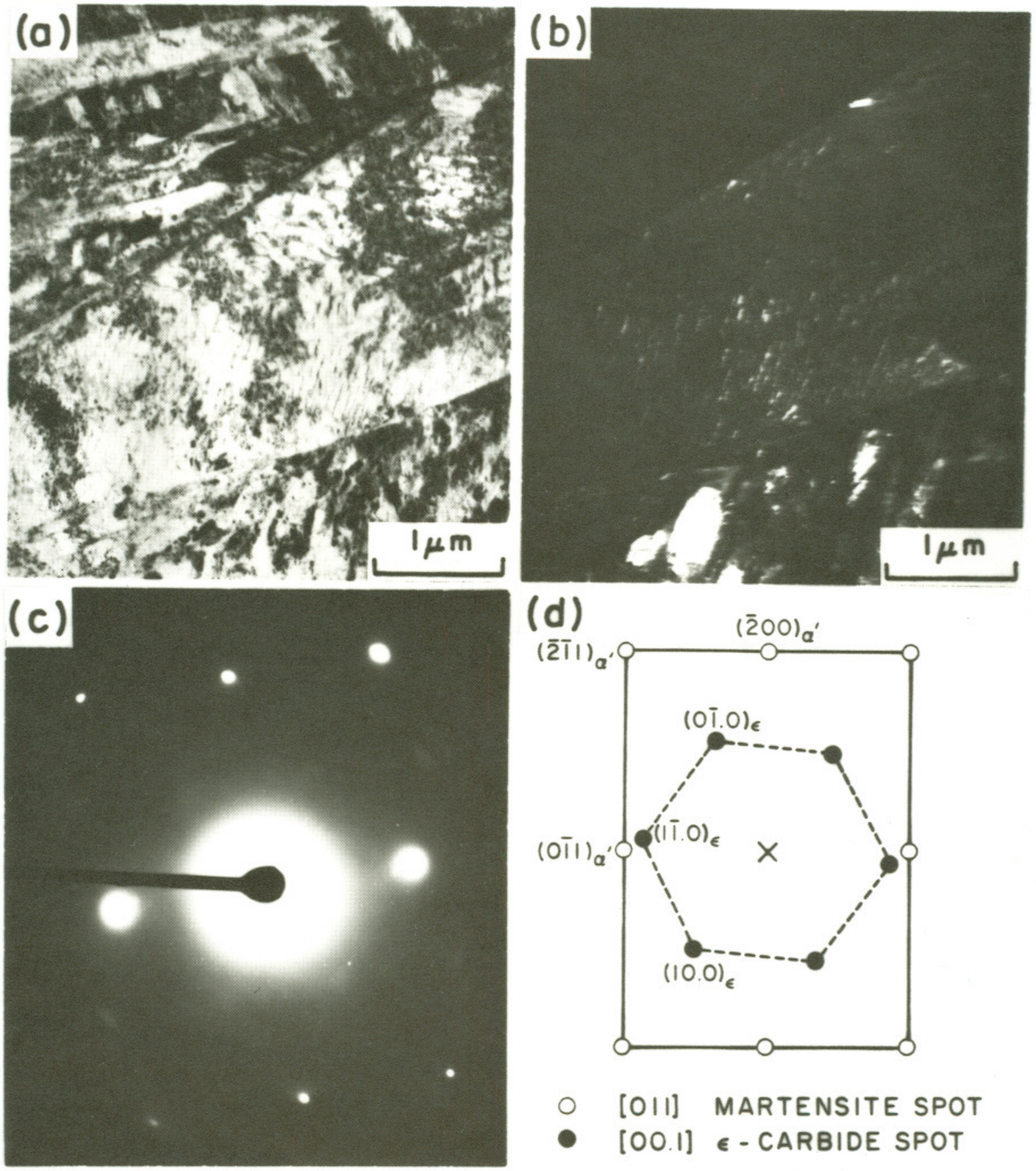

Figure 4-51: (a) BRIGHT FIELD TEM MICROGRAPH SHOWING ε-CARBIDE PRECIPITATES WITHIN A LARGE LATH IN A CONVENTIONALLY HEAT TREATED SPECIMEN, (b) DARK FIELD IMAGE, USING $(1\bar{1}00)_\epsilon$ SPOT, SHOWING ε-CARBIDE PRECIPITATION, (c) S.A.D. PATTERN FROM THE LATH AND (d) INTERPRETATION OF (c). THE GROWTH DIRECTION IS FOUND TO BE <112> AND WAS DETERMINED AS DESCRIBED IN SECTION 4.2.3.5.

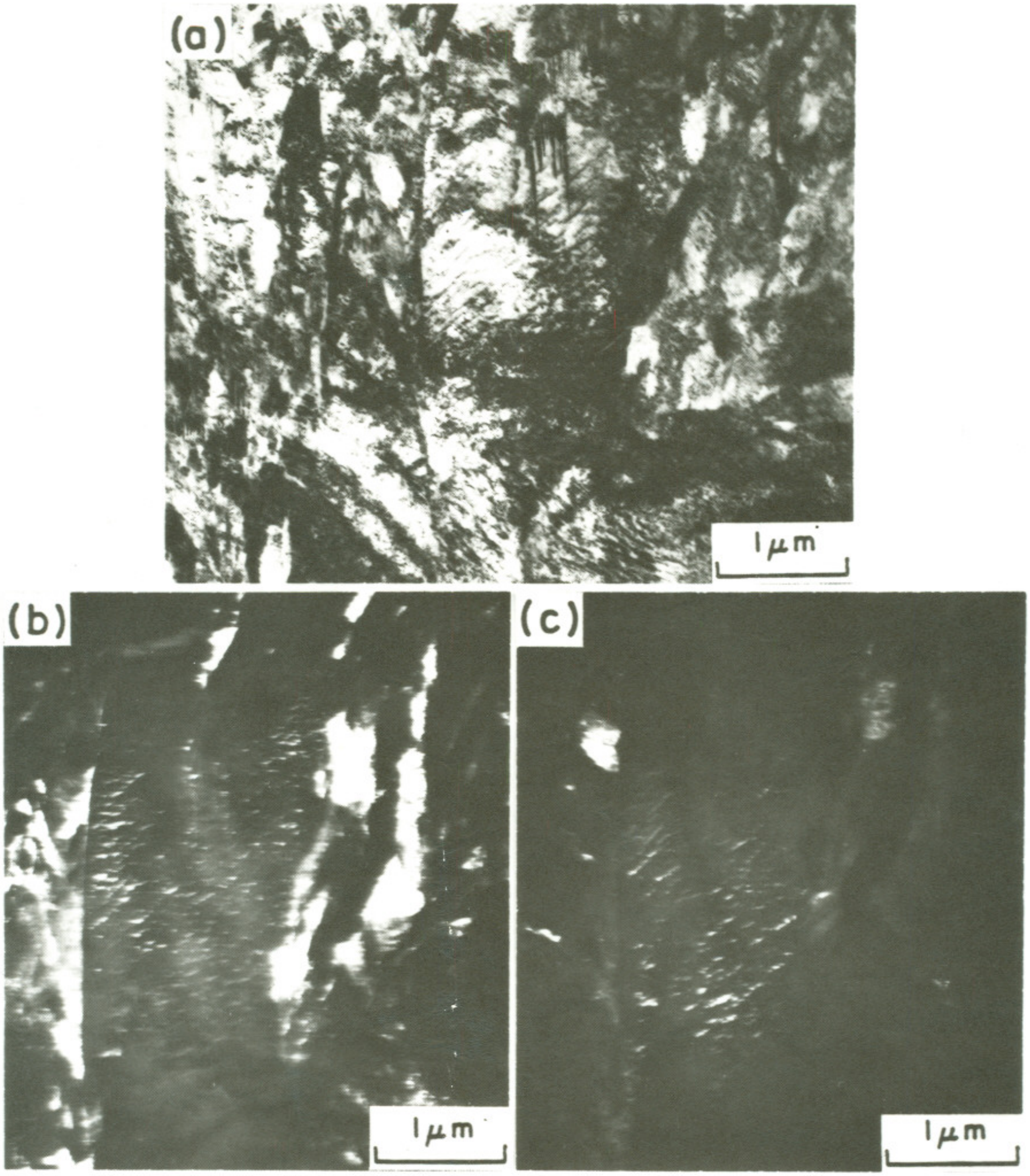

Figure 4-52: (a) BRIGHT FIELD TEM MICROGRAPH SHOWING ε-CARBIDE PRECIPITATES AND TWINS WITHIN A LARGE LATH IN A STEEL SUBJECTED TO HIGH TEMPERATURE HEAT TREATMENT, (b) & (c) DARK FIELD IMAGES, USING $(1\bar{1}00)_{\varepsilon}$ AND $(10\bar{1}0)_{\varepsilon}$ SPOTS RESPECTIVELY, HIGHLIGHTING THE CARBIDE PRECIPITATES. S.A.D. PATTERN WAS THE SAME AS IN FIGURE 4-51.

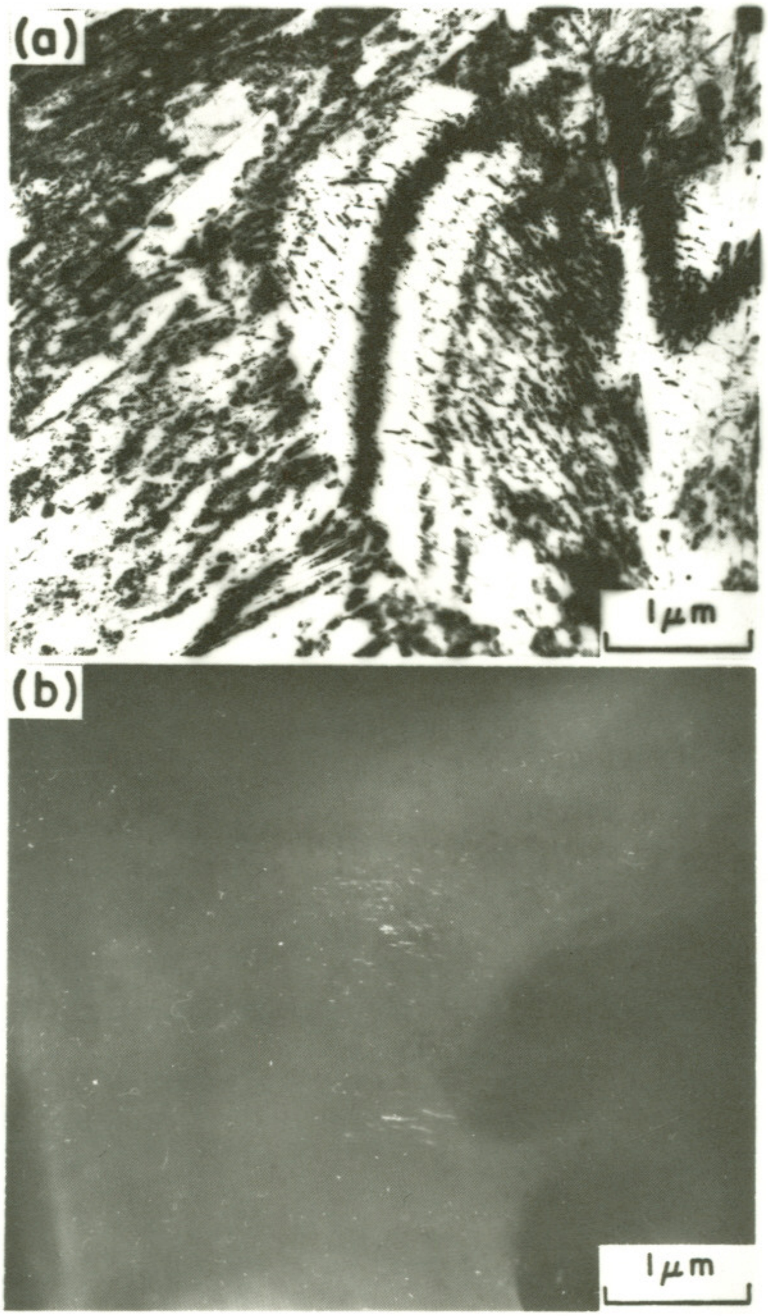

Figure 4-53: (a) BRIGHT FIELD TEM MICROGRAPH SHOWING ε-CARBIDE PRECIPITATES WITHIN A LARGE LATH IN A SPECIMEN SUBJECTED TO MODIFIED CONVENTIONAL HEAT TREATMENT AND (b) DARK FIELD IMAGE, USING $(1\bar{1}00)_\varepsilon$ SPOT, HIGHLIGHTING THE CARBIDE PRECIPITATES. S.A.D. PATTERN WAS SIMILAR TO THE ONE IN FIGURE 4-51.

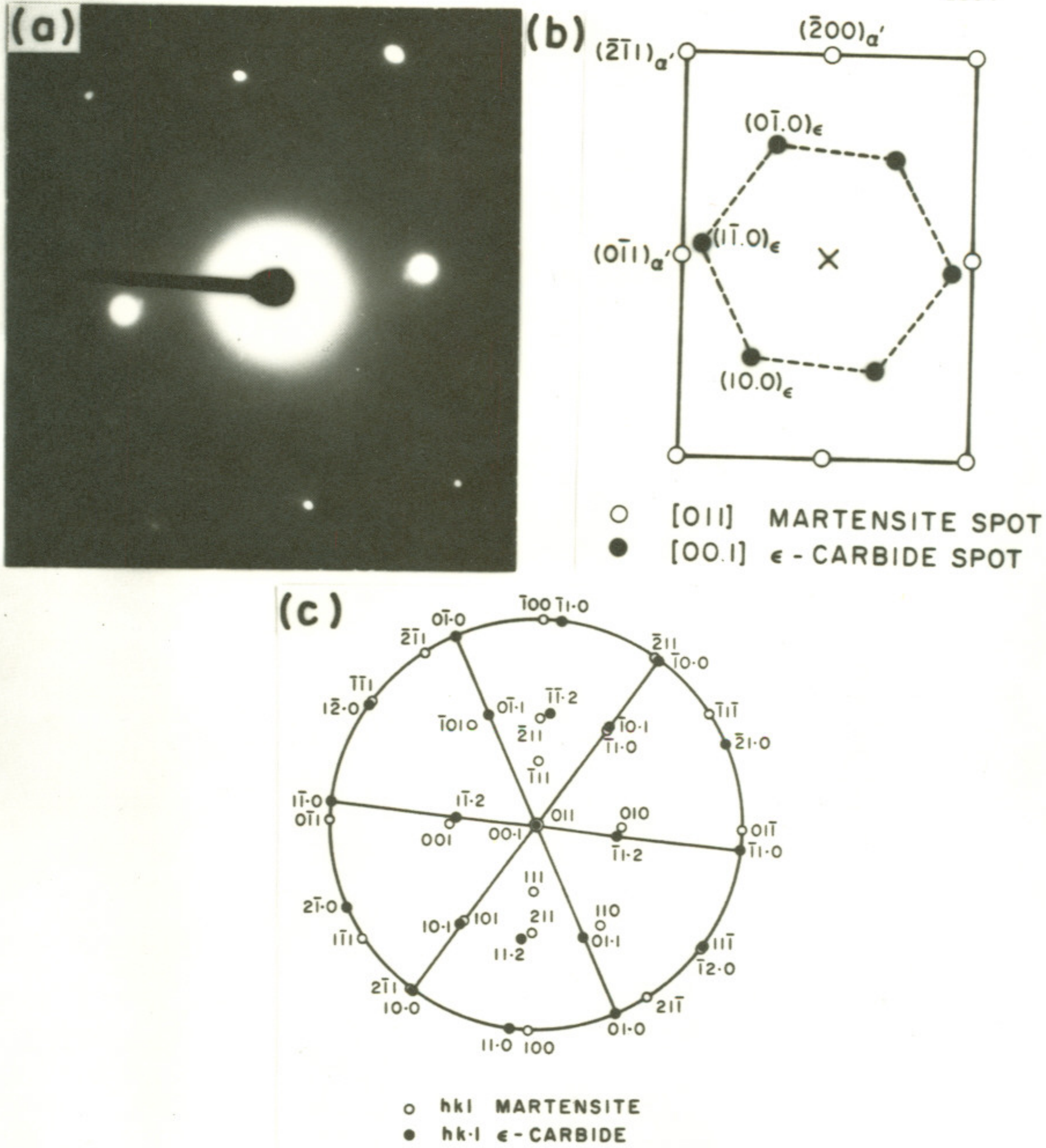

Figure 4-54: (a) SAD PATTERN FROM FIGURE 4-51, (b) INTERPRETATION OF (a), WITH [011] MARTENSITE AND [0001] ε-CARBIDE SPOTS INDEXED AND (c) STEREOGRAPHIC PROJECTION REPRESENTING ORIENTATION RELATIONSHIPS BETWEEN MARTENSITE AND ε-CARBIDE. JACK ORIENTATION RELATIONSHIP IS OBSERVED, VIZ.,

$$[011]_{\alpha'} \parallel [0001]_{\varepsilon}$$

$$(011)_{\alpha'} \parallel (0001)_{\varepsilon}$$

$$(2\bar{1}1)_{\alpha'} \parallel (10\bar{1}0)_{\varepsilon}$$

$$(101)_{\alpha'} \parallel (10\bar{1}0)_{\varepsilon}$$

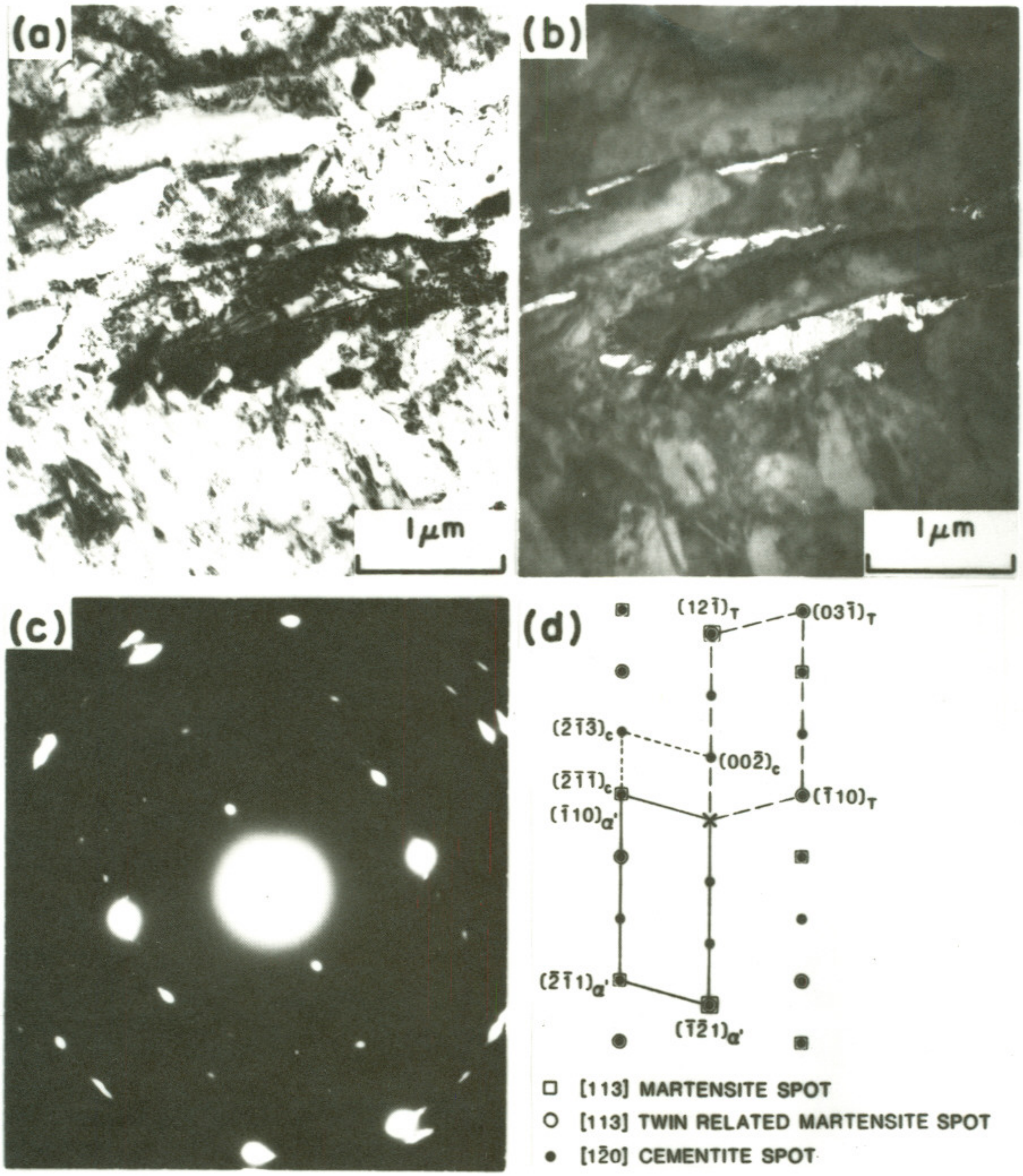

Figure 4-55: (a) BRIGHT FIELD TEM MICROGRAPH SHOWING A LATH MARTENSITIC REGION IN A CONVENTIONALLY HEAT TREATED STEEL, (b) DARK FIELD IMAGE, USING (002) Fe_3C SPOT, HIGHLIGHTING CEMENTITE PRECIPITATES WITHIN THE LATHS, (c) S.A.D. PATTERN FROM (a) AND (d) INTERPRETATION OF (c).

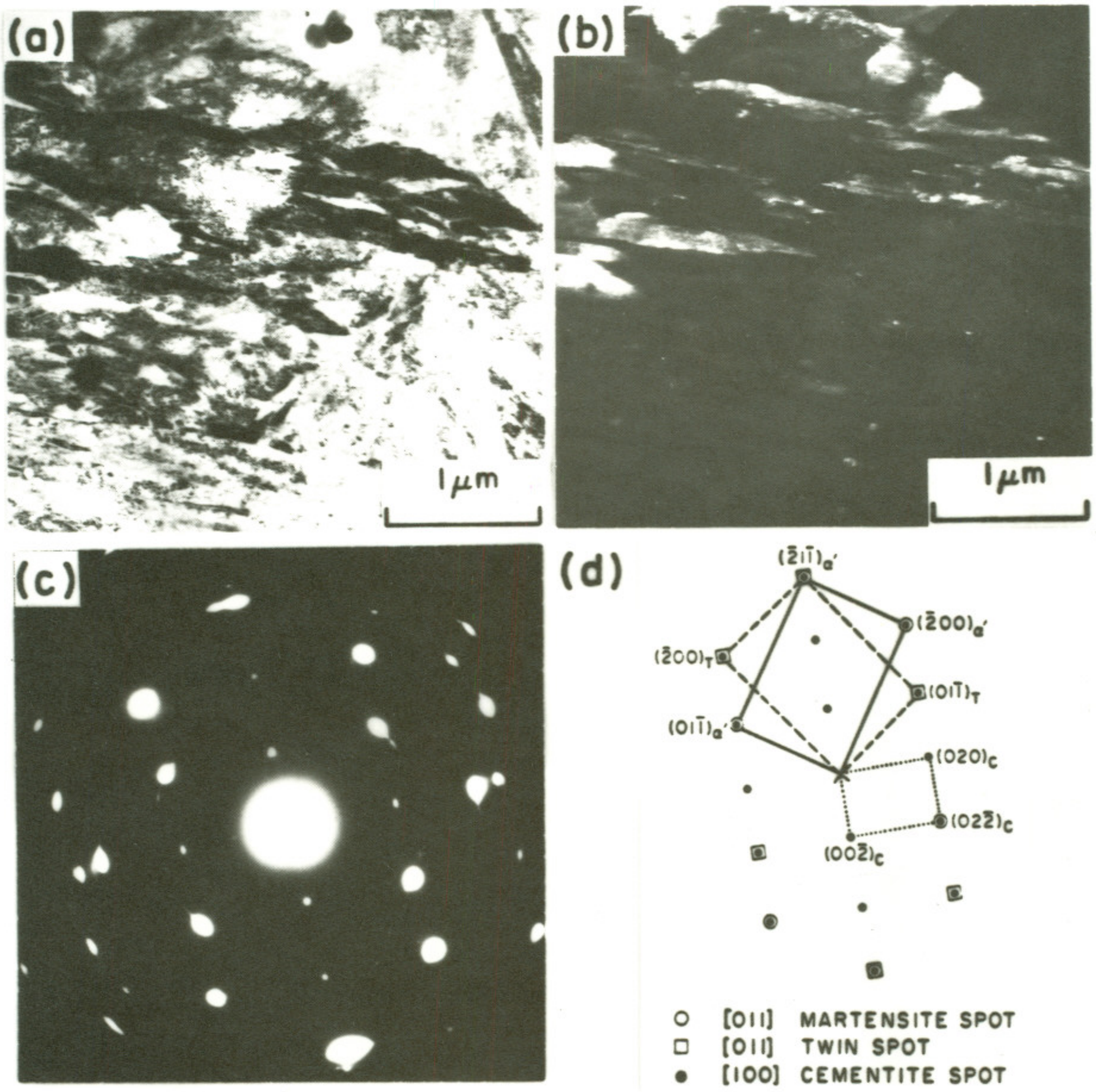

Figure 4-56: (a) BRIGHT FIELD TEM MICROGRAPH SHOWING A LATH MARTENSITIC REGION IN A CYCLICALLY HEAT TREATED SPECIMEN, (b) DARK FIELD IMAGE USING $(002)_{Fe_3C}$ SPOT HIGHLIGHTING CEMENTITE PRECIPITATION WITHIN LATHS, AND TO SOME EXTENT AT LATH AND PACKET BOUNDARIES, (c) S.A.D. PATTERN FROM (a) AND (d) INTERPRETATION OF (c). BAGARYATSKII RELATIONSHIP IS OBSERVED--VIZ., $[011]_{\alpha'} \parallel [100]_{Fe_3C}$

$(\bar{2}1\bar{1})_{\alpha'} \parallel (001)_{Fe_3C}$

$(\bar{1}\bar{1}1)_{\alpha'} \parallel (010)_{Fe_3C}$

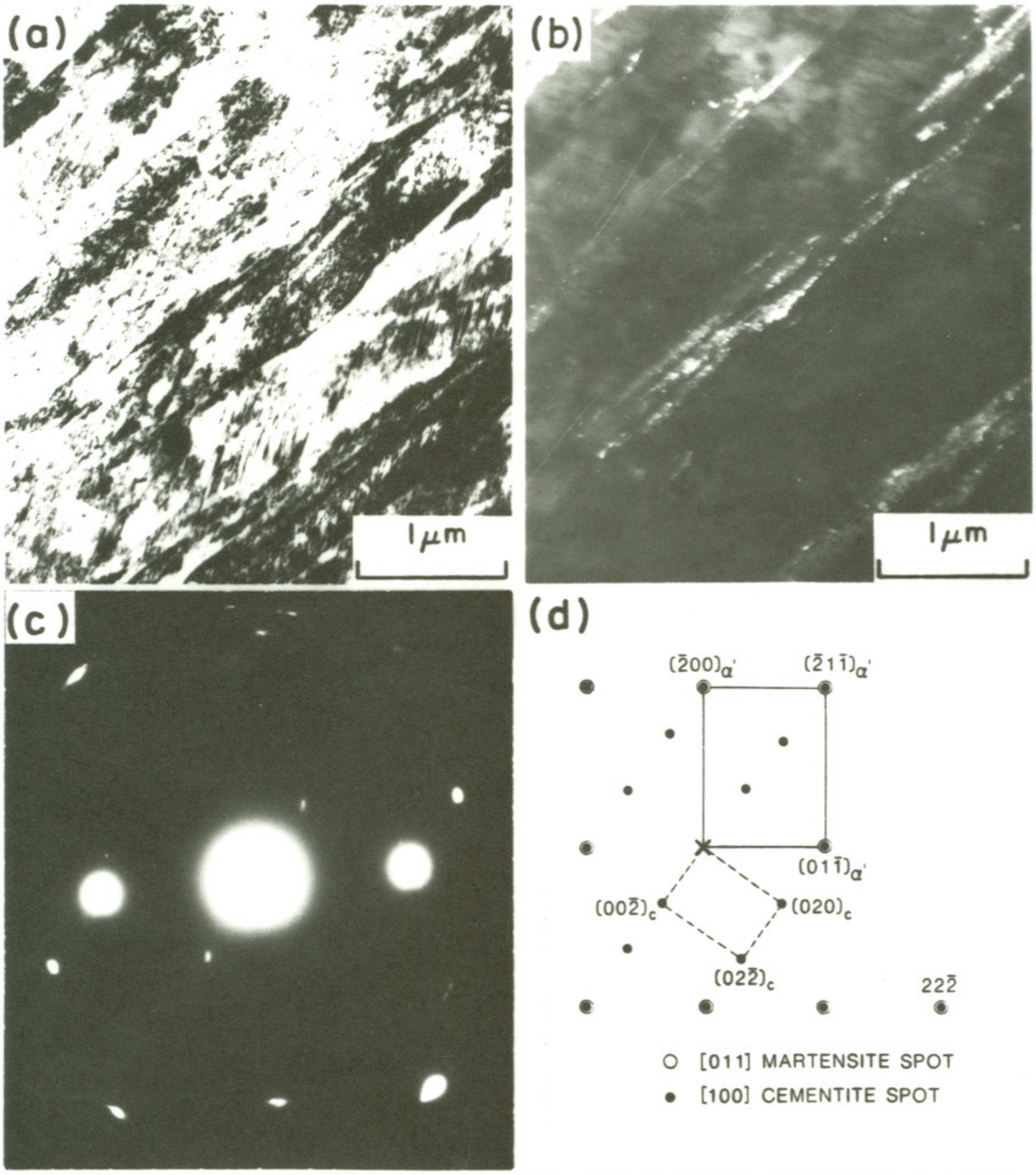

Figure 4-57: (a) BRIGHT FIELD TEM MICROGRAPH SHOWING A LATH MARTENSITIC REGION IN A SPECIMEN SUBJECTED TO HIGH TEMPERATURE HEAT TREATMENT, (b) DARK FIELD IMAGE USING $(002)_{Fe_3C}$ SPOT HIGHLIGHTING CEMENTITE PRECIPITATES WITHIN LATHS AND AT LATH BOUNDARIES, (c) S.A.D. PATTERN FROM (a) AND (d) INTERPRETATION OF S.A.D. PATTERN. BAGARYATSKII ORIENTATION RELATIONSHIP IS OBSERVED.

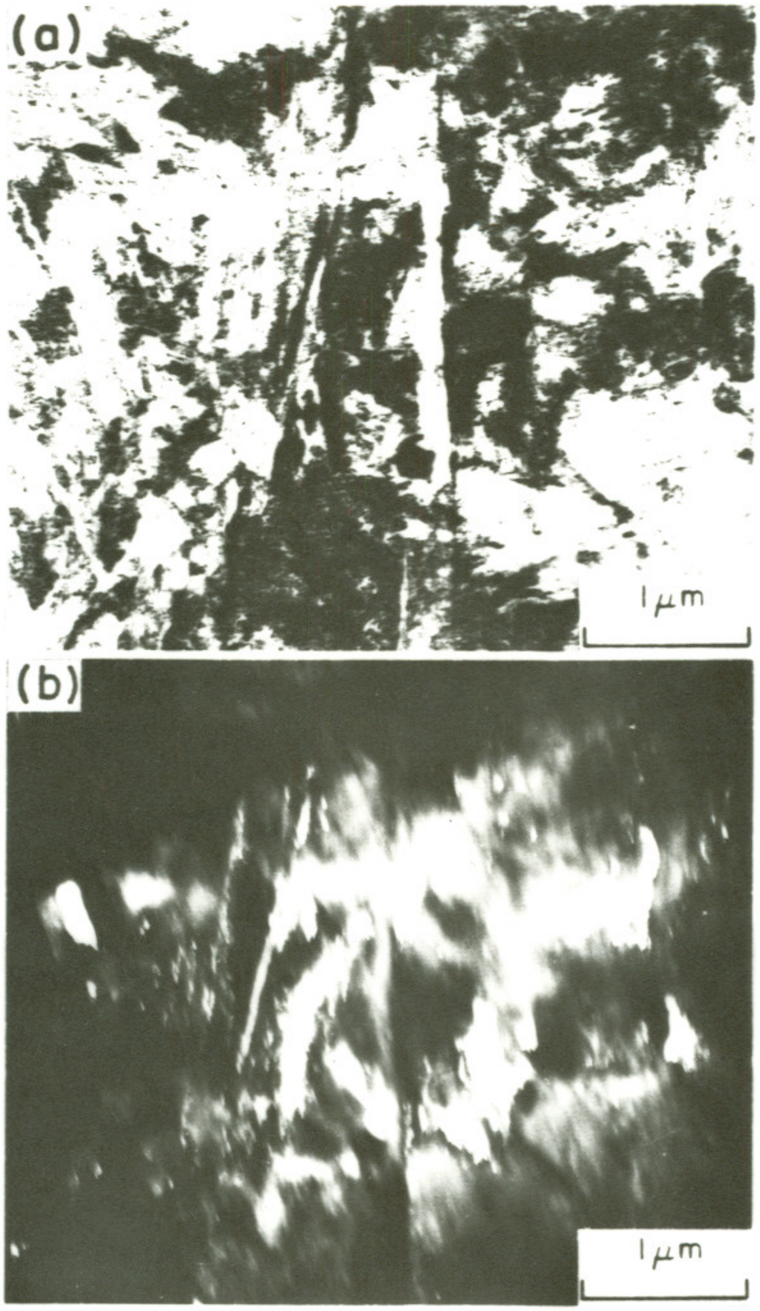

Figure 4-58: (a) BRIGHT FIELD TEM MICROGRAPH SHOWING A LATH MARTENSITIC REGION IN A SPECIMEN SUBJECTED TO STEP HEAT TREATMENT AND (b) DARK FIELD IMAGE USING $(002)_{Fe_3C}$ SPOT HIGHLIGHTING CEMENTITE PRECIPITATION WITHIN LATHS AND AT LATH BOUNDARIES. S.A.D. PATTERN WAS SIMILAR TO THE ONE IN FIGURE 4-56.

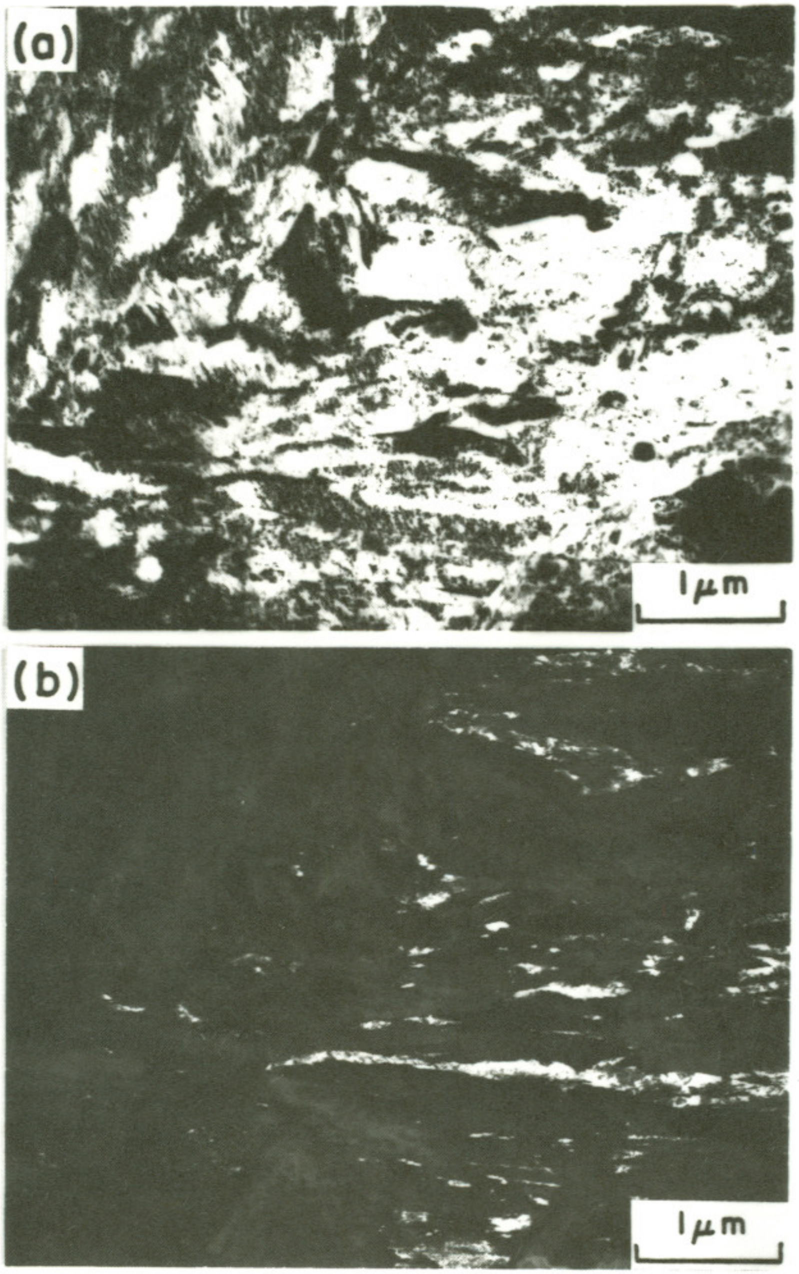

Figure 4-59: (a) BRIGHT FIELD TEM MICROGRAPH SHOWING A LATH MARTENSITIC REGION IN A SPECIMEN SUBJECTED TO MODIFIED CONVENTIONAL HEAT TREATMENT AND (b) DARK FIELD IMAGE USING $(002)_{Fe_3C}$ SPOT, HIGHLIGHTING CEMENTITE PRECIPITATION WITHIN LATHS AND TO A LESSER EXTENT AT PACKET BOUNDARIES. S.A.D. PATTERN WAS SIMILAR TO THE ONE IN FIGURE 4-56.

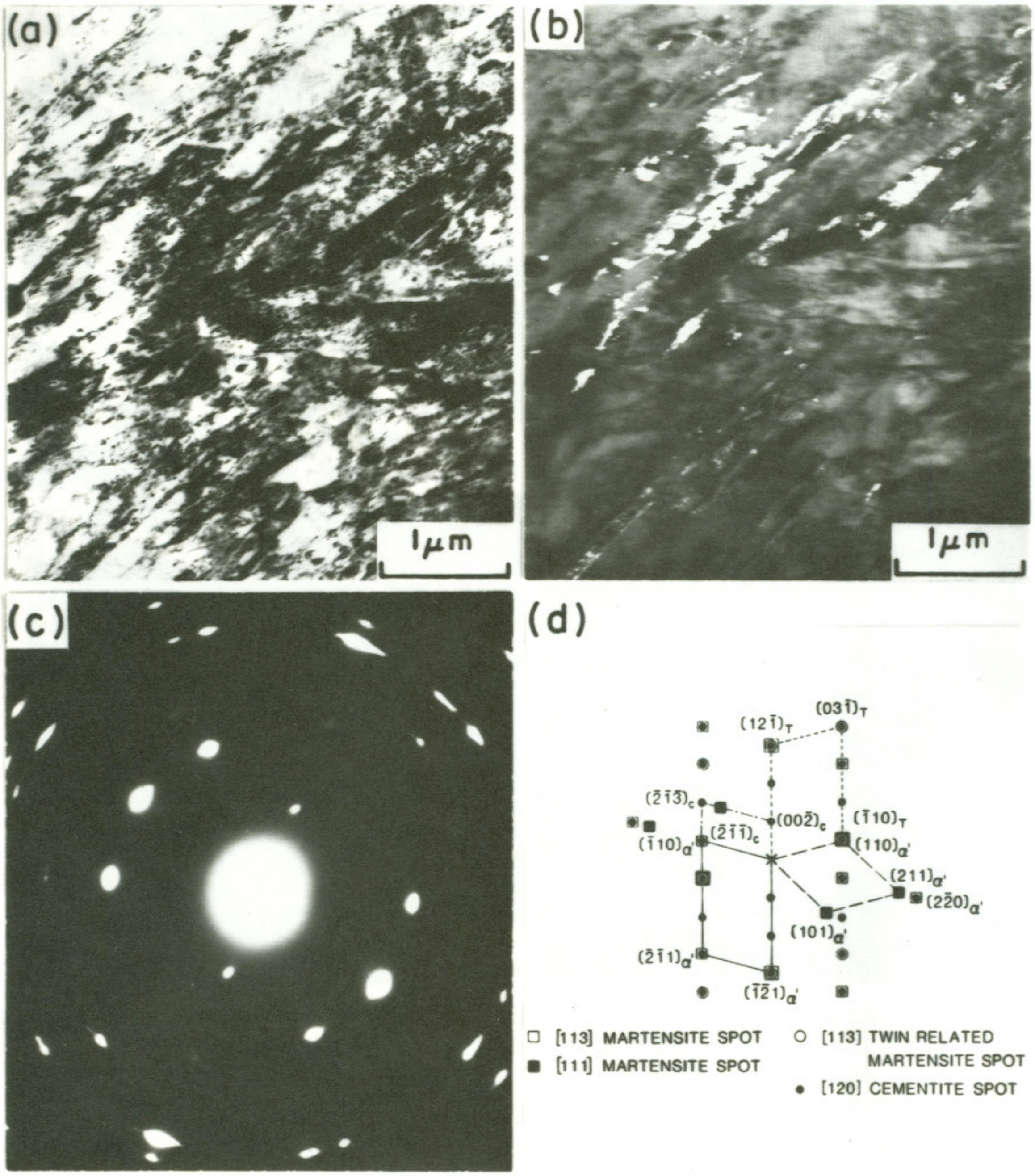

Figure 4-60: (a) BRIGHT FIELD TEM MICROGRAPH SHOWING A LATH MARTENSITIC REGION IN A SPECIMEN SUBJECTED TO MODIFIED HIGH TEMPERATURE HEAT TREATMENT, (b) DARK FIELD IMAGE USING $(002)_{Fe_3C}$ SPOT, HIGHLIGHTING CEMENTITE PRECIPITATION WITHIN LATHS, (c) S.A.D. PATTERN FROM (a)& (d) INTERPRETATION OF (c).

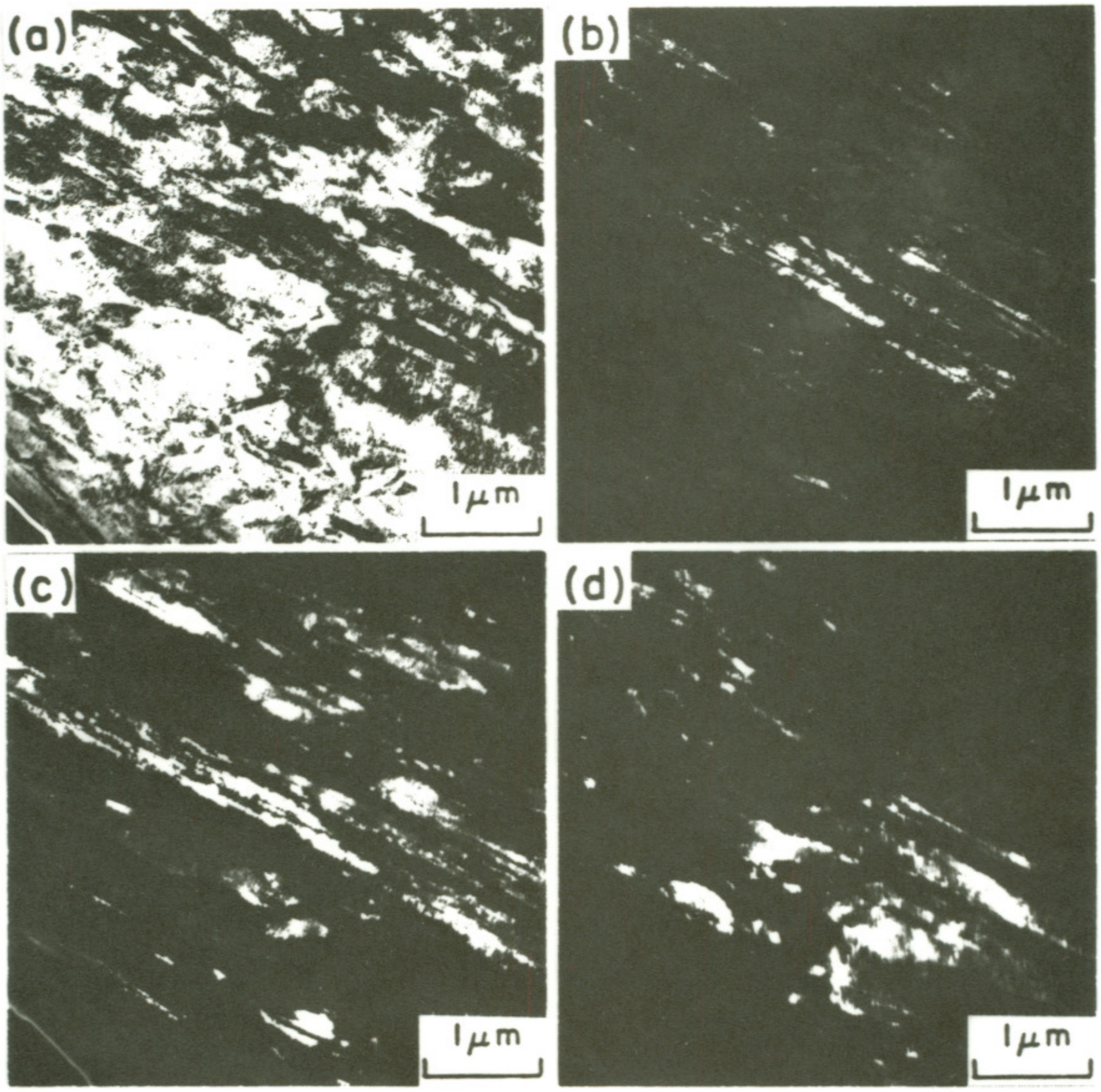

Figure 4-61: (a) BRIGHT FIELD TEM MICROGRAPH SHOWING A LATH MARTENSITIC REGION IN A SPECIMEN SUBJECTED TO MODIFIED STEP HEAT TREATMENT, (b) DARK FIELD IMAGE USING $(002)_{Fe_3C}$ SPOT, HIGHLIGHTING CEMENTITE PRECIPITATION WITHIN LATHS, (c) DARK FIELD IMAGE USING $(0\bar{1}1)_{\alpha'}$ AND $(0\bar{2}\bar{2})_{Fe_3C}$ SPOT, HIGHLIGHTING CEMENTITE PRECIPITATES WITHIN [011] MARTENSITE LATHS AND (d) DARK FIELD IMAGE USING $(200)_T$ and $(02\bar{4})_{Fe_3C}$ SPOT, HIGHLIGHTING CEMENTITE PRECIPITATES WITHIN [011] TWIN RELATED MARTENSITE LATHS. S.A.D. PATTERN WAS SIMILAR TO THE ONE IN FIGURE 4-56.

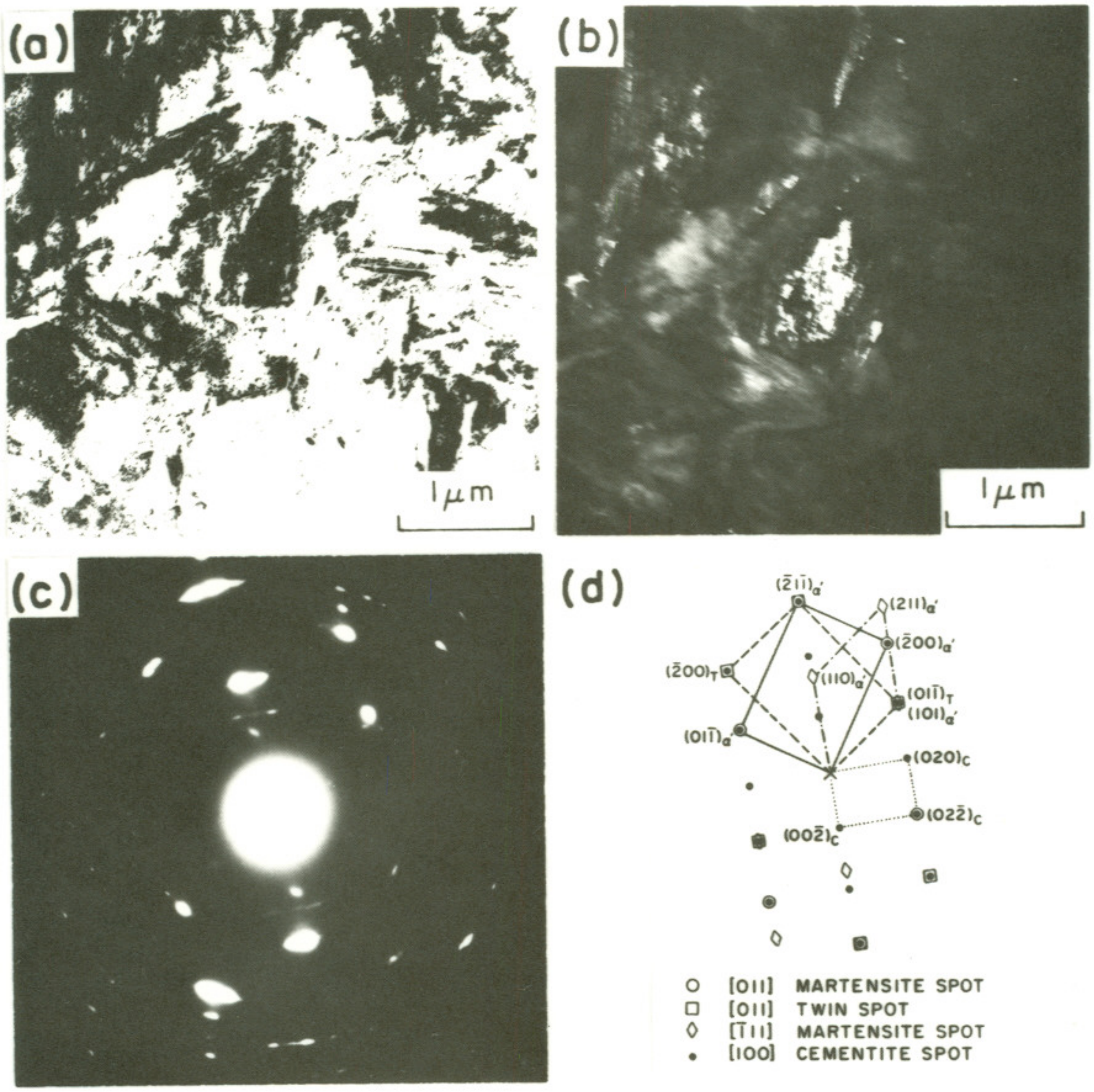

Figure 4-62: (a) BRIGHT FIELD TEM MICROGRAPH SHOWING A TWINNED PLATE MARTENSITIC REGION IN A CONVENTIONALLY HEAT TREATED STEEL, (b) DARK FIELD IMAGE USING $(002)_{Fe_3C}$ SPOT HIGHLIGHTING CEMENTITE PRECIPITATION ON TWINS, (c) S.A.D. PATTERN FROM (a) AND (d) INTERPRETATION OF S.A.D. PATTERN.

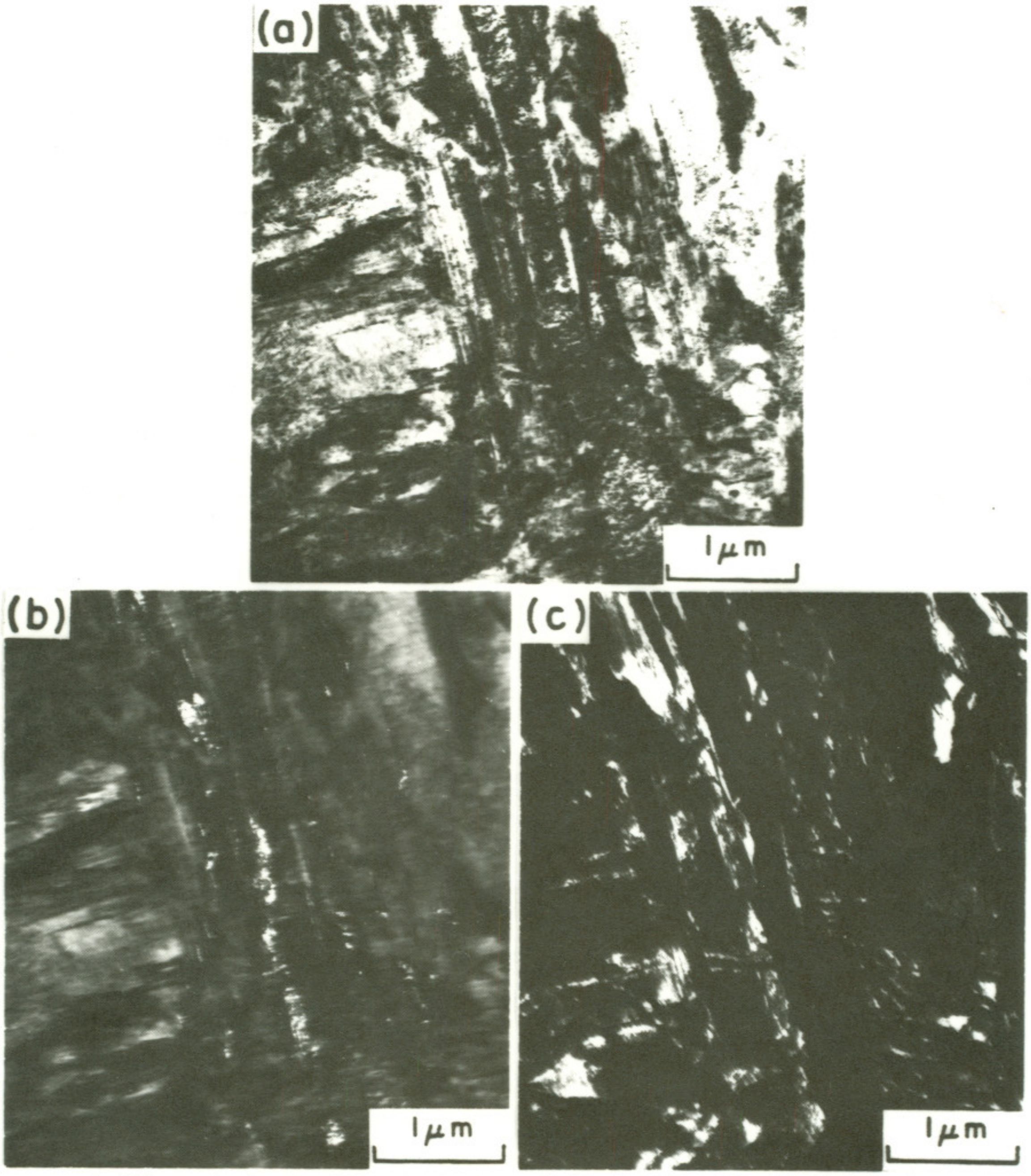

Figure 4-63: (a) BRIGHT FIELD TEM MICROGRAPH SHOWING A TWINNED REGION IN A CONVENTIONALLY HEAT TREATED STEEL, (b) DARK FIELD IMAGE USING $(002)_{Fe_3C}$ SPOT AND (c) DARK FIELD IMAGE USING $(020)_{Fe_3C}$ SPOT, HIGHLIGHTING CEMENTITE PRECIPITATION ON TWINS. S.A.D. PATTERN WAS SIMILAR TO THE ONE IN FIGURE 4-56.

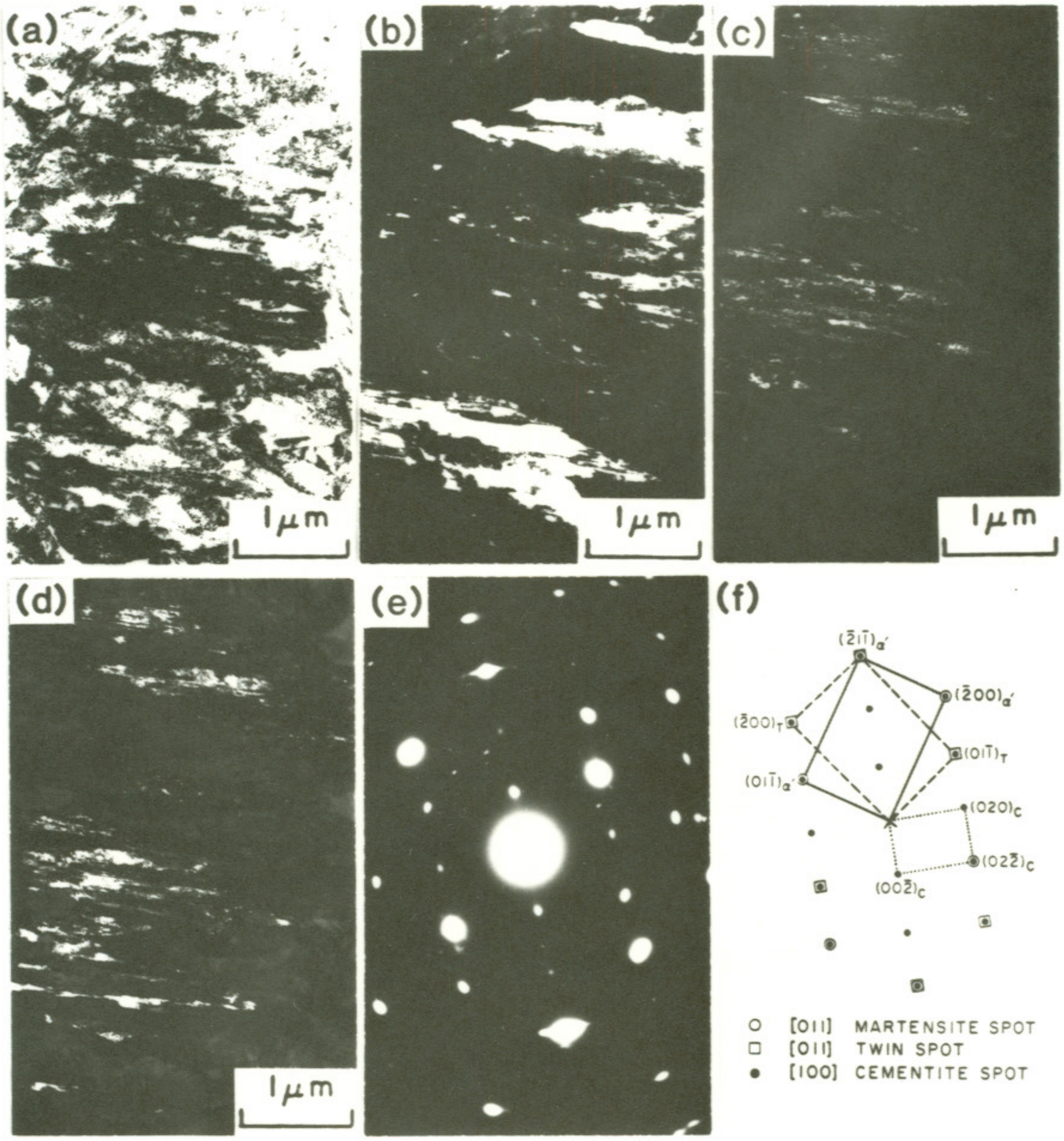

Figure 4-64: (a) BRIGHT FIELD TEM MICROGRAPH SHOWING A TWINNED REGION IN A CYCLICALLY HEAT TREATED STEEL, (b) DARK FIELD IMAGE USING $(01\bar{1})_{\alpha'}$ SPOT HIGHLIGHTING THE TWINS, (c) & (d) DARK FIELD IMAGES USING $(002)_{Fe_3C}$ AND $(020)_{Fe_3C}$ SPOTS RESPECTIVELY, HIGHLIGHTING CEMENTITE PRECIPITATION ON TWINS, (e) S.A.D. PATTERN FROM (a) AND (f) INTERPRETATION OF (e). BAGARYATSKII ORIENTATION RELATIONSHIP IS OBSERVED.

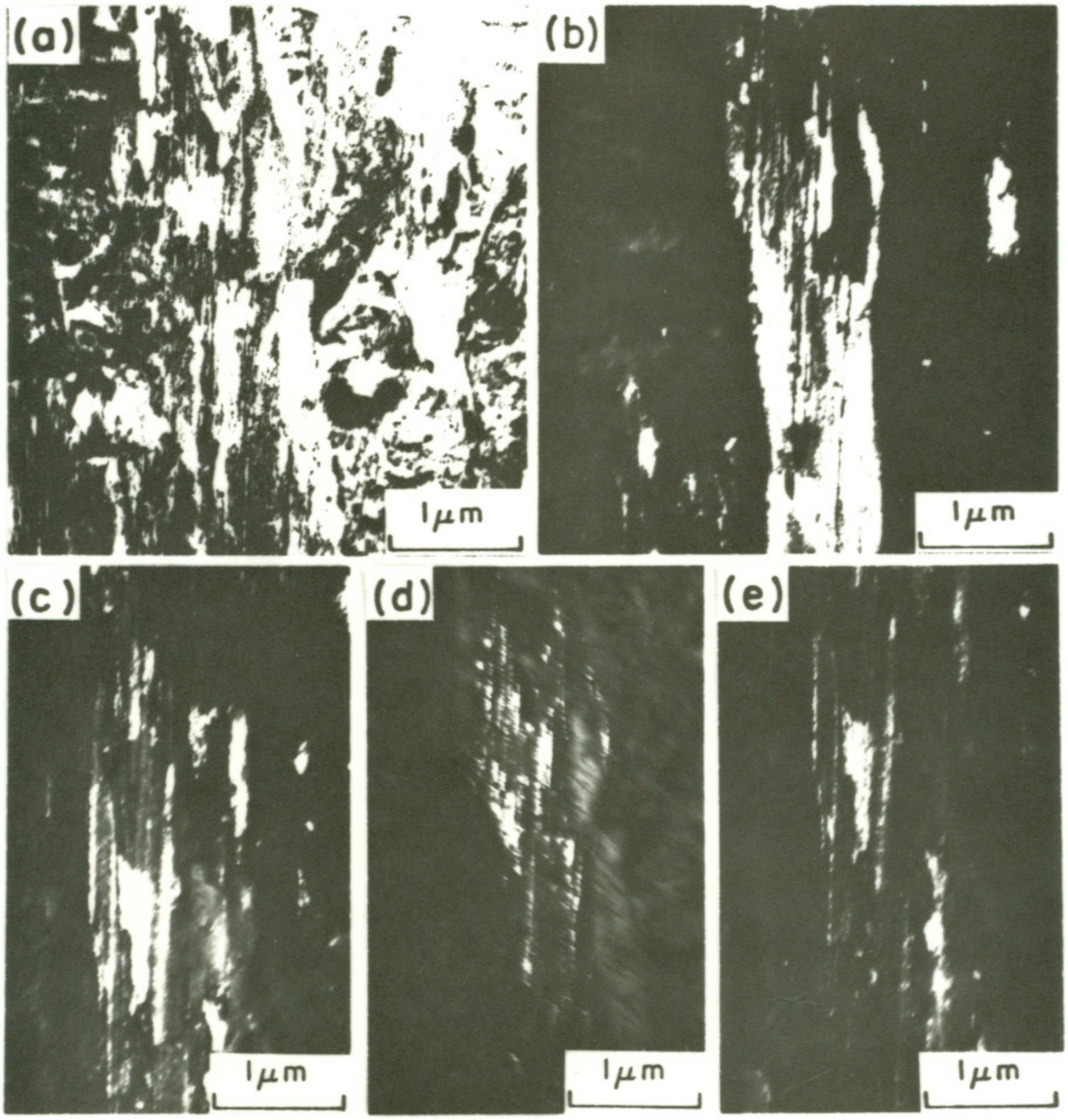

Figure 4-65: (a) BRIGHT FIELD TEM MICROGRAPH SHOWING A TWINNED REGION IN A SPECIMEN SUBJECTED TO STEP HEAT TREATMENT, (b) & (c) DARK FIELD IMAGES, USING $(0\bar{1}1)$ & (200) TYPE SPOTS, HIGHLIGHTING THE TWINS IN (a) AND (d) & (e), DARK FIELD IMAGES USING (022) AND (020) TYPE CEMENTITE SPOTS, HIGHLIGHTING THE PRECIPITATION OF CEMENTITE ON TWINS (S.A.D. PATTERN WAS SIMILAR TO THE ONE IN FIGURE 4-64).

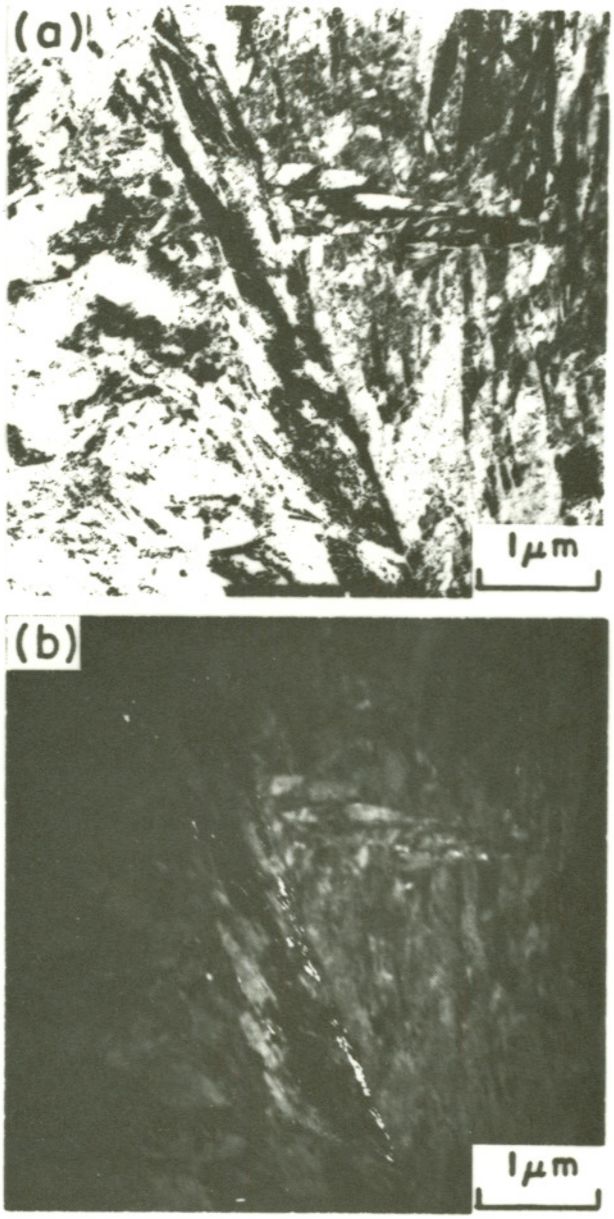

Figure 4-66: (a) BRIGHT FIELD TEM MICROGRAPH SHOWING A GENERAL REGION IN A CONVENTIONALLY HEAT TREATED STEEL AND (b) DARK FIELD IMAGE USING $(002)_{Fe_3C}$ SPOT HIGHLIGHTING CEMENTITE PRECIPITATION AT THE GRAIN BOUNDARY. S.A.D. PATTERN WAS THE SAME AS IN FIGURE 4-64.

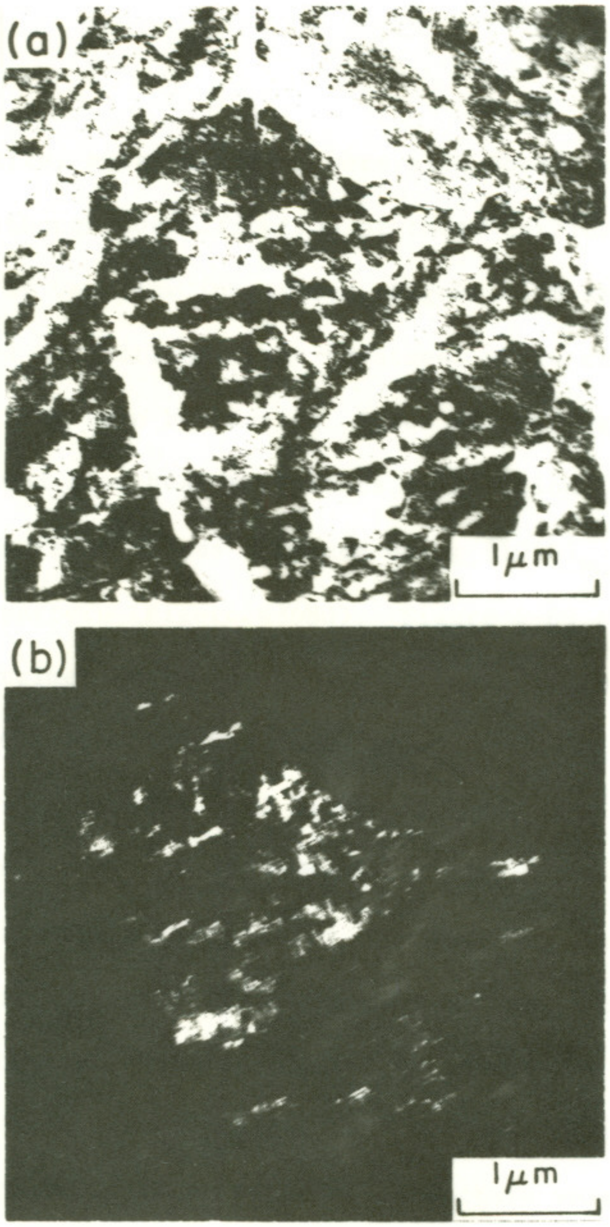

Figure 4-67: (a) BRIGHT FIELD TEM MICROGRAPH SHOWING A GENERAL REGION IN A SPECIMEN SUBJECTED TO MODIFIED HIGH TEMPERATURE HEAT TREATMENT AND (b) DARK FIELD IMAGE USING $(002)_{Fe_3C}$ SPOT, HIGHLIGHTING CEMENTITE PRECIPITATION WITHIN THE PACKET. S.A.D. PATTERN WAS SIMILAR TO THE ONE IN FIGURE 4-60.

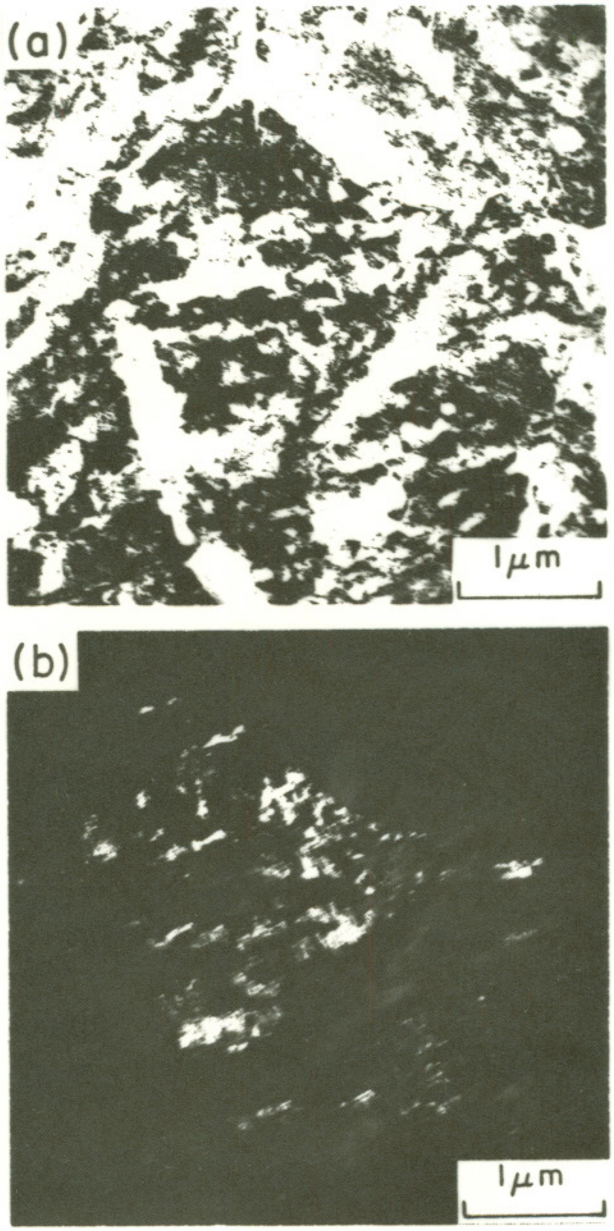

Figure 4-67: (a) BRIGHT FIELD TEM MICROGRAPH SHOWING A GENERAL REGION IN A SPECIMEN SUBJECTED TO MODIFIED HIGH TEMPERATURE HEAT TREATMENT AND (b) DARK FIELD IMAGE USING $(002)_{Fe_3C}$ SPOT, HIGHLIGHTING CEMENTITE PRECIPITATION WITHIN THE PACKET. S.A.D. PATTERN WAS SIMILAR TO THE ONE IN FIGURE 4-60.

Besides cementite, metal carbides were also observed in modified heat treatments, although identification of these carbides was difficult due to extra spots of very low intensity. Figure 4-68 shows a region in the case of modified conventional heat treatment where cementite precipitation occurred along twin boundaries. (Such twinned regions were very rarely observed in modified heat treatments.) Additionally, the dark field picture of Figure 4-68c was obtained using $(\bar{1}010)_{Mo_2C}$ as indicated in the diffraction pattern (Figure 4-68d). Figure 4-69 shows another region of the same specimen where $[00.1]_{Mo_2C}$ orientation was observed. The dark field picture was obtained using $\{\bar{1}010\}$ type Mo_2C spot. Cementite precipitation is also indicated in Figure 4-69b.

In many other regions, coarser spheroidal precipitates were also observed, as shown in Figure 4-70a,b & c, for modified conventional, modified high temperature and modified step heat treatments, respectively. However, identification of these precipitates was difficult, as extra spots in the diffraction pattern were either not visible or were not intense enough. Figure 4-70d is a bright field picture which shows these carbides even more clearly in a specimen which was subjected to modified conventional heat treatment, except that the final reaustenitization step at 850°C and the final tempering step at 280°C were not employed. Even in this sample, these particles could not be clearly identified. Hence, extraction replication was carried out for these samples and for samples subjected to modified conventional heat treatment. These results are presented in Section 4.2.3.6.

Similar to the results obtained in this study, Youngblood and Raghavan [16] also observed coarse, wavy ε-carbide precipitates in 300M

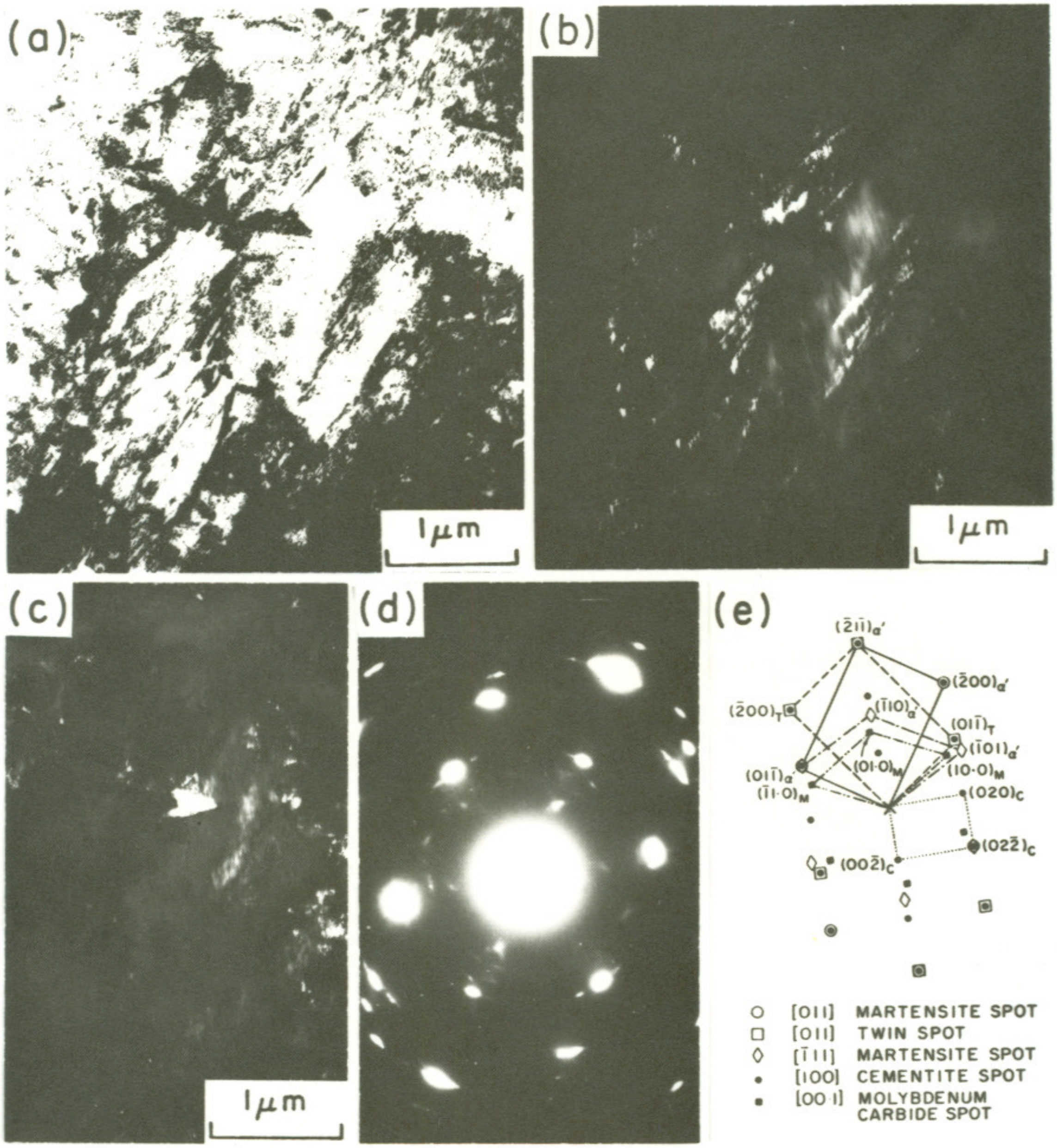

Figure 4-68: (a) BRIGHT FIELD TEM MICROGRAPH SHOWING A GENERAL REGION IN A SPECIMEN SUBJECTED TO MODIFIED CONVENTIONAL HEAT TREATMENT, (b) DARK FIELD IMAGE USING $(002)_{Fe_3C}$ SPOT, HIGHLIGHTING CEMENTITE PRECIPITATION ON TWINS, (c) DARK FIELD IMAGE USING $[\bar{1}010]_{Mo_2C}$ SPOT HIGHLIGHTING Mo_2C PRECIPITATES, (d) S.A.D. PATTERN FROM (a) AND (e) INTERPRETATION OF (d).

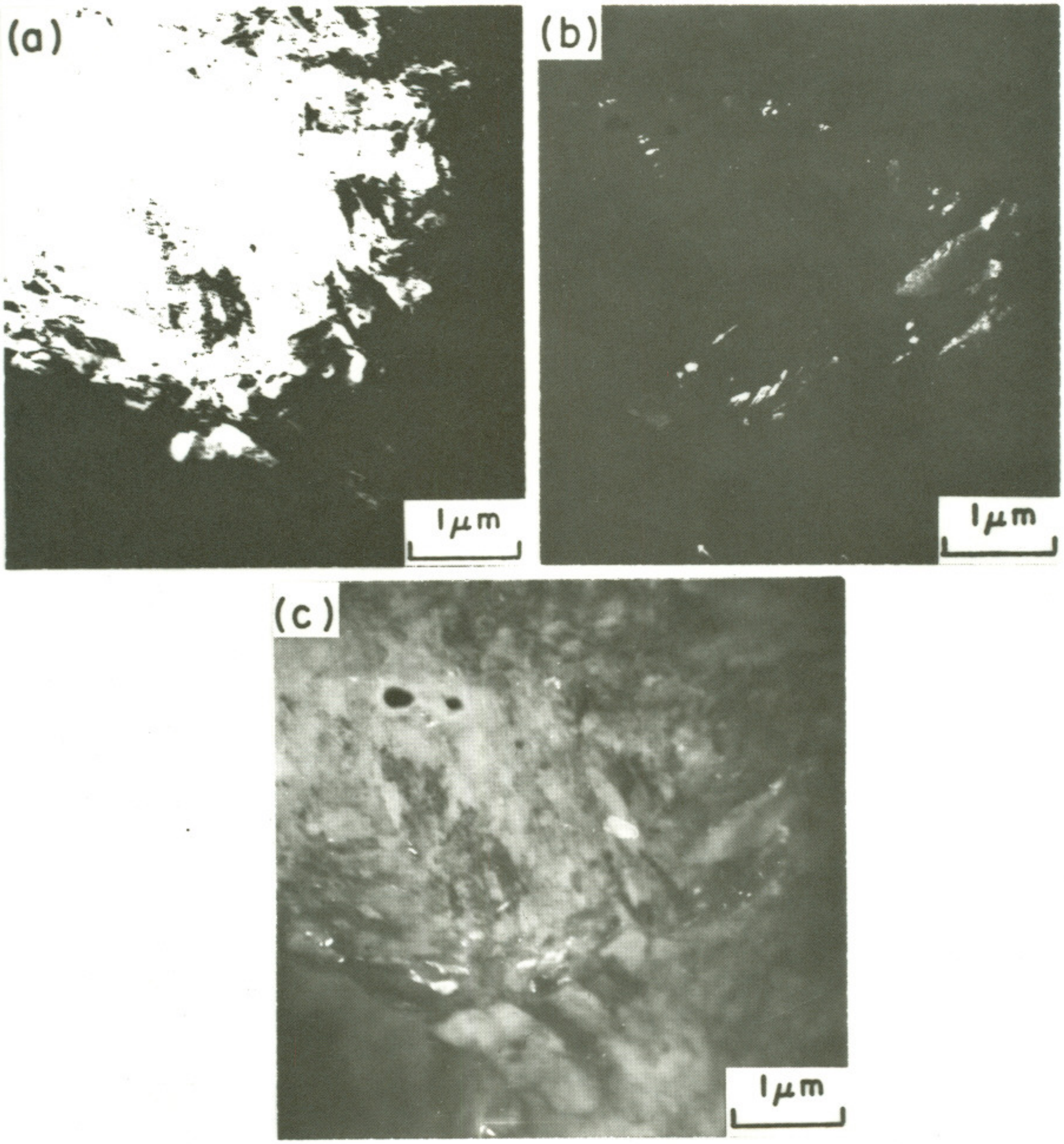

Figure 4-69: (a) BRIGHT FIELD TEM MICROGRAPH SHOWING A GENERAL REGION IN A SPECIMEN SUBJECTED TO MODIFIED CONVENTIONAL HEAT TREATMENT, (b) DARK FIELD IMAGE USING $(002)_{Fe_3C}$ SPOT HIGHLIGHTING CEMENTITE PRECIPITATES AND (c) DARK FIELD IMAGE USING $(\bar{1}010)_{Mo_2C}$ SPOT HIGHLIGHTING Mo_2C PRECIPITATES. S.A.D. PATTERN WAS SAME AS IN FIGURE 4-68.

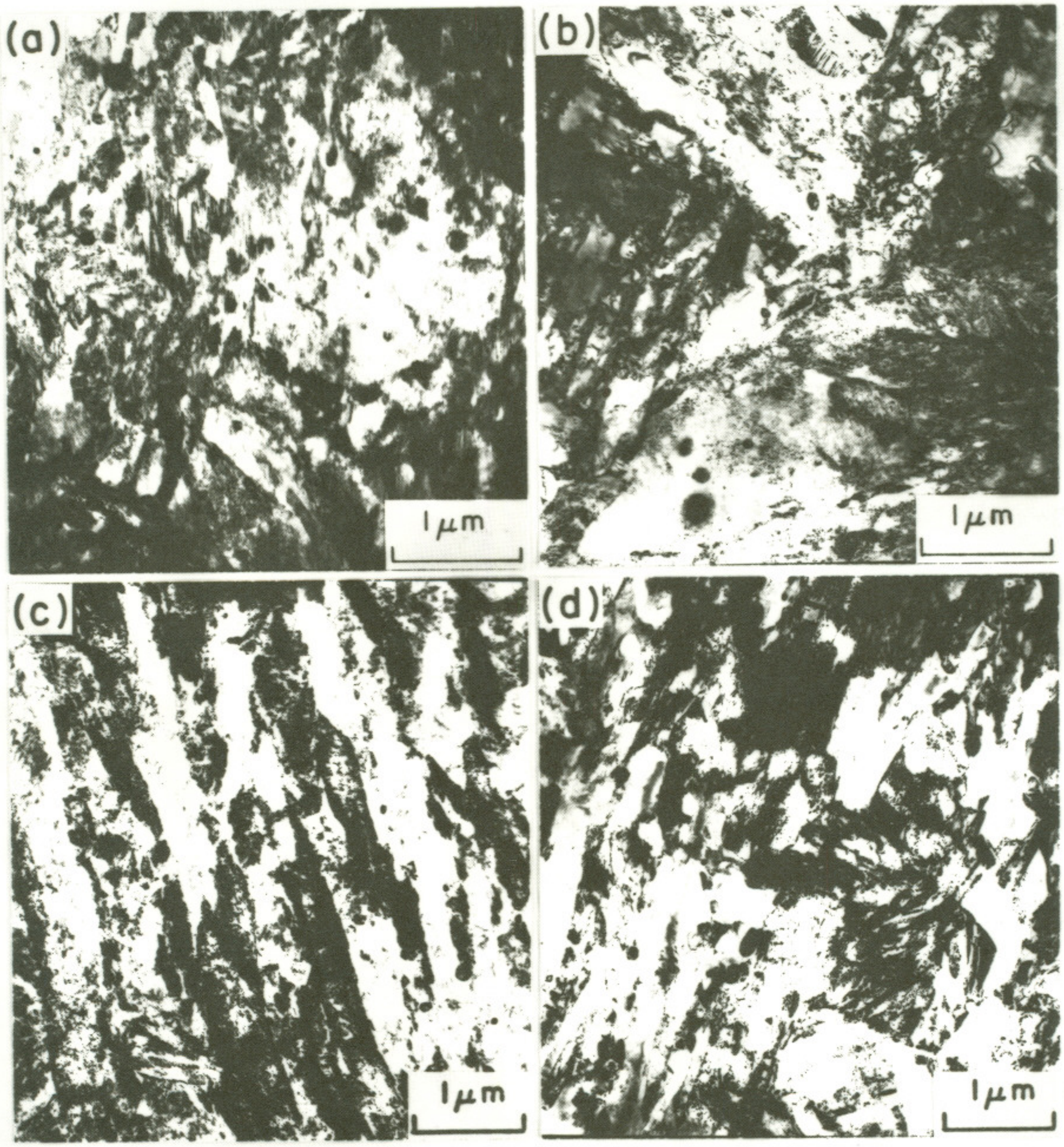

Figure 4-70: BRIGHT FIELD TEM MICROGRAPHS SHOWING SPHEROIDAL PRECIPITATES IN SPECIMENS SUBJECTED TO (a) MODIFIED CONVENTIONAL, (b) MODIFIED HIGH TEMPERATURE (c) MODIFIED STEP AND (d) SAME AS (a) BUT WITHOUT FINAL REAUSTENITIZATION (AT 850°C) AND TEMPERING (AT 280°C) STEPS, HEAT TREATMENTS RESPECTIVELY.

steel specimens tempered below 425°C. While in the range of 200°C to 310°C, they observed predominantly ε-carbide, in this investigation, cementite precipitated to a greater extent than ε-carbide for specimens tempered at 280°C. The inverse dependence on austenitization temperature of cementite precipitation on twins was also reported by other investigators [47,81], and is consistent with the observation that carbon segregation on twins decreases with increasing austenitization temperature [66]. Similarly, the slight deviation from Jack's condition for $(10\bar{1}1)_{\varepsilon}$ and $(101)_{\alpha'}$ planes was also noted by other investigators [82,83]. All the above observations are consistent with the results obtained in this investigation.

4.2.3.5. Effect of Heat Treatment on Prior Austenite Grain Boundary Nucleated Phases. As noted earlier (Sections 4.2.1 and 4.2.2), large prior austenite grain boundary nucleated phases (typically between 1 μm and 10 μm in width) were observed under optical microscope (Figure 4-30) and under SEM (Figures 4-31 and 4-32) for all the heat treatments, irrespective of grain size. Identification of this phase through optical or scanning electron microscopy was difficult and, hence transmission electron microscopy was carried out for these heat treatments and these results are now presented.

This large, irregular shaped grain boundary phase was clearly observed in all heat treatments. Bright field micrographs, Figure 4-50a-g reveal this phase for various heat treatments. ε-carbide precipitation occurred extensively within this phase, usually along parallel rows inclined at an angle of 55°-60° to the longitudinal axis of the ferrite.

These particles were typically 50 Å to 100 Å thick and 1000 Å to 1500 Å long. Although obtaining diffraction patterns with carbide spots from this phase was extremely difficult, in a few instances clear patterns were obtained and the particles were unambiguously identified as ε-carbide (Figures 4-51 to 4-53). The morphology of ε-carbide was revealed in all the dark field pictures (Figures 4-51b, 4-52b,c & 4-43b), which were all obtained using $\{1\bar{1}00\}$ type spots. The orientation relationships between ε-carbide and ferrite satisfied the Jack orientation relationship conditions [78] (Figure 4-54), viz., $[0001]_{\varepsilon} \parallel [011]_{\alpha'}$, $(0001)_{\varepsilon} \parallel (011)_{\alpha'}$, $(10\bar{1}0)_{\varepsilon} \parallel (2\bar{1}\bar{1})_{\alpha'}$, and $(10\bar{1}\bar{1})_{\varepsilon}$ was only about 1° away from $(101)_{\alpha'}$.

Figure 4-71 shows the grain boundary phase for conventional heat treatment. The region investigated was the same as shown in Figure 4-51. However, in this case, the specimen stage was tilted by 7° and a different diffraction pattern was obtained. In this orientation, the ε-carbide particles were resolved much better in the dark field image (Figure 4-71b) which was obtained using $(01\bar{1}\bar{1})_{\varepsilon}$ spot. This orientation has not been reported elsewhere in literature and a new orientation relationship, based on stereographic projection analysis (similar to Figure 4-54) is now proposed, namely, $[311]_{\alpha'} \parallel [\bar{1}1.1]_{\varepsilon}$ and $(\bar{1}03)_{\alpha'} \parallel (01.\bar{1})_{\varepsilon}$, $(311)_{\alpha'} \parallel (\bar{1}1.1)_{\varepsilon}$ and $(0\bar{1}1)_{\alpha'}$ is about 7° away from $(\bar{1}1.\bar{2})_{\varepsilon}$. Also, Figures 4-51 to 4-53 and 4-71 reveal that this blocky phase was heavily dislocated and the ε-carbide precipitation within this phase occurred in mostly two variants. To determine these variants, image-S.A.D. rotation angle calibration using MoO_3 crystal was done (Appendix III).

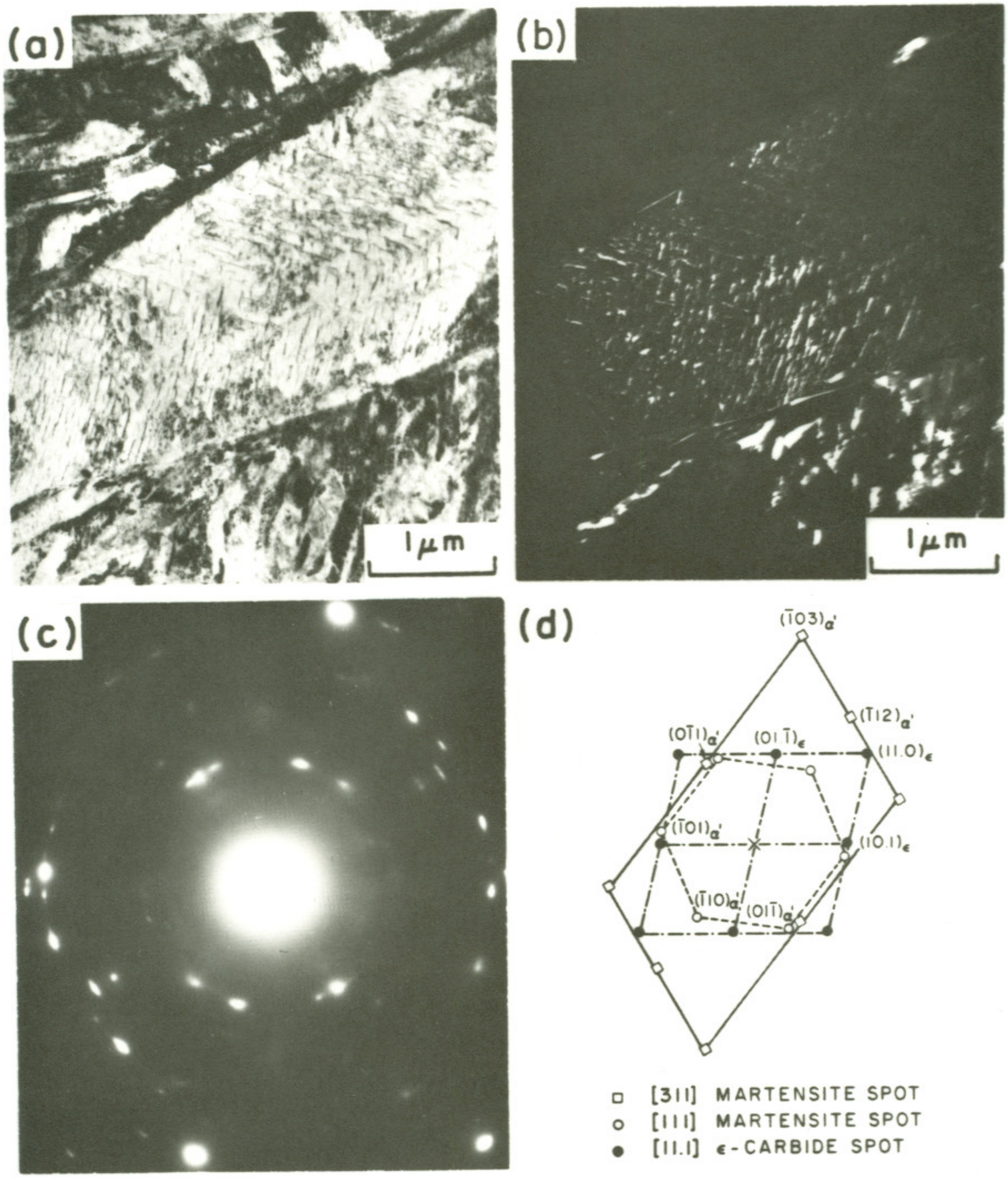

Figure 4-71: (a) BRIGHT FIELD TEM MICROGRAPH SHOWING A LARGE LATH AT A GRAIN BOUNDARY IN A CONVENTIONALLY HEAT TREATED STEEL, (b) DARK FIELD IMAGE USING $(01\bar{1}\bar{1})_{\epsilon}$ SPOT, HIGHLIGHTING ε-CARBIDE PRECIPITATATION ALONG TWO VARIANTS OF <112>, INSIDE THE LATH, (c) S.A.D. PATTERN FROM (a) AND (d) INTERPRETATION OF (c). THE GROWTH DIRECTION WAS DETERMINED AS DESCRIBED IN TEXT.

The grain boundary phase also contained twins, Figures 4-72 to 4-77. Diffraction patterns were fairly easily obtained from these twinned regions and dark field imaging was done using {011} type spots (Figures 4-73 and 4-74) to confirm the presence of these twins within the blocky ferrite. As noted in Section 4.2.2., within the blocky ferrite spheroidal particles were also occasionally seen (Figure 4-78a-c). However, these carbides could not be identified due to weak diffraction spots which were obtained. These were, however, identified through extraction replication and these results are presented in Section 4.2.3.6. Another feature was the precipitation of cementite along the boundaries of this grain boundary phase (Figure 4-79). The presence of ε-carbide in at least two variants within the blocky phase and the presence of twins within this phase (which always forms at prior austenite grain boundaries) indicates that this phase is auto-tempered blocky martensite.

Khan and Kannan [85] and Sastry [47] reported the presence of blocky martensite at prior austenite grain boundaries in 4340 steel. They also observed twinning within the blocky martensite. Kamada et al. [86] found dislocated blocky martensite in a 5% Ni steel. Other investigators found ε-carbide to have $\{100\}_{\alpha'}$ habit [286-288]. These observations conform with the results of the present investigation.

No ε-carbide or twins have been reported in upper bainite to date and cementite in upper bainite is precipitated at the ferrite boundaries, or within the ferrite, directed along, rather than at an angle to the ferrite boundaries [48-53]. In lower bainite also, the predominantly occurring carbide is cementite and ε-carbide, when identified, was reported to be present only in one variant [83,87,88]. The latter

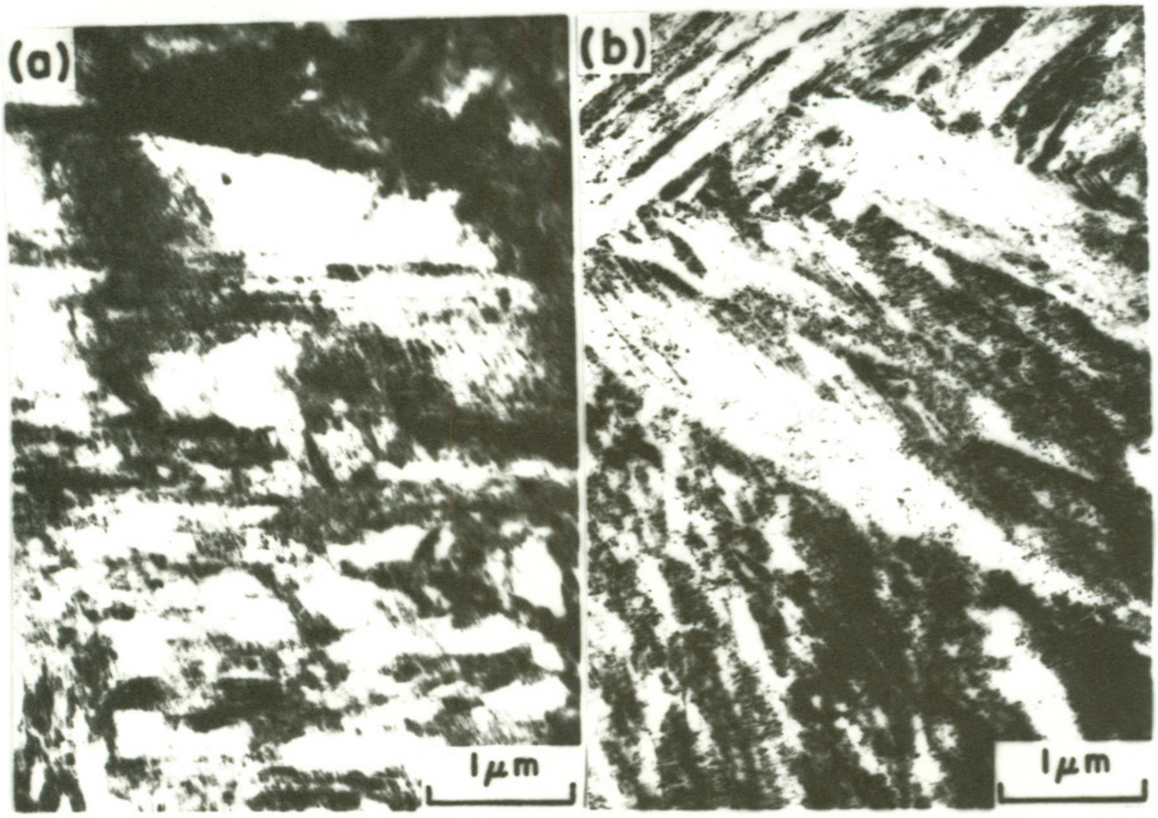

Figure 4-72: BRIGHT FIELD TEM MICROGRAPHS SHOWING EXTENSIVE TWINNING WITHIN GRAIN BOUNDARY PHASE FOR CONVENTIONAL HEAT TREATMENT.

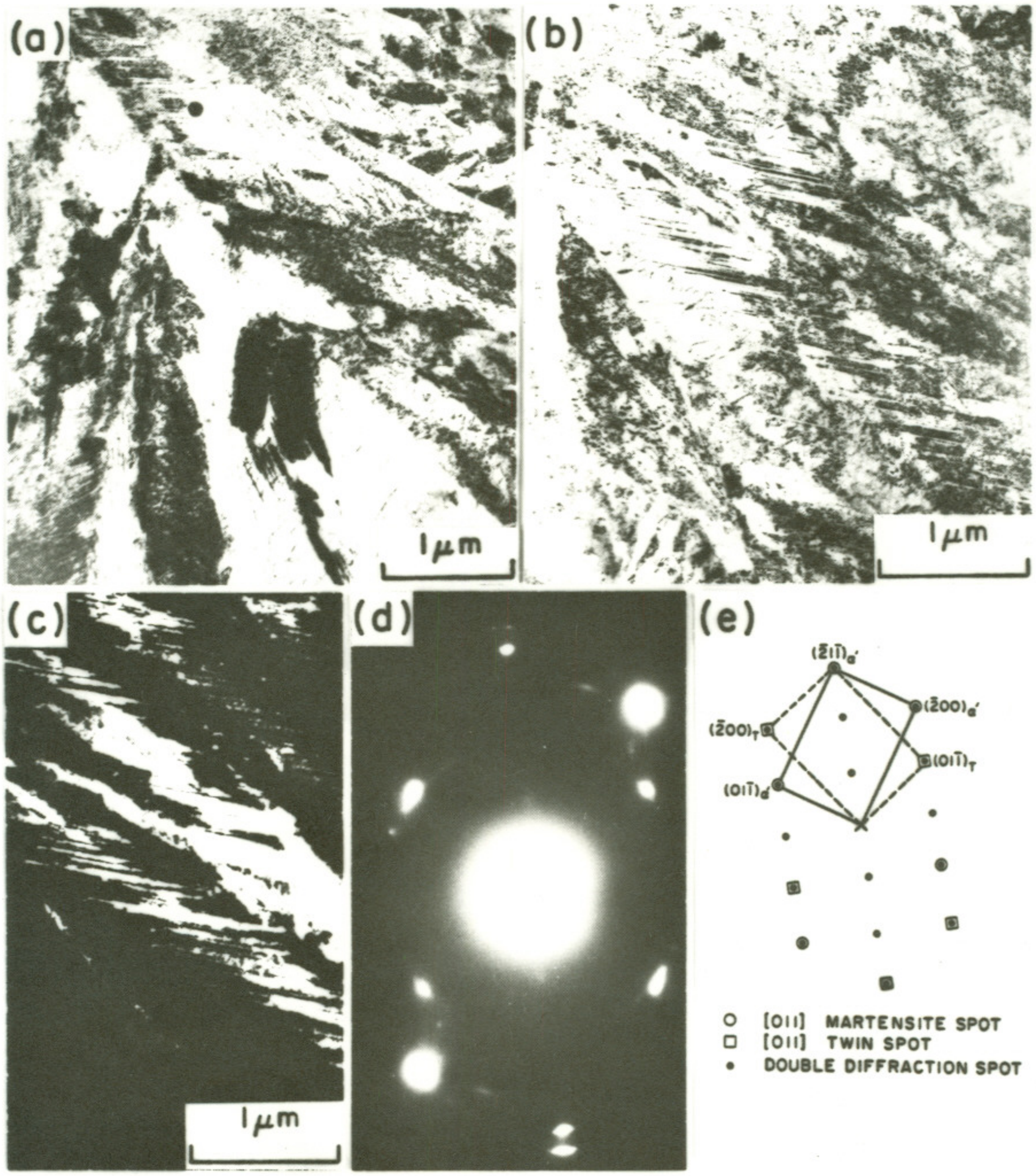

Figure 4-73: (a) & (b) BRIGHT FIELD TEM MICROGRAPHS SHOWING EXTENSIVE TWINNING WITHIN GRAIN BOUNDARY PHASE FOR CYCLIC HEAT TREATMENT, (c) DARK FIELD IMAGE USING $(01\bar{1})_T$ SPOT HIGHLIGHTING THE TWINS IN (b), (d) S.A.D. PATTERN FROM (b) AND (e) INTERPRETATION OF (d). DOUBLE DIFFRACTION SPOTS ARE ALSO FAINTLY VISIBLE.

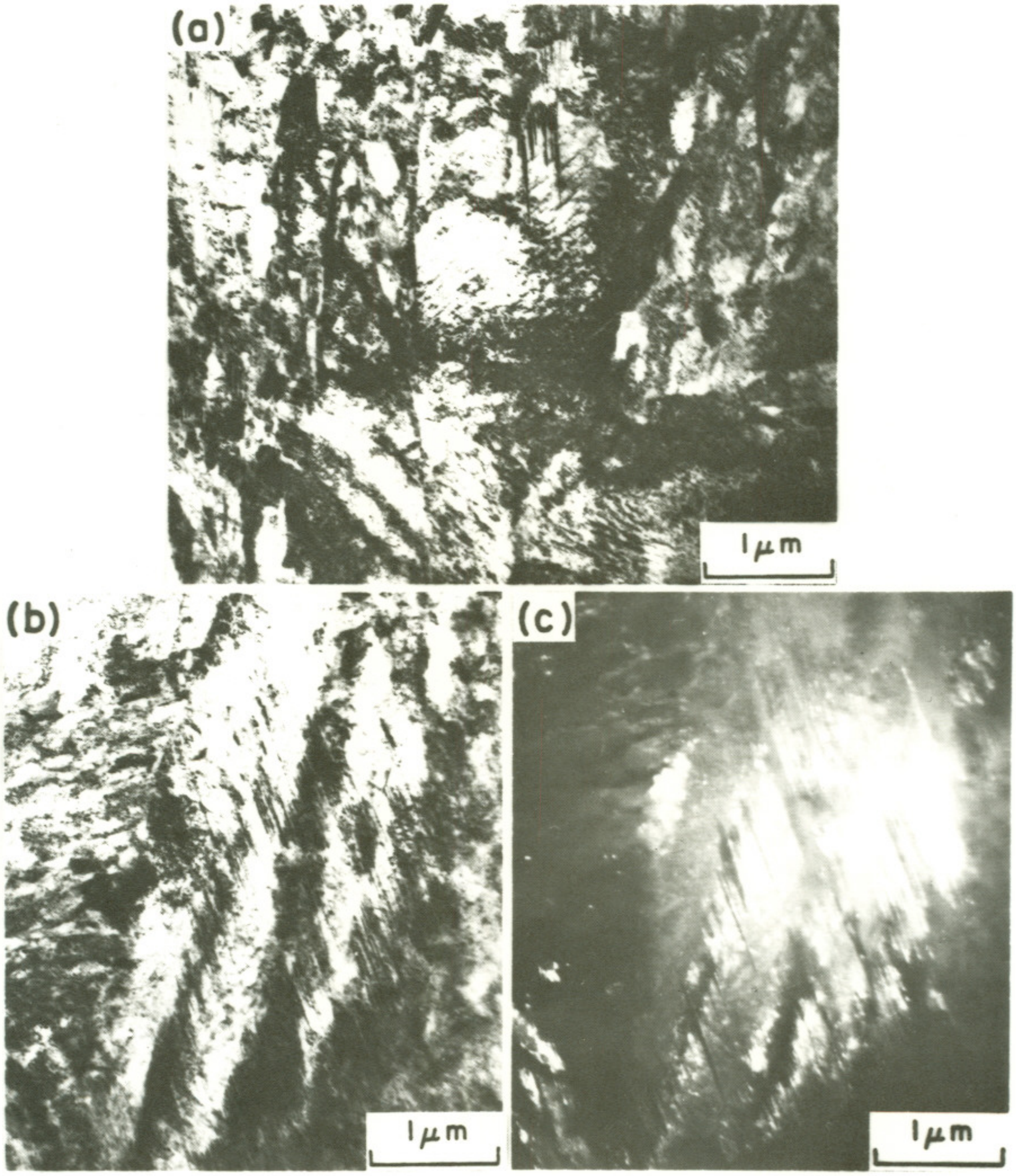

Figure 4-74: (a) & (b) BRIGHT FIELD TEM MICROGRAPHS SHOWING TWINNING WITHIN GRAIN BOUNDARY PHASE IN A SPECIMEN SUBJECTED TO HIGH TEMPERATURE HEAT TREATMENT AND (c) DARK FIELD IMAGE USING $(01\bar{1})$ TYPE SPOT HIGHLIGHTING THE TWINS WITHIN (b). S.A.D. PATTERN OBRTAINED WAS THE SAME AS IN FIGURE 4-73.

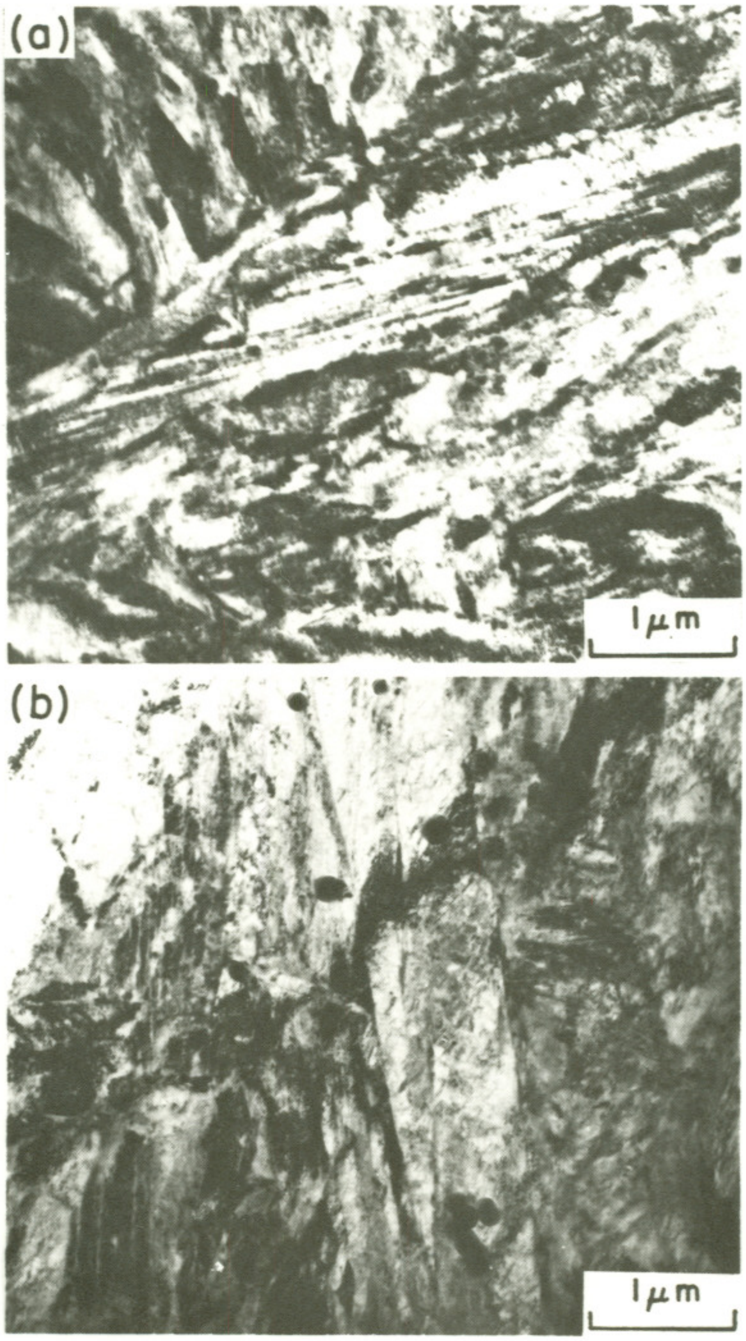

Figure 4-75: BRIGHT FIELD TEM MICROGRAPHS SHOWING TWINNING WITHIN GRAIN BOUNDARY PHASE IN A SPECIMEN SUBJECTED TO STEP HEAT TREATMENT.

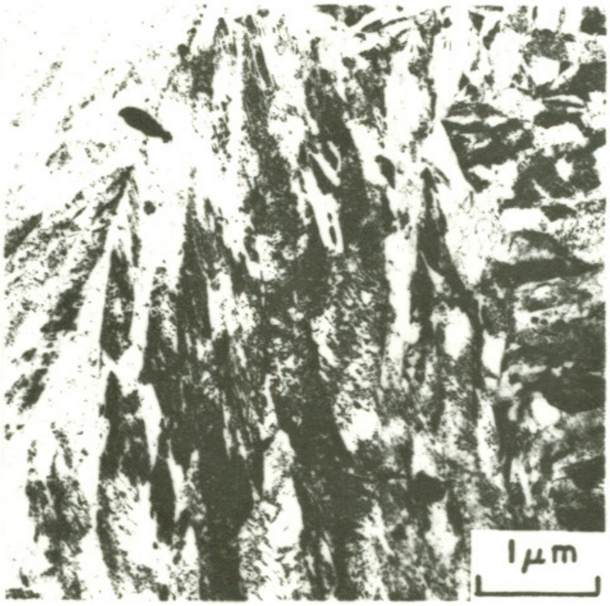

Figure 4-76: BRIGHT FIELD TEM MICROGRAPH SHOWING SOME TWINNING WITHIN GRAIN BOUNDARY PHASE IN A SPECIMEN SUBJECTED TO MODIFIED CONVENTIONAL HEAT TREATMENT.

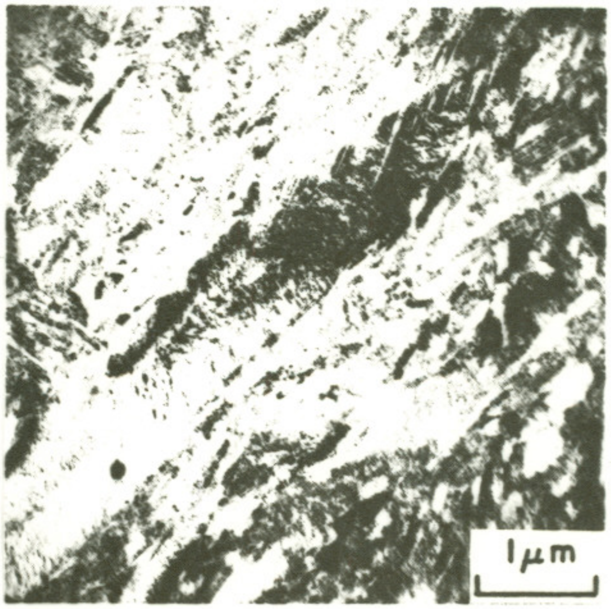

Figure 4-77: BRIGHT FIELD TEM MICROGRAPH SHOWING SOME TWINNING WITHIN GRAIN BOUNDARY PHASE IN A SPECIMEN SUBJECTED TO MODIFIED STEP HEAT TREATMENT.

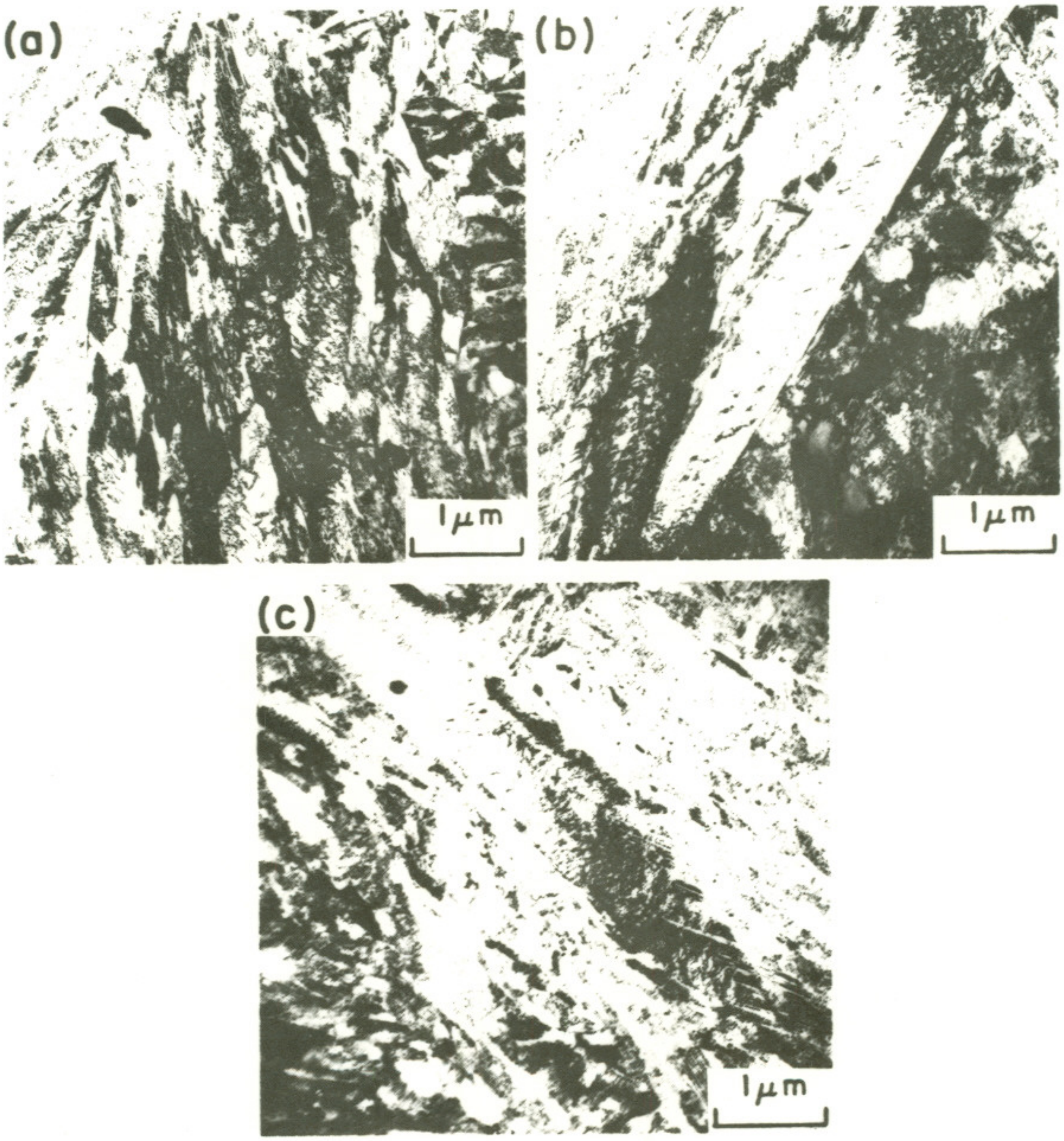

Figure 4-78: BRIGHT FIELD TEM MICROGRAPHS SHOWING SPHEROIDAL PRECIPITATES WITHIN GRAIN BOUNDARY PHASE FOR (a) MODIFIED CONVENTIONAL, (b) MODIFIED HIGH TEMPERATURE AND (c) MODIFIED STEP HEAT TREATMENTS.

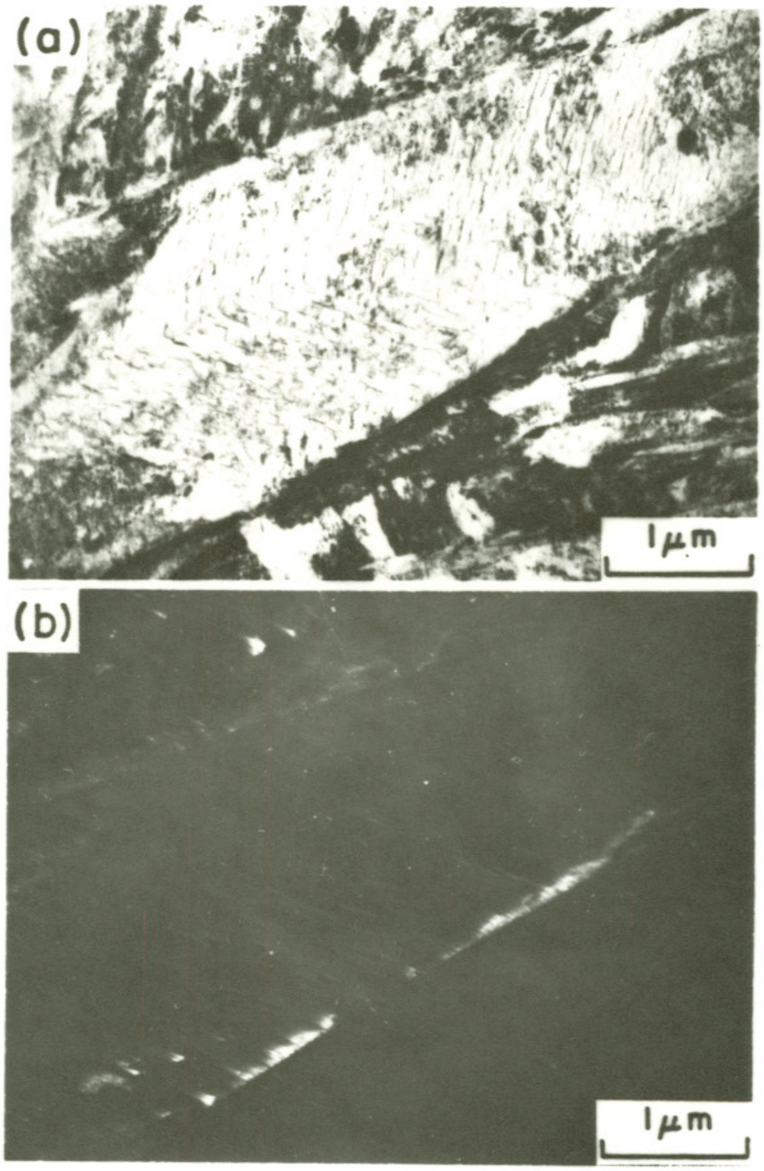

Figure 4-79: (a) BRIGHT FIELD TEM MICROGRAPH SHOWING GRAIN BOUNDARY PHASE IN A CONVENTIONALLY HEAT TREATED STEEL AND (b) DARK FIELD IMAGE USING $(002)_{Fe_3C}$ SPOT HIGHLIGHTING CEMENTITE PRECIPITATION ALONG THE BOUNDARIES OF THIS PHASE. THE CARBIDE PRECIPITATION WITHIN THIS PHASE WAS IDENTIFIED AS ε-CARBIDE (FIGURES 4-51 AND 4-71). THE S.A.D. PATTERN OBTAINED WAS SIMILAR TO THE ONE IN FIGURE 4-56. WHILE THIS PATTERN WAS OBTAINED FROM THIS GENERAL AREA, THE PATTERNS OF FIGURES 4-51 AND 4-71 WERE OBTAINED SPECIFICALLY FROM WITHIN THIS PHASE.

investigators [87,88] also reported observing twins in lower bainite, but the M_s temperature for their steel was 142°C, with the isothermal transformation temperature for obtaining lower bainite being 204°C. It is not surprising, therefore, that they did see twins in lower bainite at a temperature where the critical resolved shear stress for twinning is slightly lower than, if not equal to, that for slipping. However, no internal twins have been reported in lower bainite of steels similar to the present investigation. Based on these points, it is clear that the grain boundary phase is a blocky form of autotempered martensite.

4.2.3.6. Extraction Replication and X-Ray Results. In order to identify the spheroidal carbides observed under both SEM and thin foil TEM, extraction replication was carried out for samples subjected to modified conventional heat treatment and for samples which, after being austenitized at 870°C for 1 hour, were tempered for 1 hour at 650°C but not subsequently reaustenitized or subjected to final tempering at 280°C. The latter heat treatment was done to facilitate identification by precipitating coarse carbides at 650°C (which remained coarse and did not undergo any further dissolution or refinement due to reaustenitization at 850°C). The etching time and thickness of carbon coating during the extraction process were such that a majority of spheroidal carbides only were preferentially extracted and extraction of other carbides was minimal.

Figure 4-80 clearly shows these carbides for the modified conventional heat treatment. Since these precipitates were very fine, some high magnification micrographs were also taken (Figure 4-80b&d). The

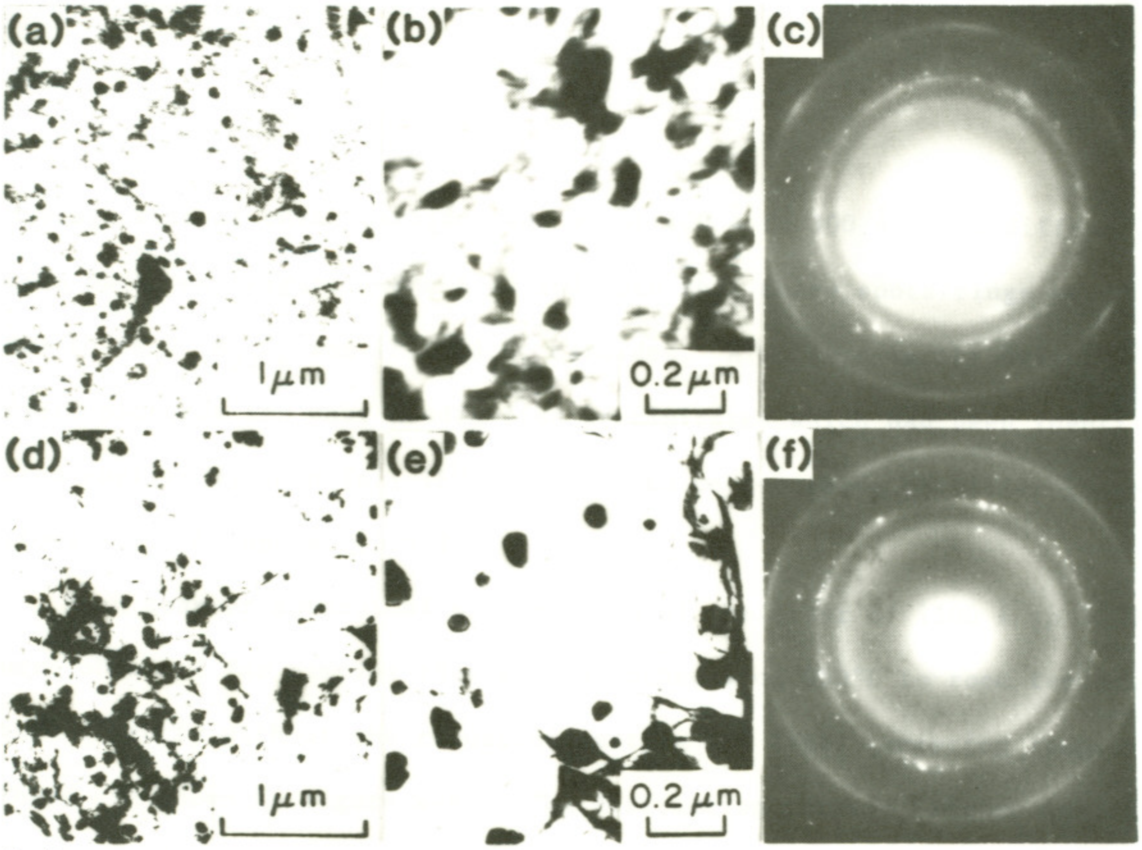

(g)

Ring #	I/I_1	Carbide Type	{hkl}
1	65	Fe_3C	112 021
2	100	Fe_3C $(Fe,Cr)_7C_3$ $M_{23}C_6$	103 600 122 333 511
3	60	$(Fe,Cr)_7C_3$	642

Figure 4-80: (a) & (b) BRIGHT FIELD TEM EXTRACTION REPLICA PICTURES FROM SPECIMEN 1, (c) S.A.D. PATTERN FROM SPECIMEN 1, (d) & (e) BRIGHT FIELD TEM EXTRACTION REPLICA PICTURES FROM SPECIMEN 2, (f) S.A.D. PATTERN FROM SPECIMEN 2 AND (g) INTERPRETATION OF THE S.A.D. PATTERNS. SPHERICAL CARBIDES ARE M_3C and M_7C_3. NEEDLE-LIKE CARBIDE IS ε-CARBIDE. BOTH SPECIMEN 1 AND 2 WERE SUBJECTED TO MODIFIED CONVENTIONAL HEAT TREATMENT.

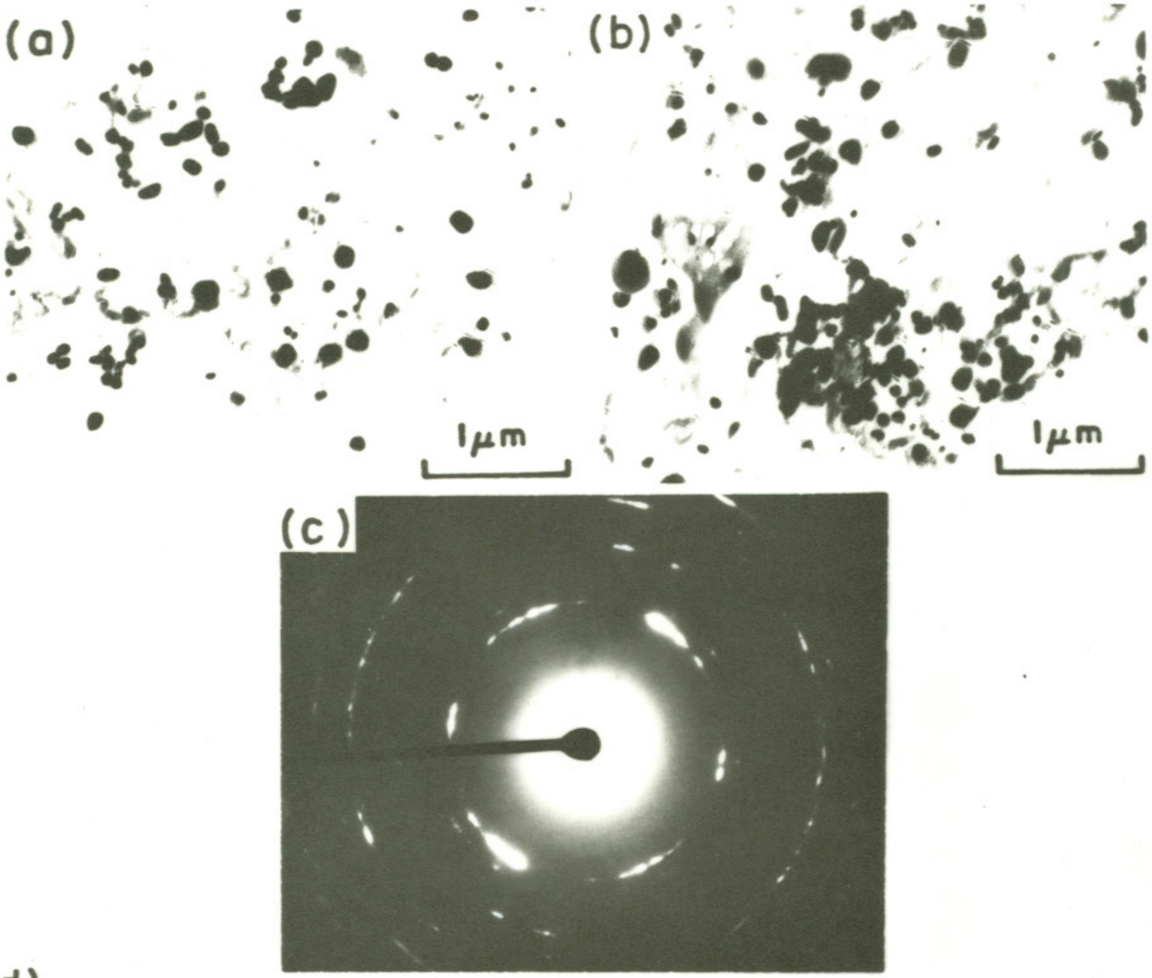

(d)

Ring #	I/I$_1$	Carbide Type	{hkl}	Ring #	I/I$_1$	Carbide Type	{hkl}
1	100	Fe$_3$C	103	4	60	(Fe,Cr)$_7$C$_3$	603
		(Fe,Cr)$_7$C$_3$	600 122	5	100	M$_{23}$C$_6$	844
		M$_{23}$C$_6$	331 511				
2	60	(Fe,Cr)$_7$C$_3$	431 402	6	60	M$_{23}$C$_6$	10 4 0
		M$_{23}$C$_6$	531				
3	18	Mo$_2$C	103	7	100	M$_{23}$C$_6$	971

Figure 4-81: (a) & (b) BRIGHT FIELD TEM EXTRACTION REPLICA PICTURES SHOWING COARSE CARBIDE PRECIPITATION IN A SPECIMEN SUBJECTED TO MODIFIED CONVENTIONAL HEAT TREATMENT (WITHOUT REAUSTENITIZING AND FINAL TEMPERING STEPS), (c) S.A.D. PATTERN FROM THIS SPECIMEN AND (d) INTERPRETATION OF S.A.D. PATTERN. CARBIDE TYPES IDENTIFIED ARE M_3C, M_7C_3, $M_{23}C_6$ AND Mo_2C.

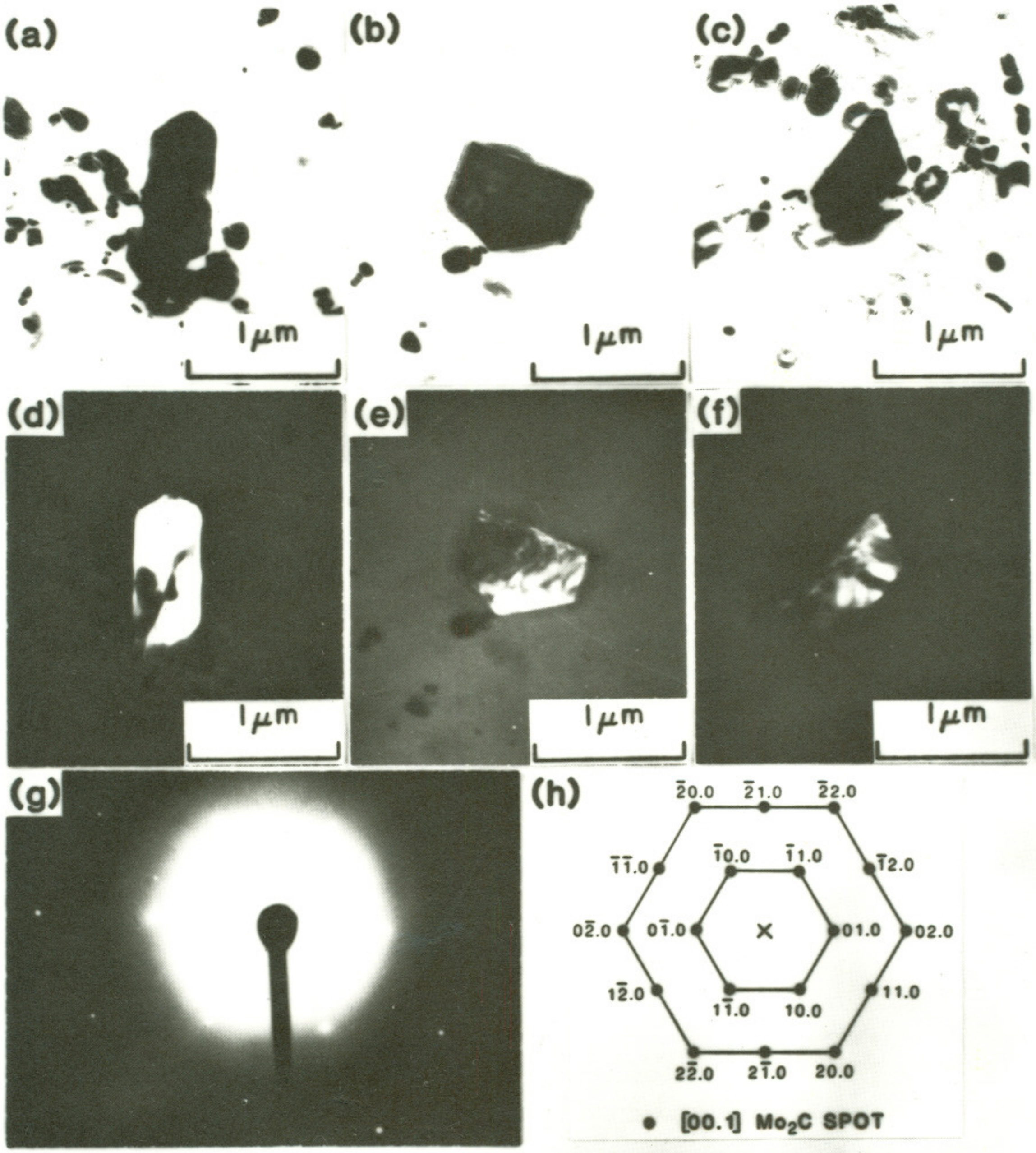

Figure 4-82: (a), (b) & (c) BRIGHT FIELD TEM EXTRACTION REPLICA PICTURES, (d),(e) & (f) DARK FIELD PICtures using $(\bar{1}1\cdot0)_{Mo_2C}$ SPOT, HIGHLIGHTING THE Mo_2C PRECIPITATE SHOWN IN (a),(b) & (c) RESPECTIVELY, (g) S.A.D. PATTERN OBTAINED FROM (a) AND (h) INTERPRETATION OF (g). S.A.D. PATTERNS FROM (b) & (c) WERE EXACTLY SIMILAR TO (g). THE SPECIMEN WAS SUBJECTED TO MODIFIED CONVENTIONAL HEAT TREATMENT, EXCEPT FOR THE REAUSTENITIZATION AND FINAL TEMPERING STEPS.

in order to confirm the presence as well as determine the morphology of Mo_2C.

X-ray powder patterns were also obtained from Debye-Scherrer cameras for these specimens to confirm the identity of the carbides. The extracted carbon films were used directly to obtain these patterns (Figure 4-83a & b). These patterns were indexed and the presence of Fe_3C, $M_{23}C_6$ and $(Fe,Cr)_7C_3$ and Mo_2C was confirmed.

4.2.4. Summary: Microstructural Analysis.

4.2.4.1. Optical.

1. High temperature and step heat treatments resulted in an order of magnitude higher prior austenite grain size, when compared with conventional heat treatment.

2. Cyclic heat treatment refined the prior austenite grain size of conventionally heat treated steel.

3. All modified heat treatments refined the prior austenite grain size of the corresponding non-modified heat treatments.

4. Conventional, high temperature and step heat treatments exhibited a dark etching constituent at the prior austenite grain boundaries.

4.2.4.2. Scanning Electron Microscopy.

1. Conventional heat treatment resulted in more lenticular, platelike martensite, whereas the high temperature and step heat treatments resulted in predominantly lath martensite.

2. Large, blocky laths, nucleated at the grain boundaries, were observed in the case of all heat treatments and these consisted of

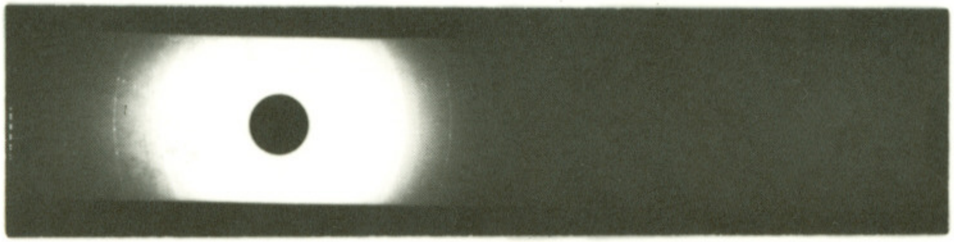

Ring #	Diameter (mm)	Measured* 'd' (Å)	Carbide Type	{hkl}	Ring #	Diameter (mm)	Measured 'd' (Å)	Carbide Type	{hkl}
1	32.80	4.055	M_3C	011	5	67.27	2.067	M_3C	210
2	35.51	3.757	M_3C	101	6	68.13	2.044	$M_{23}C_6$	333 511
3	44.53	3.022	M_3C	111	7	68.30	2.039	M_7C_3	24.1
4	65.82	2.107	M_3C	121	8	69.31	2.013	M_3C	103

Figure 4-83: (a) POWDER DIFFRACTION PATTERNS FOR MODIFIED CONVENTIONAL HEAT TREATMENT. CARBIDES IDENTIFIED: M_3C, M_7C_3, $M_{23}C_6$. *calculated from $2d \sin \Theta = \lambda$, with $\lambda = 2.2897$ for Cr K_{α_1}.

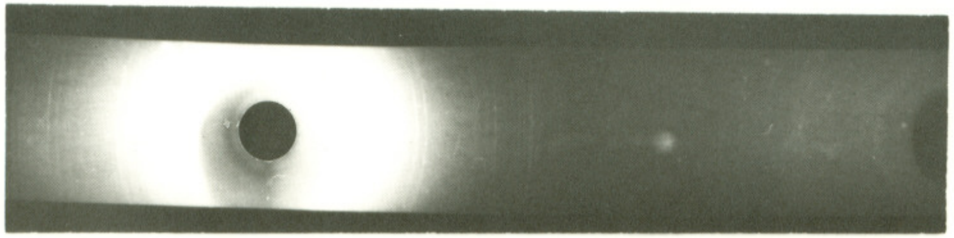

Ring #	Diameter (mm)	Measured* 'd' (Å)	Carbide Type	{hkl}	Ring #	Diameter (mm)	Measured 'd' (Å)	Carbide Type	{hkl}
1	31.48	4.220	M_7C_3	01.1	8	63.72	2.169	$M_{23}C_6$	22.4
2	35.55	3.750	M_3C $M_{23}C_6$	101 022	9	65.54	2.115	M_7C_3	02.2
3	38.19	3.500	M_7C_3	22.0	10	67.08	2.072	M_7C_3	33.1
4	39.72	3.370	M_3C	002	11	68.13	2.044	$M_{23}C_6$	333 511
5	57.37	2.384	M_3C	021	12	68.32	2.039	M_7C_3	24.1
6	60.28	2.280	M_7C_3 Mo_2C	14.1 01.1	13	69.24	2.015	M_3C	103
7	61.08	2.253	M_7C_3	00.2					

Figure 4-83: (b) POWDER DIFFRACTION PATTERNS FOR SAME AS (a), BUT NO REAUSTENITIZING AND FINAL TEMPERING HEAT TREATMENTS. CARBIDES IDENTIFIED: M_3C, M_7C_3, $M_{23}C_6$, Mo_2C. *Calculated from $2d\sin\Theta = \lambda$, with $\lambda = 2.2897$ for Cr K_{α_1}.

parallel rows of wavy carbides inclined at an angle of 55° to the longitudinal axis of the laths.

3. In the case of modified heat treatments, the large laths also contained randomly precipitated spherical carbide particles.

4.2.4.3. Transmission Electron Microscopy.

1. Conventional and cyclic heat treatments resulted in both lath and plate-like martensite with plate martensite predominating, whereas the high temperature and step heat treatments resulted in predominantly lath martensite.

2. Twins and dislocations were extensively present in conventional and cyclic heat treatments.

3. High temperature and step heat treatments resulted in a large amount of dislocations while twins were occasionally seen only in the case of step heat treatment.

4. Modified heat treatments resulted in increased lath martensite and fewer or no twins than the corresponding non-modified heat treatments.

5. The lath width was smaller for the modified and cyclic heat treatments and the laths or plates in high temperature, step and modified heat treatments rarely extended across the whole grain, unlike in the case of conventional and cyclic heat treatments.

6. Twins were generally restricted to plate martensitic regions and these regions occasionally also contained dislocations. However, a few microtwins were also seen within laths in a few instances.

7. Laths were, in general, heavily dislocated and occurred either separated from each other by low angle boundaries or in twin related fashion.

8. The predominantly occurring lath orientations were <111> and <100> although <113> and <110> zone axes were also observed regularly.

9. Laths occurred in three morphologies--convergent laths, regular parallel laths and large laths with extensive carbide precipitation within.

10. Twins occurred along {112} planes and the amount of twinning increased with decreased austenitization temperature and increased amounts of segregation.

11. All heat treatments resulted in some mostly interlath films of retained austenite, ranging in thickness from 100 Å to 200 Å. The high temperature and step heat treatments exhibited more retained austenite than conventional and cyclic heat treatments. The modified heat treatments contained more retained austenite than the corresponding non-modified heat treatments.

12. Both K-S and N-W orientation relationships were observed between retained austenite and martensite.

13. All heat treatments resulted in a mixture of ε-carbide and cementite precipitates, after tempering at 280°C.

14. Characteristic ε-carbide particles, wavy in appearance, were considerably coarser (50 Å to 100 Å thick and about 1000 Å to 1500 Å long) than cementite particles and were precipitated predominantly inside large laths and on dislocations, whereas cementite particles were found

precipitated inside laths or plates at lath, plate, packet or grain boundaries and on dislocations and twins. The precipitation of cementite on twins was an inverse function of austenitization temperature.

15. While the orientation between ε-carbide and martensite satisfied the Jack relationship, that between cementite and martensite satisfied either the Bagaryatskii or the Pitsch relationships. A new orientation relationship between ε-carbide and martensite was also determined and in this orientation the ε-carbide particles were highlighted better during dark field imaging.

16. ε-carbide precipitated inside large laths were arranged along parallel rows inclined at an angle of about 55° to the longitudinal axis of the lath. There were two definite variants for this precipitation, the growth direction coinciding with $<112>_{\alpha'}$.

17. Mo_2C precipitation (with $<00.1>_{Mo_2C}$ basal plane orientation) was also observed occasionally in the case of modified heat treatments. In these modified heat treatments, a few spheroidal precipitates were also observed.

18. Large, irregular, grain boundary nucleated laths were identified in the case of all heat treatments. In the case of non-modified heat treatments, these laths contained extensive ε-carbide precipitation along parallel rows inclined at angles of about 55° to the longitudinal axis, the growth direction coinciding with $<112>_{\alpha'}$. The boundaries of these laths often were sites for cementite precipitation.

19. Twins were also observed within these large laths, irrespective of austentitization temperature. The presence of these twins and

the occurrence of ε-carbide in two definite variants indicated that this was autotempered blocky martensite.

20. In the case of modified heat treatments, these large laths contained, in addition to ε-carbide, spheroidal shaped carbides.

21. Through extraction replication technique, the spheroidal carbides which were observed in the modified heat treatments were identified as M_3C and M_7C_3 and $M_{23}C_6$ carbides. Mo_2C particles were also identified in the case of modified heat treatments through extraction replication. X-ray powder patterns obtained using the extracted films confirmed the carbides in the modified heat treatments to be of M_3C, M_7C_3, $M_{23}C_6$ and Mo_2C types.

4.3. Fractography

4.3.1. Tensile Specimens.

Low magnification fractographs (Figure 4-84) all revealed the general fracture appearance, the extent of reduction in transverse area and the shear lip region. Also visible were the central fibrous zone and the surrounding radial zone (except for the high temperature and step heat treatments where the two zones merged). The central zone surrounded the crack origin and consisted of fine circumferential ridges, normal to the direction of crack propagation, from the origin towards the periphery of the specimen. These ridges are indicative of stable, subcritical, high energy crack extension. The radial zone consisted of fine radial marks, emanating from the periphery of the fibrous zone or the crack origin and coincided with the general direction of crack extension. This zone indicates rapid, unstable crack propagation. Since the initial cross-sectional area of all the specimens were the same, a measure of the transverse area (and the shear lip width), should be indicative of ductility. The results confirm that the transverse area was lower and shear lip width larger for specimens of higher ductility.

The fracture modes in the fibrous zone are compared in Figure 4-85. All the non-modified heat treatments exhibited a mixed failure mechanism (intergranular, quasicleavage and ductile rupture), while the modified heat treatments showed predominantly ductile rupture failure mode. Also, the amount of intergranular and quasicleavage failure was smaller for the conventional and cyclic heat treatments than for the step and high temperature heat treatments.

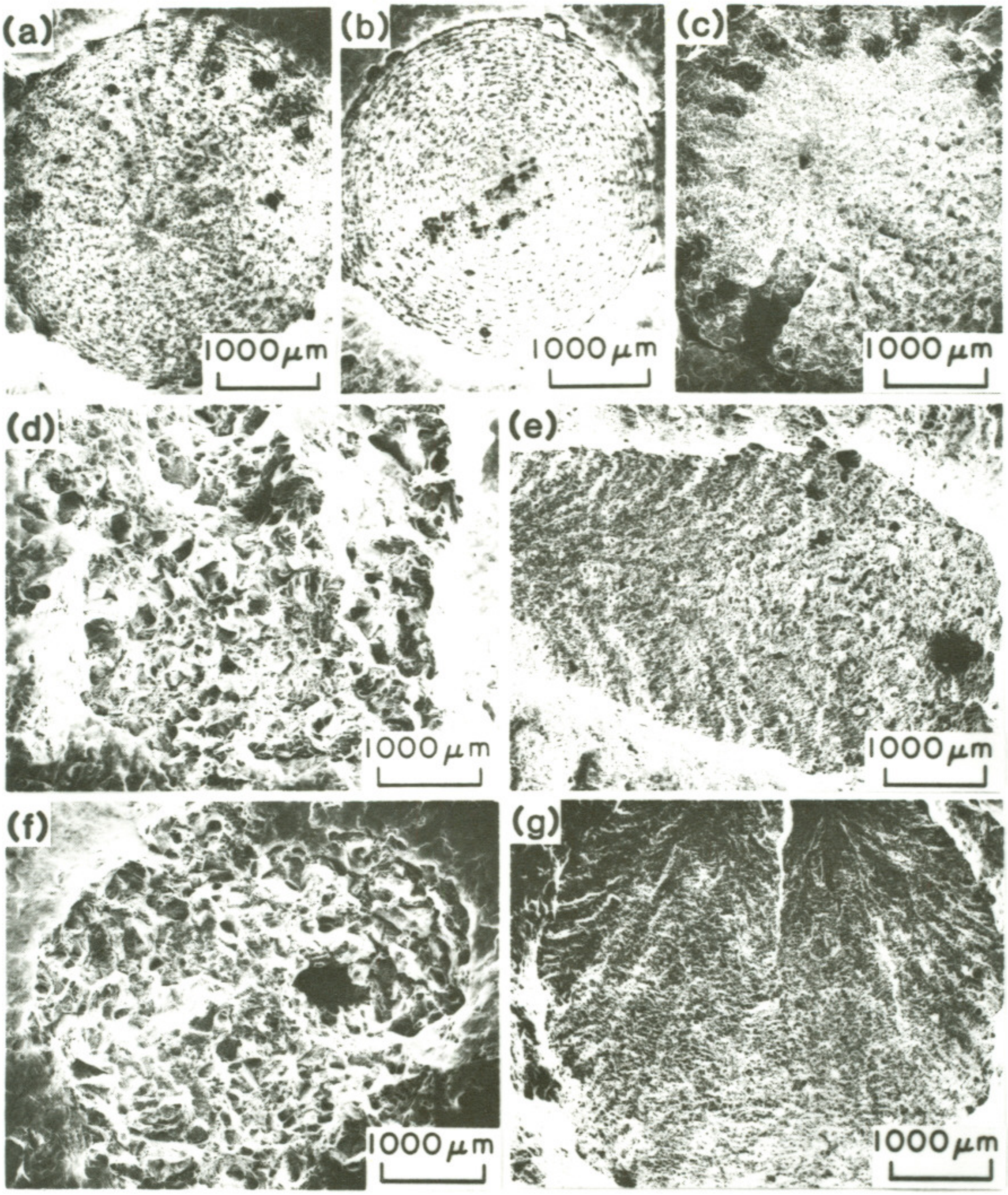

Figure 4-84: SEM FRACTOGRAPHS OF TENSILE SPECIMENS SHOWING THE MACROMODES OF FAILURE FOR a) CONVENTIONAL, b) CYCLIC, c) MODIFIED CONVENTIONAL, d) HIGH TEMPERATURE, e) MODIFIED HIGH TEMPERATURE, f) STEP & g) MODIFIED STEP HEAT TREATMENTS.

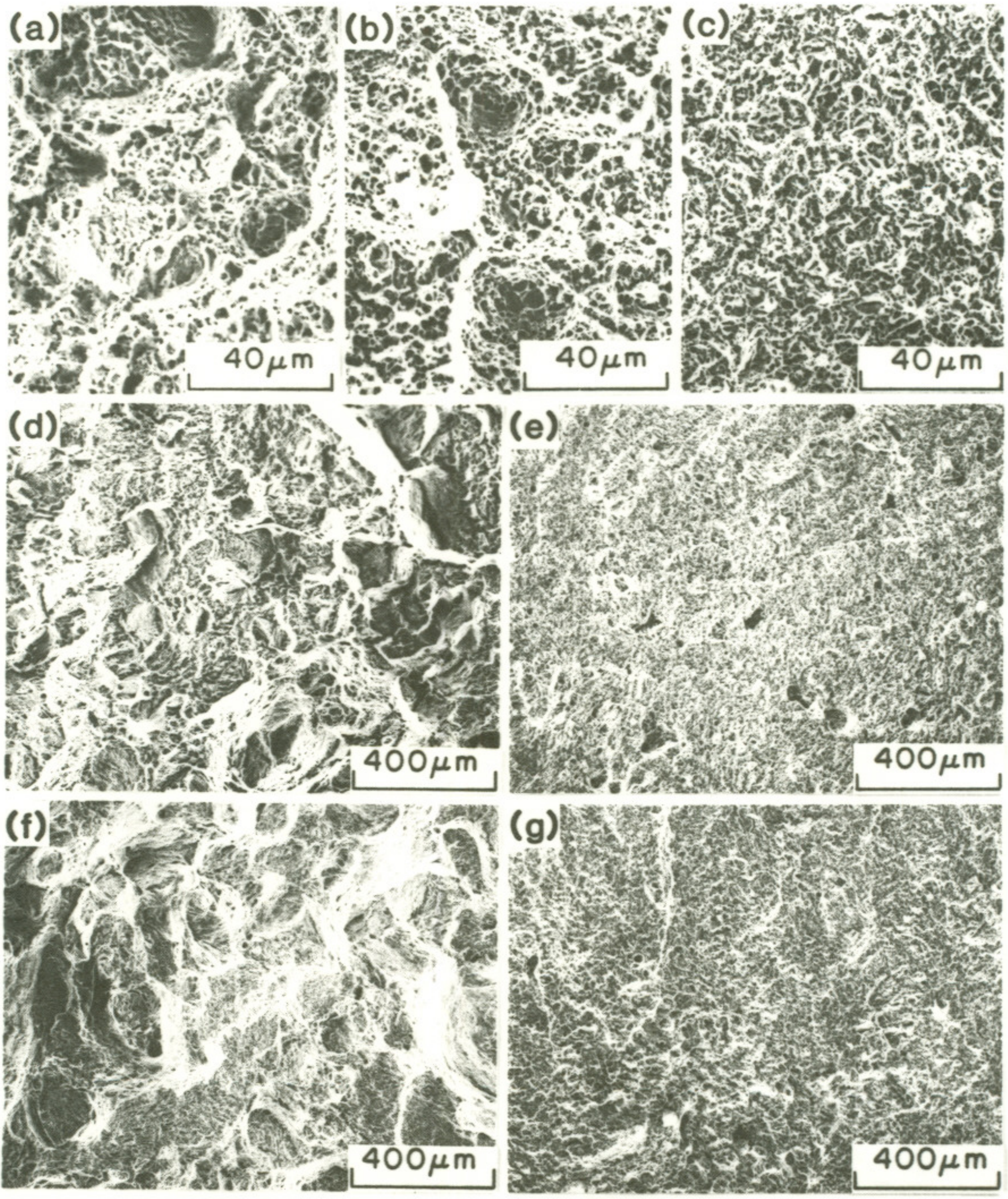

Figure 4-85: SEM FRACTOGRAPHS OF TENSILE SPECIMENS FROM CENTRAL ZONE, SHOWING A MIXED FAILURE MODE FOR a) CONVENTIONAL, b) CYCLIC, d) HIGH TEMPERATURE AND f) STEP HEAT TREATMENTS AND DUCTILE RUPTURE MODE FOR c) MODIFIED CONVENTIONAL, e) MODIFIED HIGH TEMPERATURE AND g) MODIFIED STEP HEAT TREATMENTS.

The dimple size and density are compared in Figure 4-86. The void size was higher in coarser grained structures (lower density) and the voids shallower. Also, all the modified heat treatments exhibited a much finer dimple distribution than the corresponding non-modified heat treatments. Since voids are initiated by carbides and inclusions, a higher dimple density indicates a greater volume fraction of carbides in the matrix (for a given amount of inclusions). Evidence of carbides and inclusions within voids can be found in many of these fractographs.

Coarse cleavage steps can be seen in Figure 4-87 for the high temperature and step heat treatments. These steps terminated at the prior austenite grain boundaries. Their height (about 5 μm) suggests that cleavage occurred along large laths at the grain boundaries. Such laths were identified as autotempered martensite (Section 4.2.3.5.). Several smaller steps are also seen in Figure 4-87 and these are relatable to fracture along lath and packet boundaries. These boundaries were shown to be sites of extensive carbide precipitation (Sections 4.2.3.4. and 4.2.3.5.) and the presence of these brittle carbides provided an easier fracture path along these boundaries.

Tearing, indicative of discontinuity in the advancing crack (due to necking of small ligaments behind the main crack front) were identified in many of these fractographs. Small cleavage tongues, due to cleavage across microtwins, and smooth facets, caused by plastic shear in local regions were also visible in the fractographs of non-modified heat treatments.

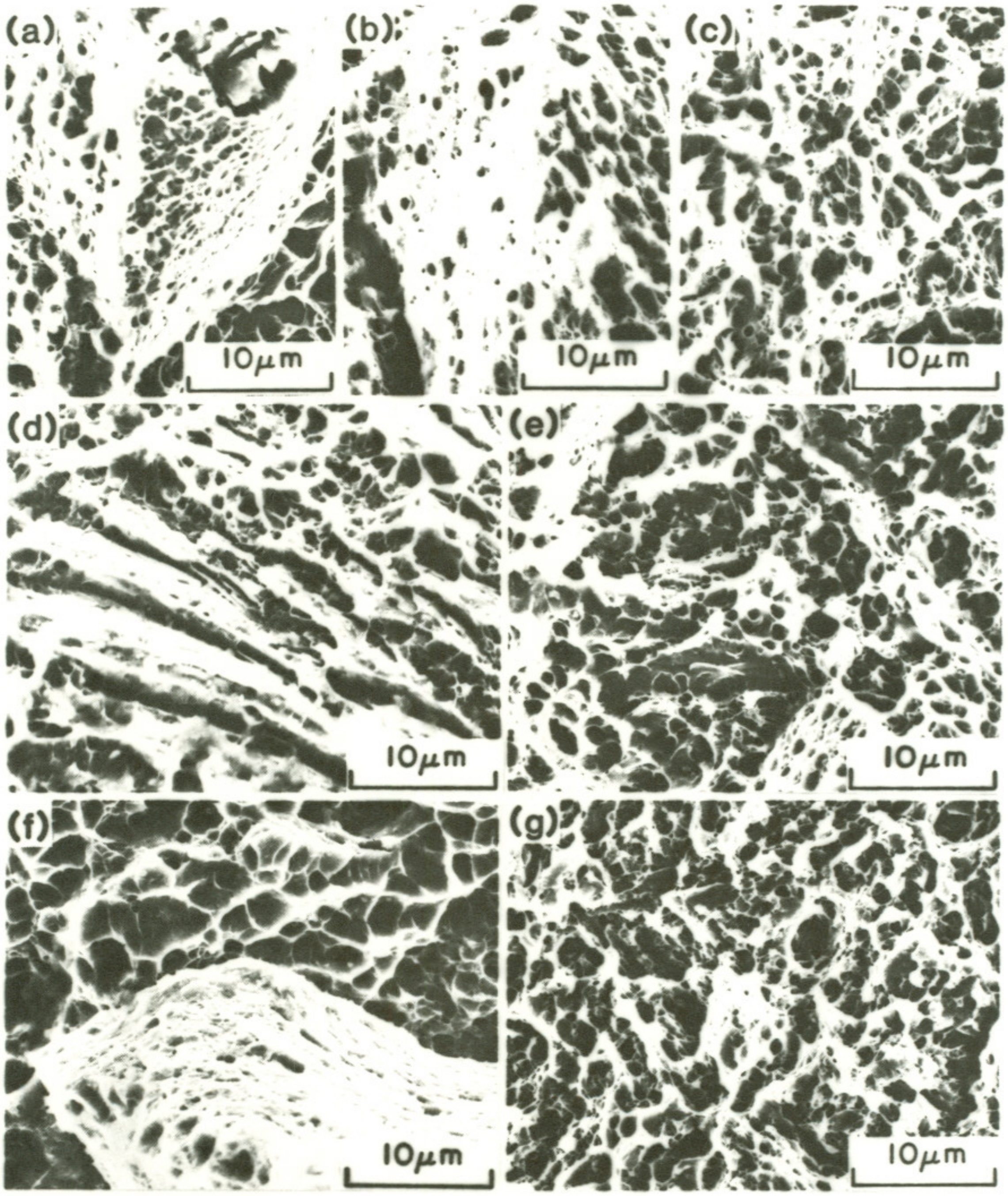

Figure 4-86: SEM FRACTOGRAPHS OF TENSILE SPECIMENS, FROM CENTRAL ZONE, COMPARING DIMPLE SIZE AND DISTRIBUTION IN (a) CONVENTIONAL, (b) CYCLIC, (c) MODIFIED CONVENTIONAL, (d) HIGH TEMPERATURE, (e) MODIFIED HIGH TEMPERATURE, (f) STEP AND (g) MODIFIED STEP HEAT TREATMENTS.

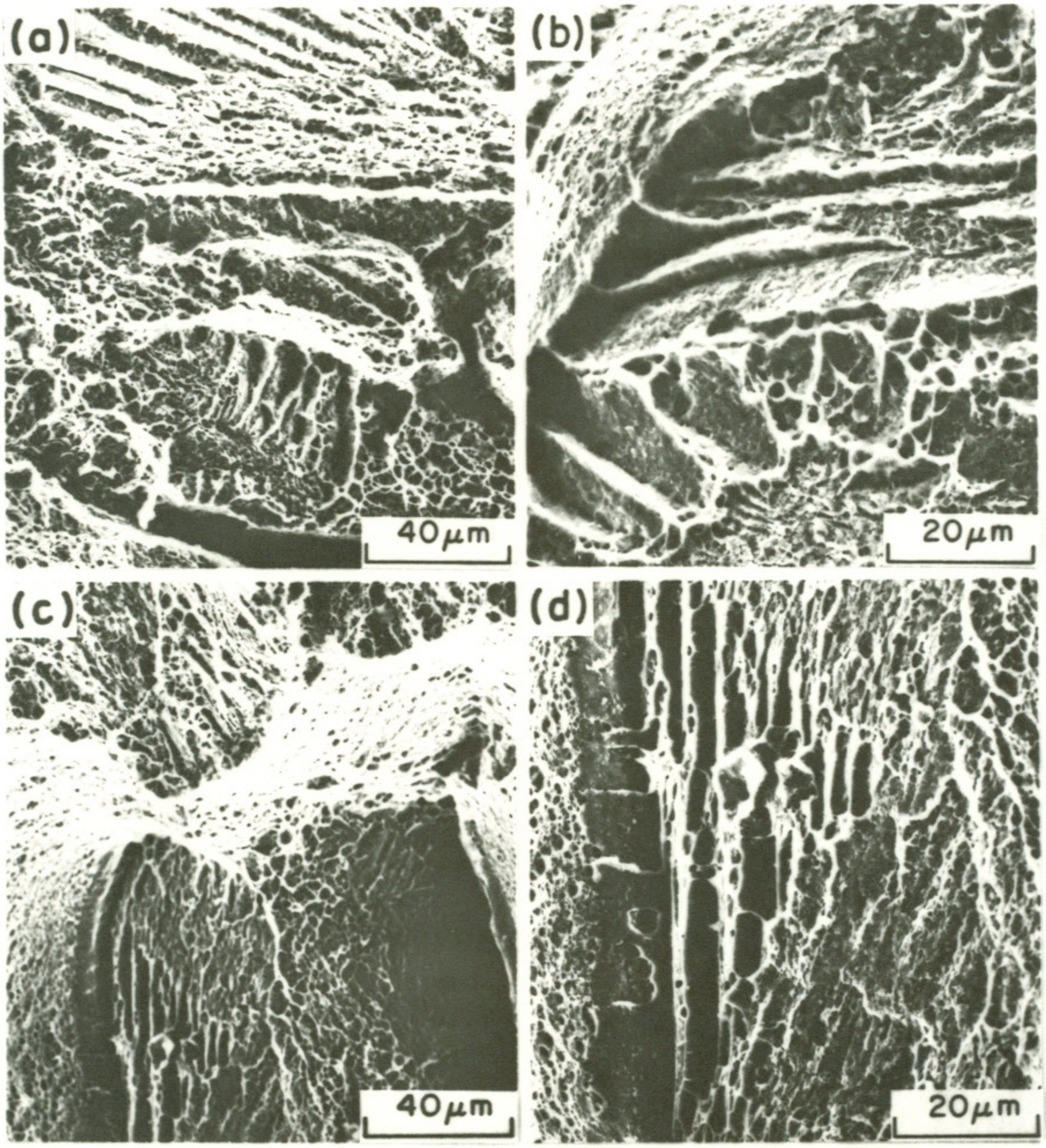

Figure 4-87: SEM FRACTOGRAPHS OF TENSILE SPECIMENS, FROM CENTRAL ZONE, SHOWING CLEAVAGE STEPS IN (a) & (b) HIGH TEMPERATURE AND (c) & (d) STEP HEAT TREATMENTS.

The first detailed topography study of tensile specimen fracture surfaces was done by Martens [95] who observed radial markings pointing back to the fracture origin. He also noted that finer grained material yielded sharper radial markings, consistent with the observations in this investigation. Classification of tensile surface marks into three zones, viz., fibrous, radial and shear lip zones, was also done by other investigators [89,90]. F. L. Carr [91] showed that for various strengths and testing temperatures, crack propagation in the central fibrous zone occurred through microvoid coalescence, again consistent with the observations in this study. However, even in this zone, quasicleavage and intergranular facets were observed in the case of conventional and cyclic heat treatments. For the high temperature and step heat treatments, no fibrous zone was identified, the central zone being predominantly intergranular in these cases.

Low magnification fractographs suggest that increased radial and shear lip zone sizes and decreased fibrous zone size resulted with increased strength level. Also, the relative coarseness and irregularity of the radial markings became finer and more regular in appearance, giving rise to a flatter surface. Similar observations were made by Nunes et al. [90]. These results also indicate that fracture mode change from intergranular to quasicleavage and ductile rupture resulted with increased strength, which agrees with the predictions of Beachem [96]. Tetelman et al. [97] showed that increasing interparticle spacing (decreasing void density) implied larger displacements associated with coalescence and, hence, higher toughness and a related drop in strength. Hodgson et al. [98] showed that the yield strength in quenched and tempered steels varied as the inverse square root of the interparticle spacing. The results in this study are consistent with the above observations.

With respect to cleavage steps, the size and orientation of available cleavage planes within a grain of prior austenite is poorly defined in a quenched and tempered steel due to precipitation of a fine network of carbide particles. True cleavage planes are replaced by smaller, ill-defined quasicleavage planes initiated at carbide particles or large inclusions. Inoue et al. [92] observed that the lath surfaces were predominantly {100} oriented, an orientation commonly encountered in this investigation, and concluded that natural cleavage perpendicular to lath surfaces was also {100} oriented. Beachem [93] observed that cementite platelets grew on {110} planes in <111> directions at angles of 45° and 90° to each other, which is consistent with TEM observations in this investigation (Figures 4-56, 4-59 and 4-62). If {110}<111> habit plane intersections are considered, then these angles of intersection should also be the same (45° and 90°), which is consistent with fractography observations. While coarse steps have not been shown in detail elsewhere, many investigators have observed the occurrence of fine steps along lath and packet boundaries and attributed this to the presence of carbide particles at these sites [76,94]. Carbide particles were seen in this investigation along the boundaries of even the coarse steps (Figure 4-87). Cementite between regular laths (Figures 4-56 to 4-58) and also along large lath boundaries (Figure 4-79) were identified through TEM studies. These carbide particles were responsible for the coarse step formation as well as the finer cleavage steps.

4.3.2. Impact Specimens. Three macroscopic failure zones, viz., a flat fibrous zone, corresponding to fracture initiation and indicating stable crack growth (parallel to the plane of the notch), a radial zone, corresponding to fracture propagation and indicating unstable crack propagation (adjacent to the fibrous zone) and a shear lip zone (at the specimen edges) were seen. These zones (excluding shear lip) can be identified in Figure 4-88. The width of the fibrous zone varied as a function of the initiation energy.

Figure 4-89 compares the fracture modes in the initiation zone. For all the heat treatments, the predominant failure mode was microvoid coalescence. A few intergranular and quasicleavage facets were also identified for the high temperature and step heat treatments. Also, in these latter heat treatments, the dimple density was lower and the voids wider and shallower than for the other heat treatments, consistent with their lower ductility.

The propagation zone fracture modes are compared in Figure 4-90. It was a mixed quasicleavage and void coalescence mode for all the heat treatments, with quasicleavage predominating. A few intergranular facets were also visible for high temperature and step heat treatments. These facets and the presence of cleavage steps (Figure 4-91) in these two heat treatments are consistent with lower fracture propagation energies. Tear ridges, typical of low energy failure in high strength steels were also seen in these fractographs.

Figure 4-91 shows coarse cleavage steps for high temperature and step heat treatments in the propagation zone. In fine grained structures, such steps were only rarely encountered and an example is also presented in

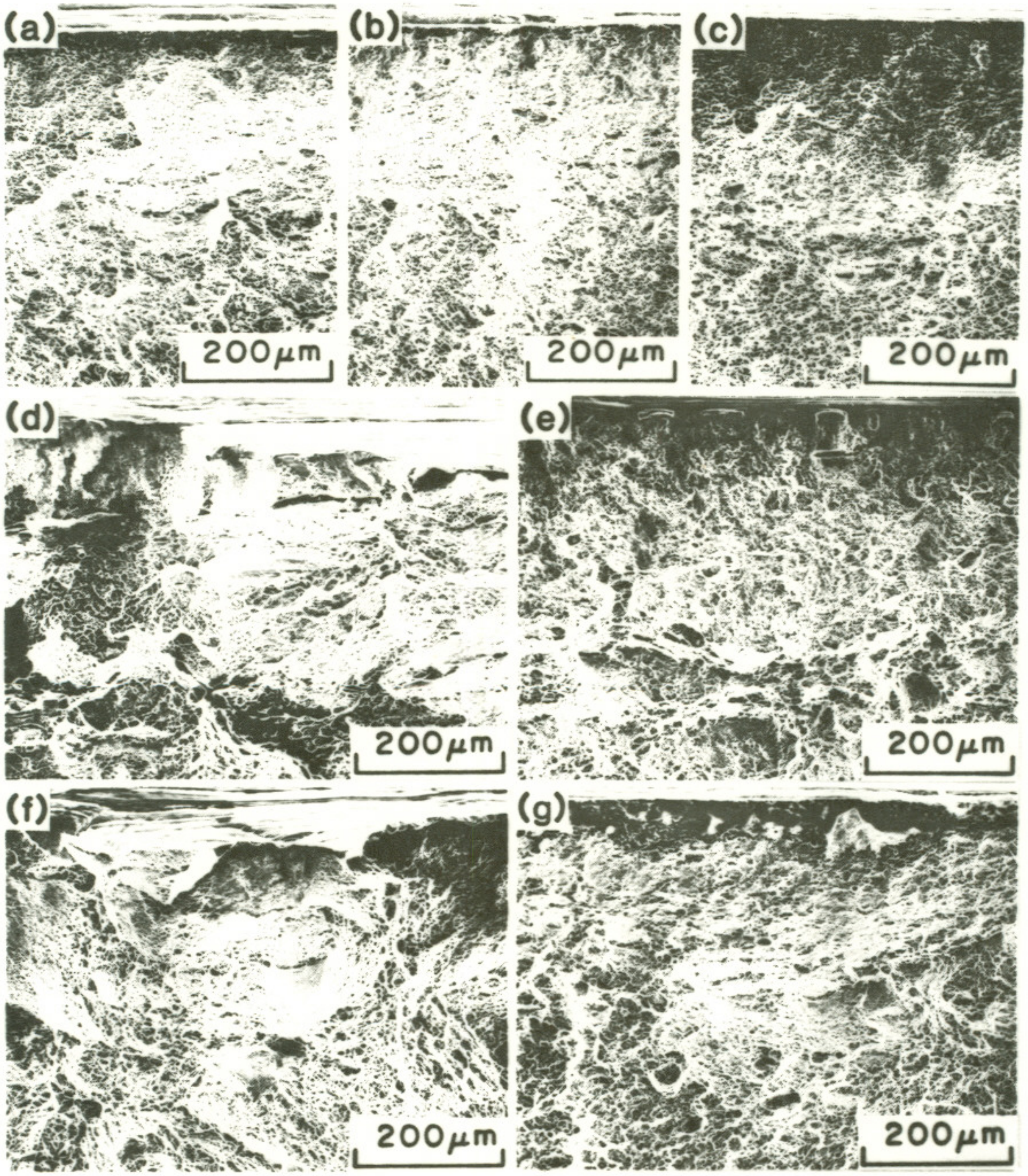

Figure 4-88: SEM FRACTOGRAPHS OF IMPACT SPECIMENS, SHOWING MACROMODES OF FAILURE FOR (a) CONVENTIONAL, (b) CYCLIC, (c) MODIFIED CONVENTIONAL, (d) HIGH TEMPERATURE, (e) MODIFIED HIGH TEMPERATURE, (f) STEP AND (g) MODIFIED STEP HEAT TREATMENTS.

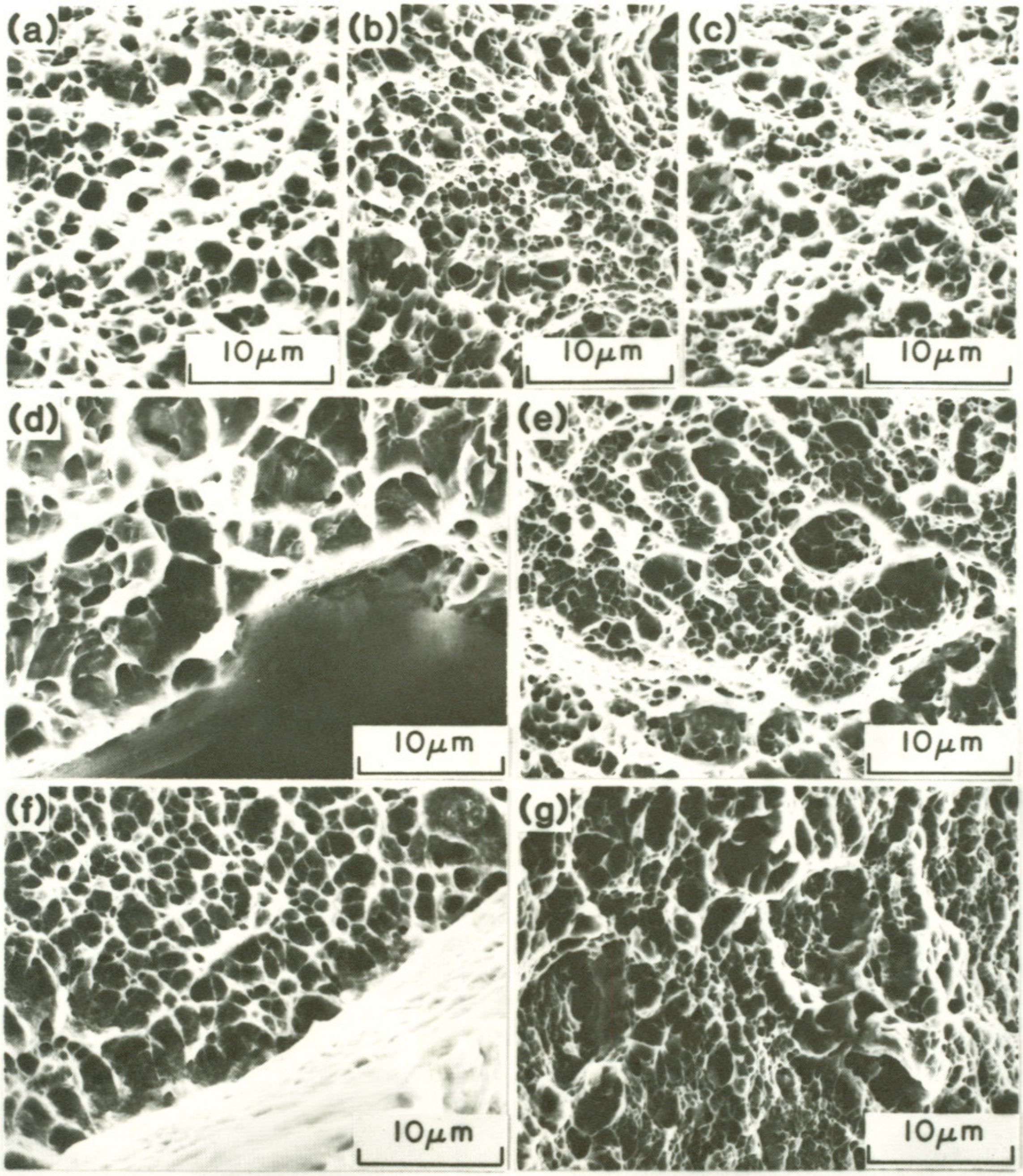

Figure 4-89: SEM FRACTOGRAPHS OF IMPACT SPECIMENS FROM INITIATION ZONE COMPARING THE FAILURE MODES (PREDOMINANTLY DUCTILE RUPTURE) FOR (a) CONVENTIONAL, (b) CYCLIC, (c) MODIFIED CONVENTIONAL, (d) HIGH TEMPERATURE, (e) MODIFIED HIGH TEMPERATURE, (f) STEP AND (g) MODIFIED STEP HEAT TREATMENTS.

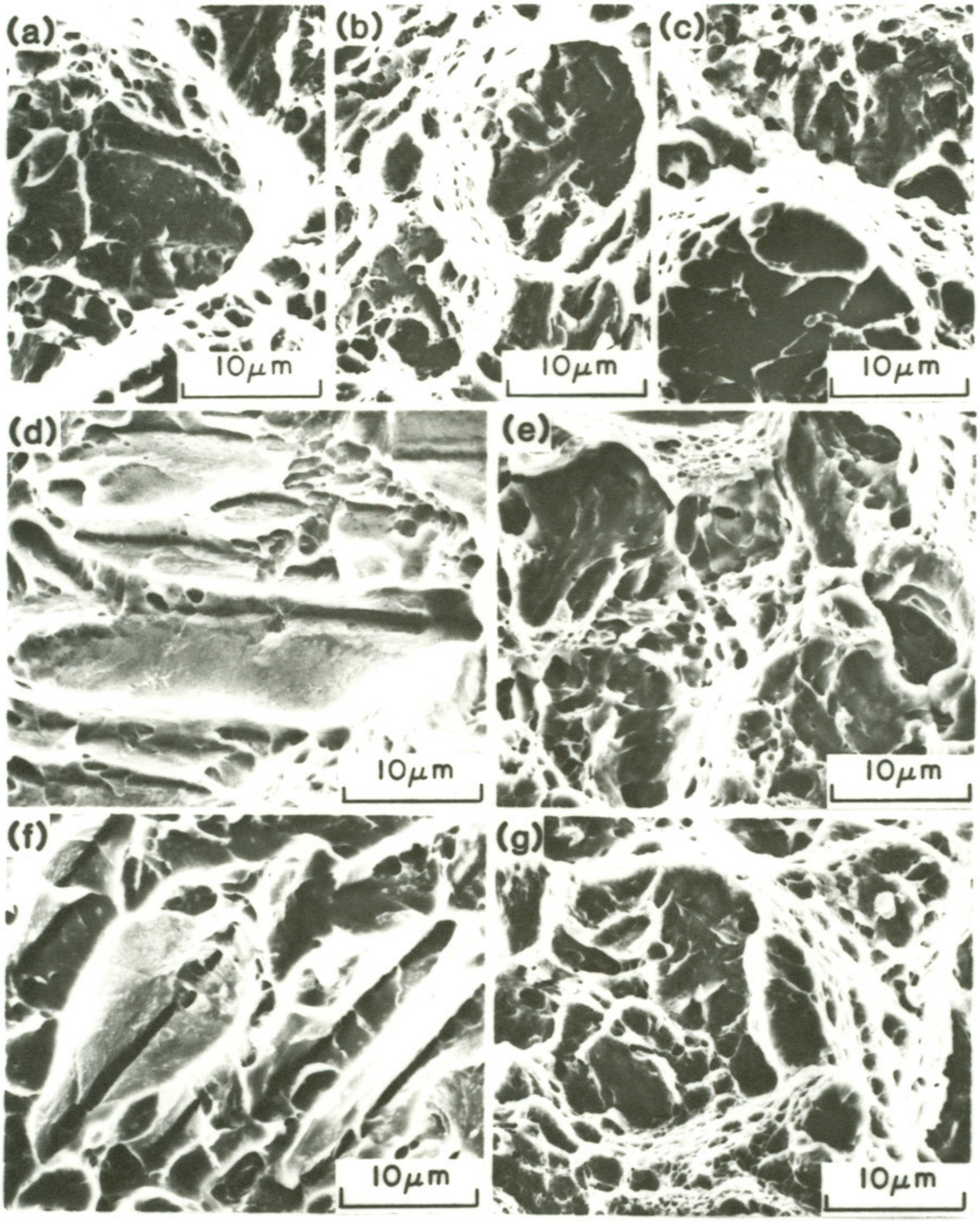

Figure 4-90: SEM FRACTOGRAPHS OF IMPACT SPECIMENS, FROM PROPAGATION ZONE, SHOWING THE FAILURE MODES (PREDOMINANTLY QUASICLEAVAGE) FOR (a) CONVENTIONAL, (b) CYCLIC, (c) MODIFIED CONVENTIONAL, (d) HIGH TEMPERATURE, (e) MODIFIED HIGH TEMPERATURE, (f) STEP AND (g) MODIFIED STEP HEAT TREATMENTS.

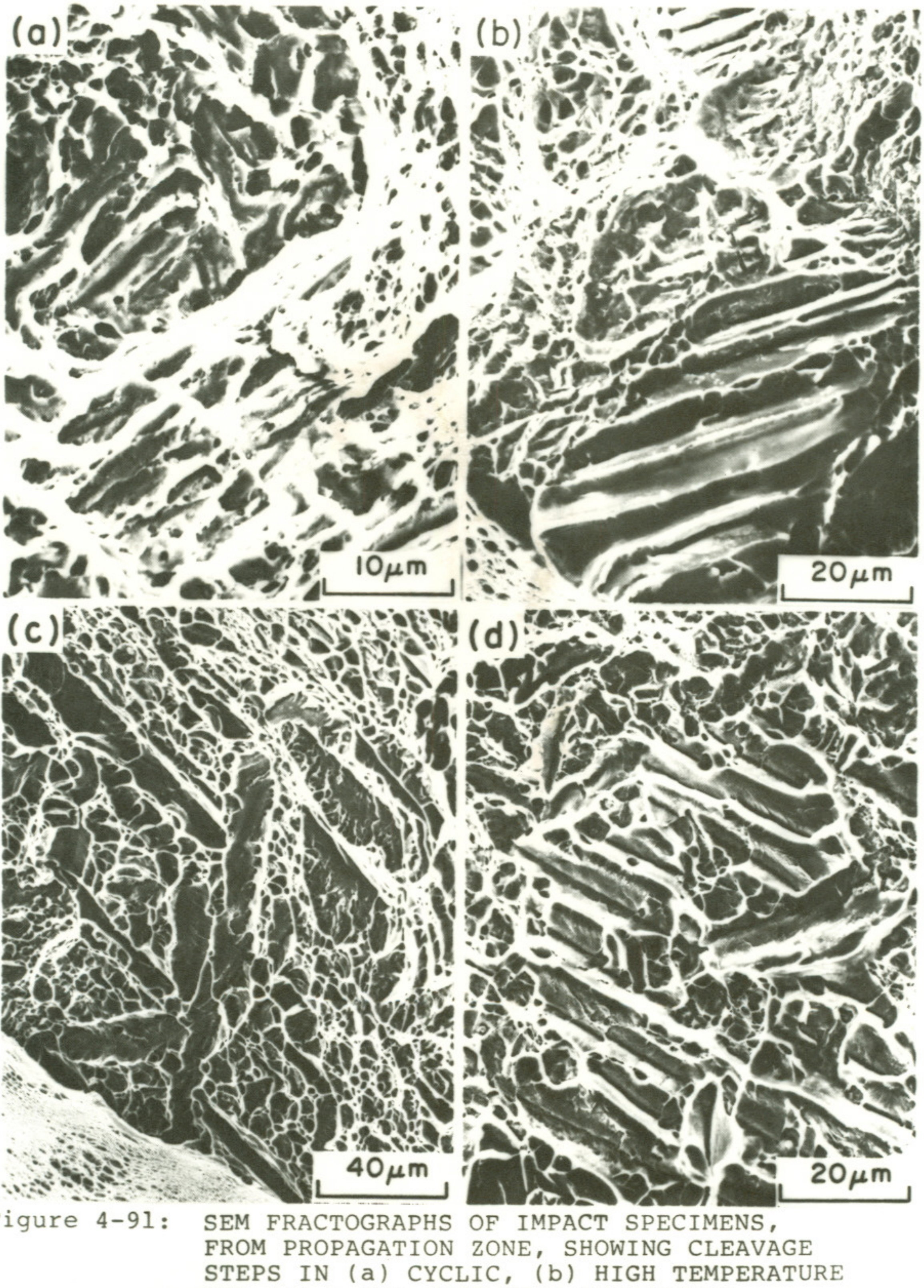

Figure 4-91: SEM FRACTOGRAPHS OF IMPACT SPECIMENS, FROM PROPAGATION ZONE, SHOWING CLEAVAGE STEPS IN (a) CYCLIC, (b) HIGH TEMPERATURE AND (c) & (d) STEP HEAT TREATMENTS.

Figure 4-91. The definite crystallographic orientations of these steps suggest that fracture occurred along coarse lath and packet boundaries. The presence of such coarse laths and brittle carbides along these boundaries were established in Section 4.2.3.5. The precipitation of epsilon carbide within coarse laths at an angle of 55° to 65° to the lath boundaries was also established in Section 4.2.3.5. Cleavage along these laths should result in fine steps or traces at an angle to these boundaries, as seen in these fractographs, consistent with cracking along epsilon carbide/ferrite interfaces. The coarse steps intersected either perpendicularly or at angles of 45° with respect to each other, indicating {110} habit plane intersection with {100} cleavage planes.

The change in fracture mode from intergranular to quasicleavage and microvoid coalescence with increasing toughness, noted in this investigation, is consistent with the observations of other investigators [4,8,19,25,96,99]. The low energy tear and quasicleavage mechanism of failure observed in the fracture propagation region was typical of high strength steels broken in impact [97,100-102]. Examination of voids revealed that increases in both dimple density and depth of dimples occurred with appreciable increase in fracture energy. Other investigators [100,103,104] also noted an increase in dimple depth with increase in toughness. Tetelman et al. [97] attributed the toughness increase with decreasing void density to the larger displacements necessary for void coalescence when void size increased. While this trend was observed from the microfractographic results of K_{Ic} specimens, for impact specimens, increased dimple density was associated with increased impact toughness. This apparent contradiction was also noted by Ritchie and

Horn [20] in the case of 4340 steel. They concluded that void density affected the toughness only when the strain rate was low as in plane strain fracture toughness testing and the increase in impact toughness with increasing prior austenite grain size (and consequently decreasing dimple density) was due to decreased critical fracture strain and not due to decreased dimple density. The present results support this latter view. The observation of carbides along coarse lath and packet boundaries as well as the observation of fine markings, corresponding to fracture along epsilon carbide particles, in this investigation, suggest that the coarse steps occurred in a similar manner as the fine steps, viz., due to fracturing along brittle carbides precipitated along the coarse lath/packet boundaries.

4.3.3. Plane Strain Fracture Toughness Specimens. Fracture initiation and propagation zones and shear lip zone were all observed for all heat treatments. The fatigue precracked region and the initiation region adjacent to it, can be seen in Figure 4-92. Unlike Charpy surfaces, there was little difference between initiation and propagation zones.

The fracture modes are better compared in Figure 4-93, obtained from the initiation region. The predominant failure mode was microvoid coalescence. All the non-modified heat treatments exhibited some quasi-cleavage and intergranular failure, and more so the step heat treatment, due to the high segregation concentration at the prior austenite grain boundaries.

The void size and densities are compared in Figure 4-94. All the coarse grained structures resulted in a lower dimple density, consistent with increased interparticle spacing, due to greater dissolution at

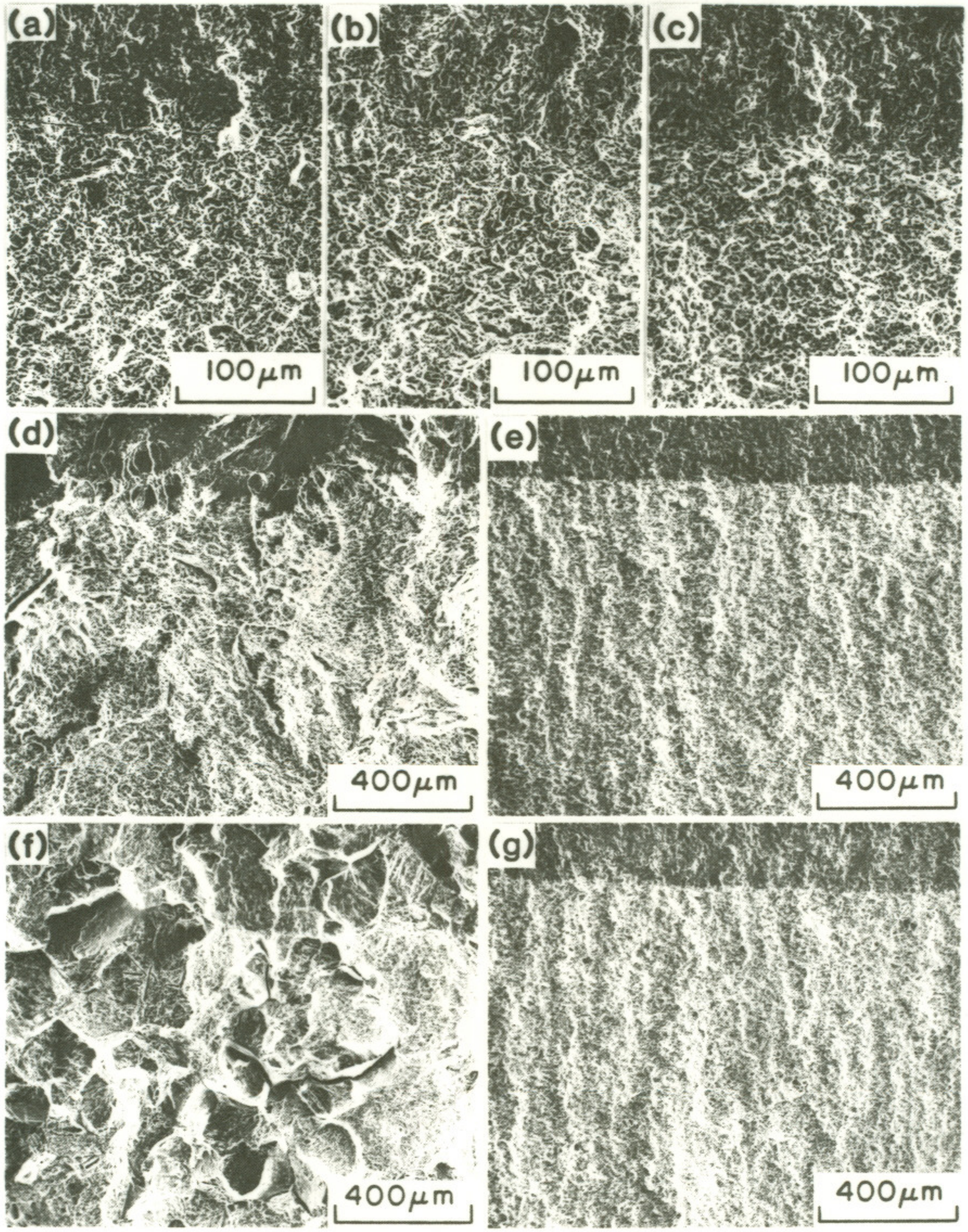

Figure 4-92: SEM FRACTOGRAPHS OF K_{Ic} SPECIMENS, SHOWING FATIGUE PRECRACKED AND INITIATION ZONES FOR (a) CONVENTIONAL, (b) CYCLIC, (c) MODIFIED CONVENTIONAL, (d) HIGH TEMPERATURE, (e) MODIFIED HIGH TEMPERATURE, (f) STEP AND (g) MODIFIED STEP HEAT TREATMENTS.

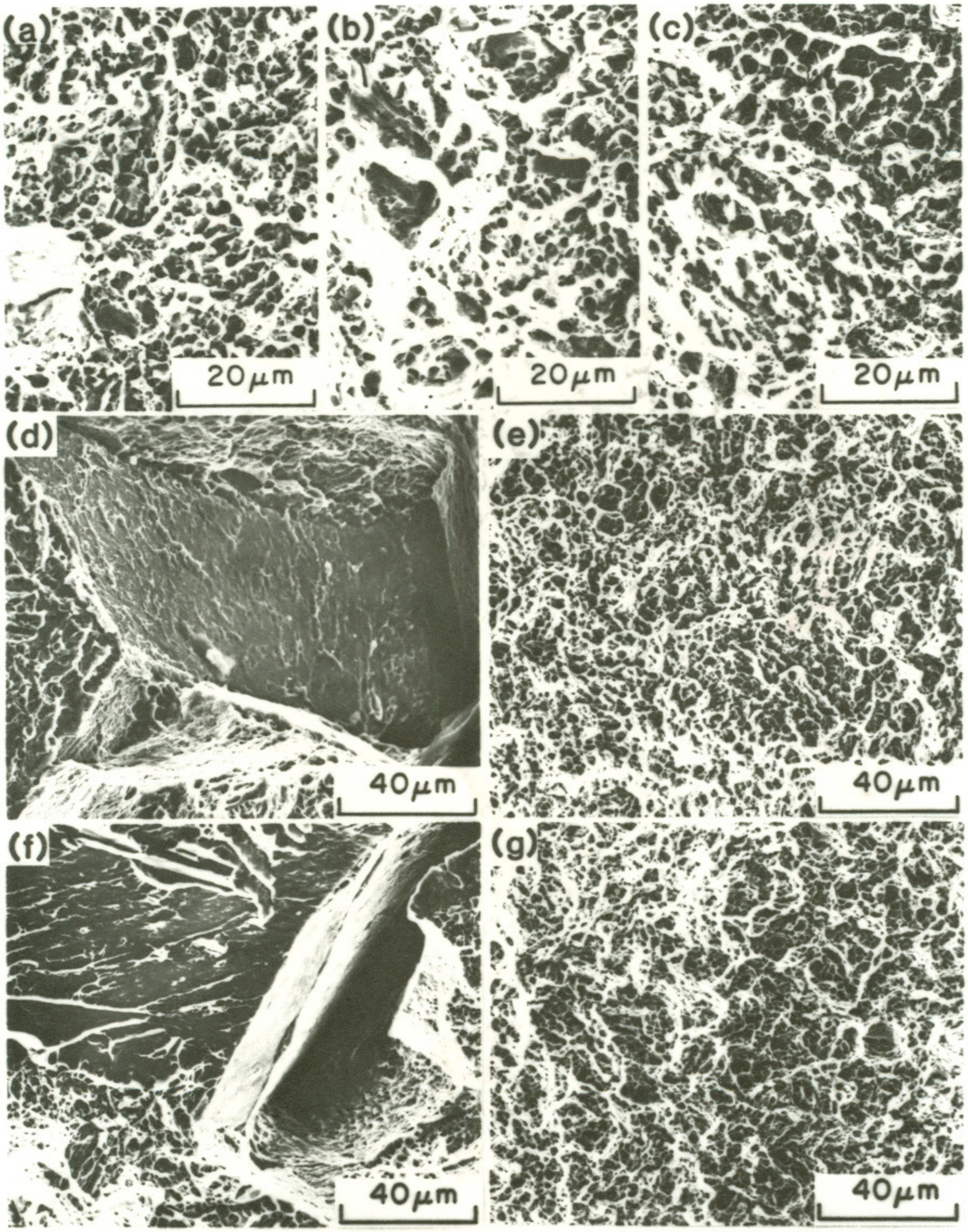

Figure 4-93: SEM FRACTOGRAPHS OF K_{Ic} SPECIMENS, SHOWING INITIATION ZONE, SHOWING A MIXED FAILURE MODE FOR (a) CONVENTIONAL, (b) CYCLIC, (d) HIGH TEMPERATURE AND (f) STEP HEAT TREATMENTS AND A PREDOMINANTLY DUCTILE RUPTURE MODE FOR (c) MODIFIED CONVENTIONAL, (e) MODIFIED HIGH TEMPERATURE AND (g) MODIFIED STEP HEAT TREATMENTS.

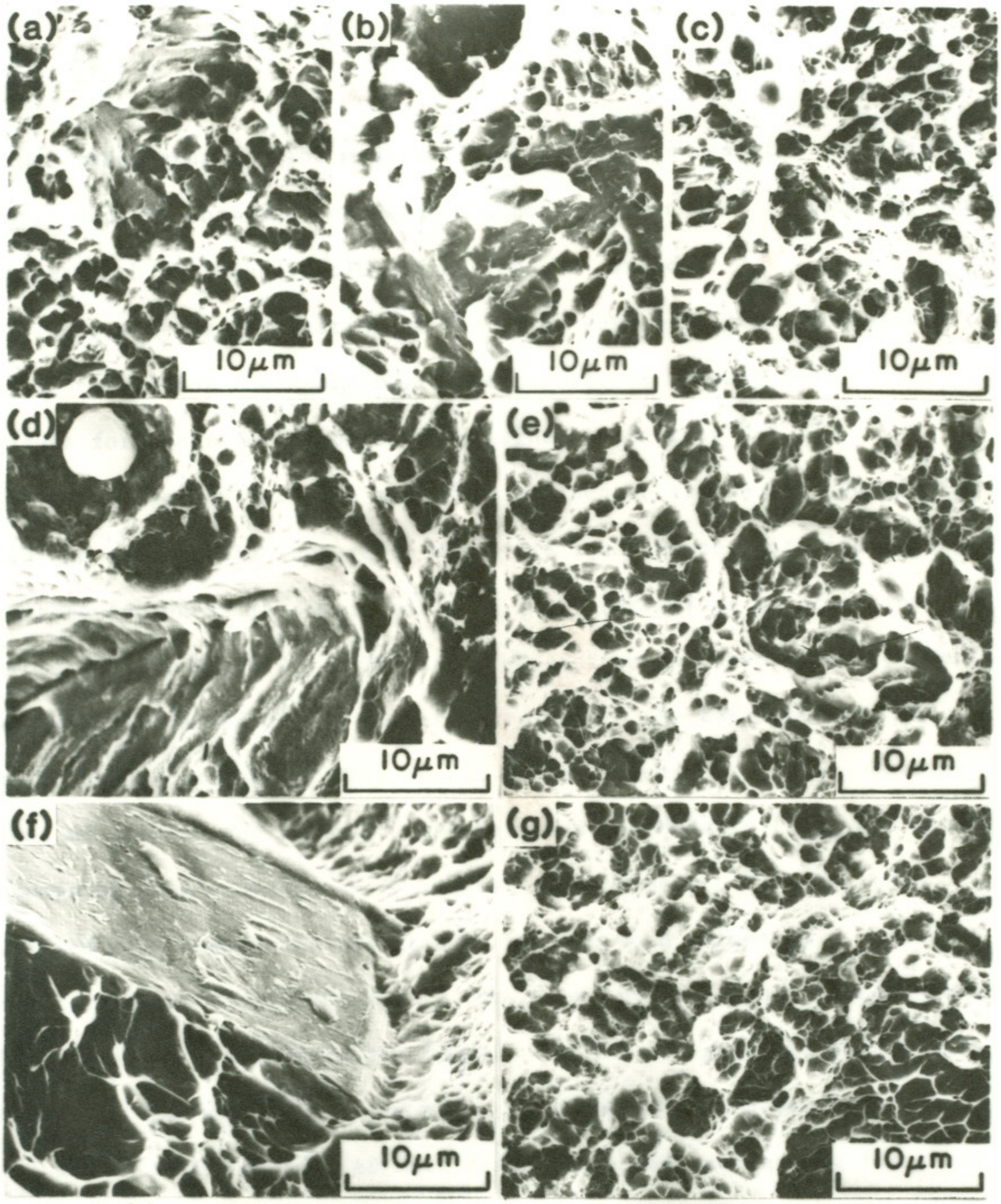

Figure 4-94: SEM FRACTOGRAPHS OF K_{Ic} SPECIMENS, FROM INITIATION ZONE, COMPARING DIMPLE SIZE AND DISTRIBUTION IN (a) CONVENTIONAL, (b) CYCLIC, (c) MODIFIED CONVENTIONAL, (d) HIGH TEMPERATURE, (e) MODIFIED HIGH TEMPERATURE, (f) STEP AND (g) MODIFIED STEP HEAT TREATMENTS.

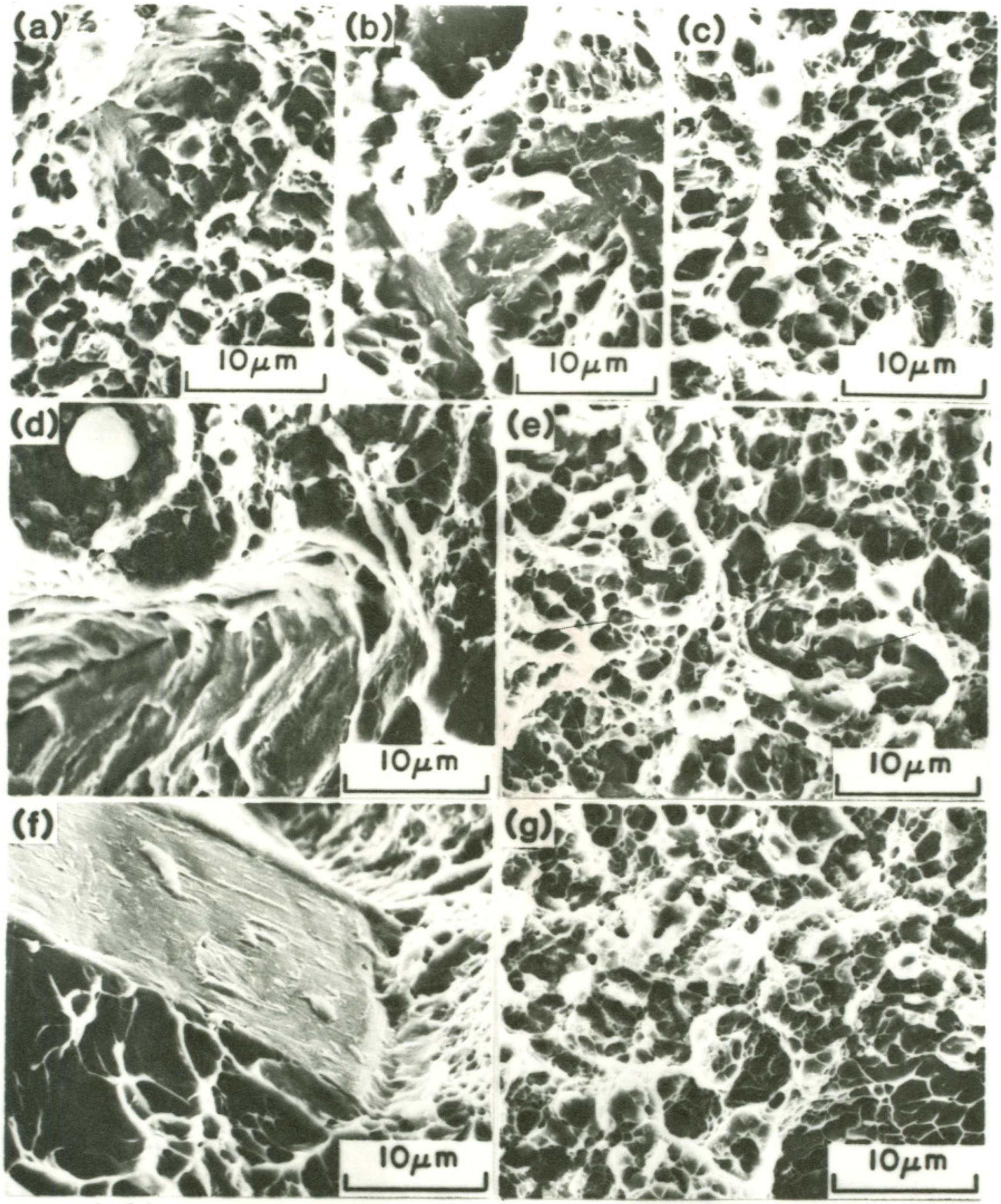

Figure 4-94: SEM FRACTOGRAPHS OF K_{Ic} SPECIMENS, FROM INITIATION ZONE, COMPARING DIMPLE SIZE AND DISTRIBUTION IN (a) CONVENTIONAL, (b) CYCLIC, (c) MODIFIED CONVENTIONAL, (d) HIGH TEMPERATURE, (e) MODIFIED HIGH TEMPERATURE, (f) STEP AND (g) MODIFIED STEP HEAT TREATMENTS.

higher temperatures. The modified heat treatments resulted in a higher dimple density than the corresponding non-modified heat treatments, consistent with the higher volume fraction of carbides.

Coarse steps terminating at the prior austenite grain boundaries can be identified for the coarser grained structures (Figure 4-95). The reasons for their formation were explained in Section 4.3.1.

The change in fracture mode from a mixed intergranular, quasicleavage and ductile rupture to microvoid coalescence, with increasing fracture toughness is consistent with the observations of other investigators [4,8,19,25,96,99]. The high temperature and step heat treatments exhibited decreased dimple density compared to the conventional, and cyclic heat treatments. This result is in agreement with the observations of Ritchie and Horn [20] and Tetelman and McEvily [97], who noted decreasing dimple density with increasing toughness. However, the modified heat treatments resulted in greater void volume as a result of more carbide precipitation due to the intermediate tempering step. While this seemingly contradicts the results for the non-modified heat treatments, the low energy fracture modes (intergranular and quasicleavage) were absent for the modified heat treatments, thus accounting for their superior fracture toughness.

4.3.4. Stress Corrosion Cracking Specimens. Unlike tensile, Charpy and K_{Ic} specimens, these specimens failed predominantly by intergranular failure under low and intermediate stress intensity levels, with complete transgranular mode occurring near the final fast fracture region. However, the modified conventional heat treatment, while failing by ductile

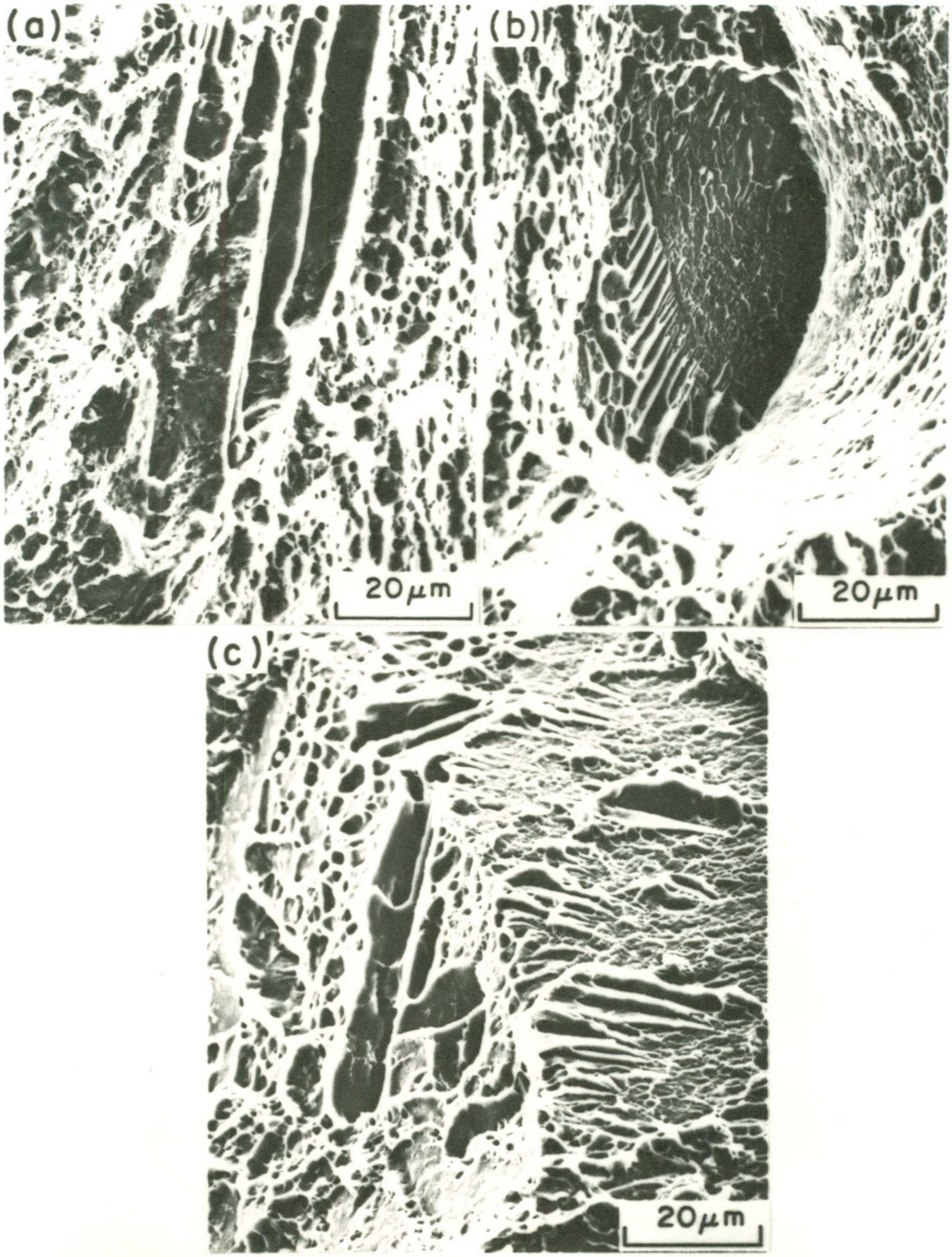

Figure 4-95: SEM FRACTOGRAPHS OF K_{IC} SPECIMENS, FROM INITIATION ZONE, SHOWING CLEAVAGE STEPS IN (a) & (b) HIGH TEMPERATURE AND (c) STEP HEAT TREATMENTS.

rupture at high stress intensity levels, exhibited a mixed failure mode consisting of both intergranular and transgranular features at low and intermediate stress intensity levels. In all cases, the amount of transgranular features increased with increasing stress intensity with the maximum intergranular failure occurring near threshold stress intensity. While the intergranular fracture was environmentally induced, the transgranular fracture was a result of triaxial stress conditions at the crack tip.

Fractographs, in the order of increasing stress intensity are presented in Figures 4-96 to 4-98, for conventional, high temperature and step heat treatments. Analysis revealed predominantly intergranular fracture mode with transgranular features increasing with increasing stress intensity. The amount of intergranular failure at equivalent stress intensities was higher for the high temperature and step heat treatments, consistent with a greater concentration of segregation at the grain boundaries (although the total amount of segregation decreases with increasing temperature). Secondary cracks and triple points can be seen in many regions. Most intergranular boundaries were smooth, while some showed cleavage and quasicleavage facets, tear ridges and dimples. The high magnification pictures showed the transition from cleavage and quasicleavage to microvoid coalescence in the transgranularly failed regions, with increasing stress intensity. The final fracture was totally by microvoid coalescence and generally the amount of tear ridges and/or dimples on the intergranular facets increased with increasing stress intensity.

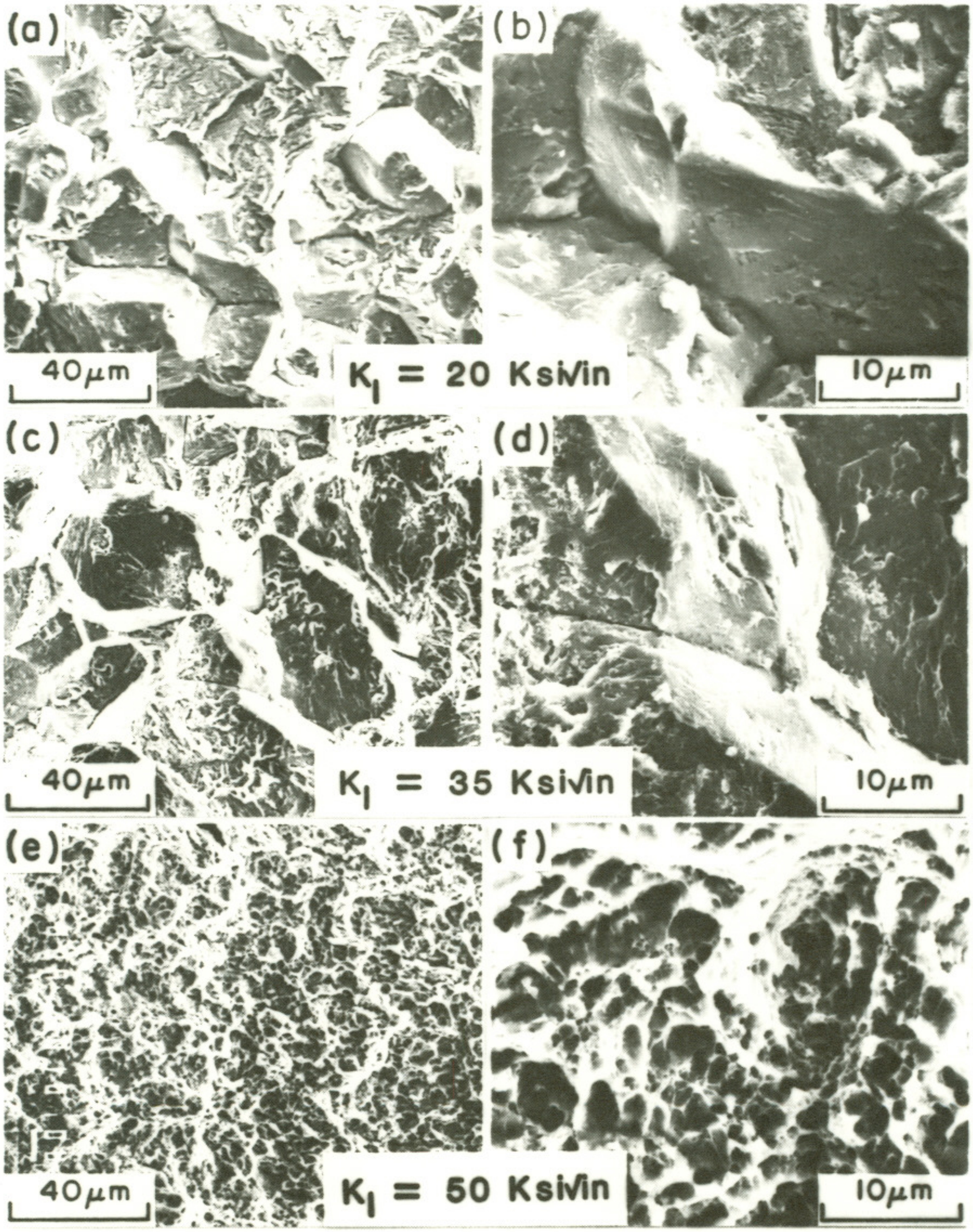

Figure 4-96: SEM FRACTOGRAPHS OF CONVENTIONALLY HEAT TREATED S.C.C. SPECIMENS, SHOWING THE CHANGE IN FAILURE MODE (INTERGRANULAR TO TRANSGRANULAR) AS A FUNCTION OF INCREASING APPLIED STRESS INTENSITY.

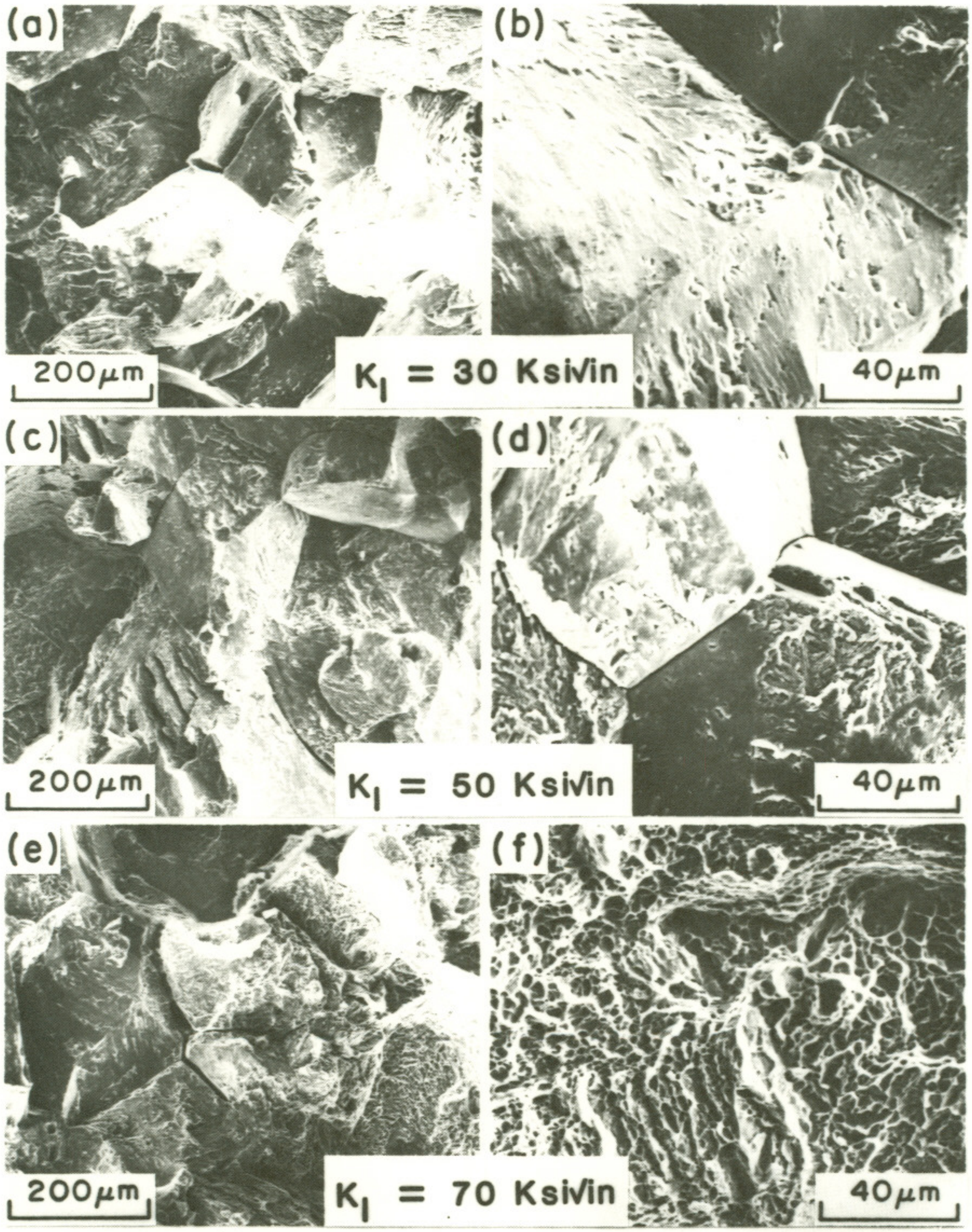

Figure 4-97: SEM FRACTOGRAPHS OF HIGH TEMPERATURE HEAT TREATED S.C.C. SPECIMENS, SHOWING THE CHANGE IN FAILURE MODE (INTERGRANULAR TO TRANSGRANULAR) AS A FUNCTION OF INCREASING APPLIED STRESS INTENSITY.

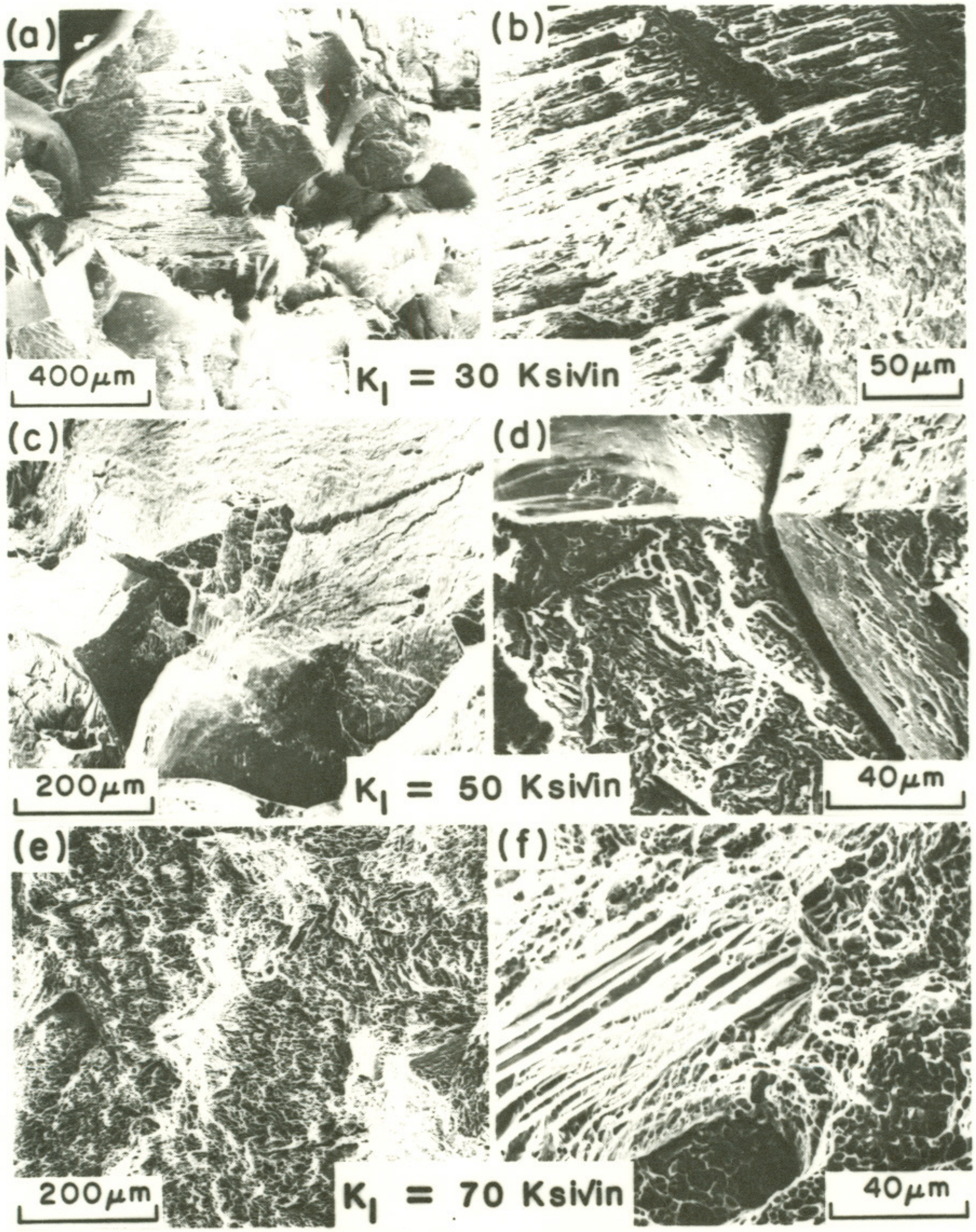

Figure 4-98: SEM FRACTOGRAPHS OF STEP HEAT TREATED S.C.C. SPECIMENS, SHOWING THE CHANGE IN FAILURE MODE (INTERGRANULAR TO TRANSGRANULAR) AS A FUNCTION OF INCREASING APPLIED STRESS INTENSITY.

As seen in Figure 4-98, steps within a grain were observed in some regions for the step heat treatment. These steps were due to a multiple crack coalescence mechanism, wherein small cracks on parallel planes coalesced to form larger cracks which in turn coalesced to form wider steps. Large steps corresponding to cracking along large lath/plate boundaries were also seen, as in the overload pictures of tensile, Charpy and K_{Ic} specimens.

The fracture surface of specimens subjected to modified conventional heat treatment could not be directly observed due to extensive corrosion on the fracture surface. The slow crack growth rate in this heat treatment allowed sufficient time for corrosion to mask the underlying fracture. Examples of this surface condition are shown in Figure 4-99. Cleaning with an aqueous solution of ammonium citrate, electrolytic cleaning in an alkaline solution containing sodium cyanide and the standard procedure recommended by ASTM Committee G-1 for preparing, cleaning and evaluating corrosion test specimens (G-1-72), wherein the specimen is electrolytically cleaned with sulphuric acid containing an organic inhibitor (diorthotolyl thiourea) were all attempted. These methods, although effective for removing sulphide products did not work as well for these corrosion products. Hence another solution containing 10 gms of 1,3-di-n-butyl-2 thiourea in 1000 cc of 37.5% HCl was used and the sample was kept immersed in this solution while ultrasonically vibrated for about 1 min. This method was very effective and the underlying fracture mode was revealed. In addition, etching was maintained at a minimal level. The results are presented in Figure 4-100

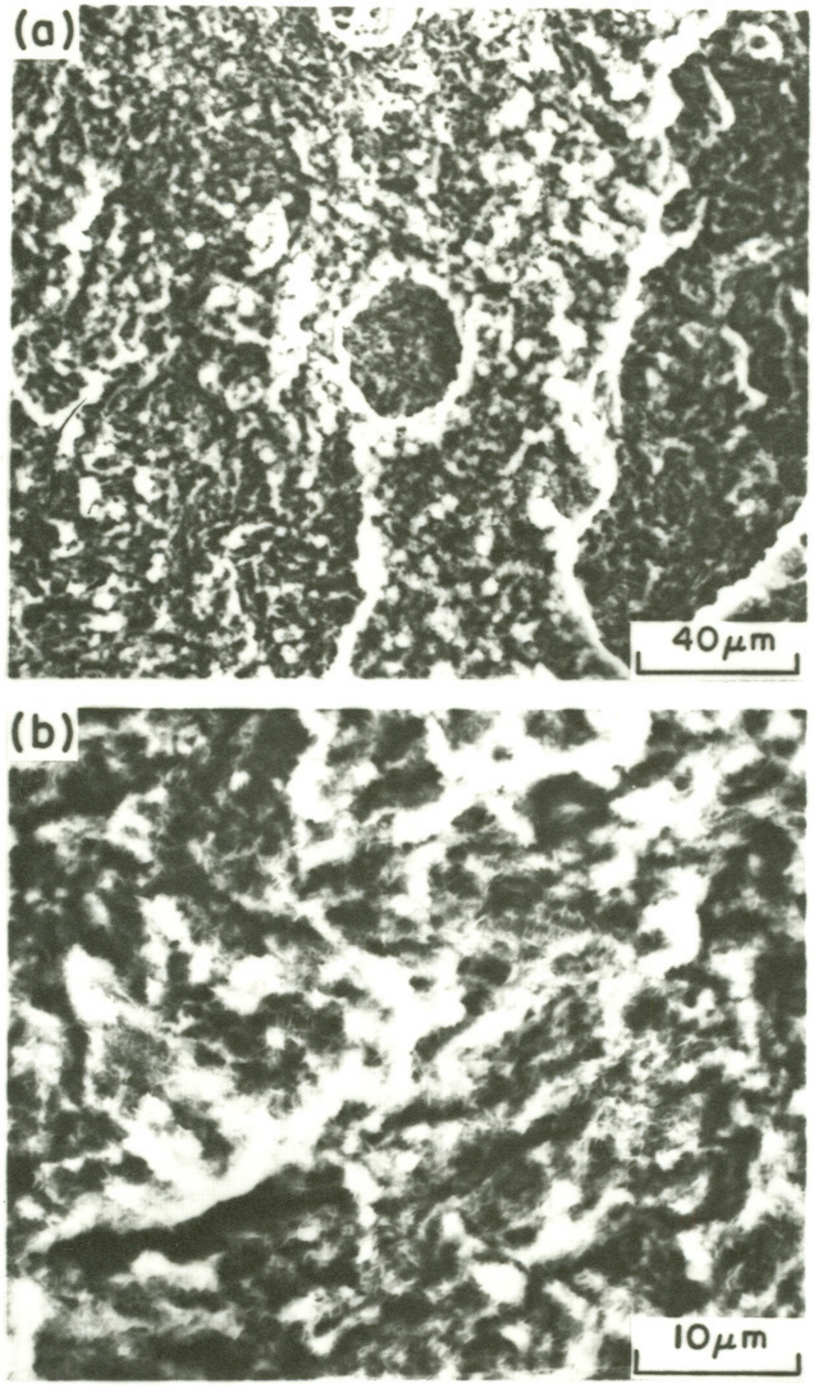

Figure 4-99: SEM FRACTOGRAPHS OF MODIFIED CONVENTIONAL HEAT TREATED S.C.C. SPECIMENS, SHOWING EXTENSIVE SURFACE CORROSION.

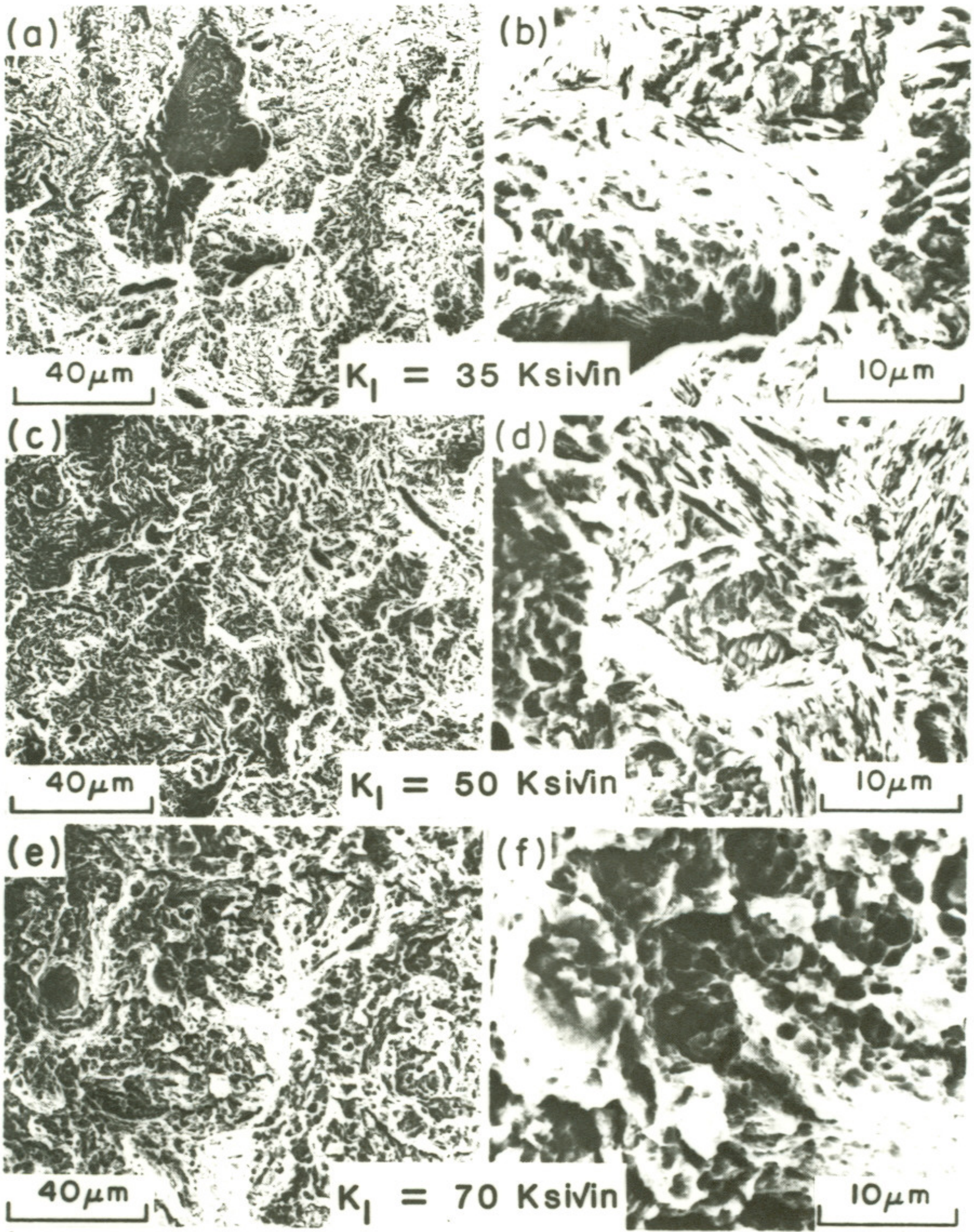

Figure 4-100: SEM FRACTOGRAPHS OF MODIFIED CONVENTIONAL HEAT TREATED S.C.C. SPECIMENS, SHOWING THE CHANGE IN FAILURE MODE (MIXED TO DUCTILE RUPTURE) AS A FUNCTION OF INCREASING APPLIED STRESS INTENSITY.

as a function of increasing stress intensity. Both intergranular and transgranular failures resulted at low and medium stress intensity levels with almost complete ductile rupture failure resulting at higher stress intensities. Extensive slot and tunnel formation was visible up to about an applied stress intensity value of 71.4 $MNm^{-3/2}$. The stress acting across the plane of tunnel formation was such that the tunnel walls were torn apart and the fracture surfaces exhibited thick torn regions between tunnels. Also, the activation of slip processes within the grain produced emergent steps which intersected the tunnel plane, leading to selective attack at these points. The initial attack at grain boundaries developed into transgranular fracture initiated at emergent {111} slip planes, leading to nearly parallel slots within one grain. At higher stress intensities, tunneling and slot formation due to corrosion were reduced and the fracture mode was then predominantly ductile rupture with limited intergranular grain boundary tearing.

Other investigators have also observed the predominant failure mode in stress corrosion cracking of high strength steels at low and intermediate stress intensities to be intergranular [17,26,27,32,33,105-107]. Beachem [107] also noted that in 4300 type steels, under aqueous environment, ductile fracture, preceded by a mixed mode of fracture was observed with increasing applied stress intensity. Wang and Staehle [108] observed a change in fracture mode with applied stress intensity for martensitic AISI 4340 steel, viz., intergranular fracture at low stress intensities in 3.5% NaCl solution and an increase in the amount of ductile rupture with an increase in applied stress intensity. The results obtained in the present investigation are consistent with these observations. Crack microbranching with crack branch separation distances of the order of one grain diameter was reported by Speidel [30] in Stage II crack growth region. He also observed occasional crack macrobranching. Carter [109] has also observed similar crack branching in high strength steels. Lessar and Gerberich [32] observed a difference in secondary features with different grain sizes for 4340 steels. They noted that smaller grained structures displayed increased tear failure than the larger grained structures. The results of this study are consistent with all the above observations. Tunneling and slot formation initiation at corrosion pits during extended exposure to corrosive environment, have also been reported by other investigators [110,111]. The model proposed by Swann and Embury [112] invoked the intersection of {111} slip planes at grain boundaries leading to slot formation, and this can be applied to this high strength steel. The absence of these features for the other heat treatments was due to accelerated crack growth rates which limit corrosion pit formation.

4.3.5. Summary: Fractography.

4.3.5.1. Tensile Specimens.

1. Three zones-viz., fibrous, radial and shear lip, were identified for all heat treatments, except high temperature and step, where the central zone merged into the shear lip zone without any intermediate zones.

2. Fractographs from the fibrous zone revealed a mixed failure mode for conventional, cyclic, high temperature and step heat treatments,

consisting of intergranular, quasicleavage and microvoid coalescence, whereas the modified heat treatments all exhibited predominantly ductile rupture.

3. The size of dimples was finer for the finer grained structures and for the modified heat treatments when compared with the corresponding non-modified heat treatments.

4. Coarse steps, along well defined crystallographic planes were observed for high temperature and step heat treatments, indicating cleavage along coarse lath and packet boundaries. Finer steps due to failure along regular laths were also observed in the case of all heat treatments.

4.3.5.2. Impact Specimens.

1. Fibrous, radial and shear lip regions were identified as in the case of tensile specimens and the width of the fibrous zone was related to the fracture initiation energy.

2. In the fibrous zone, the predominant failure mode was microvoid coalescence for all the heat treatments and in the radial zone, the failure mode was a mixed intergranular, quasicleavage and ductile rupture, with quasicleavage predominating. For modified heat treatments, however, no intergranular facets were identified.

3. Dimples were fewer and shallower for high temperature and step heat treatments, while for the other heat treatments, the dimple density and depth were more or less uniform.

4. Coarse steps were identified for high temperature and step heat treatments, as in the case of tensile specimens, indicating cleavage

along coarse laths and packet boundaries. Finer steps along regular lath boundaries were also identified.

4.3.5.3. Plane Strain Fracture Toughness Specimens.

1. All heat treatments resulted in predominantly microvoid coalescence failure mode in the initiation region, with conventional, cyclic, high temperature and step heat treatments exhibiting some intergranular and quasicleavage failure.

2. The volume fraction of dimples was higher for the modified heat treatments than for the corresponding non-modified heat treatments.

3. Coarse steps, indicative of coarse lath and packet boundary cleavage were identified for high temperature and step heat treatments.

4.3.5.4. Stress Corrosion Cracking Specimens.

1. The predominant failure mode was intergranular at low and intermediate applied stress intensities, except for the modified conventional heat treatment, which exhibited both intergranular and transgranular features.

2. The amount of transgranular features increased with increasing stress intensity, with final overload region failing by microvoid coalescence.

3. There was a transition from quasicleavage and microvoid coalescence to completely ductile rupture with increasing applied stress intensity in the transgranularly failed regions. For the modified conventional heat treatment, in these transgranularly failed regions, extensive tunnel and slot formation resulted, which changed at higher stress intensities to dimple formation.

4. Secondary cracking in Stage II crack growth region and triple points were observed frequently for all the heat treatments.

5. With increasing stress intensity, the intergranular facets showed increasing amounts of tear ridges and dimples.

6. Steps due to multiple crack coalescence and due to cleaving along coarse lath and packet boundaries were also observed for high temperature and step heat treatments.

5. DISCUSSION

5.1. Mechanical Properties

5.1.1. Tensile Properties.

Ultimate tensile strength and yield strength (true and apparent) of conventional and high temperature heat treatments were essentially the same. While an order of magnitude increase in prior austenite grain size resulted by austenitizing the steel at higher temperature, this did not reflect upon the strength values (the Hall-Petch relationship cannot be directly applied because of other microstructural variations). A higher austenitization temperature results in a greater dissolution of alloying elements and residual carbides. This chemical homogeneity should account for greater solid solution strengthening. However, higher twin density associated with the plate martensite structure of conventional heat treatment should tend to offset this effect, because a decrease in the number of available deformation systems, by a factor of four, results in twinned martensite as opposed to lath martensite [113], which should increase the strength. Often, in this study, the twin boundaries were decorated with carbides. These boundaries can act as strong barriers for the movement of dislocations and hence the dislocation pile-ups should also increase the strength [94]. On the contrary, even lath boundaries were shown to be strong dislocation barriers [114,115] and the greater amount of lath martensite obtained due to high temperature heat treatment should account for part of the strength equality. In fact, Speich and Swann [116], based upon their study of Fe-Ni martensites, reported that the strengthening effect due to twins approximately balances that lost due to increased dislocation density associated with plate martensite.

An important factor is that the prior austenite grain boundaries in martensitic structures account for only a small fraction of the total boundary surface. The low angle boundaries at plate and lath intersections and the high angle packet boundaries constitute the majority of the boundary surface. Roberts [117] showed that although the packet size is decreased by prior austenite grain refinement, this is not a linear relationship and a greater than 50 fold decrease in the grain size produces only a corresponding decrease by a factor of less than 10 in packet size.

Other factors that might affect strength are the amounts of interlath films of retained austenite and segregation effects. The reduction in strength due to an increase in retained austenite may not be significant because of the small amounts of retained austenite involved. Likewise, segregation effects may not be important, because although segregation of impurity and alloying elements are reduced by higher austenitization temperature, the amount of segregated elements/unit grain boundary area may still be the same because of the reduction in the prior austenite grain boundary area. The cumulative effect of these different factors is such that the strength of the conventional and high temperature heat treatments were almost the same.

Step heat treatment decreased strength substantially. The difference between step and high temperature heat treatments are the amounts of segregation and twins. The inverse dependence of segregation upon austenitization temperature has been established by other investigators [2,118]. In a step heat treated steel, although at the starting austenitization temperature diffusion rates are high and thermodynamic driving force for segregation small to prevent segregation, at the second lower austenitization temperature, the driving force for segregation would increase, promoting segregation to grain boundaries and other preferred sites in austenite. (1100°C is the critical temperature for this effect [2]). This would weaken the grain boundaries and decrease the strength. However, an opposing effect is the propensity for twinning with this partitioning and redistribution of alloying elements like Mn, Cr, Ni etc., as suggested by Khan et al. [18], which produce changes in local stacking fault energies. This change in stacking fault energy strongly influences the transformation characteristics of quenched iron base alloys, especially the propensity for twinning [119-121]. The microstructural results, in fact, showed an increase in twinning for step heat treatment, which should raise the strength somewhat and, in turn, balance for the loss due to decreased dislocation density. Thus, the final strength was lower than for the conventional and high temperature heat treatments chiefly due to the segregation effect alone.

Cyclic heat treatment improved the strength of the conventional heat treatment due to reduced prior austenite grain size, which was refined by about 50% and the lath width, which was slightly reduced.

All modified heat treatments showed moderate to significant strength improvement over the corresponding non-modified heat treatments. Intermediate tempering at 650°C for 1 hour precipitated coarse

M_3C, M_7C_3 and $M_{23}C_6$ particles (ranging in size from 1500 Å to 2000 Å) and lesser amounts of Mo_2C precipitates. These particles were considerably refined (100 Å - 300 Å) by the reaustenitization step at 850°C and were maintained as fine dispersions in the final microstructure. Although the transformation of the austenite after the reaustenitization step to martensite should result in decreased twinning and increased amounts of retained austenite (confirmed by transmission electron microscopy), due to decreased free carbon in the austenite which elevates the M_s temperature, the loss in strength, which would be only minimal, is outweighed by other factors. Lower free carbon in austenite results in increased lath martensite and decreased twinning because the critical resolved shear stress for slips is decreased below that of twinning [61]. Conversely, the M_s temperature is raised due to depletion of solute elements (most of which are tied up with carbon as carbides), which decreases twinning [122]. However, the lath martensite that results has a high dislocation density and the interaction of these dislocations with dispersed carbide particles acts to multiply these dislocations [123]. In addition, the fine carbides also contribute to dispersion strengthening of the matrix. A heterogeneous structure of lath martensite and fine carbides improves strength and ductility of other steels [124,125] through both increased dislocation density and dispersion hardening effects. Other relevant factors that improve the strength are the decrease in the prior austenite grain size and lath width for these modified heat treatments.

In general, the strength of tempered martensite can be considered as the sum of grain size, precipitates, interstitial and substitutional solid solution effects, substructure (twins and dislocations) and Peierls stress [126-129]. Peierls stress, which is the stress required to move a dislocation through an otherwise perfect lattice can be estimated based on a sinusoidal force [130] relation which yields a value of 10^{-4}G, where G is the shear modulus (=8.294 x 10^4 MNm^{-2}). The actual experimental values were reported to be between 13.78 MNm^{-2} and 55.11 MNm^{-2}[116,131, 132] and even if the higher values are taken, this would be still a small contribution to the yield stress. The contributions from interstitial and substitutional solid solution strengthening can also be evaluated. The equilibrium carbon content of 0.01% would yield about 1.378 x 10^2 MNm^{-2} to the yield stress, as per the calculations of Cox [133]. For a partial precipitation of cementite, the amount of free carbon in solution can be estimated using the formula:

$$\%\ \text{free C} = \left[\frac{F_V - f_V}{F_V} \right] \text{x total \% C} \qquad (5.1)$$

where F_v is the maximum volume fraction and f_v is the experimentally determined volume fraction. The hardening due to carbon in interstitial solid solution is almost linear and increases at the rate of 4.429 x 10^3 MNm^{-2} per percent of carbon. In all the heat treatments studied, the final tempering temperature was 280°C and the cementite precipitation appeared complete. In the case of the modified heat treatments, a part of the carbon was associated with metal carbides, but still the precipitation of all carbides appeared complete. Even if 10% of the carbon remained uncombined, the increase in strength would be only 48.22 MNm^{-2}, corresponding to a free carbon content of 0.042%

$\left(\left[\frac{F_v - 0.9F_v}{F_v}\right] \times 0.42\right)$, which is an exaggerated estimate, since the residual carbon in solid solution in tempered martensite is usually less than 0.02% [137].

Lacy and Gensamer [134] have studied the effects of several substitutional elements on the yield strength of iron and for only those elements present in 300M steel, if the effects are taken as additive, the maximum contribution would be about 2.518×10^2 MNm^{-2}, which would remain constant, if the solute distribution does not vary much upon tempering. In the present investigation, even for the modified heat treatments, the variation would be within limits after final tempering at 280°C.

The major substructural changes for the various heat treatments studied were in the amounts of lath and plate martensite. As explained earlier, twinning provides a strengthening effect [113]. However Speich and Swann [116] based upon their study of Fe-Ni martensites concluded that this strengthening effect due to twins would approximately balance that lost due to decreased dislocation density associated with plate martensite. These and other investigators [50,87,114,133] have reported a total contribution to the yield strength, due to substructural effect, to be between 68.89 MNm^{-2} and 20.67 MNm^{-2}, the higher value corresponding to the as-quenched state and the lower value referring to the tempered state. Work hardening also contributes to the yield strength [135]. For strains of 0.001-0.002, Smith and Hehemann [136] reported maximum values of about 82.67 MNm^{-2} for 4340 steel. In the present investigation also, strain hardening was similar to those reported by Smith and Hehmann for strain ranges between 0.001 and 0.002.

Thus, contributions to yield strength from Peierls Stress, solid solution, substructural and work-hardening effects would amount to a maximum of about 7.822×10^2 MNm^{-2}. Changes among different heat treatments with respect to any of these factors are slight and hence would not affect the yield strength significantly. Two other factors that account for a major part of the strength are dispersion strengthening from carbides and grain size effects.

The presence of fine carbides in tempered martensite has been shown to contribute a significant part of strength [126,129,135,138-140]. For an array of undeformable, incoherent precipitates, dislocations would loop around them and not cut through them, under the action of stress, and the yield stress (σ_{ys}), according to Orowan [141] could then be expressed as:

$$\sigma_{ys} = \sigma_s + \frac{4T}{bd} \tag{5.2}$$

where, σ_s is the yield stress of the matrix without the precipitates, but inclusive of solid solution strengthening, T, the line tension of a dislocation, b, the Burger's vector of a slip dislocation (= 2.48 Å), and d, the interparticle spacing of the precipitates in the slip plane. The line tension (T) of a dislocation at critical bowing is approximately equal to:

$$\frac{Gb^2}{4\pi} \left[\tfrac{1}{2}(1 + \frac{1}{1 - \nu}) \right] \ell n \left(\frac{d}{2b} \right) \tag{5.3}$$

where G is the shear modulus (=8.294 x 10^4 MNm^{-2} for iron) and ν is the Poisson's ratio [142]. Substituting for T, σ_{ys} can be rewritten as:

$$\sigma_{ys} = \sigma_s + 4\alpha Gbd^{-1} \tag{5.4}$$

where,

$$\alpha = \frac{1}{4\pi}\left[\tfrac{1}{2}(1 + \frac{1}{1 - \nu})\right] \ell n \left(\frac{d}{2b}\right) \tag{5.5}$$

Assuming that after final tempering at 280° C, only equilibrium content of carbon (0.001%) remains in solution, the interparticle spacing could then be calculated from:

$$\left(\frac{d}{2}\right)^2 = \left(\frac{r^2}{f}\right) \tag{5.6}$$

where r is the mean particle radius and f is the volume fraction of carbide. In the case of the modified heat treatments, although epsilon carbide precipitation was observed extensively within large laths, the predominant carbide was cementite with a typical size of 200 Å. The theoretical volume fraction of cementite can be estimated as shown in Appendix IV, the actual value corresponding to 0.063. The average particle size taken as 200 Å would then yield an interparticle spacing of 797 Å. Substitution of this value in Equation (5.5) yields a value of 0.504 for α. The contribution to yield strength from this dispersion strengthening effect would then be equal to $4\alpha Gb/d$ from Equation (5.4), the numerical value corresponding to 5.203 x 10^2 MNm^{-2}.

For the modified heat treatments, the amount of Mo_2C precipitates was insignificant and chromium carbides were present both as $(Fe,Cr)_7C_3$

and $(Fe,Cr)_{23}C_6$ and the remaining carbon was assumed to be present in the form of cementite. This assumption would yield a higher volume fraction of precipitates in the steel than if Mo_2C and Cr_7C_3 were to be present. On this basis, the volume fraction of the various precipitates can be calculated (Appendix IV) and the total volume fraction of the precipitates was estimated to be 0.075, giving the interparticle spacing as 730 Å. The value of α in Equation (5.5) would then be 0.495, which in turn would contribute approximately 5.581×10^2 MNm^{-2} to the total yield strength. When compared with the non-modified heat treatments, this increase is only 37.8 MNm^{-2}. This value was calculated based upon the optimum conditions for strength improvement. The actual increase depends upon the exact value of the volume fraction of the precipitates in the steel.

Strengthening by grain refinement was first predicted by Hall [143] and Petch [144], based on the hypothesis that planar obstacles like grain boundaries constitute a barrier for dislocation movement. By cyclic heat treatment procedures which refine the prior austenite grain boundaries, Grange improved the strength of various steels possessing different structures, including tempered martensite [24,46]. The constant K in the Petch relationship viz.:

$$\sigma = \sigma_o + Kd^{-\frac{1}{2}} \tag{5.7}$$

where, σ is the flow stress, σ_o is the friction stress and d is the grain diameter, was shown by Dieter [140] to be related to σ_c, the critical stress at the head of a pile-up to initiate yielding, by the equation:

$$K = \left[\frac{8Gb\sigma_c}{\pi(1-\nu)}\right]^{\frac{1}{2}} \quad (5.8)$$

where, G, b and ν carry their usual meaning. The stress σ_c depends upon the material, type of boundary (grain boundary or subgrain boundary) and relative orientation of boundary and slip plane. Values ranging from approximately 0.6044 $MNm^{-3/2}$ for grain boundary to 0.2747 $MNm^{-3/2}$ for subgrain boundary have been reported by several investigators [136,147-149]. Assuming a value of 0.6542 $MNm^{-3/2}$ for K, as reported by Grange [24], the value of $Kd^{-\frac{1}{2}}$ in the Hall-Petch equation becomes 2.067×10^2 MNm^{-2} for d = 10 μm, 1.688×10^2 MNm^{-2} for d = 15 μm, 1.461×10^2 MNm^{-2} for d = 20 μm, 73.07 MNm^{-2} for d = 80 μm and 44.06 MNm^{-2} for d = 220 μm, corresponding to various heat treatments studied in this investigation. However, the variation in the experimentally measured yield strength did not change in accordance with these predicted values. Secondly, the contribution to yield strength should be higher than the predicted values. The discrepancy can be accounted for by considering the cell size (the average size of a substructural unit) and not the prior austenite grain size, as proposed by Langford-Cohen [150]. Their model assumes that dislocation sources in the cell walls are activated more easily than at grain boundaries and the stress required to expand dislocation loops across the cell constitutes the hardening observed in tempered martensite and bainite structures. The flow stress according to this model can be written as:

$$\sigma = \sigma_o + Kd^{-1} \quad (5.9)$$

where, d is the cell size and K, the work required to generate the dislocations. Assuming a value of K = 5.9Gb (= 1.214×10^{-4} MNm^{-1}), according to Langford-Cohen, and the cell size to be the average width of the laths which was about 0.3 μm for all heat treatments (except the modified and cyclic heat treatments, for which it varied between 0.25 μm and 0.3 μm), the factor Kd^{-1} then becomes 4.046×10^2 MNm^{-2} (and 4.855×10^2 MNm^{-2} to 4.046×10^2 MNm^{-2} for modified and cyclic heat treatments).

Adding the contributions from dispersion strengthening and grain size effects, the calculated yield strength values range from 1.707×10^3 MNm^{-2} for the non-modified heat treatments to $1.826 \times 10^3 MNm^{-2}$ for the modified and cyclic heat treatments. The experimentally determined values ranged from 1.621×10^3 MNm^{-2} to 1.766×10^3 MNm^{-2} for the various heat treatments, except for the step heat treatment, which yielded 1.494×10^2 MNm^{-2}. The calculated values are slightly higher than the experimentally determined values for the corresponding heat treatments. The agreement otherwise is close indicating the applicability of the various models discussed for these heat treatments. The loss of about 127 MNm^{-2} in the case of the step heat treatment is directly attributable to the increased amounts of segregated impurities and alloying elements per unit grain boundary area as explained earlier. This loss is balanced in the case of the modified step heat treatment by the greater dilution of segregates at the prior austenite grain boundary and the final values are in fact higher for the modified heat treatments due to the dispersion strengthening and lath refinement effects.

The ultimate tensile strength of the various heat treatments varied only slightly but these variations were consistent with the changes in the yield strength for these heat treatments. Exceptions were the step and modified step heat treatments which exhibited lower values. The increased concentration of segregation at the grain boundaries should lower the overall work hardening rates for these heat treatments somewhat and the decreased ultimate tensile strength values are a direct consequence of this. For the other heat treatments work hardening rates that were obtained were almost similar and thus the ultimate tensile strength values were also similar.

Ductility variations, measured in terms of tensile elongation and reduction in area, were consistent with microstructural variations for the various heat treatments. Test conditions that affect ductility (temperature, strain rate, etc.) were constant for all the heat treatments. As shown by Carreker et al. [151], ductility increased with decreasing grain size, probably due to the small increase in strain hardening rate with reduced grain size. Local composition variations can have a deleterious effect on ductility [152] and the decreased ductility in the case of step and modified step heat treatments is attributed to this segregation effect. Second phase particles also affect ductility. While Gensamer [153] found a decrease in ductility as the interparticle spacing decreased, Edelson and Baldwin [154] concluded that ductility is only a function of the volume fraction of the second phase particles and not the nature (hard or soft), shape and size of particles, because ductility was controlled by the ability of particles to concentrate strain locally in the matrix between particles, thereby allowing fracture to occur earlier than if the strain distribution were homogeneous. However, particle shape has been shown to be a major factor in determining ductility [155] and also within a class of alloys with similar structure, as in quenched and tempered steels, ductility was found to be strongly dependent on both interparticle spacing [156] and volume fraction [157], with a decrease in the former and an increase in the latter leading to increased ductility. Fine precipitates may act as sources of fresh mobile dislocations in situations where immobility of dislocations causes brittleness, thus contributing to the improved ductility of the modified heat treatments. The theoretical analyses of Gurland [158] and Ashby [159] also indicate that ductility increases with decreasing particle size. The nature of the particles is also important, in contradiction to Edelson and Baldwin's conclusions. If the particles are weaker than the matrix, ductility would decrease due to their ease of deformation. If they are hard and tough and do not deform easily, they may improve the ductility (if numerous and small). However, if coarse, they may decrease ductility [160]. The present results have shown that the major factor in determining ductility is the prior austenite grain size, with decreasing grain size resulting in increasing ductility, by slightly increasing the work hardening rate and changing the strain distribution in the matrix at the grain boundaries. In the case of the modified heat treatments, ductility improvement can be partly attributed to the role of second phase particles (size, shape and volume fraction of carbides).

5.1.2. Impact Properties. The Charpy V-notch toughness consistently dropped as the plane strain fracture toughness (K_{Ic}) and dynamic fracture toughness (K_{Id}) increased. Various investigators have observed this trend for Ni-Cr-Mo-V, Fe-Cr-C, EN 25, 4340 and 300 M steels [4,12,19-21,161-164]. The best explanation for this apparent paradox was proposed by Ritchie [165] who suggested a model based on notch root radius effect. While the increase in K_{Ic} and K_{Id} (sharp crack toughness) can be associated with an increase in the characteristic distance ahead of the crack tip (usually related to the major microstructural feature controlling fracture, like the void size), the decrease in CVN toughness is associated with a decrease in critical fracture stress, for stress controlled (intergranular and quasicleavage) fracture and fracture strain, for strain controlled (microvoid coalescence) fracture. Fractography results showed that the predominant fracture mode for all the heat treatments was microvoid coalescence and so the latter model could be applied. Considering stress controlled fracture first, critical fracture will occur when the maximum principal stress, σ_{yy}^{max}, at the notch tip exceeds the fracture stress, σ_f. For the CVN specimen, σ_{yy}^{max} is located near the elastic-plastic interface at a distance r from the notch tip. According to slip line field theory:

$$\sigma_{yy}^{max} = \sigma_{ys}\ [1 + \ell n(1 + r/\rho)] \qquad (5.10)$$

where σ_{ys} is the yield strength and ρ, the notch root radius. For the critical plastic zone at failure, of size r_c, we can write:

$$r_c \approx 0.12(K_A/\sigma_{ys})^2 \qquad (5.11)$$

where K_A is the apparent fracture toughness. Combining Equations (5.10) and (5.11), and substituting σ_{yy}^{max} equals σ_f at failure, we get:

$$K_A \approx 2.9\ \sigma_{ys}[\exp(\sigma_f/\sigma_{ys} - 1) - 1]^{\frac{1}{2}}\rho^{\frac{1}{2}} \qquad (5.12)$$

Below a certain critical radius ρ_o, K_A becomes independent of ρ and has the same value as K_{Ic} (see Figure 5.1) and hence K_{Ic} (or K_{Id}) can be written as:

$$K_{Ic}\ (\text{or } K_{Id}) \approx 2.9\ \sigma_{ys}\ [\exp(\sigma_f/\sigma_{ys} - 1) - 1]^{\frac{1}{2}}\rho_o^{\frac{1}{2}} \qquad (5.13)$$

ρ_o is the measure of the characteristic distance 1, over which σ_f should exist to cause failure and is related to the microstructural feature which controls the fracture like slip or twin band spacings, grain size or inclusion spacing [166,168]. The minimum distance from the notch where the critical fracture event can occur is given by ℓ and only in the case of sharp notches where σ_{yy}^{max} is close to the notch tip is it important. Ahead of a blunt notch, σ_{yy}^{max} is located at, or just behind, the elastic-plastic interface [169] and at failure, fracture events occur at distances much larger than 1 from the notch tip. As the austenitization temperature is raised, σ_f decreases due to impurity induced grain boundary embrittlement [15]. Although segregation decreases with increasing austenitization temperature, the concentration of segregates/unit grain boundary area may be more because of a reduction in grain boundary area. In the case of step heat treatment, this will be even higher. The situation is schematically explained in Figure 5.2.

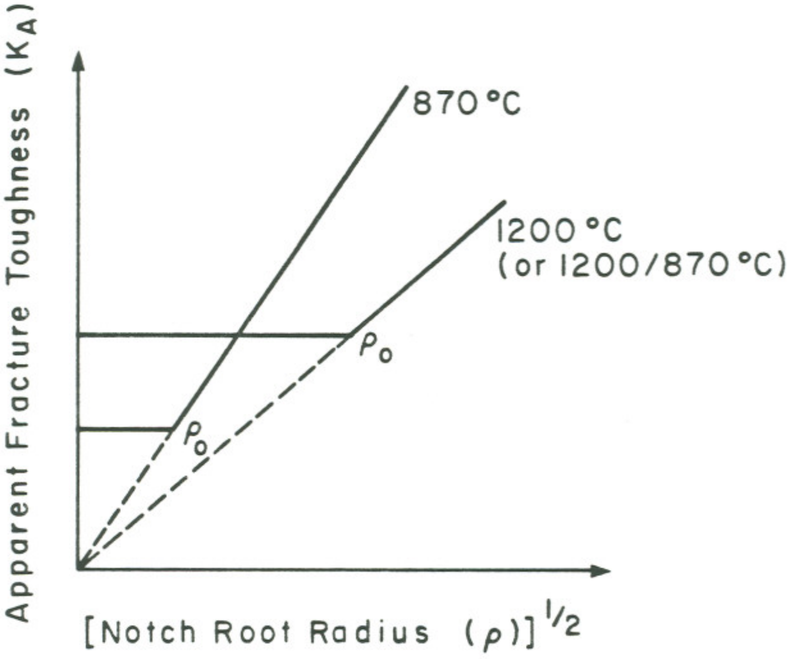

Figure 5-1: RELATIONSHIP BETWEEN APPARENT FRACTURE TOUGHNESS AND NOTCH ROOT RADIUS AS A FUNCTION OF AUSTENITIZATION TEMPERATURE [165].

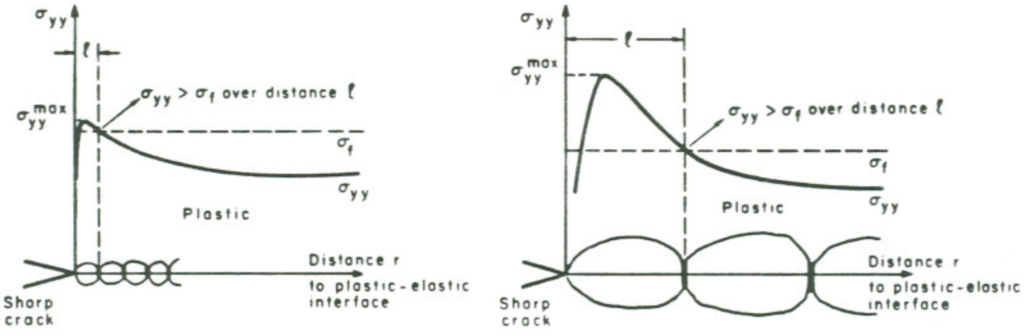

(a) 870 °C Structure (b) 1200 °C or 1200/870 °C Structure

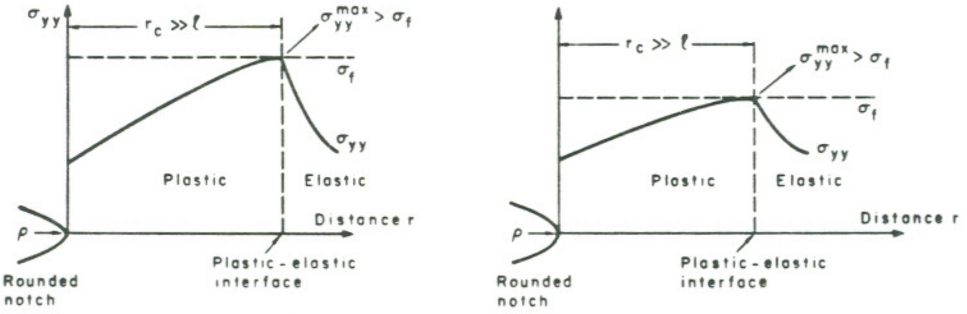

(c) 870 °C Structure (d) 1200 °C or 1200/870 °C Structure

Figure 5-2: STRESS DISTRIBUTION AHEAD OF (a) SHARP CRACK IN 870°STRUCTURE, (b) SHARP CRACK IN 1200° OR 1200/870°C STRUCTURE, (c) BLUNT NOTCH IN 870°C STRUCTURE AND (d) BLUNT NOTCH IN 1200°C or 1200/870°C STRUCTURE. $\sigma_{yy} > \sigma_f$ or $\sigma_{yy}^{max} > \sigma_f$ REPRESENTS THE FRACTURE CONDITION [165].

For strain controlled fracture, the extensional strain ε must exceed the critical fracture strain ε_f and toughness K_A can be expressed as:

$$K_A \approx (\frac{3}{2} \sigma_{ys} E \varepsilon_f)^{\frac{1}{2}} \rho^{\frac{1}{2}} \tag{5.14}$$

where E is the elastic modulus. As before, below a critical ρ_o,

$$K_{Ic} \approx (\frac{3}{2} \sigma_{ys} E \varepsilon_f)^{\frac{1}{2}} \rho_o^{\frac{1}{2}} \tag{5.15}$$

where ρ_o is the measure of the characteristic distance (like interparticle spacing) over which the critical strain should exist to cause failure. For blunt notches, with higher austenitization temperature, as ductility decreases, K_A also decreases.

Cyclic heat treatment resulted in maximum ductility and this was reflected upon the CVN toughness which was highest when compared with all other heat treatments. High temperature heat treatment resulted in a higher CVN toughness than the step heat treatment. The lower concentration of segregation at the grain boundaries for the high temperature heat treatment when compared with the step heat treatment explains this slight increase in the impact toughness. The modified conventional heat treatment resulted in higher ductility than conventional heat treatment, but the CVN toughness was the same for both the heat treatments. The increased ductility may not have been sufficient to significantly increase the CVN toughness. The modified high temperature and modified step heat treatments also improved ductility of the corresponding non-modified heat treatments and this was consistent with the observed increase in the impact toughness.

The fracture propagation energies were unchanged for all heat treatments, except for the cyclic heat treatment, which resulted in slightly higher and the step heat treatment, which yielded a slightly lower value. The CVN toughness changes were due chiefly to changes in the fracture initiation energies (FIE). The above models which rely upon critical fracture stress or strain criteria take into account only the initiation and not the propagation. After crack initiation and once a sizable crack begins to run, the rate effect takes over. The stress level induced in a neighboring grain by a running crack is much higher locally than for a stationary crack [281] and many more grains will cleave, as was confirmed by fractography studies for all heat treatments, rather than continuing to deform plastically. The process of fracture becomes catastrophic and even large reductions in applied load (or in the stress level of the region of fracture) will not stop the crack from running once it acquires enough speed. Hence, the crack propagation for all the heat treatments was not affected by microstructural variations, resulting in similar propagation energies.

Other parameters that were measured during impact testing, viz., specimen deflection at yield, apparent yield strength and dynamic fracture toughness, all changed predictably with heat treatment. Specimen deflection, which is an approximate measure of ductility, was highest for conventional, cyclic and modified heat treatments, whose grain sizes were fine. The reasons for the variations in ductility for the various heat treatments have already been explained. Apparent yield strength varied in a similar manner as the actual yield strength. Dynamic fracture toughness, generally defined as the crack resistance beyond the point of instability, was measured using the maximum load values in the load-deflection curves. The variation in this parameter generally followed the same trend as the plane strain fracture toughness. Cyclic heat treatment resulted in unusually high K_{Id} values and likewise, high temperature heat treatment yielded lower values. While it is difficult to explain this behavior, K_{Id} values measured from Charpy tests are only approximate at best [23] and even slight deviations in load measurements from the instability point yield very erroneous results. For instance, if the instantaneous energy release rate is calculated close to the static equivalent, the energy value is exaggerated. If the energy is measured near the arrest point, the measured toughness is lowered, since the arrest value is lower than the crack resistance and depends upon the crack size and speed. In general, however, K_{Id} behavior followed the K_{Ic} trends to be discussed next.

5.1.3. Plane Strain Fracture Toughness. For fracture by microvoid coalescence, the elastic strain distribution ahead of a crack tip was used by Krafft [170] to relate fracture toughness to inclusion spacing, assuming that voids nucleated at inclusions. Although in this investigation, the voids were nucleated not only by inclusions but also by carbide particles, the Krafft model is still applicable, because, it involves only interparticle spacing d. Thus if ε_i is the uniform elongation strain at the instability of a tensile specimen (which is equal to the strain hardening exponent n) then,

$$\begin{aligned} K_{Ic} &= En\sqrt{2\pi d} \\ &= E\,\varepsilon_i\sqrt{2\pi d} \end{aligned} \tag{5.16}$$

where, E is the modulus of elasticity. This equation predicts that for materials with similar modulus of elasticity and strain hardening rates, K_{Ic} increases with interparticle spacing. Rice and Johnson [171] showed that the strain distribution can be approximated by:

$$\begin{aligned} \varepsilon_y &= \frac{0.44\delta_t}{x} - 0.23 \\ &= \frac{0.22\,K_I^2}{E\,\sigma_{ys}\,x} - 0.23 \end{aligned} \tag{5.17}$$

where, δ_t is the void width, equal to d for spherical voids, K_I is the stress intensity, σ_{ys} is the yield stress and x is the distance from the crack tip. At $x = d$, $\varepsilon_y = \varepsilon_f^*$ (the fracture strain at the crack tip), and the fracture toughness according to Schwalbe [172] is then given by:

$$K_{Ic} = [4.55\,(\varepsilon_f^* + 0.23)E\,\sigma_{ys}\,d]^{\frac{1}{2}} \tag{5.18}$$

When $\delta_t = d$ (for large dimples),

$$K_{Ic} = (2E\,\sigma_{ys}\,d)^{\frac{1}{2}} \tag{5.19}$$

For finer dimples, $\delta_t > d$ and the above equation has to be modified.

A semi-empirical expression for K_{Ic} was derived by Hahn and Rosenfield [173], who used a linear strain distribution in the plastic zone and showed that

$$K_{Ic} = 5[2E\ \sigma_{ys}\ \varepsilon_f^{*}(n^2 + 0.005)10^{-3}]^{\frac{1}{2}} \tag{5.20}$$

For fracture by cleavage or quasicleavage modes, Hahn and Rosenfield [174] showed that:

$$K_{Ic} = 0.55(\sigma_{c\ell} - \sigma_{ys}) \tag{5.21}$$

A slightly modified version of the above equation is [175]:

$$K_{Ic} = \frac{1.094}{\sigma_{ys}^{\ 2}} \left(\frac{\sigma_{c\ell}}{2.35}\right)^2 \tag{5.22}$$

The cleavage stress $\sigma_{c\ell}$ is mainly dependent on the grain size. Another model of Wilshaw et al. [160] gives the relationship between K_{Ic} and $\sigma_{c\ell}$ as:

$$K_{Ic} = 2.89\ \sigma_{ys}\ [\exp(\sigma_{c\ell}/\sigma_{ys} - 1) - 1]^{\frac{1}{2}}\ \rho_o^{\ \frac{1}{2}} \tag{5.23}$$

where ρ_o is the effective root radius and is a measure of the extent of the process zone over which $\sigma_{c\ell}$ has to exceed σ_{ys} for fracture. A simple variation of this model yields [172]:

$$K_{Ic} = 3\ \sigma_{c\ell}\ \sqrt{D} \left(\frac{\sigma_{c\ell}}{\sigma_{ys}}\right) \tag{5.24}$$

Examination of Equations (5.16) through (5.19) for ductile fracture predicts that as the interparticle spacing increases, that is, as the void size increases or the void density decreases, K_{Ic} should increase. From the fractographs of K_{Ic} specimens, for the high temperature heat treatment, the void size was higher than for the conventional heat treatment.

Although quantitative estimates were not made, these voids were on an average three times larger than for the conventional heat treatment. Assuming that all the other factors are constant, K_{Ic} should then increase by $\sqrt{3}$ times (that is, from about 56 $MNm^{-3/2}$ to 97 $MNm^{-3/2}$), which is in close agreement with experimental results. Cyclic heat treatment resulted in slightly finer voids than conventional heat treatment and this is reflected in the slight drop in the K_{Ic} value. Step heat treatment, although resulting in similar sized voids as in the case of the high temperature heat treatment, resulted in an intermediate K_{Ic} value of about 79 $MNm^{-3/2}$. This suggests that apart from the simple relationship between void size and K_{Ic}, predicted by the above equations, other microstructural features are important. Similarly, for the modified heat treatments, although the void sizes were much smaller than for the conventional heat treatment, the K_{Ic} values were much higher. Thus, the above equations have to be applied carefully when predicting K_{Ic} values. Often other microstructural changes will strongly influence the fracture toughness. For step heat treatment, quasicleavage was also very pronounced. For conventional, high temperature and cyclic heat treatments, this mode was also observed but not so pronounced. When fracture occurs by cleavage or quasicleavage, Equation (5.24) predicts that K_{Ic} varies as the cleavage stress and the grain size. The factor $(\sigma_{c\ell}/\sigma_{ys})$ was introduced to account for temperature variation of $\sigma_{c\ell}$. At a given temperature, taking $\sigma_{c\ell}/\sigma_{ys}$ to be a constant, K_{Ic} should be dependent directly on the cleavage stress, for constant grain size. Segregation associated with step heat treatment should lower $\sigma_{c\ell}$, which explains the intermediate K_{Ic} value. The smaller grain size and segregation potential of conventional and cyclic heat treatments reduced their fracture toughness below the value obtained for high temperature heat treatment. However, for the modified heat treatments, these simple equations cannot predict the higher K_{Ic} values obtained, unless the factors that elevate $\sigma_{c\ell}$ are accounted for. Furthermore, quasicleavage failure mode was not the major mode of failure for the modified heat treatments. If the Hahn and Rosenfield relationship is considered [Equation (5.20)], it is clear that K_{Ic} varies directly as the fracture strain at the crack tip, ε_f^*, and the strain hardening exponent n. Both of these should be substantially higher for the modified heat treatments. While ε_f^* cannot be directly estimated, the small increase in n between the modified and the non-modified heat treatments cannot account for the increased K_{Ic} values. Reasons for the increase in ε_f^* (or, conversely, the fracture stress) will now be discussed.

For fracture by microvoid coalescence, since K_{Ic} varies as $\sqrt{d}$, where d is the interparticle spacing, it should be affected by the volume fraction v of the second phase particles, since,

$$d = 2r\left[\frac{2}{3v}\,(1 - v)\right]^{\frac{1}{2}} \qquad (5.25)$$

where, r is the particle radius [148]. When the volume fraction increases, this equation predicts a drop in K_{Ic}, which was verified for Al alloys [176-177] and steels [178-179]. In all these investigations, K_{Ic} increased as a function of material purity (that is, increasing inclusion distance, where inclusions were the major source of voids). However, the type, size and distribution of particles are also equally important. Dimple size and particle spacing may not be directly related, especially when there are different types of particles. Burghard [180] has shown that dimples could be larger than particle spacing when only a certain fraction of particles in the material contributes to the fracture process. Also, the plastic strain necessary to fracture a particle increases with decreasing particle size. In fact, particle size reduction without changing volume fraction can cause an increase in K_{Ic} in spite of decreasing interparticle spacing [181], because of the better resistance of smaller particles. The type or nature of the particle is important because ductility will be higher, the tougher the second phase particles and the better the bonding between these particles and the matrix [182]. Shape will also be important and Gladman et al. [183] showed that for steels, plate shaped or elongated particles were more detrimental than equiaxed or spherical ones.

Retained austenite is advantageous to the fracture toughness of quenched and tempered steels [4,7,9,10,75,76,184-187]. According to Antolovich et al. [188], the fracture energy (G_{Ic}) (per unit area of crack extension) of steels with structures consisting of two phases with different properties can be regarded as the sum of the fracture energies, $G_{Ic.1}$ and $G_{Ic.2}$, of each phase according to:

$$G_{Ic} = G_{Ic.1}(v_1) + G_{Ic.2}(1 - v_1) \qquad (5.26)$$

where, v_1 is the volume fraction of phase 1. Hence, K_{Ic} can be written as:

$$K_{Ic} = \left[\left(\frac{E}{1-\nu^2}\right) G_{Ic.1}\,(v_1) + G_{Ic.2}(1 - v_1)\right]^{\frac{1}{2}} \qquad (5.27)$$

For the specific case of retained austenite in martensite, they calculated theoretically the fracture energy of austenite to be about nine times that of martensite (2.94 MNm^{-1} to 25.2 MNm^{-1}). For the high temperature heat treatment, retained austenite was qualitatively estimated as 8%. Substituting $v_1 = 0.92$, K_{Ic} should increase by about 15% over the conventional heat treatment. Similarly, for the step treatment, it should increase by 12.6% and for the modified conventional, modified high temperature and modified step heat treatments, respectively by 9.6%, 20.7% and 20.7%. The actual increases are more than these predicted values but the amount of increase due to retained austenite alone can be estimated as above. A theoretical explanation for the improvement of K_{Ic} by retained austenite can also be envisaged following the model of McClintock and Irwin [189]. The harder phase (martensite) representing the bulk of the material provides high strength whereas the softer phase serves as energy absorber during crack propagation. For simplicity, considering mode III crack opening (since a simple solution for plastic deformation work W has been derived by McClintock and Irwin),

$$W = \frac{{\tau_y}^2}{\mu}\,\pi\left(\frac{w}{2}\right)^2 = \frac{{K_{III}}^4}{4\mu\pi{\tau_y}^2} \qquad (5.28)$$

where, τ_y is the shear stress ($= \sigma_{ys}/2$), w, the length of the plastic zone and μ, the shear modulus. Because of the different yield stresses of both phases, two plastic zones have to be distinguished. If v designates the volume fraction of the soft phase, the contribution of the hard phase to plastic work at a given stress intensity is given by:

$$W_1 = \frac{c}{(\sigma_{ys.1})^2}(1 - v) \tag{5.29}$$

and that due to the soft phase is given by:

$$W_2 = \frac{c}{(\sigma_{ys.2})^2}\cdot v \tag{5.30}$$

where, c is a constant and $\sigma_{ys.1}$ and $\sigma_{ys.2}$ are yield stresses of the hard and soft phases respectively. Taking $\sigma_{ys.1}$ to be at least 1378 MNm^{-2} and $\sigma_{ys.2}$ to be 276 MNm^{-2} [186], if v is 10%, W, the total plastic work (= W_1 + W_2) is given by:

$$W = c\left[\frac{0.9}{1.9 \times 10^6} + \frac{0.1}{7.62 \times 10^4}\right]$$

$$= c \times 10^{-6}(0.47 + 1.31) \tag{5.31}$$

This indicates that in spite of this small amount, austenite can contribute about three times more to the plastic work than the hard phase does. In other words, when the failure mode is predominantly void nucleation and growth and when retained austenite is present, an additional increment of plastic work must be done if the voids in the martensite are to link up. Thus retained austenite limits the nucleation of emissary cracks ahead of the main crack front and the material is effectively toughened.

Qualitative explanations have also been put forth by Webster [190] who attributes the improvement in toughness by retained austenite to its crack arresting ability. By high magnification movie techniques, he observed that cracks propagating through martensite were stopped upon intersecting a region of retained austenite. With further loading, the cracks branched and grew around the austenitic area. This crack motion necessarily involves more energy absorption than straight propagation through martensite plates.

Koo et al. [185] proposed that the presence of a highly coherent retained austenite-lath martensite interface prevents the formation of brittle carbides and disrupts the continuity of cleavage planes across various laths in a packet. Thomas and Rao [68] proposed that the austenite/martensite boundary is highly coherent. In the absence of austenite, adjacent laths impinge laterally to form a rotation boundary, creating high energy interfaces for crack propagation and/or segregation and precipitation. The above explanations assume that retained austenite is stable. In the present investigation, retained austenite was thermally stable up to 280°C (the final tempering temperature employed). However, no attempts were made to verify the mechanical stability. Even if the austenite films are assumed to be mechanically unstable, it is still possible to achieve toughness enhancement. Studies by Gerberich et al. [191] and Antolovich et al. [192] indicate that about five times more energy is absorbed when austenite is converted to martensite by a strain (or stress) induced transformation, than for the plastic deformation of a stable metal matrix. Another indirect benefit of retained austenite is its ability to dissolve large amounts of interstitial and substitutional elements which would prevent the formation of brittle lath boundary carbides.

Increased amounts of retained austenite for high temperature and step heat treatments are due to the increased M_s temperature (due to the larger grain sizes obtained by austenitizing at high temperature). The grain boundary atoms are relatively stable to martensitic transformation because they are free from restriction by neighboring atoms and tend not to take part in the coordinated atom movements of such transformations. Also, the lattice defects near the grain boundaries can migrate to the boundaries and disappear decreasing the number of nucleation sites [193]. Hence, the M_s temperature should decrease with decreasing grain size. On the contrary, several investigators have experimentally observed an increase in M_s temperature with higher austenitization temperatures for many steels including UHSLA steels [4,61-64,194-202] and attributed this to the increase in the number of frozen-in vacancies with higher quenching temperature (and hence increase in the number of nucleation sites), a larger thermal strain with increased quenching temperature and the reduction of energy needed for complementary shear during transformation, which originates in the elimination of lattice imperfections due to heating to a higher temperature [193]. As opposed to the general stabilization of austenite by finer grains [196,198,199], in this investigation additional retained austenite was obtained for the coarser grains. Most of the qualitative TEM estimates of retained austenite also point to increased amounts of retained austenite with increasing austenitization temperatures [3-5,7,9,10,19]. Lai [203] attributed this increase in retained austenite as being a direct consequence of the increased amounts of lath martensite. The growing martensite laths, during the austenite-martensite transformation induce a compressive stress on the untransformed austenite. Since approximately 3% volume expansion is involved when austenite transforms to martensite, this compressive stress would stabilize the austenite.

For the modified, high temperature and step heat treatments, the structure was predominantly lath martensite. Lai's model for retained austenite stabilization by laths can be applied for these heat treatments, which would explain partly the improved K_{Ic}. While the increase in M_s temperature for high temperature and step heat treatments has been explained earlier, the increase for modified heat treatments (fine grains), which also increased the amount of retained austenite, cannot be similarly explained. When the grain size increased approximately tenfold, the M_s temperature increased only by about 10°C for 4340 steel [4]. For the modified high temperature and modified step heat treatments, the grain size increased only fourfold when compared with the conventional heat treatment. Although actual measurements of M_s temperatures were not made, judging from the amounts of lath martensite which resulted and the almost total absence of twins in the modified heat treatments, it is estimated that M_s temperature should have increased by at least 10°C. Only at higher M_s temperatures can the critical resolved shear stress for slip be below that for twinning (Figure 5.3), producing dislocated lath martensite, as opposed to twinned plate martensite [65]. This increase in M_s temperature for modified heat treatments can only be attributed to the lowering of free carbon content of austenite by precipitation of carbides during the intermediate tempering step. It was shown earlier that even if a

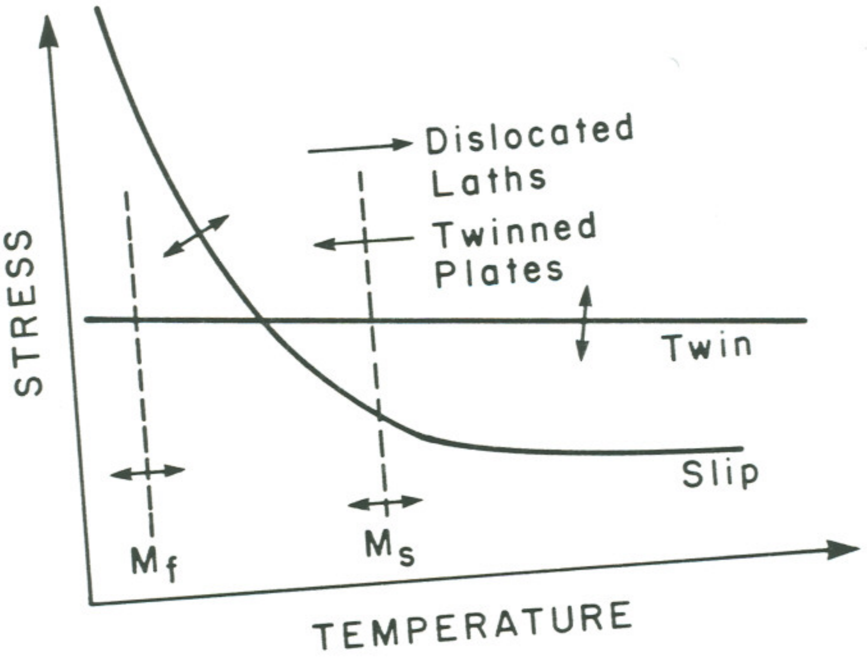

Figure 5-3: VARIATION OF STRESS FOR SLIP AND TWIN AS A FUNCTION OF TEMPERATURE [65].

0.075 volume fraction of carbides were formed, the carbon content would decrease to the equilibrium value of 0.01% in the ferrite. From the approximation for M_s temperature [204], viz.:

$$M_s(°C) = 561 - 474C - 33Mn - 17Ni - 17Cr - 21Mo \tag{5.32}$$

even if the free carbon content were decreased by 0.1%, the increase in M_s temperature could be as high as 47.4°C. But, the final reaustenitization temperature at 850°C would dissolve most of the carbides and hence the actual drop in free carbon content would be much smaller, of the order of about 0.02% to 0.03% corresponding to about 10°C to 15°C.

Other microstructural features that could influence the toughness are the twin density and lath/packet size. No quantitative estimates of the effects on K_{Ic} with twin density are available. However, qualitative explanations have been proposed by many investigators [63-65,94,113]. Kelly and Nutting [113] showed that the number of available deformation systems is decreased by a factor of four for twinning and this results in an increase in strength and a concurrent drop in toughness. Also, the twin boundaries, when decorated with carbides, as was often the case in this investigation, act as strong barriers for the movement of dislocations and the pile-up of these dislocations at these boundaries lead to crack nucleation [94]. It was also suggested that the mode of deformation of twinned martensite is likely to be mechanical twinning rather than slip [64,65] and the subsequent intersection of transformation and deformation twins leads to microcracks [63]. All these would lower the fracture toughness of the steel and hence the improvement in K_{Ic} of the high temperature, step and modified heat treatments, could be partly attributed to the reduction or elimination of twins. In this study, for the step heat treatment, the twin density was observed to be higher than for the high temperature heat treatment but still lower than for the conventional heat treatment. The reasons for this were already discussed in Section 4.2.3.2. This is consistent with the resultant intermediate fracture toughness.

A reduction in both lath width and packet size has been shown to increase toughness by Naylor [114] and Roberts [117]. For the propagation of a crack of critical length c, the fracture stress σ_f may be written as:

$$\sigma_f = \left(\frac{1.4\ E\ \gamma}{c}\right)^{\frac{1}{2}} \tag{5.33}$$

according to the Griffith-Orowan relationship [205], where, E is the Young's modulus and γ is the surface energy. For propagation across a grain boundary, this becomes:

$$\sigma_f = \left(\frac{1.4\ E\ \gamma}{d}\right)^{\frac{1}{2}} \tag{5.34}$$

where, d is the grain diameter and γ, the effective surface energy will encompass the energy for grain boundary tearing [206]. This formula assumes that crossing the first grain boundary is the critical event controlling σ_f. However, often, secondary microcracks can exist over a few grains. Then, if the critical length for fracture involves n grains, then:

$$\sigma_f = \left(\frac{1.4\ E\ \gamma}{nd}\right)^{\frac{1}{2}} \qquad (5.35)$$

However, fracture along grain boundaries was only a small portion of the total fracture in all the heat treatments. Hence, the packet diameter d_p and the lath width ε_ℓ should now be considered. When a crack reaches a packet boundary, a major crack deviation is required and for subsequent propagation across the boundary,

$$\sigma_f = \left(\frac{1.4\ E\ \gamma_p}{d_p}\right)^{\frac{1}{2}} \qquad (5.36)$$

where, γ_p is the energy needed to create a crack that will cross a packet boundary. If the critical event involves n packets, this becomes:

$$\sigma_f = \left(\frac{1.4\ E\ \gamma_p}{n\ d_p}\right)^{\frac{1}{2}} \qquad (5.37)$$

Major deviations between packets are created by the difference in orientation of their groups of fracture planes permitting small angle deviations between laths inside a packet, although the laths in any one packet may adopt any of the six possible Kurdjumov-Sachs orientations (one $\{111\}_\gamma$ plane resulting in one $\{110\}_{\alpha'}$ plane, and one of three possible $<110>_\gamma$ directions producing one of two possible $<111>_{\alpha'}$ directions [58,87,116, 207-209]). Fracture will then continue by large angle deviations across the first few laths of the neighboring packet until a group of fracture planes is found that will allow small angle crack deviations. Hence,

$$\sigma_p = x\ \gamma_\ell' \qquad (5.38)$$

where, x is the average number of laths per packet near a packet boundary, where high angle deviations are necessary and γ_ℓ' is the energy needed to accomplish high angle crack deviations across these laths. After undergoing these deviations, the crack will reach a critical length L after which it will automatically propagate to the next packet boundary. Using the approximation

$$x = \frac{L}{\varepsilon_\ell} \tag{5.39}$$

where ε_ℓ is the lath width, σ_f can be written as:

$$\sigma_f = \left(\frac{1.4\ L\ E\ \gamma_\ell'}{n\ d_p\ \varepsilon_\ell} \right)^{\frac{1}{2}} \tag{5.40}$$

The above equation predicts that a decrease in either lath width or packet diameter or both leads to an increase in toughness. As an example, for the modified heat treatments, when the lath width decreases from about 0.3 μm to about 0.25 μm, σ_f should increase by about 5.5 $\mathrm{MNm}^{-3/2}$ due to this drop alone. However, d_p also decreases and γ_ℓ' the energy needed to achieve deviations across the laths and L the critical length of the crack should both increase. Hence, the actual improvement in K_{Ic} will be much higher. Further, $\gamma_{\ell'}$ will also increase because of increases in dislocation density, precipitation hardening and decreased carbon in solution. Qualitatively, the above equation predicts that major crack deviations occur only at packet boundaries and due to the small angle deviations across laths, a relatively straight fracture would occur across a packet. However, finding another group of fracture planes involves plastic tearing at a certain number of lath boundaries and hence when lath width decreases, this should constitute an increase in fracture stress.

5.1.4. Mechanical Properties of Trial Heat Treatments. The behavior of trial heat treatments (Figures 4.4 - 4.8) is now explained. Intermediate tempering at 650°C precipitated coarse M_3C, M_7C_3, $M_{23}C_6$ and Mo_2C carbides (ranging in size from 1500 Å to 2000 Å). The size of these precipitates depend upon both the tempering temperature and the hold time. Since time was constant, the size is directly dependent upon the temperature, with lower temperatures yielding finer size and vice versa. After a 3 min. reaustenitization at 850°C, the precipitate size was reduced to about 100 Å to 300 Å. This final size also depends upon the temperature and time of reaustenitization. Since the temperature was constant at 850°C, the size depends upon the time only, with longer times resulting in total dissolution.

Precipitate strengthening depends upon the size, distribution and coherency strains. Mott and Nabarro [210] developed theories for interpreting this strengthening effect and these were modified further by Kelly and Nicholson [142] for predicting the strengthening behavior throughout the size range. Qualitatively, the relationship between strength, particle size and coherency strains is depicted in Figure 5.4.

Case•1: When the intermediate tempering temperature was 675°C, as the reaustenitization time increased, strength continuously increased, as a direct consequence of decreasing particle size. This increasing strength with decreasing particle size is direct evidence that the

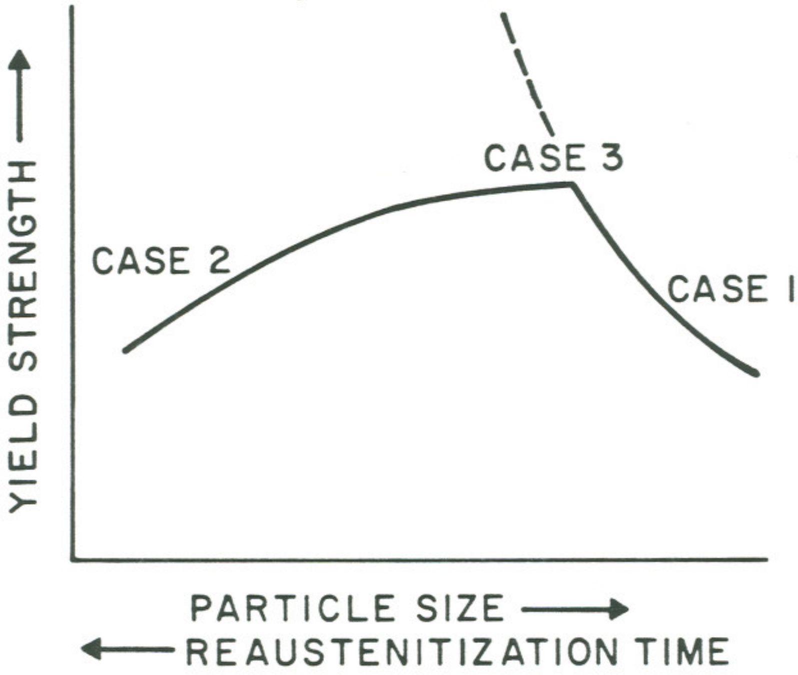

Figure 5-4: RELATIONSHIP BETWEEN YIELD STRENGTH AND PARTICLE SIZE OR REAUSTENITIZATION TIME.

carbides after 675°C tempering are large and widely separated, and can be categorized as incoherent precipitates, wherein the mean particle distance between the particles is much larger than the limiting radius of the dislocations. The dislocations can then bow out between the particles, leaving loops of dislocations around the particles. This Orowan looping occurs because the size of precipitates is such that they can not be sheared by dislocations crossing their slip plane. The yield stress varies as 1/d, where d is the interparticle spacing, or, more rigorously according to:

$$\tau = \tau_s + \frac{Gb}{4\pi}\,\varphi\,\ell n\left(\frac{d - 2r}{2b}\right)\left(\frac{1}{(d - 2r)/2}\right) \tag{5.41}$$

where, τ is the initial yield stress of the alloy, τ_s, the yield stress of the matrix, G, the shear modulus, b, the Burger's vector, r, the particle radius and φ is given by:

$$\varphi = \tfrac{1}{2}\left(1 + \frac{1}{1 - \nu}\right) \tag{5.42}$$

where, ν is the Poisson's ratio. Ductility also increased as the particles get refined at higher austenitization times [158,159], as already explained in Section 5.1.1 and fracture toughness decreased with increasing reaustenitization times, consistent with the decrease in strength.

Case•2: When the tempering temperature was 600°C, the strength varied directly as a function of increasing reaustenitization time (and conversely with decreasing particle size). This indicates that these particles are coherent with the matrix and allow shearing by dislocations (deformable). Orowan looping does not occur because the stresses required to bend the dislocations around each particle are too high. Instead these dislocations are forced through the precipitates and the yield stress is governed by this work done in forcing the dislocations through the precipitates according to:

$$\tau b^2 d = \gamma_p \, \ell \, b + (bn) b \gamma_s + \left(\frac{Gb^3}{2}\right) \cos^2 \alpha \qquad (5.43)$$

where, τ is the stress required to move the dislocation through the particle, b, is the Burger's vector, d, the interparticle spacing, ℓ, the mean thickness of the precipitate ($= \frac{\pi r}{\sqrt{6}}$, with r, the particle radius), n, the unit vector normal to the precipitate-matrix interface, γ_s, the precipitate-matrix interfacial energy (including the energy of misfit of the dislocation produced) and α, the angle between the moving dislocation line and its Burger vector. The left hand side of the equation gives the energy needed to move the dislocation through the precipitate. On the right hand side, the first term represents the work done in disordering the precipitate, the second term gives the energy for producing the additional precipitate-matrix interface area (and predicts that the resistance to dislocation motion is dependent upon the orientation of the precipitate) and the last term represents the energy for the dipole produced as the dislocation moves through a distance b (which is the effect due to the orientation of the dislocation in the matrix with respect to its Burger's vector). Thus, the work done in forcing the dislocations through the precipitates (which governs the final strength of the alloy) is related to the coherency stresses, internal ordering of the precipitate and interface effects. As the precipitate particles decrease in size, the internal structure and the nature of the interface are changed (with respect to the matrix) and the work done in cutting the particles is decreased, leading to lowering of strength. Also, the strains that can be accommodated at the particle-matrix interface are progressively reduced with decreasing particle size (and decreasing volume fraction of the precipitates), leading to lowered ductility, with increasing reaustenitization times. Toughness consistently varied as an inverse function of strength except in the initial region, where it decreased with increasing reaustenitization time, as did the strength. This is because, for strain-controlled fracture, where void size (which depends on interparticle distance and particle size) governs the fracture toughness (see Sections 5.1.2 and 5.1.3), up to the point where total dissolution of the finest sized carbides occurs, the interparticle distance does not change appreciably. However, the void size itself is reduced with decreasing carbide size, lowering the toughness in this range.

Case•3: When the intermediate tempering temperature was 650°C, strength initially decreased and then increased to a maximum value corresponding to completely homogenized solid solution, with increasing reaustenitization times. This clearly indicates that these precipitates can be classified under the coherent or semi-coherent group, corresponding to particles that are either sheared through by dislocations or which allow Orowan looping or both. Strength was initially at a high value, corresponding to the critical size and dispersion of the precipitates. With initial increase in reaustentization time, strength decreased because the size is decreased (and the particles behave like coherent, deformable precipitates). Ductility and fracture toughness also decreased in this range as explained earlier for Case 2 precipitates. However, subsequently, strength again increased, because of two reasons. During the reaustenitization process itself, the movement of dislocations become turbulent, since, interface dislocations are left behind at the particles, or in the case of slightly oversized precipitates, dislocation loops are left around the precipitates, due to bowing out. This produces a high density of dislocations which resist the passage of further slip, thereby forcing the dislocation to bow out between particles and not shear through them. This corresponds to the situation explained in Case 1 and, hence, size reduction results in strength increment. However, a second, more probable reason is the depression of M_s temperature with dissolution of carbides, during the reaustenitization step, making twinned plate martensite the favored substructure (for increasingly greater dissolution of carbides). As explained in Section 5.1.1., the strength loss due to decreased dislocation density by changing from dislocated lath to twinned plate martensite is not compensated for by strength gain associated with twins in the initial stages, due to a decrease in the number of available deformation systems, as postulated by Kelly and Nutting [113]. However, with a greater reduction in the volume fraction of carbides at higher reaustenitization times, the amount of twinned martensite is substantial and the gain in strength far exceeds the loss from the marginal reduction in the dislocation density. Consequently, in this higher range, toughness decreased with increasing reaustenitization time and ductility increased due to the associated reduction in particle size. The final values corresponded approximately to the values of the conventionally heat treated structure, indicating complete dissolution of carbides.

5.2. Stress Corrosion Cracking Properties

5.2.1. Threshold Stress Intensity. The threshold stress intensity is affected by the strength level, substructural effects, prior austenite grain size, composition, type of environment, solution pH, etc. In all cases, bulk composition of the steel was the same (but not the grain boundary composition) and the type of environment and solution pH were all maintained same. The effect of the other parameters upon K_{Iscc} will now be discussed.

The dominant parameter in defining the susceptibility of high strength steels to stress corrosion cracking is the strength level. Several investigators [36,211-213], have studied the effect of strength level upon K_{Iscc} of high strength steels and have reported a decreasing trend in K_{Iscc} with increasing strength, up to strength levels of about 1515 MNm^{-2} (Figure 5.5). This has been related to the increasing hydrogen pick-up by the steel ahead of the crack tip due to the diffusion gradient set up under the action of the hydrostatic stress. The concentration gradient of hydrogen ahead of the crack tip is directly related to the plastic stress field and from Hill's slip line field equation for plane strain conditions [214]:

$$\left\{\begin{aligned} \sigma_x &= \ell n\ [1 + (x/\rho)] \\ \sigma_y &= \sigma_{ys} + \ell n\ [1 + (x/\rho)] \\ \sigma_z &= \frac{\sigma_{ys}}{2} + \ell n\ [1 + (x/\rho)] \end{aligned}\right\} \qquad (5.44)$$

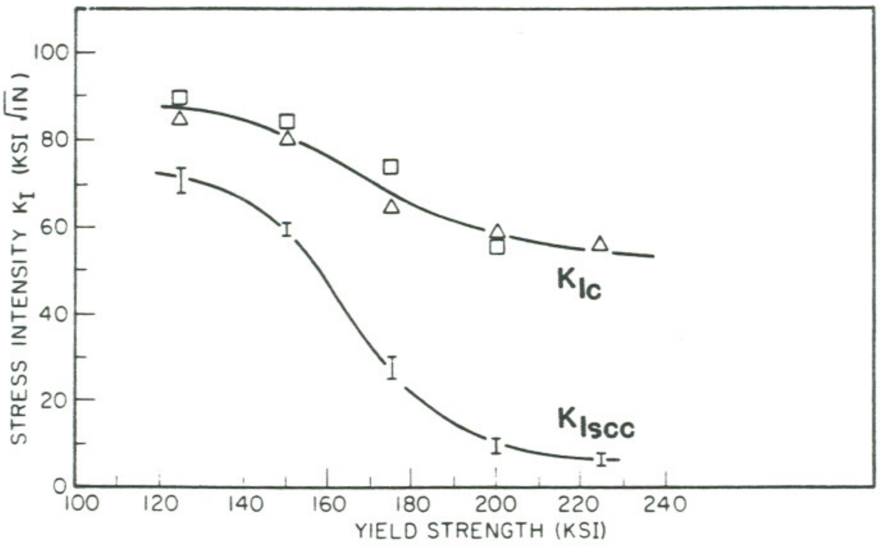

Figure 5-5: VARIATION OF K_{Ic} AND K_{Iscc} WITH YIELD STRENGTH [36].

where, x is the distance ahead of the crack tip, ρ is the root radius, σ_{ys} is the yield strength, and σ_x, σ_y and σ_z are normal stresses in the x, y and z direction respectively. If p is the stress tensor normal to the crack tip which constitutes the hydrostatic tension,

$$p = (\sigma_x + \sigma_y + \sigma_z)/3 \qquad (5.45)$$

Substituting for σ_x, σ_y and σ_z from Equation (5.44),

$$p = \left(\frac{\sigma_{ys}}{2}\right) + \ell n \; [1 + \left(\frac{x}{\rho}\right)] \; , \qquad (5.46)$$

giving,

$$\frac{dp}{dx} = \left[\frac{\sigma_{ys}}{\rho + x}\right] \qquad (5.47)$$

Thus, as the yield strength is increased, the concentration gradient is increased and, hence, more hydrogen pick-up will occur ahead of the crack tip. However, beyond a certain level, no additional pick-up occurs due to strength increment and this prompted some investigators to predict an exponential relationship of K_{Iscc} with strength [42,215]. Gerberich and Chen [212] derived a theoretical relationship between these two parameters as follows:

$$K_{Iscc} = \frac{RT}{\alpha V_H} \; \ell n \; \left(\frac{C_{cr}}{C_o}\right) - \frac{\sigma_{ys}}{2\alpha} \qquad (5.48)$$

with,

$$\frac{C_{cr}}{C_o} = \frac{\beta}{\sigma_{ys}} \qquad (5.49)$$

where, T is the absolute temperature, V_H, the partial molar volume of hydrogen, R, the gas constant, α, a constant ($= 50.8 \sqrt{\text{mm}}$), β a constant dependent upon the material and environment (= 3169 MNm^{-2} for 300M steel and 3.5% NaCl solution), C_{cr}, the concentration of hydrogen in the vicinity of the crack required to embrittle the steel (the critical concentration), C_o, the equilibrium concentration of hydrogen in the material and σ_{ys}, the yield strength. The above equation predicts a greater variation in K_{Iscc} at lower values of yield strength and vice versa. In the present investigation, the strength of the steel for the various heat treatments studied varied between 1495 MNm^{-2} and 1729 MNm^{-2}. In this range, consistent with the above arguments, K_{Iscc} should not be affected by strength. Experimental results obtained in this investigation revealed a higher K_{Iscc} for the modified conventional heat treatment (with the highest yield strength) and no particular pattern with strength for the other heat treatments. Thus, the variations in strength did not affect the threshold values.

With respect to the martensite substructure, only limited information is available. Wang and Staehle [108] reported a difference in crack growth rates of quenched and tempered martensite and lower bainite in a 0.4C1.8Ni steel, possessing the same yield strength and attributed this effect to twins in martensite. Boniszewski et al. [216,217] showed that in 1C9Ni steels, where it is possible to have both lath and twinned martensites, twinned martensite is always more severely embrittled. Watkinson et al. [218] also reported similar results. Twinned martensite, favored at lower transformation temperatures, leads to higher internal stresses [113]. Twinned martensite is indicative of an enhanced temperature dependence of the flow stress in both martensite and austenite [219]. Also, the dislocation density of twinned martensite is much lower than that of the lath martensite [220] and the presence of closely spaced twin boundaries effectively inhibits dislocation movement [221]. Twin boundaries provide neither many additional preferred sites for hydrogen, nor a possible short circuit diffusion path. Combined with high internal stresses and low dislocation mobility, the overall tendency for embrittlement will be high [222]. Conventional heat treatment resulted in a high twin density, followed by step and high temperature heat treatments, with modified conventional heat treatment resulting in only few twins. While K_{Iscc} also increased in the same order, it may not have been entirely due to this effect, since the influence at best may be only marginal [47].

All heat treatments, except the modified conventional heat treatment, produced the same carbides. Cementite occurred predominantly, with epsilon carbide present only in large laths. The carbide type could affect stress corrosion cracking susceptibility [27,100,224]. However, Ritchie et al. [27] and Carter [29] did not observe any change in K_{Iscc} due to a change in carbide type (epsilon carbide vs. cementite) in their study of high strength steels. The important factor in determining whether the carbide is an effective trap for hydrogen is its coherency with the lattice. Thompson [225] showed that the interaction energy between hydrogen atoms and a potential trap is determined by its coherency, with lower energies (0.1-0.3 eV) existing for coherent precipitates (reversible traps) and higher energies (0.35-1 eV), for incoherent, as well as semicoherent precipitates (irreversible traps). The metal carbides formed during intermediate tempering of modified conventional heat treatment were semi-coherent (Section 5.1.4) and cementite is also incoherent. Since the volume fraction of epsilon carbide was constant and small (the coherent precipitate), and the total volume fraction of the carbides was almost the same for all the heat treatments, the stress corrosion properties should not be affected by the carbide types for any of these heat treatments.

The diffusivity of hydrogen is an order of magnitude lower in the fcc structure of austenite than in the bct structure of martensite and the solubility of hydrogen is also higher in austenite [226,227]. These factors should combine to reduce the diffusion of hydrogen, as the amount of retained austenite increases and thus improve the stress corrosion cracking resistance. The amount of retained austenite transformed to martensite during loading at low stress intensities is small, since the plastic zone size (r_p) ahead of the crack tip is small compared to the grain size (d) and the distance to the nearest triple point, since

$$r_p = \frac{1}{6\pi}\left(\frac{K_I}{\sigma_{ys}}\right)^2 \tag{5.50}$$

where K_I is the applied stress intensity and σ_{ys}, the yield strength. For instance, at $K_I = 16.5$ MNm$^{-3/2}$, r_p is roughly 5 μm and, hence, over twice this distance ($2r_p$), the stress would exceed σ_{ys}, making retained austenite mechanically unstable in this region. Retained austenite transformation ahead of the crack tip could liberate dissolved hydrogen near the crack tip, which would be detrimental for stress corrosion cracking resistance. However, this is significant only for the fine grained structures. For structures with coarser grains, this distance is only a small fraction of the grain size and, hence, there could be an improvement in K_{Iscc} with an increase in the retained austenite amounts. For the high temperature and step heat treatments, this was experimentally verified. For the conventional heat treatment, K_{Iscc} was lower and, hence, the transformation of austenite ahead of the crack tip could be significant. For the modified conventional heat treatment, this loss was offset by other factors, to be discussed subsequently.

Prior austenite grain size is also very important in determining the K_{Iscc} values, since the fractography studies suggest that the predominant failure mode was intergranular for all heat treatments (except the modified conventional heat treatment, where a greater amount of transgranular failure resulted). While McDarmaid [17] and Proctor and Paxton [26] did not observe a grain size effect of K_{Iscc}, Carter [29], Lessar and Gerberich [32] and Dilip Kumar [33] all observed an increase in K_{Iscc} with an increase in the prior austenite grain size. In this study, except for the modified conventional heat treatment, increased K_{Iscc} occurred with increasing prior austenite grain size. The predominantly intergranular failure mode obtained suggests that the grain boundaries (which are already weakened due to the presence of segregated elements) are the sites where the critical concentration of hydrogen necessary for embrittlement is achieved first. The pressure-expansion theory of Zapffe and Sims [229], developed further by others [230-233], considers that very large hydrogen pressures generated in internal microcracks and voids force their expansion either by plastic deformation or cleavage, leading to coalescence of the microcracks or microvoids.

The observed cracking of high strength steels by gaseous hydrogen at pressures of about 10^8 MNm^{-2} [234] and at about 1.3 x 10^6 MNm^{-2} [235] cannot be explained by this thermodynamically motivated generation of large internal pressures, because no equilibrium hydrogen activity exists between the gas phase and the metal lattice, such that internal hydrogen pressures, sufficient for lattice bond decohesion, can exist within the steel. The decohesion theory of Oriani [236,237] considers that at any stress state, a value of hydrogen pressure exists above which it is possible to have hydrogen assisted cracking. Once this critical concentration is achieved, the maximum cohesive force between the iron atoms at the crack tip is decreased and the crack advances, atom by atom. The discontinuous and jerky crack propagation noted in actual crack measurement, fractography and acoustic emission studies in this investigation, as well as by other investigators [32,238] is contradictory to this postulate. Furthermore, it assumes decohesion to occur within atomic distances of the crack tip surface, whereas, in many steels, decohesion occurs deep within the plastic enclave. Petch and Stables [282,286] assume that the surface free energy of an atomically clean metal is lowered by adsorption of hydrogen and, thus, the fracture stress is lowered. It may be argued that the idea that adsorption lowers the energy required to create new surfaces is not necessarily linked to any one mechanism for the generation of new crack surface and, hence, could be applicable to a mechanism, involving the breaking of interatomic bonds and one in which the new surface is created by plastic tearing. Also, for materials with yield strength less than the theoretical cohesive strength of the lattice, the effect of surface energy on the total fracture energy is negligible [97]. Again, the lowering of surface energy by gas adsorption, implies that a higher heat of adsorption for the gas species will result in a greater reduction of metal surface energy. However, oxygen is known to adsorb on iron more strongly than iron [283] and yet halts cracking in gaseous environments [234,284,285]. Other decohesion models [239-242] are based on the accumulation of hydrogen followed by a secondary crack nucleation at a region of maximum triaxial state of stress and subsequent joining of the main and secondary cracks. These models do not explain how a microcrack (and the embrittled region associated with it) at a small distance away from the crack tip can be responsible for intergranular separation, unless the entire grain boundary is also weakened due to hydrogen transport, as proposed by Richards et al. [243]. Also these theories utilize a stress criterion, postulating that dissolved hydrogen in iron at sufficiently large concentrations decrease the maximum cohesive force between the iron atoms. Emphasis is thus on the shape of the cohesive force-distance curve, because hydrogen lowers the maximum force along this curve. That the area under this curve is smaller when iron is in equilibrium with hydrogen, than in the absence of hydrogen, is a thermodynamically necessary consequence of the lowering of the surface free energy by hydrogen but not a sufficient condition. However, the decohesion theories stated above could be modified to explain the grain size effect of K_{Iscc} as follows.

Rice [168,244] has calculated the location of maximum triaxial stress ahead of a sharp crack approximately as $2\delta_t$ (where δ_t is the crack tip opening displacement) from the crack tip. This distance can be derived from the relationship:

$$\delta_t = \frac{0.5\ K_I{}^2}{E\ \sigma_{ys}} \tag{5.51}$$

where, K_I is the applied stress intensity, E, the elastic modulus and σ_{ys}, the yield strength. This relationship shows that this distance is independent of grain size at a given stress intensity. The location of maximum triaxial stress governs the region of accumulation of hydrogen, but unlike Troiano's postulation [239] does not coincide with the nucleation site of the secondary crack ahead of the main crack, because there is a considerable distance beyond the point of maximum triaxiality, where the actual stress exceeds σ_{ys}, the yield stress (Figure 5.6). Within this distance, depending upon the value of the stress, the hydrogen concentration will vary with position. However, this region is weakened by the accumulation of hydrogen by the stress gradient. If, for intergranular failure, at least a significant portion of the prior austenite grain boundary is assumed to be weakened by the diffusion of hydrogen, then this condition would be satisfied first for a smaller grained structure (at a given stress intensity). For coarser grained structures, the stress intensity has to be increased in order to weaken the prior austenite grain boundaries to the same extent as for the finer grained structures (in relation to the actual grain size). This explains why when the fracture mode is intergranular, K_{Iscc} is higher for structures possessing coarser grains. However, the modified conventional heat treatment, exhibited a significant amount of transgranular

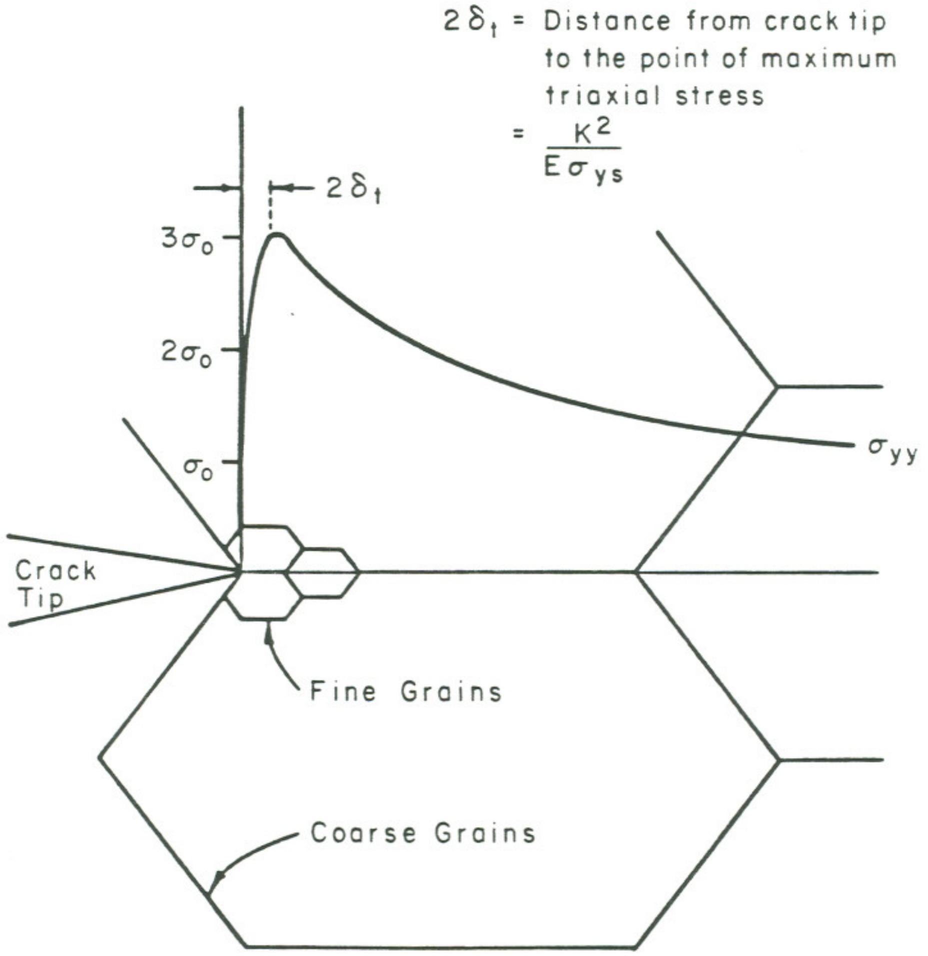

Figure 5-6: STRESS DISTRIBUTION AHEAD OF A SHARP CRACK, IN RELATION TO THE GRAIN SIZE.

failure, despite the fine grain size. K_{Iscc} was highest in this case and this requires further explanation.

Segregation of impurity elements including P and S, to prior austenite grain boundaries has an additive effect upon stress corrosion cracking [245], by reducing intergranular cohesion. Yoshino and McMahon [246] suggested that hydrogen is trapped at the grain boundaries due to the presence of segregated impurity elements and this interaction of impurity and hydrogen atoms prevents hydrogen diffusion into the bulk. Banerji et al. [238], through Auger electron spectroscopy of fractured HY130 impact specimens, detected that temper embrittled specimens exhibited segregation of Si, P, N and Sn upon the surface of the grains and that such specimens consequently failed intergranularly at low stress intensities under about 2×10^8 MNm^{-2} of gaseous hydrogen. Their work with 4340 steel also showed that segregation of P and N to the prior austenite grain boundaries after one step temper embrittlement (OSTE) at 260°C is pronounced. Because commercial 4340 steel subjected to about 10^8 MNm^{-2} of gaseous hydrogen always (independent of OSTE) cracked intergranularly and high purity NiCrMoC alloy of the same basic composition as 4340 steel cracked by cleavage and rupture under the action of hydrogen and then only at much higher stress intensities (the actual improvement in the threshold value was about five times) and did not exhibit OSTE, the authors [238] concluded that segregation of P (and N, wherever applicable) is responsible for the susceptibility of 4340 steel to gaseous hydrogen. Dautovich and Floreen [213] also noted an improvement of K_{Iscc} with a reduction of S content of the steel and attributed this to the segregation of S to the prior austenite grain boundaries and its ability to increase hydrogen intake. The driving force for this segregation of impurity elements to the grain boundaries can be either thermodynamic in nature (Gibbs adsorption) or from non-equilibrium or kinetic causes. For Gibbs adsorption, the driving force is a decrease in the total free energy of the system. If an alloying element or an impurity element can decrease the grain boundary energy, by being adsorbed into or very near the grain boundary, there will be a driving force for segregation. This equilibrium segregation can be expressed by Gibbs adsorption isotherm [247]:

$$\sum_i N_i \, d \, \ell n \, a_i x_i = - \frac{d\gamma}{kT} \qquad (5.52)$$

where, N_i is the number of adsorbed 'i' species atoms/unit area, a_i is the activity coefficient of 'i' species in bulk matrix, x_i is the atom fraction of 'i' species in the bulk matrix, γ is the grain boundary energy and k, the Boltzmann's constant, with T, the absolute temperature.

For non-equilibrium segregation, the driving force is a solute-vacancy interaction mechanism proposed by Aust et al. [248] which considers grain boundaries as sinks for vacancies and other defects. During quenching, the equilibrium concentration of vacancies (corresponding to the higher austenitization temperature) will be drastically reduced, resulting in a supersaturatoin of vacancies. Those vacancies within a diffusion distance of the grain boundaries will be annihilated at such grain boundaries. As these vacancies migrate to the grain boundaries, they will drag along solutes (impurity and alloying elements) whose vacancy-solute binding energy is positive. Effective uphill diffusion of the solute occurs and solute enrichment over the diffusion distance near the boundaries occurs in the form of solute clusters. Since most alloy and impurity elements in iron have a high positive binding energy with vacancies in iron, preferential grain boundary enrichment of these elements occurs.

From the foregoing arguments, it is clear that segregation has an important effect on the stress corrosion cracking susceptibility of high strength steels. As to the variation of segregation with austenitization temperature, Wood [8] suggested that higher austenitization temperatures decrease segregation and partitioning of impurity and alloying elements, thus decreasing lean zones which tend to transform earlier to different structures, during cooling/quenching, than the more highly alloyed zone. Through selective etching techniques, Ogura et al. [66] demonstrated decreased segregation of impurity elements at prior austenite grain boundaries and twin boundaries, with increasing austenitization temperature. Ritchie et al. [109] postulated that austenitizing above 1100°C, followed by fast quenching, prevents segregation of impurities to grain boundaries and Clark et al. [2] suggested that the thermodynamic driving force for segregation is too small above 1100°C to drive the embrittling species to the grain boundaries but below this temperature, substantial segregation to the grain boundaries takes place. While these were postulates, Briant et al. [249], through Auger spectroscopy reported that the P segregation in steels containing 0.06% and 0.03% P respectively, decreased with increasing austenitization temperature and with decreasing P content of the steel. The steel used in this investigation contained about 0.01% P. This suggests that segregation differences among the various heat treatments may not be significant. However, if segregation is considered in terms of unit grain boundary area, it would increase for high temperature heat treatment compared to the conventional heat treatment. This increase would be even higher for the step heat treatment. On the contrary, for the modified conventional heat treatment, the dilution of segregation at the grain boundaries due to the increased grain boundary area would be maximum, resulting in a very low concentration of the embrittling elements per unit grain boundary area.

It is proposed that a certain critical concentration of segregation per unit area of the grain boundary exists above which predominantly intergranular fracture occurs under stress corrosion cracking conditions and below which mixed failure or transgranular failure occurs. For conventional, high temperature and step heat treatments, failure was predominantly intergranular, indicating that this critical concentration is exceeded. The lower K_{Iscc} for conventional heat treatment is due to the domination of grain size effect, viz., the attainment of the critical embrittled zone, extending over a significant portion of the grain boundary area (and which is related to the maximum triaxial stress ahead of the crack tip) at a lower applied stress intensity level than for the coarser grained structures. The almost identical values of K_{Iscc} for high temperature and step heat treatments indicate that either segregation differences between these two heat treatments are minimal (when measured over unit grain boundary area) or what is more likely, that once the critical concentration of segregation for intergranular separation is exceeded, further increases in the concentration contributes little to the lowering of K_{Iscc}. The high value of K_{Iscc} for the modified conventional heat treatment, coupled with significant amounts of transgranular failure (even at low stress intensitites), suggests a different mechanism. The reduction of surface energy by hydrogen to the level for crack growth occurs first at the grain boundary junctions or triple points only when these sites are already weakened due to the presence of critical amounts of embrittling species. Otherwise, the surface energy of the lattice as a whole has to be decreased and this can happen only at higher stress intensities (at higher hydrogen concentrations), as for the modified conventional heat treatment. Since the grain size for this heat treatment was considerably smaller than for any other heat treatment, for a similar amount of segregation (as in the case of conventional heat treatment), it is reasonable to assume that the critical concentration at the grain boundaries is not attained. The transgranular nature of failure supports this postulation.

Another factor is the influence of the fracture toughness (K_{Ic}) in the absence of hydrogen. Brown [36] has shown a decrease in K_{Ic} and a corresponding one-to-one decreasing trend of K_{Iscc} (Figure 5-5), with increasing strength level for AISI 4340 steel. Sandoz [250] has studied the fracture toughness and stress corrosion cracking susceptibility of high strength steels and his work also shows a direct relationship between K_{Iscc} and K_{Ic}. Other investigators have also observed this relationship [29,211,251] between K_{Ic} and K_{Iscc}. Since K_{Ic} is a measure of the fracture energy, a higher K_{Ic} implies a higher fracture energy and consequently, in corrosive environments, a higher energy for decohesion (or to the level necessary for reducing the fracture energy to the critical level for crack initiation). The results of this investigation agree well with this prediction. Both K_{Ic} and K_{Iscc} were highest for modified conventional heat treatment, followed by high temperature, step and conventional heat treatments.

5.2.2. Crack Growth Rates. All the heat treatments exhibited limited Stages I and III and, hence, the discussion is confined to Stage II region only (the average crack velocity in this region being defined at a point midway between K_{Ic} and K_{Iscc}).

All factors that affect threshold intensity affect the crack growth rates also. Strength variations among these heat treatments did not affect the crack growth rates. As explained in Section 5.2.1, the strength effect is not significant above about 1515 MNm^{-2} for these high strength steels. Lessar and Gerberich [32] noted an increase in the crack velocities with a decrease in grain size (that is, increasing strength). However, the yield strength changes were in the ranges of 1240 MNm^{-2} to 1481 MNm^{-2}, a range where the strength effect is predominant. Proctor and Paxton [26] and Dilip Kumar [33] in their study of 4340 steel reported either negligible variation or a slight decrease in the crack growth rates with decreasing grain size (increasing yield strength). The yield strength variations in their study was above 1515 MNm^{-2}. These observations are consistent with the above postulation.

With respect to substructure, prior discussion of the effect of twinning and carbides (Section 5.2.1) are applicable for the interpretation of crack velocities also. The effect of twinning, while marginal, should enhance crack growth rates [108,216,217,222]. However, this was not observed in the experimental results, due to other effects, which will be discussed next. Likewise, since the volume fraction of carbides was the same for all heat treatments, and the total volume fraction of the carbides also almost the same, the effect of carbides upon crack growth rates was negligible.

While it has been proposed that retained austenite, due to its higher solubility for hydrogen (and lower diffusion rate for hydrogen through austenite than in martensite) can improve stress corrosion resistance [32,47,226,227], its stability has to be considered. For instance, Lessar and Gerberich [32] attributed the decrease in crack velocity of 4340 steel with increasing austenitization temperature to the presence of higher retained austenite resulting at higher austenitization temperatures. However, the tempering temperature of 300°C utilized by them would transform the retained austenite [252,253]. Hence, the beneficial effect of retained austenite is questionable. Ritchie et al. [27] observed no changes in the crack growth rates of 300M steel in which the amount of retained austenite was varied between 2% and 12% at similar strength levels. This investigation shows that while retained austenite may influence K_{Iscc} (higher K_{Iscc} with more austenite), it did not affect the Stage II crack growth rates. Other investigators have shown that in the plastic zone ahead of the crack tip, as long as the stresses exceed the yield strength, all austenite within this zone would transform [20,47]. The size of this zone within which retained austenite would transform can be computed from Equation (5.50), Section 5.2.1. At intermediate stress intensities, corresponding to Stage II region, the size of the zone becomes significant in relation to the grain size. For example, at $K_I = 33\ MNm^{-3/2}$, $r_p = 21\ \mu m$ and hence, over a region extending to at least 42 μm from the crack tip, retained austenite would transform. This transformation of austenite to either untempered martensite or lower bainite may actually increase the susceptibility for stress corrosion cracking. Also, all dissolved hydrogen in this austenite would now be liberated into a matrix whose solubility for hydrogen is much lesser, and this would provide additional hydrogen for stress corrosion cracking, in the vicinity of the crack tip. Thus, retained austenite may be detrimental for stress corrosion cracking resistance at stress intensity levels corresponding to or exceeding Stage II region, where it is mechanically unstable. The results of conventional, high temperature and step heat treatments corroborate this hypothesis. However, the modified conventional heat treatment, possessing more retained austenite than the corresponding non-modified conventional heat treatment, still exhibited a lower crack growth rate in this region. The impurity content due to segregation at grain boundaries is much lesser for this heat treatment, requiring a greater amount of hydrogen to cause cracking and the hydrogen released from the transformed austenite region would still not be sufficient to meet the critical level for embrittlement. In this case, the accumulation of hydrogen to this level depends upon diffusion from regions where stresses are still low enough for retained austenite to be mechanically stable. This should lower the crack growth rates further. However, this assumption may be questionable because the hydrogen supply is predominantly from the crack tip into a region where retained austenite has already transformed and the amounts diffusing into this region from other regions in the bulk would not be significant. Thus, retained austenite, by itself, cannot account for the observed crack growth rates.

The mechanism proposed earlier (Section 5.2.1) to explain the dependence of K_{Iscc} on the prior austenite grain size cannot be applied for predicting crack growth rates. This is because, although for coarse grained structures, critical hydrogen concentrations ahead of the main crack occur only at higher stress intensities than for finer grained structures, this effect affects only K_{Iscc}. At higher stress intensities, corresponding to Stage II and beyond, sufficient hydrogen is attained for coarse as well as for fine grains, and the actual crack growth rate should be independent of the prior austenite grain size. This, however, was not the case in this investigation. This is explained by considering triple points as constraint points, where the advancing crack has to change its direction. For a given traverse, fine grained structures will contain more such constraint points and hence, the crack growth rate will decrease, in agreement with this and other investigations [26,33]. In the modified conventional heat treatment, this effect is even more pronounced, since propagation occurs transgranularly rather than intergranularly and involves additional constraint points (the microstructural feature which controls fracture in this case is the interparticle spacing and hence, the void size).

Segregation and K_{Ic} effects which affect K_{Iscc} does not affect Stage II kinetics. Increasing segregation concentration at grain boundaries decreases the critical amount of hydrogen necessary for decohesion. Likewise, decreasing K_{Ic} also lowers the cohesive stress (Section 5.2.1). However, these determine only the threshold value and at stress intensities exceeding this value, no longer influence the actual crack growth kinetics, since the crack will propagate only after the minimum concentration for hydrogen is exceeded.

In this study, a slight decrease in Stage II growth rates with increasing applied stress intensities was noted. Other investigators [42, 254] have also noted a similar effect. Dunegan and Tetelman [254] found that in Stage II, island cracks form in front of the main crack and grow both ahead and back toward the main crack front. If this were true, the creation of such cracks and their growth, in addition to the growth of the main crack would need higher energy, thus slowing down the overall growth rate. Often in this study, as well as in other investigations [30,109], secondary cracking and crack branching were observed in Stage II. Since the creation of these additional cracks and the propagation of such cracks also require additional energy, there would be a retardation of the cracking velocity, as reflected in the stress corrosion cracking curves. In addition to this phenomenon of slightly decreasing crack velocity with increasing applied stress intensity, the actual crack growth curve, in Stage II, exhibited several peaks and valleys (indicative of intermittent crack growth) whose amplitude decreased with increasing applied stress intensity. Fractography and acoustic emission studies also confirmed the occurrence of such slow and burst (fast) regions of growth. Since the growth rates were computed for increases in crack lengths of 5 μm, which was smaller than the finest grain size achieved in any heat treatment, such intermittent crack growth must have occurred within a grain itself. Steps on many intergranular facets, indicating crack arrest, confirm this. Non-uniform cohesive strength and non-uniform plastic behavior due to internal flaws and interfaces and variations in solute and dislocation disturbances, are the reasons for the intermittent crack growth. Further, microcracks, voids, second phase particles and grain boundaries act as stress raisers, complicating the simple pattern of stress distribution. Thus, the actual crack propagation is jerky and intermittent, giving rise to the peaks and valleys. Towards higher stress intensities, the effect of such inhomogeneities will in part be overcome by the higher stresses existing ahead of the crack tip, establishing a more uniform growth rate.

5.3. Acoustic Emission Properties

Acoustic emission (A.E.) analysis has been widely applied to study stress corrosion cracking behavior [33,40,254-267]. However, no consistent analysis techniques exist and most proposed relationships are applicable only for specific cases. In this study, an independent method for analyzing A.E. results is proposed.

Several investigators [268-270] have observed that an A.E. source, operating once and isolated in time from other acoustic emissions, excites the transducer in a ring-down mode (Figure 5-7), and the resulting signal follows the form:

$$V = V_o e^{-\beta t} \sin \lambda t \tag{5.53}$$

where, V is the instantaneous voltage at time t, V_o is the peak (initial) voltage, β is the exponential decay time constant and λ is the angular frequency. Also, the number of such ring-down counts generated from a single source could be given by the relationship:

$$n = \frac{\lambda}{2\pi\beta} \ \ell n \left(\frac{V_o}{V_t} \right) \tag{5.54}$$

where, V_o is now the amplitude (initial) of the damped sinusoid and V_t, the threshold voltage at which the counter is triggered. Since λ/β is a constant for a given transducer, Equation (5.54) could be rewritten as:

$$n = \varphi_1 \ \ell n \left(\frac{V_o}{V_t} \right) \tag{5.55}$$

where, φ_1 is a constant ($= \lambda/2\pi\beta$). β might decrease at higher stress intensities (corresponding to Stage III), if the A.E. counter is not able to resolve rapidly occurring events, thus inflating the counts per event data. β may also decrease when the A.E. event lasts longer than the natural period of the transducer. However, since Stage III was limited to very short time intervals and since the grain size of even the coarsest grained structure was such that the A.E. event generated was

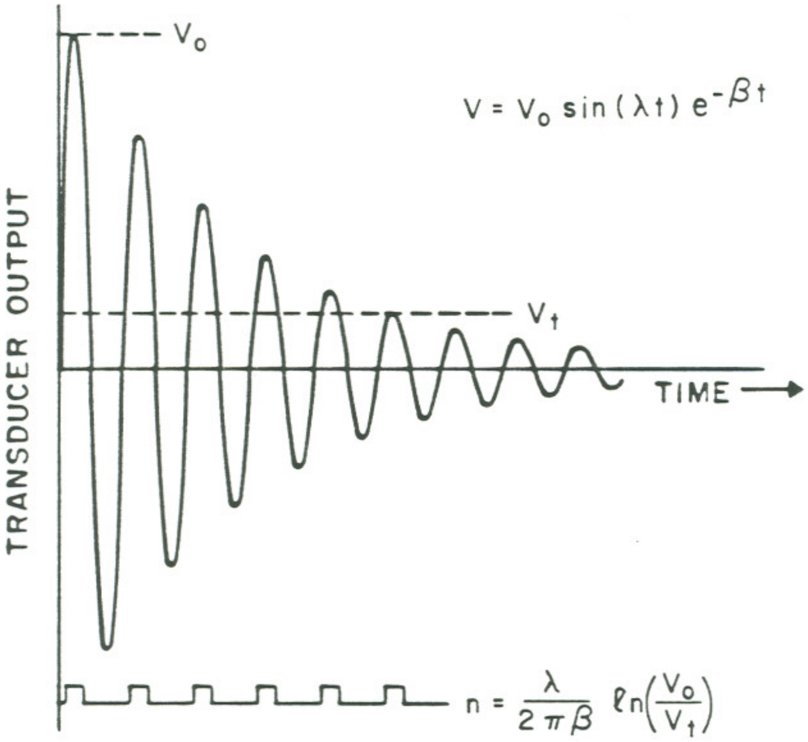

Figure 5-7: TYPICAL ACOUSTIC EMISSION WAVEFORM.

restricted to well below the natural period of the transducer, β is assumed to be constant. Since 'n' represents the number of counts generated by a single event whose peak amplitude is given by V_o, Equation (5.55) can be rewritten as:

$$n \left(= \frac{dc}{de}\right)$$

$$= \varphi_1 \; \ell n\left(\frac{V_o}{V_t}\right) \tag{5.56}$$

where, dc/de represents the ratio of the cumulative number of A.E. counts due to all generated events, to the cumulative number of events. A moving crack, as a first order approximation, releases energy W, proportional to the square of the crack velocity as:

$$W = \varphi_2 \left(\frac{da}{dt}\right)^2 \tag{5.57}$$

where, da/dt is the crack extension per unit time and φ_2 is a material constant. V_o, the peak amplitude is also related to W by the relationship:

$$W = \varphi_3 \; V_o^{\,2} \tag{5.58}$$

where, φ_3 is the constant of proportionality. Comparing Equations (5.57) and (5.58)

$$V_o = \varphi_4\left(\frac{da}{dt}\right) \tag{5.59}$$

where,

$$\varphi_4 = (\varphi_2/\varphi_3)^{\frac{1}{2}} \tag{5.60}$$

Substituting for V_o in Equation (5.56), we obtain,

$$\frac{dc}{de} = \varphi_1 \left(\ln \frac{da}{dt} - \ln V_t + \ln \varphi_4\right) \tag{5.61}$$

Since V_t, the threshold voltage was constant for all heat treatments, the second and third terms of Equation (5.61) are constants and dc/de should be directly proportional to $\ln$ (da/dt) and a plot of either dc/de vs. K_I or $\ln$ (da/dt) vs. K_I where K_I is the applied stress intensity, should yield similar results. This was experimentally verified in this investigation, wherein the counts/event curve followed exactly the same trend as the crack velocity curve, as a function of the applied stress intensity. Also, dc/de decreased with a decrease in the grain size, d. From linear elastic fracture mechanics, the energy released for a crack extension of da is given by [271]:

$$W = \frac{\sigma^2}{E} \delta a \; da(1 - \nu^2) \tag{5.62}$$

where δa represents the height of the crack, ν is the Poisson's ratio and E is the modulus of elasticity. The term ($\delta a da$) represents the new area created due to crack extension and will be equal to πd^2 or $\frac{\pi d^2}{4}$ for intergranular or transgranular failure respectively, d being the grain size for intergranular fracture (or the void size for fracture through microvoid coalescence). Hence, Equation (5.62) can be written as:

$$W = \eta_1 \sigma^2 d^2 \tag{5.63}$$

where,

$$\eta_1 = \frac{\pi(1 - \nu^2)}{E} \tag{5.64}$$

for intergranular failure ($= \frac{\pi(1 - \nu^2)}{4E}$, for transgranular failure). Comparing Equations (5.58) and (5.63),

$$V_o = \eta_2(\sigma d) \tag{5.65}$$

where,

$$\eta_2 = \left(\frac{\eta_1}{\varphi_3}\right)^{\frac{1}{2}} \tag{5.66}$$

Substitution this value of V_o in Equation (5.56):

$$\frac{dc}{de} = \varphi_1(\ell n\ \sigma + \ell n\ d - \ell n\ V_t + \ell n\ \eta_2) \tag{5.67}$$

This equation predicts that, when the grain size remains constant (for a given heat treatment), dc/de will vary directly as $\ell n\ \sigma$, and consequently as $\ell n\ K_I$ since [271]

$$K_I = \sigma\sqrt{\pi a} \tag{5.68}$$

Also, for a given applied stress intensity, dc/de will vary directly as $\ell n(d)$. These predictions were verified experimentally.

A consequence of Equations (5.67) and (5.61) is that at a given applied stress intensity, the crack growth rate should be maximum for the coarsest grained structures and least for the finest grain sized structures, since:

$$\frac{dc}{de} \propto \ell n\ d$$

$$\propto \ell n\ (da/dt),$$

giving,

$$\ell n\ d \propto \ell n\ (da/dt) \tag{5.69}$$

It was pointed out that conflicting claims were made [26,32,33] as to the relationship between crack velocity and grain size (Section 5.2.2). Through A.E. techniques, this ambiguity could be resolved as shown theoretically above (and as verified experimentally in this investigation).

The cumulative counts (and events) and counts rate with respect to both time and crack extension (and events rate) exhibited a nearly exponential increase with time, crack length and applied stress intensity. This is due to two reasons. A.E. generation within the material depends upon the actual stress state, which is related to the applied stress intensity, K_I . Hence, with increasing K_I, the A.E. activity should increase. Secondly, the amplitude V_o of the acoustic signal depends upon the grain size d [Equation (5.65)]. If V_{cr} (= V_t, the threshold voltage) represents the critical amplitude which should be exceeded for detection by the sensor, as K_I increases, the critical grain size which will generate an event with an amplitude equal to or greater than V_{cr} will decrease, according to Equation (5.65). This will result in more grains in the material contributing to detectable A.E. activity. Since, for any heat treatment, the grain size distribution varies in general as a normal or a log-normal distribution [33,272], both distributions involving exponential terms, the A.E. activity should also vary exponentially with respect to the crack length, time or applied stress intensity. Thus finer grained structures give rise to lesser A.E. activity. The above situations are explained in Figure 5-8.

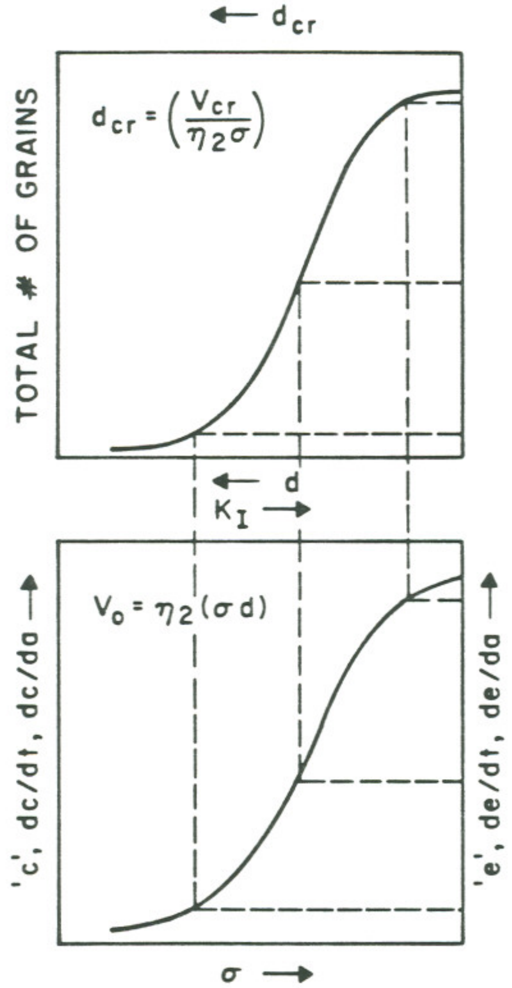

Figure 5-8: RELATIONSHIP BETWEEN ACOUSTIC EMISSION PARAMETERS, APPLIED STRESS INTENSITY AND CRITICAL GRAIN SIZE.

6. CONCLUSIONS

A comprehensive summary is given following each subsection in Section 4. In this section the main conclusions are listed.

6.1. Tensile, Impact and Fracture Toughness Properties

High temperature and step heat treatments improved the plane strain fracture toughness markedly when compared with conventional heat treatment. While high temperature heat treatment resulted in considerably lower ductility and impact properties at similar strength as the conventional heat treatment, step heat treatment resulted in not only decreased ductility and impact properties, but also decreased strength. Cyclic heat treatment improved strength, ductility and impact properties but fracture toughness decreased.

When compared with the corresponding non-modified heat treatments, all the modified heat treatments improved all the properties significantly.

6.2. Stress Corrosion Cracking Properties

High temperature and step heat treatments exhibited almost identical and higher threshold stress intensity values when compared with the conventional heat treatment. The modified conventional heat treatment resulted in the highest threshold stress intensity.

Stage II crack velocities were highest for high temperature and step heat treatments and lowest for modified conventional heat treatment. Conventional heat treatment resulted in an intermediate value. The actual crack growth rate in Stage II region exhibited several sharp peaks and valleys (indicative of intermittent growth), whose amplitude decreased with increasing stress intensity.

6.3. Acoustic Emission Characteristics

The counts per event vs. applied stress intensity curves showed a remarkable similarity to the stress corrosion crack growth rate vs. applied stress intensity curves. The counts per event values were dependent upon the actual crack growth rate and the Stage II value was highest for high temperature and step heat treatments and lowest for modified conventional heat treatment, with conventional heat treatment exhibiting an intermediate value.

The counts and counts rate and the events and events rate (with respect to both time and crack length) increased exponentially with respect to the applied stress intensity. The x-axis intercept coincided with the threshold stress intensity value for the particular heat treatment.

6.4. Microstructure

The prior austenite grain size increased with increasing austenitization temperatures (high temperature and step heat treatments) and decreased with thermal cycling (cyclic and modified heat treatments). The general structure consisted of predominantly lath martensite for high temperature, step and modified heat treatments and predominantly plate martensite for conventional and cyclic heat treatments. Extensive twinning occurred in the case of conventional and cyclic heat treatments, with step, high temperature and modified heat treatments exhibiting increasingly less twinning. All modified heat treatments resulted in increased interlath films of retained austenite than the corresponding non-modified heat treatments. The amount of retained austenite was generally higher for coarser grained structures. All the heat treatments resulted in extensive precipitation of cementite and epsilon carbide. The modified heat treatments, in addition, also resulted in $(Fe,Cr)_3C$, $(Fe,Cr)_7C_3$, $(Fe,Cr)_{23}C_6$, and Mo_2C precipitation. Epsilon carbide precipitation occurred only within large laths along definite growth directions and specific habit planes. Such large laths were identified at the prior austenite grain boundaries.

6.5 Fractography

The fracture initiation zone of tensile, Charpy and K_{Ic} specimens all exhibited predominantly microvoid coalescence mode of failure in the case of all heat treatments. However, all non-modified heat treatments generally revealed a mixed failure mode consisting of intergranular and quasicleavage failure, in addition to microvoid coalescence, when compared with the modified heat treatments, which revealed no such mixed failure. Additionally, the tensile specimens of high temperature and step heat treatments exhibited a high amount of intergranular failure in the initiation region. In the propagation zone, the predominant failure mode was quasicleavage for all heat treatments. Dimple size was consistently finer for finer grained structures and when compared with the corresponding non-modified heat treatments, all the modified heat treatments possessed finer and deeper dimples. Coarse lath boundary cleavage steps, cleavage tongues and tearing in association with tear ridges were all identified in many cases.

In the case of stress corrosion cracking specimens, the predominant failure mode was intergranular at low and intermediate applied stress intensities, with increasing amount of transgranular features at higher stress intensities, the final overload region failing by microvoid coalescence. However, the modified conventional heat treatment exhibited both intergranular and transgranular features even at low stress intensities, with extensive tunnel and slot formation in the transgranular regions at intermediate stress intensities. Secondary cracking, triple points, crack coalescence and associated cleavage steps were all observed.

6.6 Hypotheses

Although the strength of 300M steel is a function of Peierl's stress, solid solution effects, substructural effects (twins vs. dislocations) and work hardening effects, changes in strength for different heat treatments with respect to any of these factors were slight. Strength was a strong function of dispersion strengthening from carbides (and hence, the size, volume fraction, interparticle spacing and nature of carbides) and grain size (inclusive of lath width and packet diameter). Ductility was a function of prior austenite grain size, homogeneity of steel, interparticle spacing, volume fraction, size and nature of carbides. A model based upon the characteristic distance ahead of the crack tip for sharp cracks and a critical fracture stress (or strain) criterion for blunt cracks adequately explained the variation of plane strain fracture toughness and impact toughness of the steel as a function of heat treatment. Impact toughness varied directly with ductility, for the strain-controlled fractures observed in this investigation. However, the plane strain fracture toughness was dependent upon the void size and spacing (and hence, the carbide dispersion), grain size (inclusive of lath width and packet size), amounts of retained austenite (both stable and unstable) and twin density. The behavior of modified heat treatments as a function of intermediate tempering temperature and time was observed to be consistent with a model which takes into account the size, distribution and coherency strains of the carbides.

Threshold stress intensity was independent of the changes in the strength and carbide dispersion for this high strength 300M steel and only slightly dependent upon the substructure. It was a major function of the plane strain fracture toughness, prior austenite grain size and amounts of segregation and retained austenite. A model was proposed to explain the variations of threshold stress intensity with heat treatments, based upon a critical segregation concentration criterion. The crack growth rate was also independent of strength, carbide dispersion, substructure and K_{Ic} and only slightly dependent upon retained austenite amount and segregation. Only the number of constraint points (prior austenite grain size and interparticle spacing) exerted a major influence on the crack growth rates. The relationships between the acoustic emission responses of the steel and crack growth rate, applied stress intensity and prior austenite grain size (or void size) were also explained through a model based on an energy criterion.

REFERENCES

1. V. F. Zackay, E. R. Parker, R. D. Goolsby and W. E. Wood, Nat. Phy. Sci., 236(1972)108.

2. R. A. Clark, R. O. Ritchie and J. F. Knott, Nat. Phy. Sci., 239 (1972)104.

3. W. E. Wood, E. R. Parker and V. F. Zackay, An Investigation of Metallurgical Factors Which Affect the Fracture Toughness of Ultra High Strength Steels, Rep. #LBL-1474, Lawrence Berkeley Laboratory, Univ. of California, Berkeley, CA, May 1973.

4. G. Y. Lai, W. E. Wood, R. A. Clark, V. F. Zackay and E. R. Parker, Metall. Trans., 5A(1974)1663.

5. V. F. Zackay, E. R. Parker and W. E. Wood, The Microstructure and Design of Alloys: Proc. Inst. of Met. and ISI 3rd Int. Conf. on the Strength of Metals and Alloys, Cambridge, England, August 1973, The Met. Soc. (London), 1(1974)175.

6. N.E. Clark and W. G. Ferguson, Metallurgy in Australasia: Proc. 27th Ann. Conf. of Australian Inst. of Met., Christchurch, New Zealand, May 1974, J. S. Smaill (Ed.), 1974, 53.

7. E. R. Parker, V. F. Zackay, G. Y. Lai and R. M. Horn, Untempered Ultra High Strength Steels of High Fracture Toughness, Army Mat. and Mech. Res. Ctr. Rep. #AMMRC CTR 74-33, April 1974 (LBL-2715, Lawrence Berkeley Laboratory, Univ. of California, Berkeley, CA, April 1974.

8. W. E. Wood, Eng. Fr. Mech., 7(1975)219.

9. G. Y. Lai, V. F. Zackay and E. R. Parker, Enhancement of Fracture Toughness by Retained Austenite in 300M Steel, Rep. #4513, Lawrence Berkeley Laboratory, Univ. of California, CA, November 1975.

10. E. R. Parker and V F. Zackay, Eng. Fr. Mech., 7(1975)371.

11. J. L. Youngblood and M. R. Raghavan, Influence of Heat Treatment on Mechanical Properties of 300M, paper presented at AIAA/ASME/SAE 16th Structures, Structural Dynamics and Materials Conf., Denver, CO, May 1975.

12. R. O. Ritchie, B. Francis and W. L. Server, Metall. Trans., 7A (1976)831.

13. D. S. McDarmaid, Effects of High Austenitization Treatments Upon the Plane Strain Fracture Toughness and Other Mechanical Properties of 300M Bar, RAE Tech. Rep. #TR 76104, Royal Aircraft Establishment, Farnborough, Hants, England, 1976.

14. V. F. Zackay and E. R. Parker, Alloy and Microstructural Design, J. K. Tien and G. S. Ansell (Eds.), A.P. (London), 1976, 213.

15. M. F. Carlson, B. V. N. Rao, R. O. Ritchie and G. Thomas, Improvements in Strength and Toughness of Experimental Fe-Cr-C Steels, Rep. #LBL-5111, Lawrence Berkeley Laboratory, Univ. of California, Berkeley, CA, April 1976.

16. J. L. Youngblood and M. R. Raghavan, Metall. Trans., 8A(1977)1439.

17. D. S. McDarmaid, Met. Tech., 5(1978)7.

18. K. H. Khan and W. E. Wood, Metall. Trans., 9A(1978)899.

19. W. E. Wood, Mechanism of Enhanced Toughness in Martensitic Alloys, OGC Tech. Rep. #N00019-77-C-0135, Oregon Graduate Center, Beaverton, OR, February 1978.

20. R. O. Ritchie and R. M. Horn, Metall. Trans., 9A(1978)331.

21. W. G. Ferguson, N. E. Clark and B. R. Watson, Met. Tech. 3(1976)208.

22. D. S. McDarmaid, Effects of Notch Root Radius and High Temperature Austenitizing Treatments Upon the Impact Strength of 300M Steel, RAE Tech. Rep. #TR 79076, Royal Aircraft Establishment, Farnborough, Hants, England, June 1979.

23. K. P. Datta, Effects of Microstructural and Mechanical Testing Variables on the Toughness of Quenched and Tempered 4340 Steel, Ph.D. Thesis, Oregon Graduate Center, Beaverton, OR, September 1979.

24. R. A. Grange, Trans. ASM, 59(1966)26.

25. J. N. Robinson and C. W. Tuck, Eng. Fr. Mech., 4(1972)377.

26. R. P. M. Proctor and H. W. Paxton, Trans. ASM, 62(1969)989.

27. R. O. Ritchie, M. H. C. Cedeno, V. F. Zackay and E. R. Parker, Metall. Trans. 9A(1978)35.

28. M. H. C. Cedeno, The Effect of Silicon on the Environmental Cracking Behavior of a High Strength Steel, Rep. #LBL-6012, Lawrence Berkeley Laboratory, Univ. of California, Berkeley, CA, May 1977.

29. C. S. Carter, Corrosion, 25(1969)423.

30. M. O. Speidel, Proc. Int. Conf. on Hydrogen in Metals, Paris, France, May-June 1972, Paul Bastien (Ed.), Editions Science et Industrie (Paris), 1972, 290.

31. S. Mostovoy, H. R. Smith, E. J. Ripling and R. G. Lingwall, Eng. Fr. Mech., 1(1971)291.

32. J. F. Lessar and W. W. Gerberich, Metall. Trans., 7A(1976)953.

33. D. Dilip Kumar, Effect of Microstructure on Internal and External Hydrogen Embrittlement of an Ultrahigh Strength Steel, Ph.D. Thesis, Oregon Graduate Center, Beaverton, OR, February 1980.

34. E. P. Dahlberg, ARPA Coupling Program on Stress-Corrosion Cracking, NRL Mem. Rep. #1941, Naval Research Laboratory, Washington, D.C., November 1968.

35. R. P. Wei, S. R. Novak and D. P. Williams, Mat. Res. and Std., 12(1972)25.

36. B. F. Brown, NATO Sci. Comm. Res. Eval. Conf. on the Theory of Stress Corrosion Cracking in Alloys, Ericeira, Portugal, March-April 1971, J. C. Scully (Ed.), NATO Scientific Affairs Div. (Brussels), 1971, 186.

37. M. O. Speidel, ibid., 289.

38. J. A. Feeney and M. J. Blackburn, ibid., 355.

39. M. J. Blackburn, J. A. Feeney and T. R. Beck, Adv. in Corr. Sci. and Tech., Plenum Press, (N.Y.), 3(1973)67.

40. A Symp. on Stress Corrosion - New Approaches: 78th Ann. Meet. of ASTM, Montreal, Canada, June 1975, ASTM STP 610, H. L. Craig, Jr. (Ed.), ASTM (Philadelphia), 1976.

41. M. O. Speidel, Metall. Trans., 6A(1975)631.

42. W. W. Gerberich, Y. T. Chen and C. St. John, Metall. Trans., 6A(1975)1485.

43. C. S. Carter, Corrosion, 27(1971)471.

44. W. G. Reuter and C. E. Hartbower, Eng. Fr. Mech., 3(1971)493.

45. H. P. van Leeuwen, Corrosion, 31(1975)42.

46. R. A. Grange and E. R. Shackelford, Method of Producing Ultrafine-Grained Steel, U.S. Pat. #3178324, April 1965.

47. C. N. Sastry, Effect of Microstructure and Internal Hydrogen on Fatigue Crack Propagation of Ultrahigh Strength Steels, Ph.D. Thesis, Oregon Graduate Center, Beaverton, OR, September 1980.

48. F. B. Pickering, Proc. 4th Int. Conf. on Electron Microscopy, Berlin, East Germany, September 1958, Springer-Verlag(Berlin), 1(1960)626.

49. L. Habraken, ibid., 621.

50. R. M. Fisher, ibid., 579.

51. First Prog. Rep. of Sub-Comm. XI, ASTM Comm. E-4, Proc. ASTM, 50(1950)444.

52. Second Prog. Rep. of Sub-Comm. XI, ASTM Comm. E-4, Proc. ASTM, 52(1952)543.

53. Fourth Prog. Rep. of Sub-comm. XI, ASTM Comm. E-4, Proc. ASTM, 54(1954)568.

54. P. M. Kelly and J. Nutting, Proc. Roy. Soc. (London), 259A(1960)45.

55. A. R. Marder and G. Krauss, Trans. ASM, 60(1967)651.

56. S. K. Das and G. Thomas, Metall. Trans., 1A(1970)325.

57. N. C. Law, R. P. Howell and D. V. Edmonds, Mat. Sci., 13(1979)507.

58. J. M. Chilton, C. J. Barton and G. R. Speich, JISI, 208(1970)184.

59. B. V. N. Rao, J. Y. Koo and G. Thomas, Proc. 33rd Ann. Meet. of EMSA, Las Vegas, NV, August 1975, G. W. Bailey (Ed.), Claitor's Publishing Div. (Baton Rouge), 1975, 30.

60. M. F. Carlson, B. V. N. Rao and G. Thomas, Metall. Trans., 10A (1979)1273.

61. A. S. Sastri and D. R. F. West, JISI, 203(1965)138.

62. A. Ankara, JISI, 208(1970)819.

63. T. Maki, S. Shimooka, M. Umemoto and I. Tamura, Metall. Trans., 2A(1971)2944.

64. J. D. Bolton, E. R. Petty and E. B. Allen, JISI, 207(1969)1314.

65. G. Thomas, Metall. Trans., 2A(1971)2373.

66. T. Ogura, C. J. McMahon, H. C. Feng and V. Vitec, Acta Met., 1 (1978)3.

67. G. Krauss and W. Pitsch, Acta Met., 12(1964)278.

68. D. Hull, Acta Met., 8(1960)11.

69. M. Bevis, P.C. Rowlands and A. F. Acton, Trans. AIME, 242(1968)1555.

70. P. M. Kelly, Trans. AIME, 233(1965)264.

71. M. A. Jawson and D. B. Dove, Acta Cryst., 9(1956)621.

72. G. Kurdjumov and G. Sachs, Z. Physik, 64(1930)325.

73. Z. Nishiyama, Sci. Rep., IRTU, Tohoku Univ. (Japan), 23(1934)638.

74. G. Wassermann, Archiv. Fur das Eisenhutt, 16(1933)647.

75. G. Thomas and B. V. N. Rao, Proc. Int. Conf. on Martensitic Transformations, Keive, Naukora, USSR, May 1977, 1978, 57 (Morphology, Crystallography and Formation of Dislocated (Lath) Martensites in Steels, Rep. #LBL-6242, Lawrence Berkeley Laboratory, Univ. of California, Berkeley, CA, May 1977).

76. G. Thomas, Metall. Trans., 9A(1978)439.

77. B. V. N. Rao, Metall. Trans., 10A(1979)645.

78. K. H. Jack, JISI, 169(1951)26.

79. Yu. A. Bagaryatskii, Dokl. Akad. Nauk., USSR, 73(1950)1161.

80. W. Pitsch, Acta Met., 10(1962)79.

81. C. N. Sastry, Proc. 37th Ann. Meet. of EMSA, San Antonio, TX, August 1979, G. W. Bailey (Ed.), Claitor's Publishing Div. (Baton Rouge), 1979, 644.

82. S. Murphy and A. Whiteman, Metall. Trans., 1A(1970)1469.

83. G. Y. Lai, Metall. Trans., 6A(1975)1469.

84. A. K. Seal and R. W. K. Honeycombe, JISI, 188(1958)9.

85. K. H. Khan and V. C. Kannan, Proc. 35th Ann. Meet. of EMSA, Boston, MA, August 1977, G. W. Bailey (Ed.), Claitor's Publishing Div. (Baton Rouge), 1977, 256.

86. A. Kamada, N. Koshizuka and T. Fumakoshi, Trans. ISI (Japan), 16(1976)407.

87. D. H. Huang and G. Thomas, Metall. Trans., 8A(1977)1661.

88. D. H. Huang, Bainitic Transformations in Steels, Ph.D. Thesis, Univ. of California, Berkeley, CA, May 1975.

89. F. R. Larson and F. L. Carr, Met. Prog., 85(1964)74.

90. J. Nunes, F. L. Carr and F. R. Larson, Techniques for the Direct Observation of Structure and Imperfections: Techniques of Metals Research (Vol. 2, Part 1), R. F. Bunshah (Ed.), Wiley (N.Y.), 2(1)(1968)379.

91. F. L. Carr, D. Biehler, A. Connolly, R. Dragen, J. Faller, O. Johari, R. Morais, M. T. Parker and R. H. Sailors, Symp. on Applications of Electron Microfractography to Materials Research: 73rd Ann. Meet. of ASTM, Rep. of ASTM E24.2 Task Group, ASTM STP 493, Toronto, Ont., Canada, June 1970, W. Wiebe (Ed.), ASTM (Philadelphia), 1971, 36.

92. T. Inoue, S. Matsuda, Y. Okamura and K. Aoki, Trans. Jpn. Inst. of Met., 11(1970)36.

93. C. D. Beachem, Metall. Trans., 4A(1973)1999.

94. T. B. Cox and J. R. Low, Metall. Trans., 5A(1974)1457.

95. A. Martens, Handbook of Testing Materials, Parts I and II, Wiley (N.Y.), 1889.

96. C. D. Beachem, Microscopic and Macroscopic Fundamentals (Vol. 1): Fracture - An Advanced Treatise, H. Liebowitz (Ed.), A.P. (N.Y.), 1(1968)243.

97. A. S. Tetelman and A. J. McEvily, Jr., Fracture of Structural Materials, J. H. Hollomon, J. E. Burke, B. Chalmers, R. L. Sproull and A. T. Toboisky (Eds.), Wiley (N.Y.), 1967.

98. D. E. Hodgson and A. S. Tetelman, Fracture 1969: Proc. 2nd Int. Conf. on Fracture, Brighton, England, April 1969, P. L. Pratt (Ed.), Chapman and Hall (London), 1969, 266.

99. D. H. Huang and G. Thomas, Metall. Trans., 2A(1971)1587.

100. W. S. Pellini, R. J. Goode, P. P. Puzak, E. A. Lange and R. W. Huber, Review of Concepts and Status of Procedures for Fracture-Safe Design of Complex Welded Structures Involving Metals of Low to Ultra-High Strength Levels, NRL Rep. #6300, Naval Research Laboratory, Washington, D.C., June 1965.

101. F. R. Larson and F. L. Carr, Trans. ASM, 55(1962)599.

102. F. L. Carr and F. R. Larson, Proc. ASTM, 62(1962)1210.

103. C. D. Beachem and R. M. N. Pelloux, ASTM Symp. on Fracture Toughness Testing and Its Applications: 67th Ann. Meet. of ASTM, Chicago, IL, June 1964, W. F. Brown, Jr. (Ed.), ASTM STP 381, ASTM (Philadelphia)1965, 210.

104. A. J. Edwards, NRL Rep., Naval Research Laboratory, Washington, D.C., November 1963.

105. R. A. Davis, G. A. Dreyer and W. C. Gallaughen, Corrosion, 20(1964)93.

106. W. A. Van der Sluys, Eng. Fr. Mech., 1(1969)447.

107. C. D. Beachem, Metall. Trans., 3A(1972)347.

108. M. T. Wang and R. W. Staehle, Proc. Int. Conf. on Hydrogen in Metals, Paris, France, May-June 1972, Paul Bastien (Ed.), Editions Science et Industrie (Paris), 1972, 342.

109. C. S. Carter, Eng. Fr. Mech., 3(1972)1.

110. P. R. Swann, NATO Sci. Comm. Res. Eval. Conf. on the Theory of Stress Corrosion Cracking in Alloys, Ericeira, Portugal, March-April 1971, J. C. Scully (Ed.), NATO Scientific Affairs Div. (Brussels), 1971, 113.

111. J. C. Scully, ibid., 127.

112. P. R. Swann and J. D. Embury, High Strength Materials, V. F. Zackay (Ed.), Wiley (N.Y.), 1965, 351.

113. P. M. Kelly and J. Nutting, JISI, 197(1961)199.

114. J. P. Naylor, Metall. Trans., 10A(1979)861.

115. M. J. Roberts and W. Jolley, Metall. Trans., 1A(1970)1389.

116. G. R. Speich and P. R. Swann, JISI, 203(1965)480.

117. M. J. Roberts, Metall. Trans., 1A(1970)3287.

118. R. O. Ritchie, L. C. E. Geniets and J. F. Knott, The Microstructure and Design of Alloys: Proc. Inst. of Met. and ISI 3rd Int. Conf. on the Strength of Metals and Alloys, Cambridge, England, August 1973, The Met. Soc. (London), 1(1974)124.

119. G. B. Olson and M. Cohen, Metall. Trans., 7A(1976)1905.

120. G. V. Kurdjumov and A. G. Khachaturyan, Acta Met., 23(1975)1077.

121. F. Lecrroisey and A. Pineau, Metall. Trans., 3A(1972)387.

122. O. Johari and G. Thomas, Trans. ASM, 58(1965)563.

123. I-Lin Cheng and G. Thomas, Metall. Trans., 3A(1972)503.

124. P. Pahuta, L. Hyspecka and K. Mazanee, Metall. Mat., 8(1970)259.

125. F. Habrovec, J. Skarek and P. Rys, JISI (London), 205(1967)861.

126. K. J. Irvine and F. B. Pickering, Proc. BISRA and ISI Conf. on Physical Properties of Martensite and Bainite, Scarborough, England, May 1965, ISI Spec. Rep. #93, C. H. Inman (Ed.), Percy Lund, Humphries (London), 1965, 110.

127. P. M. Kelly and J. Nutting, ibid, 166.

128. P. G. Winchell and M. Cohen, Trans. ASM, 55(1962)347.

129. M. Cohen, JISI, 201(1963)833.

130. F. R. N. Nabarro, Proc. Phy. Soc., 59(1947)256.

131. L. Heslop and N. J. Petch, Phil. Mag., 1(1956)866.

132. J. F. W. Bishop, J. Mech. Phy. Sol., 3(1955)259.

133. A. R. Cox, Trans. Jpn. Inst. of Met., 9(1968)118.

134. C. E. Lacy and M. Gensamer, Trans. ASM, 32(1944)88.

135. W. C. Leslie and R. J. Sober, Trans. ASM, 60(1967)459.

136. D. W. Smith and R. F. Hehemann, JISI, 6(1971)476.

137. R. W.K. Honeycombe, Structure and Strength of Alloys, Climax Moly. Co., (London), 1974.

138. W. R. Tyson, Acta Met., 11(1963)61.

139. T. Kunitake, Trans. I.S.I. (Japan), 7(1967)254.

140. G. S. Ansell, Precipitation from Iron Base Alloys, G. R. Speich (Ed.), Gordon and Breach (N.Y.), 1965, 231.

141. E. Orowan, Symp. on Internal Stresses in Metals and Alloys, London, October 1947, Inst. of Met. (London), 1948, 47, 451.

142. A. Kelly and R. B. Nicholson, Precipitation Hardening, Prog. Mat. Sci., B. Chalmers (Ed.), Pergamon Press (N.Y.), 10(1963)149.

143. E. O. Hall, Proc. Phy. Soc., 64B(1951)747.

144. N. J. Petch, JISI, 174(1953)25.

145. W. B. Morrison, JISI, 201(1963)317.

146. G. E. Dieter, Mechanical Metallurgy, B. J. Clark and M. Gardner (Eds.), McGraw-Hill (N.Y.), 1961, 186.

147. I. Codd and N. J. Petch, Phil. Mag., 42(1951)351.

148. J. D. Baird, JISI, 204(1966)44.

149. D. H. Warrington, JISI, 201(1963)610.

150. G. Langford and M. Cohen, Trans. ASM, 62(1969)623.

151. R. P. Carreker, Jr. and W. R. Hibbard, Jr., Trans. AIME, 209 (1957)1157.

152. F. C. Quigley and P. J. Ahearn, Modern Castings, 47(1965)813.

153. M. Gensamer, Trans. ASM, 36(1945)30.

154. B. I. Edelson and W. M. Baldwin, Jr., Trans. ASM, 55(1962)230.

155. E. C. Bain and H. W. Paxton, Alloying Elements in Steel (2nd ed.), ASM (Metals Park), 1961.

156. E. J. Janitzky and M. Baeyertz, Metals Handbook (6th ed.), ASM (Metals Park), 1939, 519.

157. M. F. Hawkes, Iron Age, 152(1943)49.

158. J. Gurland, Trans. AIME, 227(1963)1146.

159. M. F. Ashby, Phil. Mag., 14(1966)1157.

160. H. C. Rogers, Proc. ASM Sem. on Ductility, October 1967, H. W. Paxton (Ed.), ASM (Metals Park), 1968, 31.

161. D. Dulieu, The Microstructure and Design of Alloys: Proc. 3rd Int. Conf. on the Strength of Metals and Alloys, Cambridge, England, August 1973, The Met. Soc. (London), 2(1974)383.

162. S. Ensha and A. S. Tetelman, The Effect of Microstructure on the Fracture Toughness of Low Alloy Steels, UCLA Tech. Rep. #14 UCLA-ENG-7435, Univ. of California, Los Angeles, CA, May 1974.

163. M. F. Carlson, B. V. N. Rao, R. O. Ritchie and G. Thomas, Proc. 4th Int. Conf. on the Strength of Metals and Alloys, Nancy, France, August-September 1976, Laboratoire de Physique du Solide (Nancy), 2(1976)509.

164. R. O. Ritchie, B. Francis and W. L. Server, Metall. Trans., 8A(1977)1197.

165. R. O. Ritchie, Proc. Ann. Meet. of AIME, 1978, 54.

166. T. R. Wilshaw, C. A. Rau and A. S. Tetelman, Eng. Fr. Mech., 1(1968)191.

167. J. Malkin and A. S. Tetelman, Eng. Fr. Mech. 3(1971)151.

168. R. O. Ritchie, J. F. Knott and J. R. Rice, J. Mech. Phy. Sol., 21(1973)395.

169. J. R. Griffiths and D. R. J. Owen, J. Mech. Phy. Sol., 19(1971)149.

170. J. M. Krafft, App. Mat. Res., 3(1964)88.

171. J. R. Rice and M. A. Johnson, Inelastic Behaviour of Solids, M. F. Kanninen, W. F. Adler, A. R. Rosenfield and R. I. Jaffee (Eds.), McGraw-Hill (N.Y.), 1970.

172. K. H. Schwalbe, Eng. Fr. Mech., 9(1977)795.

173. G. T. Hahn and A. R. Rosenfield, ASTM Symp. on Applications Related Phenomena in Titanium and its Alloys, Los Angeles, April 1967, ASTM STP 432, ASTM (Philadelphia), 1968.

174. G. T. Hahn and A. R. Rosenfield, Trans. ASM, 59(1966)909.

175. G. T. Hahn, R. G. Hoagland and A. R. Rosenfield, Metall. Trans., 2A(1971)537.

176. J. H. Mulherin and H. Rosenthal, Metall. Trans., 2A(1971)427.

177. J. R. Low, Jr., R. H. Van Stone and R. H. Merchant, NASA TR#2, NASA Grant NGR-39-087-003, 1972.

178. A. J. Birkle, R. P. Wei and G. E. Pellissier, Trans. ASM, 59(1966)981.

179. A. H. Priest, British Steel Corp. and ISI Proc. Conf. on the Effect of Second Phase Particles on the Mechanical Properties of Steel, Scarborough, England, March 1971, M.J. May (Ed.), ISI (London), 1971, 134.

180. H. C. Burghard, Jr., Metall. Trans., 5A(1974)2083.

181. T. B. Cox, An Investigation of the Plastic Fracture of High-Strength Steels, NASA Grant NGR-39-087-003, Rep. #NSRDC-4296, Naval Ship Research and Development Center, Annapolis, MD, June 1974.

182. G. T. Hahn, M. F. Kanninen and A. R. Rosenfield, Amer. Rev. Mat. Sci., 2(1972)381.

183. T. Gladman, B. Holmes and I. D. McIvor, British Steel Corp. and ISI Proc. Conf. on the Effect of Second Phase Particles on the Mechanical Properties of Steel, Scarborough, England, March 1971, M .J. May (Ed.), ISI(London), 1971, 68.

184. S. H. Hwang, Sungho Jin and J. W. Morris, Metall. Trans., 6A(1975)2015.

185. J. Koo, B. V. N. Rao and G. Thomas, Met. Prog., 116(1979)66.

186. V. F. Zackay, Fundamental Considerations in the Design of Ferrous Alloys, Rep. #LBL-3595, Lawrence Berkeley Laboratory, Univ. of California, Berkeley, CA, 1975.

187. D. Webster, Trans. ASM, 61(1968)816.

188. S. D. Antolovich, A. Saxena and G. R. Chanani, Metall. Trans., 5A(1974)623.

189. F. A. McClintock and G. R. Irwin, ASTM Symp. on Fracture Toughness Testing and Its Applications: 67th Ann. Meet. of ASTM, Chicago, IL, June 1964, W. F. Brown, Jr. (Ed.), ASTM STP 381, ASTM (Philadelphia), 1965, 84.

190. D. Webster, Metall. Trans., 2A(1971)2097.

191. W. W. Gerberich and J. P. Birat, Int. J. Fr. Mech., 7(1971)108.

192. S. D. Antolovich and B. Singh, Metall. Trans., 2A(1971)2135.

193. Z. Nishiyama, Martensitic Transformations, M. E. Fine, M. Meshii and C. M. Wayman (Eds.), A. P. (N.Y.), 1978.

194. W. J. Barrett and A. R. Troiano, Trans. AIME, 175(1948)175.

195. M. R. Meyerson and S. J. Rosenberg, J. Res. Nat. Bur. Std., 55(1955)177.

196. W. C. Leslie and R. L. Miller, Trans. ASM, 57(1964)972.

197. M. Izumiyama, Sci. Rep., IRTU, Tohoku Univ. (Japan), 14(1962)11.

198. G. Krauss, Jr. and M. Cohen, Trans. AIME, 224(1962)1212.

199. G. Krauss, Jr. and M. Cohen, Trans. AIME, 227(1963)278.

200. Z. Nishiyama, J. Jpn. Inst. Met., 2(1938)202.

201. Y. Imami and M. Izumiyama, Sci. Rep., IRTU, Tohoku Univ. (Japan), 11(1959)393.

202. A. R. Entwisle and J. A. Feeney, Inst. Met. Monogr, Rep. Ser. #33, 1969, 156.

203. G. Y. Lai, Mat. Sci. and Eng., 19(1975)153.

204. W. Steven and A. G. Haynes, JISI, 183(1956)349.

205. G. T. Hahn, B. L. Averbach, W. S. Owen and M. Cohen, Fracture: Proc. Int. Conf. on the Atomic Mechanisms of Fracture, Swampscott, MA, April 1959, B. L. Averbach, D. K. Felbeck, G. T. Hahn and D. A. Thomas (Eds.), MIT Press (Cambridge), Wiley (N.Y.), 1959, 91.

206. W. S. Owen, Yield and Fracture of Mild Steel, ISI Spec. Rep. #81, London, England, 1963, 1.

207. D. Guttmann and P. R.. Krahe, Mem. Sci. Rev. Metall., 7(1973)559.

208. C. A. Apple, R. N. Caron and G. Krauss, Metall. Trans., 5A(1974)593.

209. S. Matsuda, T. Inoue and M. Ogasawara, Trans. Jpn. Inst. of Met., 9(1968)343.

210. N. F. Mott and F. R. N. Nabarro, Dislocation Theory and Transient Creep: Report of a Conf. on the Strength of Solids, Phy. Soc. (London), 1948, 1.

211. G. Sandoz, Metall. Trans., 3A(1972)1169.

212. W. W. Gerberich and Y. T. Chen, Metall. Trans., 6A(1975)271.

213. D. P. Dautovich and S. Floreen, Proc. Int. Conf. on Stress Corrosion Cracking and Hydrogen Embrittlement in Iron Base Alloys, Unieux-Firminy, France, June 1973, R. W. Staehle, J. Hochmann, R. D. McCright and J. E. Slater (Eds.), NACE (Houston), NACE-5, 1977, 798.

214. A. J. Wang, Quart. App. Mech., 11(1954)427.

215. D. P. Dautovich and S. Floreen, Metall. Trans., 4A(1973)2627.

216. T. Boniszewski and F. Watkinson, Met. and Mat., 7(1973)90.

217. T. Boniszewski and R. G. Baker, Brit. Weld. J., 12(1965)349.

218. F. Watkinson, R. G. Baker and H. F. Tremlett, Brit. Weld. J., 10(1963)54.

219. R. G. Davis and C. L. Magee, Metall. Trans., 1A(1970)2927.

220. W. S. Owen, E. A. Wilson and T. Bell, High Strength Materials, V. F. Zackay (Ed.), Wiley (N.Y.), 1965, 167.

221. A. H. Cottrell, Trans. Inst. Weld., 7(1944)69.

222. A. P. Miodownik, Proc. Int. Conf. on Stress Corrosion Cracking and Hydrogen Embrittlement in Iron Base Alloys, Unieux-Firminy, France, June 1973, R. W. Staehle, J. Hochmann, R. D. McCright and J. E. Slater (Eds.), NACE (Houston), NACE-5, 1977, 272.

223. B. D. Craig, Acta. Met., 25(1977)1027.

224. P. C. Hughes, I.R. Lambern and B. B. Liebert, JISI, 203(1965)728.

225. A. W. Thompson, Proc. Conf. on Environmental Degradation of Engineering Materials, Blacksburg, VA, October 1977, M. R. Louthan, Jr. and R. P. McNitt (Eds.), Virginia Tech. (Blacksburg), 1977, 3.

226. R. A. Oriani, Proc. Conf. on Fundamental Aspects of Stress Corrosion Cracking, Columbus, OH, September 1967, R. W. Staehle (Ed.), NACE (Houston), 1967, 32.

227. J. K. Tien, Proc. Int. Conf. on the Effect of Hydrogen on Behaviour of Materials, Moran, WY, September 1975, A. W. Thompson and I. M. Bernstein (Eds.), TMS AIME (N.Y.), 1976, 309.

228. D. Broek, Elementary Engineering Fracture Mechanics, Noordhoff International Publishing (Layden), 1974, 91.

229. C. Zapffe and C. Sims, Trans. AIME, 145(1941)225.

230. F. J. deKazinsky, JISI, 177(1954)83.

231. F. Garofalo, Y. T. Chen and R. Ambegaokar, Acta Met., 8(1960)504.

232. B. A. Bilby and J. Hewitt, Acta Met., 10(1962)587.

233. A. S. Tetelman and W. D. Robertson, Acta Met., 11(1963)415.

234. G. G. Hancock and H. H. Johnson, Trans. AIME, 236(1966)513.

235. G. E. Kerns, M. T. Wang and R. W. Staehle, Proc. Int. Conf. on Stress Corrosion Cracking and Hydrogen Embrittlement in Iron Base Alloys, Unieux-Firminy, France, June 1973, R. W. Staehle, J. Hochmann, R. D. McCright and J. E. Slater (Eds.), NACE (Houston), NACE-5, 1977, 700.

236. R. A. Oriani, Ber. Bunsenges. Phy. Chem., 76(1972)848.

237. R. A. Oriani, Proc. Int. Conf. on Stress Corrosion Cracking and Hydrogen Embrittlement in Iron Base Alloys, Unieux-Firminy, France, June 1973, R. W. Staehle, J. Hochmann, R. D. McCright and J. E. Slater (Eds.), NACE (Houston), NACE-5, 1977, 351.

238. S. K. Banerji, C. J. McMahon and H. C. Feng, Metall. Trans., 9A(1978)237.

239. A. R. Troiano, Trans. ASM, 52(1960)54.

240. P. Blanchard and A. R. Troiano, Mem. Sci. Rev. Metall., 57(1960)409.

241. R. P. Frohmberg, W. J. Barnett and A. R. Troiano, Trans. ASM, 47(1955)892.

242. E. R. Slaughter, E. E. Fletcher, A. R. Elsea and G. K. Manning, An Investigation of the Effects of Hydrogen on the Brittle Failure of High-Strength Steels, WADC Tech. Rep. #56-83, Wright Air Development Center, Wright Patterson Air Force Base, Dayton, OH, April 1956.

243. R. J. Richards, S. Purushothaman, J. K. Tien, J. D. Frandsen and O. Buck, Metall. Trans., 9A(1978)1107.

244. J. R. Rice, Proc. Int. Conf. on Stress Corrosion Cracking and Hydrogen Embrittlement in Iron Base Alloys, Unieux-Firminy, France, June 1973, R. W. Staehle, J. Hochmann, R. D. McCright and J. E. Slater (Eds.), NACE (Houston), NACE-5, 1977, 11.

245. C. J. McMahon, Jr., C. L. Briant and S. K. Banerji, Fracture 1977: Proc. 4th Int. Conf. on Fracture - Advances in Research Strength and Fracture of Materials, Univ. of Waterloo, Canada, June 1977, D.M.R. Taplin (Ed.), Pergamon Press (N.Y.), 1(1977)363.

246. K. Yoshino and C. J. McMahon, Jr., Metall. Trans., 5A(1974)363.

247. M. E. Fine and H. L. Marcus, Metall. Trans., 2A(1971)1473.

248. K. T. Aust, R. E. Hanneman, P. Niessen and J. H. Westbrook, Acta Met., 16(1968)291.

249. C. L. Briant and S. K. Banerji, Metall. Trans., 10A(1979)1729.

250. G. Sandoz, Stress Corrosion Cracking in High Strength Steels and in Titanium and Aluminum Alloys, B. F. Brown (Ed.), NRL (Washington, D. C.), 1972, 79.

251. D. Webster, Trans. ASM, 62(1969)759.

252. R. D. Goolsby, W. E. Wood, E. R. Parker and V. F. Zackay, Electron Microscopy and Structure of Materials: Proc. 5th Int. Mat. Symp. on the Structure and Properties of Materials - Techniques and Applications of Electron Microscopy, Berkeley, CA, September 1971, G. Thomas (Ed.), Univ. of Cal. Press (Berkeley), 1972, 798.

253. R. M. Horn and R. O. Ritchie, Metall. Trans., 9A(1978)1039.

254. H. L. Dunegan and A. S. Tetelman, Eng. Fr. Mech., 2(1971)387.

255. H. H. Chaskelis, W. H. Cullen and J. M. Krafft, Fracture Toughness and Slow-Stable Cracking: ASTM Committee E-24 7th Nat. Symp. on Fracture Mechanics, Part-1, College Park, MD, August 1973, ASTM STP 559, ASTM (Philadelphia), 1974, 31.

256. C. E. Hartbower, W. W. Gerberich and P. O. Crimmins, Weld. J., 47(1968)1.

257. D. G. Chakrapant and E. N. Pugh, Metall. Trans., 6A(1975)1155.

258. H. N. G. Wadley and C. B. Scruby, Acta Met., 27(1979)613.

259. P. McIntyre and G. Green, Brit. J. of NDT, 20(1978)135.

260. W. W. Gerberich and C. E. Hartbower, Proc. Conf. on Fundamental Aspects of Stress Corrosion Cracking, Columbus, OH, September 1967, R. W. Staehle (Ed.), NACE (Houston), 1967, 420.

261. C. E. Hartbower, W. G. Reuter, C. F. Morais and P. P. Crimmins, ASTM Symp. on Acoustic Emission, Bal Harbour, FL, December 1971, R. G. Liptai (Ed.), ASTM STP 505, ASTM (Philadelphia), 1972, 187.

262. H. R. Dunegan and A. S. Tetelman, Res. Dev., 22(1971)20.

263. R. W. Staehle and G. E. Kerns, Specialists Meet. on Stress Corrosion Testing Methods, AGARD Conf. Proc. #98, NATO Advisory Group for Aerospace Research and Development, Paris, France, January 1972, 182 (Paper presented at the Structures and Materials Panel 33rd Meet., Brussels, Belgium, October 1971.).

264. C. E. Hartbower, W. G. Reuter and P. P. Crimmins, Mechanisms of Slow Crack Growth in High-Strength Steels and Titanium, AFML Tech. Rep. #AFML-TR-67-26, Vol. 2, Aerojet-Gen. Corp. for Met. and Cer. Div., Sacramento, CA, June 1969.

265. C. E. Hartbower, W. W. Gerberich and P. P. Crimmins, Mechanisms of Slow Crack Growth in High-Strength Steels, AFML Tech. Rep. #AFML-TR-67-26, Vol. 1, Aerojet-Gen. Corp. for Met. and Cer. Div., Sacramento, CA, February 1967.

266. W. J. Zarella, Jr., Stress Wave Emission from Non- and Irradiated Hydrogen Embrittled Reactor Steels, M. S. Thesis, Univ. of Idaho, Moscow, ID, May 1969.

267. T. R. Tucker and C. T. Fujii, Acoustic Emissions and Stress-Corrosion Cracking in High-Strength Alloys, NRL Mem. Rep. #2879, Naval Research Laboratory, Washington, D.C., August 1974.

268. D. O. Harris, A. S. Tetelman and F. A. I. Darwish, ASTM Symp. on Acoustic Emission, Bal Harbour, FL, December 1971, R. G. Liptai (Ed.), ASTM STP 505, ASTM (Philadelphia), 1972, 238.

269. A. A. Pollock, Acoustics and Vibrations Progress, R. W. B. Stephens and H. G. Leventhal (Eds.), Chapman and Hall (London), 1(1974)63.

270. A. A. Pollock, Non-destructive Testing, 6(1973)264.

271. J. F. Knott, Fundamentals of Fracture Mechanics, Wiley (N.Y.), 1973.

272. R. C. Bill and J. R. Frederick, Use of Acoustic Emission in Nondestructive Testing: 4th Semiannual Rep. #01971-4-P, March 1 - August 31, 1970, Advanced Research Projects Agency Contract F33615-68-C-17703, Univ. of Michigan, Ann Arbor, MI, December 1970.

273. A. J. McEvily, R. M. Bush, F. W. Shaller and D. J. Schmatz, Trans. ASM, 56(1963)753.

274. G. Venkataraman and A. K. Mallik, Mat. Sci., Eng., 16(1974)133.

275. F. Habrovec, J. Skarek and P. Rys, Metall. Mat., 10(1972)129.

276. F. Habrovec, J. Skarek and P. Rys, Hutnicke Listy. 24(1969)671.

277. B. V. N. Rao and G. Thomas, Mat. Sci. and Eng., 20(1975)195.

278. B. V. N. Rao, R. W. Miller and G. Thomas, Heat Treatment '76: Proc. 16th Int. Heat Treatment Conf., Stratford-upon-Avon, May 1976, The Met. Soc. (London), 1977, 75.

279. G. Thomas and Yen-Lung Chen, Metall. Trans., 12A(1981)933.

280. W. F. Brown, Jr. and J. E. Srawley, Plane Strain Crack Toughness Testing of High-Strength Metallic Materials, B. F. Brown (Ed.), ASTM STP 410, ASTM (Philadelphia), 1966.

281. D. C. Drucker, Microscopic and Macroscopic Fundamentals (Vol. 1): Fracture - An Advanced Treatise, H. Liebowitz (Ed.), A.P. (N.Y.), 1(1968)473.

282. N. J. Petch, Phil. Mag., 1(1956)331.

283. B. M. W. Trapnell, Proc. Roy. Soc. (London), A218(1953)566.

284. G. E. Kerns, Stress Corrosion Cracking in Gaseous and Aqueous Environments, Ph.D. Thesis, Ohio State Univ., Columbus, OH, 1973.

285. V. R. Sawicki, Jr., Hydrogen Induced Cracking in a High-Strength Steel, Ph.D. Thesis, Cornell Univ., Ithaca, N.Y., 1971.

286. N. J. Petch and P. Stables, Nature, 169(1952)842.

287. H. R. Smith and D. E. Piper, Stress Corrosion Cracking in High-Strength Steels and in Titanium and Aluminum Alloys, B. F. Brown (Ed.), NRL (Washington, D.C.), 1972, 17.

APPENDIX I

METHOD FOR CALIBRATION OF INSTRUMENTED TUP SYSTEM

Compare the impact energy (W_t) recorded on the instrument dial with the energy as calculated from the area under the load-time trace on an oscilloscope, where the energy (W_c) in ft. lbs. is related to the area (A) in sq. inch under the trace by the expression:

$$W_c = AC_xC_yP_dV_{eff}/C_a$$

where C_x is the time sweep rate/div., C_y is the vertical sensitivity/div., V_{eff} is the effective velocity of the tup during the impact [$= (V_e + V_i)/2$, where V_e and V_i are the final and initial velocities of the tup], P_d is the proportionality constant, having the units of lbs/V, $V_e = \sqrt{2gh_e}$ and $V_i = \sqrt{2gh_i}$, where g = acceleration due to gravity and h_i and h_e are the drop height and rise height of the hammer before and after impact, respectivley.

Ideally, a material with an impact energy value of about 20 ft. lbs. (27 Nm) is chosen for this calibration purpose, since at higher values, V_{eff} is not equal to $(V_e + V_i)/2$ and at lower values, error in measuring the area under load-time trace would increase.

APPENDIX II

PROGRAM FOR EVALUATING CRACK VELOCITY AND VARIOUS A.E. RATES

```
C       This program reads data from KISFIL and calculates
          DA/DT,DC/DT,DE/DT,DC/DA,DE/DA,DC/DE and AVK.
C       Slope is evaluated only if DA .GE. 0.005".
C       Compliance equation is valid upto A/W=0.81.
C       When x-axis full range is 1 hr., scale factor is 14.0625.
C       When y-axis full range is 100,000 counts, scale factor is
          390.625.
C       When y-axis full range is 16,000 events, scale factor is
          62.5.
C       For 0.005"/V COD output, scale factor is 0.00019531.
        DIMENSION T(2000),V(2000),C(2000),E(2000)
        DIMENSION A(2000),K(2000)
        REAL G1,G2,G3,AOW1,AOW2,AOW3,AOW4,AOW,K,COMP
        REAL DA,DT,DAT,DCT,DET,AVK,DCA,DEA,DCE
        CALL SEARCH (1,'KISFIL',1,0)
        CALL SEARCH (2,'KISOU1',2,0)
        CALL SEARCH (2,'KISOU2',3,0)
        WRITE (1,10)
10      FORMAT ('ENTER LOAD IN 0000.00 FORMAT')
        READ (1,20)P
20      FORMAT (F7.2)
        WRITE (1,30)
30      FORMAT ('ENTER THICKNESS IN 0.000 FORMAT')
        READ (1,40)B
40      FORMAT (F5.3)
        WRITE (1,50)
50      FORMAT ('ENTER TIME INTERVAL IN 14.06250 FORMAT')
        READ (1,60)TI
60      FORMAT (F8.5)
        WRITE (1,70)
70      FORMAT ('ENTER COUNT INTERVAL IN 390.6250 FORMAT')
        READ (1,80)CI
80      FORMAT (F8.4)
        WRITE (1,90)
90      FORMAT ('ENTER EVENT INTERVAL IN 62.5000 FORMAT')
        READ (1,100)EI
100     FORMAT (F7.4)
        WRITE (1,110)
110     FORMAT ('ENTER COD INTERVAL IN 00.00019531 FORMAT')
```

```
      READ (1,120)VI
120   FORMAT (F11.8)
      WRITE (1,130)
130   FORMAT ('ENTER CODDIFF IN 00.0000000 FORMAT')
      READ (1,140)VD
140   FORMAT (F10.7)
      WRITE (1,150)
150   FORMAT ('INPUT NUMBER OF DATA POINTS IN 0000 FORMAT')
      READ (1,200)ID
200   FORMAT (4I5)
C     Read input file one line at a time and calculate A(I)
       and K(I).
      I=1
250   READ (5,*,END=400,ERR=950)T(I),V(I),C(I),E(I)
      T(I)=T(I)*TI
      C(I)=C(I)*CI
      E(I)=E(I)*EI
      V(I)=V(I)*(VI-VD)
      G=30.0E+06
      COMP=(V(I)*B*(G/100))/(P)
      IF (COMP .LE. 2.5) GO TO 300
      AOW=0.49+(0.157E-02)*COMP*100-(0.213E-01)*COMP**2
      GO TO 350
300   CONTINUE
      AOW1=0.15136+8.70914E-01*COMP
      AOW2=-5.70479E-01*COMP**2
      AOW3=1.83754E-01*COMP**3
      AOW4=-2.26238E-02*COMP**4
      AOW=AOW1+AOW2+AOW3+AOW4
350   CONTINUE
      A(I)=AOW*2.0
      G1=(29.6*AOW**0.5)-(185.5*AOW**1.5)
      G2=(655.7*AOW**2.5)-(1017.0*AOW**3.5)
      G3=(638.9*AOW**4.5)
      K(I)=((G1+G2+G3)*P)/((1.414*B)*1000)
      I=I+1
      GO TO 250
400   CONTINUE
      WRITE (1,450)I
450   FORMAT (I4)
C     Calculate DA and compute DA/DT, etc.
      M=1
500   CONTINUE
      I=M
      J=M
550   DA=A(J+1)-A(M)
      IF ((J+1) .GE. ID) GO TO 900
```

```
      IF (DA .GE. 0.005) GO TO 600
      J=J+1
      GO TO 550
600   CONTINUE
      DT=(T(J+1)-T(I))
      DAT=(A(J+1)-A(I))/DT
      DCT=(C(J+1)-C(I))/DT
      DET=(E(J+1)-E(I))/DT
      DCA=DCT/DAT
      DEA=DET/DAT
      IF (DET .EQ. 0) GO TO 650
      DCE=DCT/DET
      AVK=(K(J+1)+K(I))/2.0
      GO TO 700
650   CONTINUE
      DCE=00000.000
700   WRITE (6,750)K(I),T(I),A(I),E(I),C(I)
750   FORMAT (F6.2,1X,F10.1,1X,F7.5,1X,F11.0,1X,F12.0)
      WRITE (7,800)AVK,DAT,DET,DCT,DEA,DCA,DCE
800   FORMAT (F6.2,1X,F8.7,1X,F9.3,1X,F10.3,1X,
        F11.0,1X,F12.0,1X,F9.3)
      M=J+1
      IF (M .GE. ID) GO TO 900
      WRITE (1,850)M
850   FORMAT (I6)
      GO TO 500
900   CONTINUE
      CALL SEARCH (4,0,1,0)
      CALL SEARCH (4,0,2,0)
      CALL SEARCH (4,0,3,0)
C     Error Message
950   WRITE (1,1000)I
1000  FORMAT (I4)
      CALL EXIT
      END
```

APPENDIX III

IMAGE-S.A.D. ROTATION ANGLE CALIBRATION

α-MoO_3 single crystals were prepared by heating ammonium molybdate to red heat in a crucible and washing small crystals from the lid into an aqueous suspension. A drop of this was dried on a grid covered with a carbon support film. MoO_3 is pseudoorthorhombic and forms as a ribbon with long edges parallel to $\langle 001 \rangle$ and surface normal to $\langle 010 \rangle$. A series of double exposed pictures were produced (Figure A-1), each with a S.A.D. pattern from a thin crystal and the image of the crystal superimposed at a fixed magnification. The (010) spot in the S.A.D. pattern was indexed, since d_{010} (0.0156 µin or 3.966 Å), and the camera constant (0.0057 inµin or 37 mmÅ) for these specific conditions (secondary electron accelerating voltage of 100 kV, projector lens current of 130 mA, objective lens current of 127 mA, and pole piece number 2 corresponding to 66.9 mils or 1.7 mm diameter) are known. The angle (φ) between [001] direction thus determined from the diffraction pattern and the long edge of MoO_3 crystal was measured for each set and plotted as a function of magnification (Figure A-2). From Figure A-2, for a magnification of 15,500x, the correction for image rotation was found to be 13.5° counterclockwise. When this correction was applied to Figure 3-51a and 3-71a, the direction of ε-carbide precipitation coincided with two variants of $\langle 112 \rangle_{\alpha'}$. The habit planes also coincided with $\{010\}_{\alpha'}$.

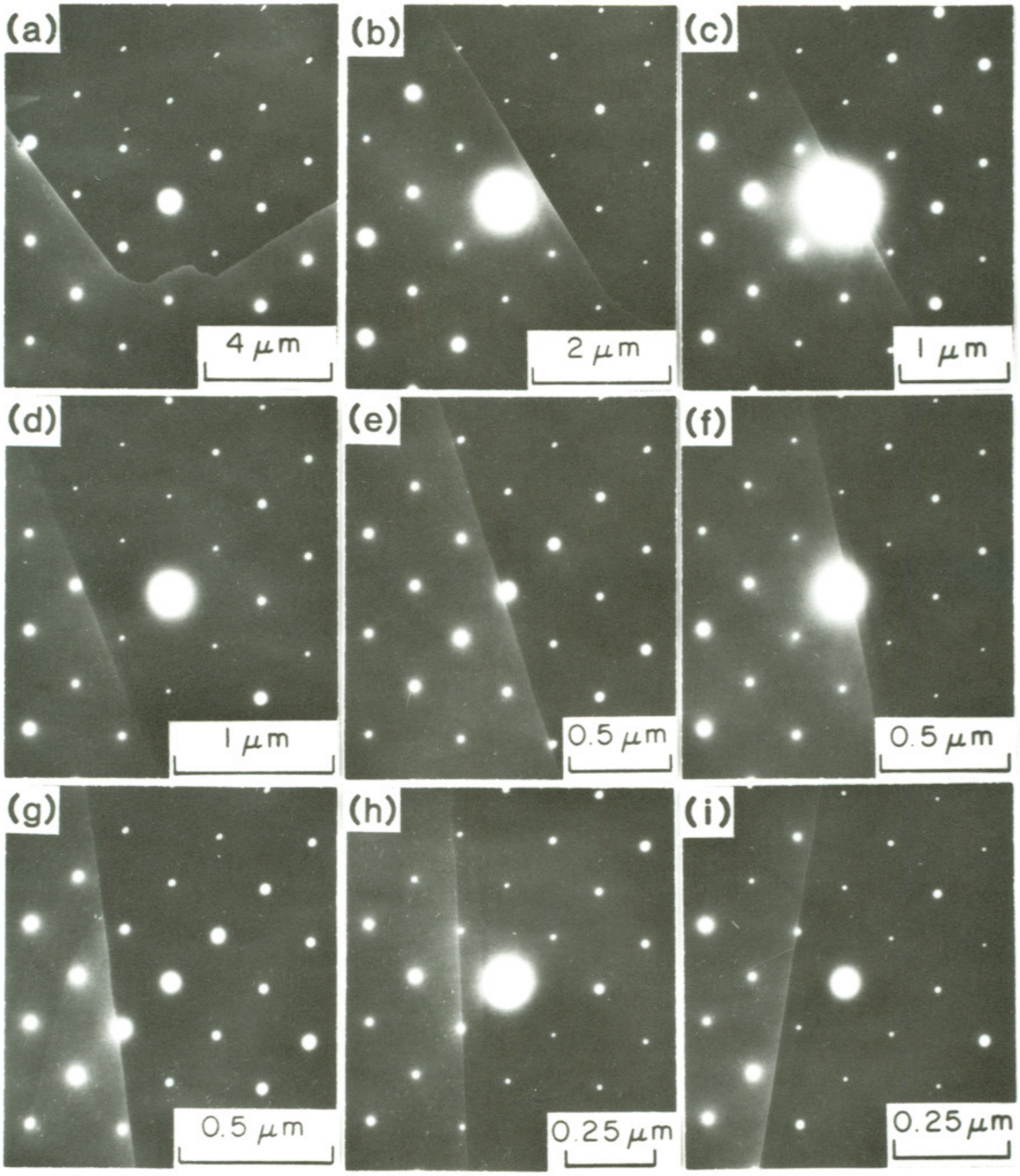

Figure A-1: BRIGHT FIELD TEM PICTURES, AT VARIOUS MAGNIFICATIONS, OF MoO_3 CRYSTAL, WITH S.A.D. PATTERN SUPERIMPOSED, FOR IMAGE-S.A.D. ROTATION ANGLE CALIBRATION.

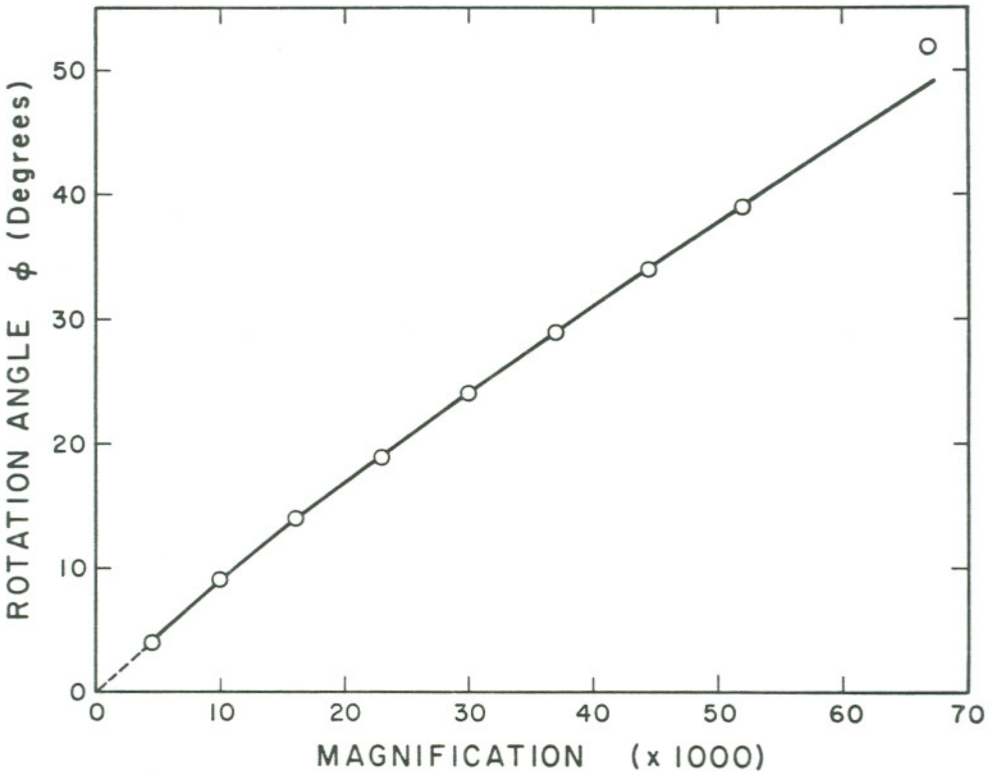

Figure A-2: ROTATION ANGLE AS A FUNCTION OF MAGNIFICATION.

APPENDIX IV

CALCULATION OF VOLUME FRACTION OF CARBIDES

Let m equal wt%, ρ equal density and f, the volume fraction.

Case 1: Theoretical volume fraction of cementite (assuming 0.41 wt. % carbon is available):

$$3Fe + C = Fe_3C$$

$$m_{Fe_3C} = \frac{0.41 \times 179.56}{12.01}$$

$$= \underline{6.13\%}$$

$$f_{Fe_3C} = \frac{\left[\dfrac{m_{Fe_3C}}{\rho_{Fe_3C}}\right]}{\left[\left(\dfrac{m_{Fe_3C}}{\rho_{Fe_3C}}\right) + \left(\dfrac{m_{Fe}}{\rho_{Fe}}\right)\right]}$$

$$= \underline{0.063}$$

Case 2: Total volume fraction of carbides (assuming only $Cr_{23}C_6$ and Fe_3C are present):

(a) $23\ Fe + 23\ Cr + 6C = (Fe,Cr)_{23}C_6$

From Table 3-1, $m_{Cr} = 0.79\%$.

Hence, $$m_{Cr_{23}C_6} = \frac{0.79 \times 2552.61}{1196}$$

$$= \underline{1.69\%}$$

$$\text{Amount of C used up} = \frac{0.79 \times 72.06}{1196}$$

$$= \underline{0.048\%}$$

(b) $$3Fe + C = Fe_3C$$

$$\text{Amount of C available} = 0.41 - 0.048$$

$$= 0.362\%$$

Hence, $$m_{Fe_3C} = \frac{0.362 \times 179.56}{12.01}$$

$$= \underline{5.41\%}$$

(c) $$f_{Cr_{23}C_6} = \frac{\left[\dfrac{m_{Cr_{23}C_6}}{\rho_{Cr_{23}C_6}}\right]}{\left[\left(\dfrac{m_{Cr_{23}C_6}}{\rho_{Cr_{23}C_6}}\right) + \left(\dfrac{m_{Fe_3C}}{\rho_{Fe_3C}}\right) + \left(\dfrac{m_{Fe}}{\rho_{Fe}}\right)\right]}$$

$$= \underline{0.019}$$

(d) Similarly,

$$f_{Fe_3C} = \frac{\left[\dfrac{m_{Fe_3C}}{\rho_{Fe_3C}}\right]}{\left[\left(\dfrac{m_{Fe_3C}}{\rho_{Fe_3C}}\right) + \left(\dfrac{m_{Cr_{23}C_6}}{\rho_{Cr_{23}C_6}}\right) + \left(\dfrac{m_{Fe}}{\rho_{Fe}}\right)\right]}$$

$$= \underline{0.056}$$

(e) Total volume fraction of precipitates

$$= f_{Cr_{23}C_6} + f_{Fe_3C}$$

$$= \underline{0.075}$$

<u>Note</u>: ρ_{Fe} = 7.86 gms/cc

ρ_{Fe_3C} = 7.67 gms/cc

$\rho_{Cr_{23}C_6}$ = 6.97 gms/cc

BIOGRAPHICAL NOTE

The author was born on March 5, 1953, in Ambattur, India. He attended the Universal Children's Convent School between 1956 and 1962, and Sir Ramaswamy Mudaliar High School between 1962 and 1968 and graduated with a S.S.L. Certificate in April 1968. He then joined the Loyola College at Madras, India, and obtained a B.S. degree in Physics with Distinction in March 1972. The author then moved to Bangalore, India and enrolled at the Indian Institute of Science, where he pursued the B.E. course in Metallurgy, graduating in June 1975 with Distinction and First Rank and obtaining the K. K. Malik Gold Medal for the best B.E. Student. He subsequently joined the Bharat Electronics Ltd. at Bangalore, India, as a Deputy Engineer, Materials Development, in which capacity he worked until August 1977. At that juncture, he accepted a Research Fellowship in Materials Science at the Oregon Graduate Center, Beaverton, Oregon, U.S.A., where he completed the requirements for the Doctor of Philosophy degree in March 1982. The author is now employed at the Oregon Graduate Center as a Research Scientist and Instructor.